Phase Transition and Conductivity Modification of Porous Silicon via CO_2 Laser Processing

Haifa Ali Ibrahim Qadi

Supervisors: Prof. Noel Healy

Prof. Jonathan Goss

Dr Benjamin Horrocks

School of Mathematics, Statistics and Physics

Newcastle University

This dissertation is submitted for the degree of

Doctor of Philosophy

March 2025

Abstract

This study investigates how laser irradiation modifies the optical, structural and electrical properties of porous silicon (PS). PS samples were fabricated by electrochemically etching p-type crystalline silicon wafers at a current density of 63 mA/cm^2 for 20 minutes. A continuous wave CO_2 laser (10.6 μm, 5–40 W) was then applied. A comprehensive suite of characterisation techniques, including scanning electron microscopy (SEM), atomic force microscopy (AFM), X-ray diffraction (XRD), X-ray photoelectron spectroscopy (XPS), secondary ion mass spectrometry (SIMS), Kelvin probe force microscopy (KPFM), Raman spectroscopy and current-voltage (I-V) measurements was used to analyse the samples before and after laser irradiation.

The unique interaction between the 10.6 μm CO_2 laser and PS is attributed to the significant IR absorption of PS at this wavelength, unlike bulk silicon. Upon laser irradiation, vibrational excitation triggers localised heating and the formation of heat zones, which induce two distinct stages. During the pre-melting consolidation stage, localised heating leads to partial melting of pore walls, causing adjacent pores to merge. As pores coalesce, the number of individual pores decreases, and the material between them consolidates, resulting in thicker pore walls, wider remaining pores, and an overall reduction in porosity. SEM and AFM analyses reveal a decrease in PS layer thickness and a smoother surface, with a roughness decreasing from 1.48 to 0.82 nm, approaching that of the underlying crystalline silicon substrate.

In the melting stage, where the temperature exceeds the melting point of the silicon, the AFM images show a complete pore collapse, indicating that the silicon has fully melted. Raman spectroscopy transitions from a broadened, redshifted spectrum with an additional lower-frequency peak to a sharp crystalline peak at 520 cm^{-1} (with a 2.8 cm^{-1} full width at half maximum) in the laser-modified regions. Increasing laser intensity and exposure further broadens the peak and induces a redshift, accompanied by the emergence of a secondary peak, suggesting stress effects. XRD confirms the reformation of a single-crystalline structure, while XPS analysis reveals significant oxidation and the formation of a silicon oxide layer in the laser-irradiated areas, a layer that when removed by HF etching restores the Raman spectral profile.

Electrical characterisation shows that the laser-processed areas exhibit metallic-like behaviour, as evidenced by I-V measurements and KPFM data indicating a high-work function network. This behaviour is attributed to the uneven distribution of boron during electrochemical etching, leading to the formation of heavily doped silicon nanowires. Upon laser irradiation, these regions melt and recrystallise, resulting in localised metallic-like conduction because of the high density of charge carriers and a reduced bandgap. Overall, the controlled laser irradiation process offers a precise means of tailoring PS properties, with significant implications for advanced applications in optical waveguides, biosensors, photovoltaics, microelectronics, energy storage, and plasmonic devices.

For my father, whose memory lives on

Declaration

I hereby declare that except where specific reference is made to the work of others, the contents of this dissertation are original and have not been submitted in whole or in part for consideration for any other degree or qualification in this, or any other university. This dissertation is my own work and contains nothing which is the outcome of work done in collaboration with others, except as specified in the text and Acknowledgements. This dissertation contains fewer than 65,000 words including appendices, bibliography, footnotes, tables and equations and has fewer than 150 figures.

Haifa Ali Ibrahim Qadi

March 2025

Acknowledgements

I would like to begin by expressing my deepest gratitude to Allah, whose infinite guidance, mercy, and blessings have been the cornerstone of my strength and perseverance throughout this journey. His presence has illuminated my path and given me the courage to overcome every obstacle.

I am deeply grateful to my supervisors, Jon Goss, Noel Healy, and Benjamin Horrocks, whose unwavering support, insightful feedback, and expert guidance have been instrumental in shaping my research. Their dedication and commitment to my academic development have not only enriched this work but also inspired me to strive for excellence in all aspects of my life.

I also acknowledge the invaluable contributions of my esteemed colleagues. My heartfelt thanks go to Dr. Osama El Zubir, Dr. Naseem Alsaif, Dr. Christian Johnson-Richards, Dr. Luke Stocks, and Dr. Safeyah Alshehri. Their collaboration, constructive criticism, and stimulating discussions have significantly broadened my perspectives and improved the quality of my research.

My sincere appreciation extends to my family, whose love and support have been unwavering throughout this process. I am forever grateful to my mother, Wasfia Kurdy, for her endless care, encouragement, and belief in my abilities. I also wish to express my deep gratitude to my husband, Akram Owaidah, for his patience, understanding, and constant support during the highs and lows of this journey.

Finally, I dedicate this work to my sons, Rayan and Yousef, and to my daughter, Aroob, who have continued to inspire me with their wisdom and strength. Their unwavering support and the example they set in their own pursuits have been a constant source of motivation.

To everyone who has contributed to my journey, be it through guidance, support or simply believing in me, I extend my heartfelt thanks. This thesis stands as a testament to the collective efforts of all those who have walked alongside me.

Table of Contents

List of Figures

Nomenclature

AFM	Atomic Force Microscop
CPD	contact potential difference
CT	Charge Transfer
CW	Continuous-wave
EM	Electromagnetic Enhancement
FTIR	Fourier Transform Infrared Spectroscopy
FWHM	Full Width at Half Maximum
KPFM	Kelvin Probe Force Microscopy
LED	Light-Emitting Diode
LINAC	linear particle accelerator
LSPR	Localised Surface Plasmon Resonances
MACE	Metal-Assisted Chemical Etching
PS	Porous silicon
PZT	Piezoelectric
RIE	Reactive-Ion Etching
RMS	Root Mean Square
SCLC	Space-Charge Limited Currents
SEM	Scanning Electron Microscope
SERS	Surface-Enhanced Raman Spectroscopy

SIMS	Secondary Ion Mass Spectrometry
XPS	X-ray photoelectron Spectroscopy
XRD	X-ray Diffraction

Introduction

Since its initial observation, porous silicon has intrigued researchers due to its extraordinary properties, which stand in stark contrast to those of bulk silicon. Early studies discovered that through electrochemical etching [101], silicon could be transformed into a material with a highly porous structure. This finding not only expanded our fundamental understanding of silicon chemistry but also paved the way for a host of new applications. Over the decades, the unique optical, electrical, and structural characteristics of porous silicon have been extensively explored, highlighting its potential in areas such as optoelectronics [32], sensing [74], and energy conversion[228].

Porous silicon exhibits a range of unique properties that have intrigued researchers over time. The optical properties, including tunable photoluminescence and varied light absorption, are mainly due to quantum confinement processes within its nanostructured framework, which makes it highly appealing for optoelectronic applications [74, 99]. Porous silicon exhibits a wide spectrum of electrical conductivity behaviours, ranging from semiconducting to nearly metallic, depending upon its porosity, surface chemistry, and subsequent treatments [16]. The material has a high surface area and a modifiable pore structure that can be precisely adjusted by electrochemical etching settings, affecting its reactivity and response to external forces [113]. These interconnected properties highlight the adaptability of porous silicon and establish a foundation for its incorporation into sophisticated technological applications.

Electrochemical etching, the primary method for fabricating porous silicon, allows precise control over parameters such as etching time and current density. The pore size, porosity, and surface chemistry of silicon can be customised by adjusting these factors, directly affecting its overall performance [113]. Despite the progress achieved using conventional etching techniques, optimising the intrinsic properties of porous silicon for advanced applications remains a challenge. Understanding and controlling the phase transitions and electrical conductivity of porous silicon is crucial in this endeavour.

In recent years, laser processing has emerged as a potential technique for controlling the characteristics of porous silicon. Using a CO_2 laser allows for non-contact and highly regulated

phase transitions and conductivity changes. By varying the laser power and scanning speed, it is possible to tailor the crystal structure, chemical composition, optical behaviour, and electrical characteristics of porous silicon. This approach provides a novel means to overcome the limitations of traditional post-etching treatments and opens new avenues for the development of silicon-based devices.

This thesis explores how laser processing affects the phase transition and conductivity of porous silicon. Porous silicon samples are generated by electrochemical etching, with etching parameters varied in a systematic manner to produce a variety of architectures. Continuous CO_2 laser irradiation is used to study the effects of laser power and scanning speed on material properties. Characterisation techniques such as SEM, FTIR, AFM, KPFM, Raman spectroscopy, XRD, SIMS, and current-voltage This effort intends to promote porous silicon research by clarifying the fundamental principles underlying laser-induced phase transitions and conductivity changes. The findings are intended to inform the design of next-generation silicon-based devices, resulting in improved performance in applications ranging from microelectronics to optoelectronics, and beyond.

1. Aims and Objectives

The primary aim of this research is to investigate the phase transition and conductivity modification of porous silicon induced by CO_2 laser processing, thereby advancing our understanding of the underlying mechanisms and contributing to the design of next-generation silicon-based devices. To achieve this aim, porous silicon is first fabricated using electrochemical etching, with systematic variations in etching time and current density employed to yield a range of pore structures and porosities. This approach allows for a controlled exploration of how fabrication parameters affect the intrinsic properties of the material.

The prepared porous silicon is comprehensively characterised using advanced techniques such as SEM, FTIR, AFM, KPFM, Raman spectroscopy, XRD, secondary SIMS, current-voltage measurements and XPS. These characterisation methods are used to assess the optical, electrical, chemical, and structural attributes of the material, thereby establishing a baseline for subsequent modifications.

The next stage of the research involves subjecting the porous silicon samples to continuous CO_2 laser irradiation. By varying parameters such as laser power and scanning speed, the study aims to induce controlled phase transitions and modify the electrical conductivity of the material. Finally, the research seeks to correlate the processing conditions, both from electrochemical

etching and laser irradiation, with the resulting changes in the properties of the material. Through this integrated approach, the thesis aims to elucidate the fundamental mechanisms driving laser-induced modifications in porous silicon, ultimately paving the way for enhanced performance in applications ranging from microelectronics to optoelectronics and sensing technologies.

2. Thesis Outline

Chapter 1 provides a comprehensive overview of porous silicon, beginning with its historical discovery and the fundamental principles behind its formation. The chapter discusses the evolution of porous silicon research, highlighting the extraordinary optical, electrical, structural, and thermal properties that distinguish it from bulk silicon. In addition, it reviews the various fabrication methods, such as anodic etching, metal-assisted chemical etching, stain etching, reactive ion etching, and laser ablation and introduces the key applications of porous silicon in optoelectronics, sensing, and energy conversion.

Chapter 2 outlines the experimental procedures used throughout the research. This chapter describes the electrochemical etching process for the formation of porous silicon, including the systematic variation of parameters like etching time and current density to obtain a range of pore structures. The chapter also details the laser processing setup, where continuous CO_2 laser irradiation is employed to modify the porous silicon, and presents the characterisation techniques—such as SEM, FTIR, AFM, KPFM, Raman spectroscopy, XRD, SIMS, I–V measurements, and XPS—that are used to evaluate the material's properties before and after laser processing.

Chapter 3 focuses on the fabrication of porous silicon via electrochemical etching. It details the cleaning and preparation of the silicon substrate, the etching process, and the subsequent rinsing and drying steps. The chapter then presents an in-depth analysis of the porous silicon's thickness, porosity, colour, surface chemistry, and overall structure, employing both conventional and alternative characterisation techniques to establish a baseline understanding of the material's intrinsic properties.

Chapter 4 examines the effect of CO_2 laser processing on porous silicon, focusing on the consolidation process. This chapter begins by discussing the thermal and optical properties of both silicon and porous silicon, followed by an analysis of heat distribution within the porous layer during laser irradiation. It describes the experimental procedure for laser-induced consolidation and presents results from structural and spectroscopic characterisation (including Raman analysis) to demonstrate the changes in the material following laser processing.

Chapter 5 investigates the phase transitions in porous silicon under high-intensity CO_2 laser processing. The chapter presents a detailed discussion of the heat distribution, microscopic and optical changes, and the melting and recrystallisation phenomena observed in the material. It includes an analysis of surface roughness, the formation of silicon clusters, and the evolution of the Raman and XRD profiles, elucidating the mechanisms that underpin the laser-induced transformations in porous silicon.

Chapter 6 is dedicated to the study of electrical properties following laser processing. This chapter explores how laser-induced melting and recrystallisation affect the conductivity and charge carrier dynamics of porous silicon. Detailed electrical characterisation including current–voltage measurements, temperature-dependent studies, work function mapping, and morphological assessments is presented to correlate the structural changes with the observed electrical behaviour. A specific focus is placed on the hypothesis that boron enrichment may play a critical role in enhancing the material's conductivity.

The thesis concludes with a synthesis of the research findings, discussing the implications of the laser-induced modifications on porous silicon for future device applications. The conclusion highlights the key contributions of the work, outlines potential areas for further research, and suggests how the insights gained may inform the development of next-generation silicon based technologies.

3. Contribution

The author is responsible for all the work presented in this thesis under the supervision of Prof. Noel Healy, Prof. Jonathan Goss and Dr Benjamin Horrocks The author gratefully acknowledges assistance in the following areas: Prof. Noel Healy assisted with Raman and XRD analysis. Dr Benjamin Horrocks presented a simulation of the heat distribution using Fortran, which was reprogrammed by the author using Python with the incorporation of heat distribution as a function of distance. Dr Elisabetta Arca provided expertise in X-ray photoelectron spectroscopy (XPS). Dr Toby Hallam provided assistance with the KPFM measurements and analysis.

Chapter 1. Background

1.1. Introduction to Porous Silicon

Porous silicon (PS) is a nanostructured material with unique properties, which have enabled its use in a wide range of technological applications, including microelectronics, optoelectronics, energy storage, and biomedical devices [211]. Its high surface area, tunable porosity, and photoluminescence have made PS a subject of significant scientific interest since its discovery [216]. Understanding its structural characteristics, fabrication methods, and potential applications is essential for exploring its role in advanced material science and technology.

The discovery of PS dates back to 1956, when the Uhlirs, a husband-and-wife team at Bell Laboratories, investigated an electropolishing process for silicon wafers in an HF-based solution [216]. During their experiments, an unexpected drop in current resulted in the formation of a dark, matte layer on the silicon surface. Initially, this layer was hypothesised to be a subfluoride $(SiF_2)_x$, formed during anodic dissolution. However, subsequent research revealed that the layer was composed of voids, creating a porous structure through the electrochemical dissolution of silicon [101].

Despite its early discovery, the material remained relatively obscure until the 1990s, when Leigh T. Canham demonstrated that porous silicon could emit visible light at room temperature [34]. This discovery was transformative, shifting perceptions of silicon from an inefficient light-emitting material to one with significant potential for optoelectronic applications. It marked a pivotal moment in the development of the material, sparking global research into its properties and applications. Since then, PS has received widespread attention for its remarkable properties, such as its high reactivity, biocompatibility, and ability to emit light efficiently at room temperature [136]. These attributes, combined with its compatibility with silicon-based technology, make PS an adaptable material for a variety of fields, including biosensing, drug delivery, and energy conversion [13, 228].

The structural characteristics of PS are defined by four terms: geometry, morphology, porosity, and thickness. Geometry refers to the pore size and the spacing between the pores. Based on pore size, PS can be categorised as microporous (pores smaller than 2 nm), mesoporous (2

to 50 nm) or macroporous (greater than 50 nm) [8]. Morphology as illustrated in Figure 1.1 encompasses the shape, orientation, and interaction of the pores, which can be observed using scanning electron microscopy (SEM) as shown in Figure 1.2 [65]. Porosity, defined as the ratio of pore volume to total volume, is a key factor in determining a material's reactivity and functionality. [55].

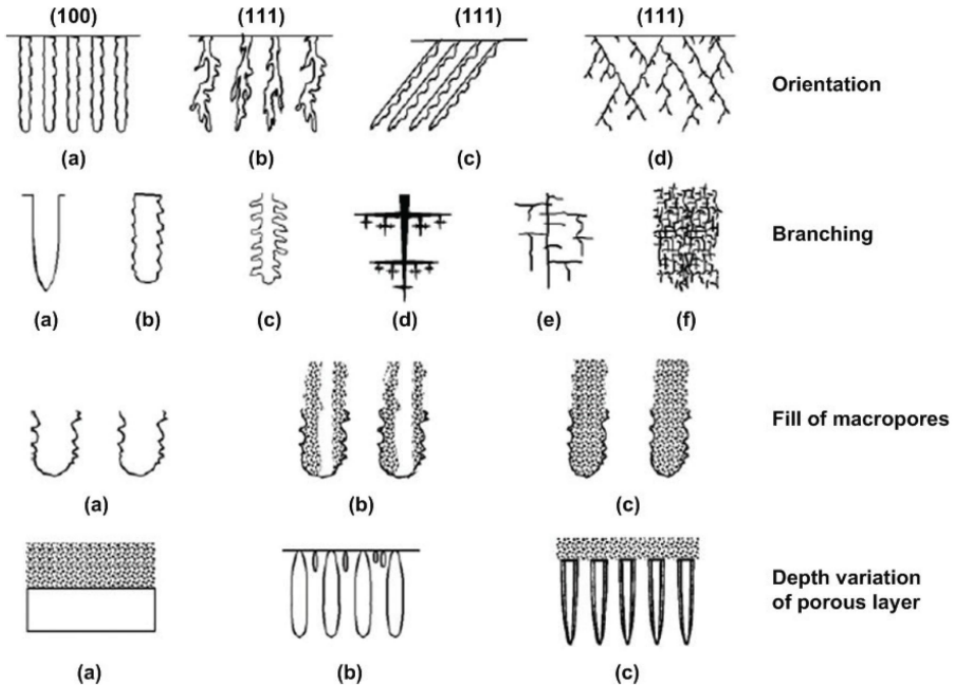

Figure 1.1 Morphological characteristics of PS: **Orientation:**(a) Aligned to $\langle 100 \rangle$ direction and source of holes (b) Roughly aligned to source of holes (c) Partially aligned to $\langle 100 \rangle$ direction and source of holes (d) Aligned only to $\langle 100 \rangle$ direction. **Branching:** (a) Smooth pore walls (b) Branches shorter than diameter (c) Second-level branches only (d) Dendritic branches; (e) Main pores with second- and third-level branches (f) Dense, random, and short branches. **Fill of Macropores:** (a) Unfilled (b) Partially filled with microporous silicon (c) filled with microporous silicon. **Depth Variation of Porous Layer:** (a) Single layer of microporous silicon (b) Single layer of macroporous silicon with smaller pores near the surface (c) A layer of microporous silicon atop macroporous silicon (macropores may be filled by microporous silicon). This Figure taken from [242].

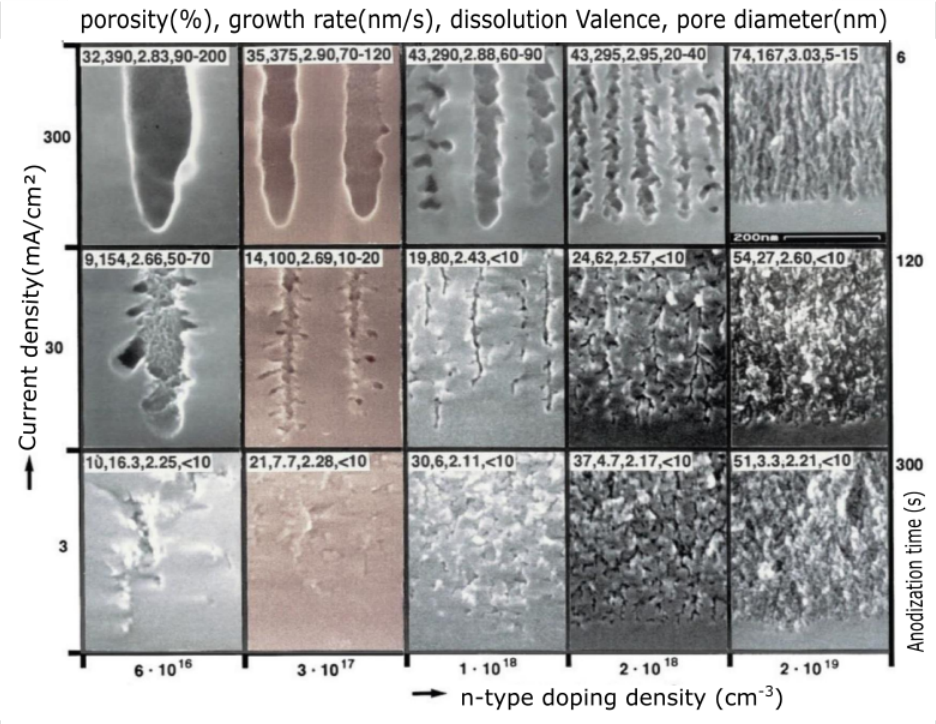

Figure 1.2 Cross-sectional SEM micrographs of various PS structure. This Figure taken from [101].

The properties of PS are closely related to its fabrication method. More than 30 fabrication techniques have been developed, broadly classified as top-down and bottom-up approaches [101]. Top-down methods involve removing silicon atoms from a monocrystalline wafer, creating voids that form a porous structure. This process often employs chemical or physical removal techniques, such as electrochemical etching, which is widely used because of its precision and scalability. In contrast, bottom-up approaches assemble silicon clusters, leaving empty spaces while forming a crystalline structure, typically producing PS powders [101]. These methods enable precise control over the properties of PS, ensuring its suitability for a wide range of applications.

PS is a versatile and indispensable material in modern science and engineering [63]. Its exceptional properties, combined with advanced fabrication techniques, continue to drive innovations in various fields, from energy and electronics to healthcare and environmental science [63].

1.2. Properties of Porous Silicon

PS has a unique combination of morphological, optical, chemical, and electrical properties that make it a highly versatile material for a wide range of scientific and technological applications. Its tunable features, including porosity, surface chemistry, and nanoparticle size, are closely related to the fabrication techniques used, enabling precise tailoring of its properties for specific uses in areas such as optoelectronics, drug delivery, and environmental sensing [63].

1.2.1. Morphological Properties

The morphology of PS is significantly influenced by various electrochemical etching parameters. The etching time plays a crucial role, affecting the evolution of the pore structure, the roughness of the surface, and the porosity [89]. The current density affects the formation of pores and surface characteristics, with higher densities leading to more rapid etching [237]. Electrolyte composition, typically involving hydrofluoric acid and ethanol, influences the etching process and resulting PS structure [236]. Wafer doping levels also affect PS formation, with different behaviours observed in n- and p-type silicon [236]. The ability to adjust these parameters provides precise control over the pore size, distribution, and overall morphology, making PS a versatile material for a wide range of applications.

PS morphologies are classified on the basis of pore size and distribution. According to IUPAC definitions, PS can be categorised as microporous (pores smaller than 2 nm), mesoporous (2 to 50 nm) or macroporous (greater than 50 nm) [175]. Classification is critical to tailor PS to specific applications. For instance, microporous PS is ideal for gas sensing as a result of its high adsorption capacity [204], while macroporous PS is often used in photonic crystals and MEMS devices because of its uniform pore alignment [223]. Scanning Electron Microscopy (SEM) reveals a sponge-like morphology, with pore diameters increasing with longer etching times [217]. This variability allows for precise control of properties such as surface area, reactivity, and mass transport, which are crucial for applications such as catalysis and drug delivery.

The sponge -like structure of PS evolves during fabrication, as shown in Figure 1.3. At lower magnifications (Figure 1.3a), the surface reveals large clusters of silicon, while higher magnifications (Figure 1.3b) display finer details and smaller clusters. These irregular surfaces provide numerous active sites for chemical interactions, contributing to the high reactivity of PS [35].

Morphological properties play a pivotal role in applications such as catalysis, where the high surface area enhances reaction rates, and drug delivery, where the ability to control pore size governs the release kinetics of therapeutic agents.

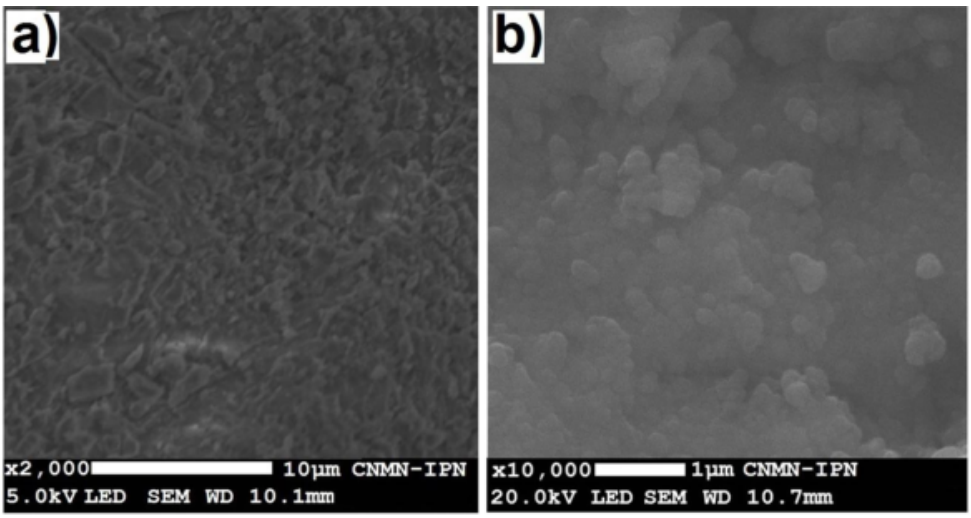

Figure 1.3 SEM images of the PS surface. (a) Magnification of 2000 ×, showing silicon clusters and uneven texture. (b) Magnification of 10,000 ×, revealing smaller clusters compared to (a). Images taken from [35].

1.2.2. Optical Properties

PS is characterised by its unique optical properties, which arise from its nanostructured architecture and distinctive surface chemistry. These features enable a wide range of applications in optoelectronics, sensing, and photonics [96].

One of the most notable optical properties of PS is its ability to emit light across a broad wavelength range, a phenomenon known as photoluminescence. The visible photoluminescence at room temperature was first observed by Leigh T. Canham in 1990. This effect results from quantum confinement in silicon nanocrystallites [34]. When crystallite dimensions approach the silicon Bohr exciton radius, the mobility of electrons and holes becomes restricted, leading to a narrowing of the emission spectrum and a widening of the bandgap. Consequently, smaller crystallites emit blue light, while larger ones emit red [128]. This tunability makes PS ideally suited for wavelength-specific applications such as multicolour LEDs and optical filters [99, 29].

Figure 1.4 shows the photoluminescence spectra of PS produced at etching durations of 15 and 25 minutes. The difference in spectrum shape and intensity highlights how the etching time, as well as, in general, the size of nanocrystallite and the surface passivation, can significantly influence the photoluminescence performance [225].

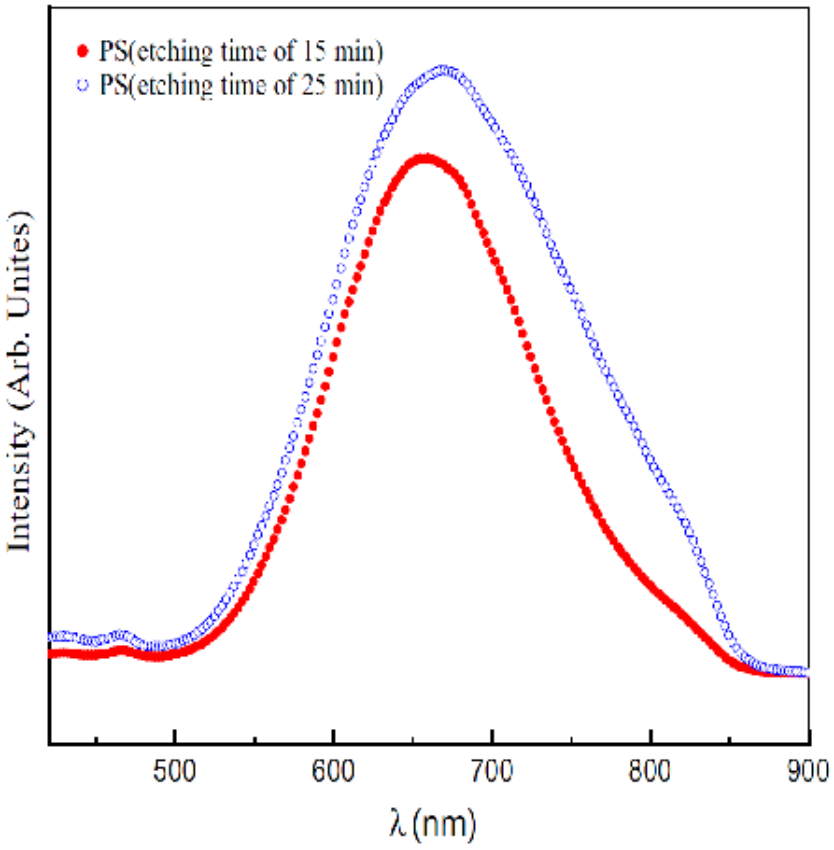

Figure 1.4 Photoluminescence spectra of PS produced at etching durations of 15 and 25 minutes. The Figure adapted from [225].

The optical absorption spectra of PS support the quantum confinement model, revealing an inverse relationship between the band gap energy and the size of the nanoparticle [128]. Moreover, increasing the porosity of PS lowers its refractive index, allowing the design of customised optical components such as anti-reflective coatings and wavelength-selective sensors [65]. This feature is particularly advantageous in photovoltaics, where the reduced reflectivity enhances light absorption and improves energy conversion efficiency. By controlling the porosity and nanocrystallite size, the optical bandgap of PS can be engineered for specific applications. For instance, smaller nanocrystallites with larger band gaps are ideal for ultraviolet absorption, whereas larger nanocrystallites with narrower bandgaps are better suited for infrared devices [128].

Multiple mechanisms influence photoluminescence in PS, including quantum confinement, surface state emissions, and defect-related phenomena. Surface passivation methods, such as hydrogenation or oxidation, significantly enhance photoluminescence by reducing non-radiative recombination pathways [138]. Additionally, surface states introduced by functional groups, such as Si-H_x and Si-OH, shape the intensity and spectral profile of the photoluminescence profile[212].

Photoluminescence lifetime and quantum efficiency are also critical parameters, as they describe how long the excited carriers remain in an emissive state before returning to the ground state and what fraction of absorbed photons are ultimately re-emitted, respectively. These factors significantly influence the overall brightness, stability, and performance of photoluminescent materials in applications such as LEDs, sensors, and lasers, where maximising light output and minimising nonradiative losses are essential [220]. Well-passivated PS exhibits longer photoluminescence lifetimes, making it suitable for time-resolved imaging applications. In contrast, defects or impurities can introduce nonradiative pathways that reduce quantum efficiency [138].

Surface chemistry strongly affects the optical behaviour of PS. Infrared spectroscopy detects functional groups wavenumber such as Si-H_x, Si-O, and Si-OH, which influence light absorption and enhance photoluminescence [138]. Modifying these functional groups, for example, through silanisation or coating with organic dyes, allows further optimisation of PS for specific applications.

Additionally, thermal oxidation serves as an effective surface passivation technique, improving the long-term stability of PS and ensuring consistent optical performance. The functionalisation of PS with organic or inorganic molecules expands its scope in various fields, notably biosensing, where selective binding to target biomolecules is crucial [225].

Future research on the optical characteristics of PS focusses on improving its stability and investigating new applications. Recent ultrafast spectroscopy studies offer deeper insight into carrier dynamics, paving the way for PS use in quantum information systems. Meanwhile, the integration of PS with innovative nanomaterials such as graphene and perovskites shows potential for next-generation optical devices. Although challenges persist, most notably in scalability and photoluminescence degradation, advances in surface passivation and fabrication techniques continue to address these issues [199].

1.2.3. Chemical Properties

The chemical properties of PS are critical to its functionality in areas such as catalysis, drug delivery, and environmental sensing [95]. Its high surface-to-volume ratio, combined with reactive surface chemistry, allows significant interaction with chemical species.

PS surfaces are typically terminated with silicon hydride (Si-H_x) groups formed during electrochemical etching. These groups can be oxidised to form Si-OH or Si-O bonds [138], improving stability and biocompatibility [235]. Functionalisation of the surface with organic

or inorganic groups further enhances its utility for specific applications, such as biosensors and drug delivery systems [35].

The oxidation behaviour of PS is another critical feature. When exposed to ambient conditions, PS naturally forms a silica (SiO_2) layer, enhancing its chemical stability. More importantly, PS gradually corrodes into silicate anions, which are harmless and excreted from the body, making it highly biocompatible and suitable for long-term biomedical applications [224].

In addition, the reactive surface of PS supports various chemical reactions, such as hydrosilylation, which facilitate the attachment of functional groups or the synthesis of hybrid materials. This versatility expands the scope of PS applications in advanced material science.

1.2.4. Electrical Properties of Porous Silicon

PS exhibits unique electrical properties due to its nanostructured morphology, which influences charge transport, carrier concentration, and conductivity [212]. These properties make PS suitable for applications in electronic and optoelectronic devices, such as sensors, photovoltaic cells, and microelectronics. In addition, the electrical characteristics of PS are highly tunable and depend on factors such as fabrication methods, porosity, doping level, and surface treatments.

The electrical resistivity of PS is significantly influenced by its porosity, doping type, and pore morphology. As porosity is a major factor that affects PS resistivity, with resistivity increasing exponentially as porosity increases due to the reduced silicon content and interrupted crystalline network. For example, the resistivity reaches approximately 1×10^9 Ω cm at room temperature when porosity exceeds 60% [143]. Figure 1.5 illustrates the relationship between electrical conductivity and porosity.

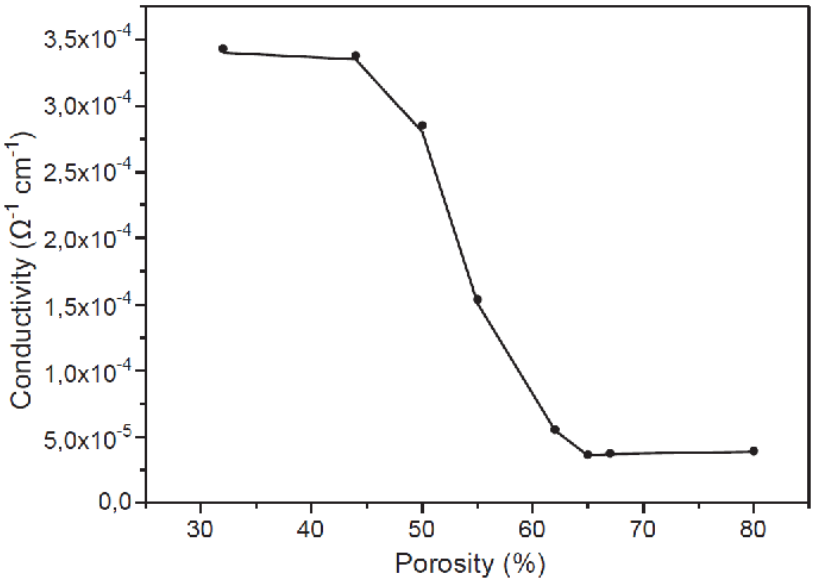

Figure 1.5 Relationship between electrical conductivity and porosity (the figure copied from [103]).

The doping concentration of the silicon wafer plays a critical role in determining the conductivity of PS. Highly doped substrates introduce a larger number of charge carriers, which can influence the electrochemical properties of PS-based sensors. While this can enhance sensitivity in certain applications, the observed over-Nernstian behaviour may be more directly related to deviations in the effective charge number (z) rather than changes in conductivity, as the sensor response exceeds the theoretical limit predicted by the Nernst equation.The Nernst equation, given as:

$$E = E^{\circ} - \frac{RT}{zF} \ln Q,$$

relates the equilibrium potential E (in volts) of an electrochemical reaction to the standard electrode potential E° (the potential under standard conditions, also in volts), the reaction quotient Q (a ratio of the concentrations of products to reactants) and the number of electrons transferred in the reaction (z). The constant 0.059 is derived from the gas constant, temperature, and Faraday's constant, assuming a temperature of 298 K (25°C).

In the case of over-Nernstian behaviour, the response surpasses this theoretical prediction due to enhanced surface reactions or charge transport properties [241].

The type of doping also affects the transport mechanisms of the carriers. P-type PS typically exhibits higher resistivity compared to n-type due to the lower mobility of holes, while n-type PS benefits from higher electron mobility, resulting in lower resistivity [10].

Charge transport in PS involves complex mechanisms, including space-charge limited currents (SCLC), tunnelling, and trapping-detrapping dynamics. The SCLC mechanism occurs

under high electric fields when the injected carrier density exceeds the thermally generated carrier density, resulting in a current that follows a quadratic dependence on voltage under ideal conditions [100].

In tunnelling, charge carriers move through potential barriers via quantum tunnelling, a process that dominates in structures with thin silicon oxide layers or narrow pore walls. PS nanowires embedded with silicon quantum dots exhibit enhanced tunnelling conduction [168]. The predesigned structure of these nanowires allows for a distinct tunnelling mechanism that is more efficient than bulk PS. This increased efficiency is attributed to the large internal surface area and the high density of quantum dots, which facilitate electron transport through tunnelling [168].

Charge carriers in PS are frequently captured by traps, localised energy states caused by defects or impurities, before being released back into the conduction or valence band. This process, known as trapping-detrapping dynamics, significantly impacts carrier mobility and contributes to dispersive transport behaviour. Trapping centres, including donor and acceptor states, are distributed on the surface and within most PS, making them a critical factor in modulating the discharge current. These dynamics are strongly influenced by external conditions, such as electric field strength and temperature, which govern the rates of trapping and detrapping. Understanding these mechanisms is essential for optimising the electrical performance of PS in applications such as sensors, memory devices, and other electronic systems [87].

1.2.5. Thermal Properties of Porous Silicon

PS exhibits unique thermal properties because of its nanostructured morphology, which includes features such as porosity and pore size. These structural characteristics directly influence its thermal conductivity, heat capacity and thermal stability, making it a highly versatile material for applications in thermal management, energy storage and thermoelectric devices [133].

The thermal conductivity of PS is significantly lower than that of bulk silicon, primarily due to the scattering of phonons at the interfaces of the pores [232]. Increased porosity disrupts the silicon network, enhancing phonon scattering and subsequently reducing thermal conductivity. Furthermore, smaller pores amplify this effect by creating a dense network of interfaces, which limits phonon transport [190].

The specific heat capacity of PS is generally higher than that of bulk silicon, owing to the large internal surface area associated with its pores. Studies have shown that the heat capacity increases monotonically, by up to 30%, as the inner surface area of the pores expands [58]. This enhancement is attributed to surface phenomena that dominate the thermal behaviour

of nanostructured materials, providing advantages for applications that demand efficient heat storage.

Thermal stability is another critical aspect of PS, particularly in high-temperature environments. PS remains stable at moderate temperatures but undergoes structural changes, such as pore collapse and oxidation, at elevated temperatures exceeding 800 °C. These changes result in the formation of silicon dioxide, altering its thermal and mechanical properties [152]. Such behaviour is crucial for applications like thermoelectric devices and high-temperature coatings, where maintaining structural integrity and performance under extreme conditions is essential.

The distinctive combination of morphological, optical, chemical, electrical, and thermal properties in PS underscores its versatility for a wide range of applications. Its tunable porosity, surface chemistry, and nanostructured features enable precise control of its properties, fostering advances in fields such as optoelectronics, energy storage, catalysis, and biomedical devices. Using these properties through innovative fabrication techniques, researchers can continue to unlock the potential of PS for next-generation technologies, cementing its role as a cornerstone in modern material science.

1.3. Fabrication Techniques for Porous Silicon

The development of PS depends on a variety of fabrication methods, each designed to achieve particular structural properties and uses. These methods aim to control important variables, such as the pore size, morphology, and porosity, that affect the material's performance. Over the years, several methodologies have been developed that use chemical, physical, and hybrid methods to produce PS in multiple forms, ranging from thin layers to powders. Although many options are available, several are distinguished by their efficiency, scalability, and adaptability. The following sections explore five of the most widely used techniques for forming PS, highlighting their principles and advantages.

1.3.1. Anodic Etching

Anodic etching is the most widely used method for the fabrication of PS due to its ability to produce highly uniform structures with fine control over the pore parameters. This electrochemical process involves dissolving a crystalline silicon wafer in a hydrofluoric acid-based electrolyte under an applied electric current. Parameters such as current density, electrolyte composition, and etching duration can be adjusted to control pore size, porosity, and layer thickness. Anodic etching is especially valued for producing uniform and reproducible PS layers (more details

in Chapter 2 and Chapter 3), making it ideal for applications in optoelectronics, photonics and drug delivery systems. Its ability to create well-defined porous structures ensures its continued dominance among fabrication techniques [66].

1.3.2. Metal-Assisted Chemical Etching

Metal-assisted chemical etching (MACE) leverages a metal catalyst, such as gold or silver, to guide the etching process. In this method, a metal film is deposited onto the silicon wafer, and the etching reaction occurs preferentially at the metal interface when exposed to HF and an oxidising agent. Figure 1.6 shows the PS fabrication process using metal-assisted etching, applying highly ordered gold nanoparticle arrays as an etching mask. MACE allows for the creation of high-aspect ratio structures and intricate nanostructures, making it ideal for advanced photonic devices, sensors, and microfluidic systems [19].

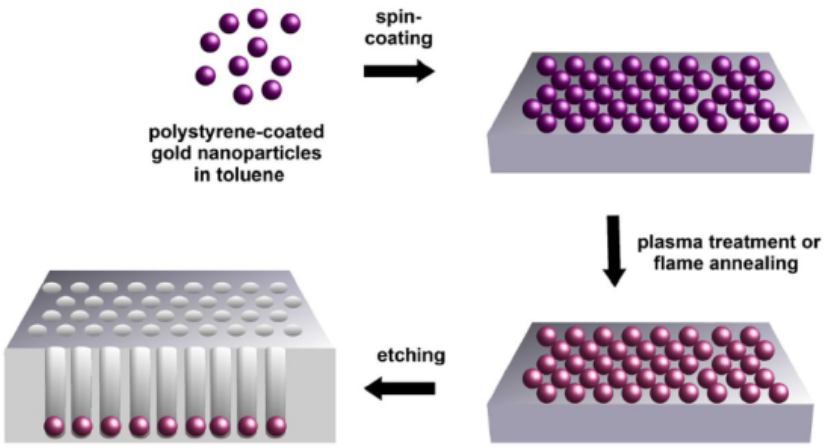

Figure 1.6 Metal-assisted chemical etching using gold nanoparticle arrays to fabricate PS (the figure taken from [187])

1.3.3. Stain Etching

Stain etching is a purely chemical process that does not require an external power source. In this method, silicon is immersed in a solution containing hydrofluoric acid and an oxidising agent, such as nitric acid, which chemically reacts with the silicon surface to create a porous layer. Although stain etching is less precise and less scalable than techniques such as anodic etching, it remains a cost-effective option to produce PS [97]. This approach is particularly well suited for applications where strict uniformity is not essential but simplicity and low cost are paramount, such as in antireflective coatings, gas sensors and certain biomedical devices[161].

1.3.4. Reactive-Ion Etching

Reactive-ion etching (RIE) employs plasma to etch silicon surfaces with exceptional precision in patterning and shaping silicon surfaces [56]. This method combines reactive chemical species and physical ion bombardment to achieve well-defined patterns and controlled porosity. Figure 1.7 shows that the sequential RIE process for producing PS involves three stages: an etching step followed by two passivation steps, namely oxidation and fluorination. RIE offers excellent control over the geometry, depth and distribution of the pores, which makes it essential for microfabrication [126]. Applications of RIE include photonic crystals, optical sensors, and microelectromechanical systems (MEMS), where intricate designs and fine features are critical. Its versatility ensures its continued use in cutting-edge silicon technology.

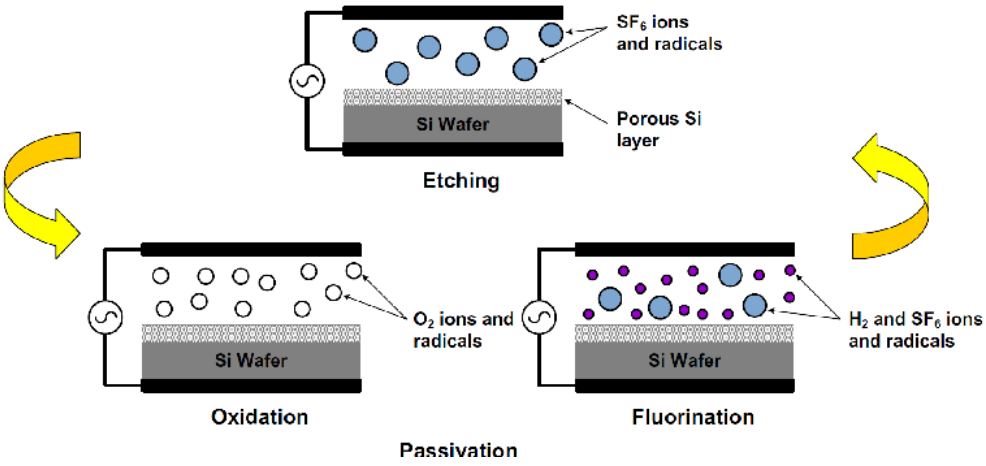

Figure 1.7 RIE method to fabricate PS (the Figure used from [102])

1.3.5. Laser Ablation

Laser ablation employs high-intensity laser pulses to vaporise silicon and form porous structures. By adjusting laser parameters such as intensity, duration, and wavelength, this technique offers precise control over pore formation [184]. Laser ablation is beneficial for creating PS layers on irregular substrates and for rapid prototyping applications. Its adaptability makes it a valuable tool for the fabrication of PS in niche areas, including flexible photonic and optoelectronic devices [171].

In addition to the five primary methods, numerous other fabrication techniques have been developed to produce PS for specific applications or to achieve unique PS characteristics. These include photoetching, which uses light to enhance pore formation [91]; vapour etching, which avoids liquid immersion using HF vapours [177]; and mechanical synthesis, which induces porosity through mechanical processes [92]. Advanced methods such as spark erosion, plasma

hydrogenation, and oblique-angle deposition offer innovative ways to create PS for specialised uses. Although less commonly used than primary methods, these approaches continue to expand the versatility and applicability of PS in modern materials science.

1.4. Oxidation and Stability of Porous Silicon

The oxidation and stability of PS are critical for its long-term performance and applicability in various environments. Due to its high surface-to-volume ratio and reactive surface, PS is particularly susceptible to oxidation, significantly influencing its structural, chemical, and electrical properties. This section explores the formation of silicon oxide and the role of environmental conditions in affecting the stability of PS.

1.4.1. Formation of Silicon Oxide

PS exhibits a high susceptibility to oxidation, because of its intrinsic properties, such as porosity and surface reactivity. The large surface area provided by the porous structure facilitates the interaction of oxygen molecules with the silicon substrate, enabling faster and more extensive oxidation compared to bulk silicon [125].

The higher porosity of PS provides a large surface area, allowing for more interaction sites for oxygen molecules with the silicon substrate. The interaction is vital for the oxidation process, allowing more extensive and faster oxidation than non-porous silicon [125].

Oxidation occurs when silicon reacts with oxygen or water vapour, leading to the formation of a silicon dioxide layer. This process can be induced thermally, chemically, or by exposure to ambient air. Thermal oxidation, in particular, allows precise control over the thickness and uniformity of the oxide layer. At temperatures above 400°C, the oxidation rate increases significantly, producing a robust SiO_2 layer that enhances the material's stability [152].

Thermal oxidation yields a stable surface with minimal degradation over extended periods. For example, no surface degradation was observed for thermally oxidised PS over a year, as confirmed by techniques such as scanning electron microscopy and photoluminescence [4].

1.4.2. Impact of Environmental Conditions on the Stability of Oxidised Porous Silicon

The stability of oxidised PS is influenced by environmental factors such as temperature, humidity, and exposure to reactive chemicals. These factors can enhance or degrade the performance of PS, depending on the specific conditions.

In humid environments, PS undergoes natural oxidation at an accelerated rate, forming a thin oxide layer even at room temperature. The natural oxide thickness increases from about 2 nm to around 4 nm [60]. Although this natural oxidation improves the chemical stability of the material, it also affects its porosity and reactivity. Oxidation increases the sensitivity of PS to humidity by improving its adsorption capacity. This is attributed to improved wetting properties and increased surface area of the oxidised layers, allowing greater interaction with water molecules [107]. These characteristics make oxidised PS highly valuable in humidity sensors.

However, long-term exposure to moisture can alter the electrical characteristics and sensitivity of humidity sensors based on thermally carbonised PS. In particular, sensitivity tends to decrease over several months, although the sensors eventually stabilise, exhibiting only minor variations in capacitance [214].

Thermal oxidation also improves the resistance of PS to further atmospheric oxidation and improves its chemoresistive response to specific vapours, such as isopropanol [17]. This increased stability broadens the potential applications of oxidised PS in various environmental conditions.

1.5. Laser Interaction with Porous Silicon

The interaction of lasers and PS causes considerable structural, optical, and chemical modifications, increasing its potential for use in optoelectronics, sensing, and biomedical technologies [206]. Laser exposure changes the microstructure of PS, influencing properties such as pore size, crystallinity, and chemical content. These modifications are dependent on laser parameters such as wavelength and energy, as well as environmental conditions, allowing for precise control over the material's final properties.

Different laser wavelengths control the absorption and distribution of energy within PS, influencing the results of processes like material consolidation, surface patterning, and functionalisation. The interaction can be optimised by adjusting the laser parameters and fabrication procedures to generate application-specific alterations.

1.5.1. Long-Wavelength Lasers

Long-wavelength lasers, such as CO_2 lasers operating at 10.6 μm, interact with PS primarily through thermal effects. The absorption of laser energy by the silicon lattice results in localised heating, which can induce consolidation, melting, recrystallisation and thermal oxidation. PS

consolidation occurs when the porous structure partially collapses, reducing porosity and enhancing the mechanical stability of the material.

Additionally, combining CO_2 lasers with chemical vapour deposition (a process that uses reactive gas-phase precursors to deposit thin films on a substrate through chemical reactions) facilitates the formation of silicon nanoclusters within a silicon oxide matrix. By adjusting the laser power, the size and properties of these clusters can be precisely controlled, directly influencing the photoluminescence characteristics of the material [122].

The melting threshold of PS decreases significantly with increased porosity, highlighting the influence of structural characteristics on its thermal response to laser irradiation. For example, the threshold decreases from 35 to 11 mJ/cm^2 as porosity increases from 45% to 82%, a stark contrast to the much higher threshold of 750 mJ/cm^2 for crystalline silicon. This reduction is primarily attributed to the diminished thermal conductivity and lower melting temperatures associated with the porous structure [209]. The reduced thermal conductivity in PS enhances localised heating during laser exposure, allowing for precise thermal modifications at lower energy levels. These properties make PS particularly suitable for applications that require controlled melting, recrystallisation, or structural modification using laser techniques.

CO_2 lasers are capable of melting PS, inducing significant changes on its surface. Controlled energy input during the laser process can facilitate recrystallisation, allowing for precise tailoring of the material's properties [85].

During laser writing, the high temperatures generated in an oxygen-rich environment can result in the formation of a silicon dioxide layer. This oxide layer not only enhances the chemical stability of PS but also broadens its applicability in environments requiring long-term durability [156].

1.5.2. Short-Wavelength (UV) Lasers

Short-wavelength lasers, such as ultraviolet lasers operating at wavelengths below 400 nm, interact with PS primarily through non-thermal mechanisms, including photon absorption and surface photochemical effects.

UV laser irradiation can alter the chemical composition of PS by removing hydrides (Si-H_x) and forming silicon oxides (SiO_x) or hydroxides (Si-OH), as confirmed by FTIR spectroscopy. These modifications enhance the chemical stability and functionalisation potential of the material, making it suitable for sensing and biomedical applications [206].

Short-wavelength lasers can also influence the optical properties of PS, such as photoluminescence. UV laser irradiation, such as that from excimer lasers, can create periodic surface structures on silicon, which have been shown to enhance photoluminescence by increasing the crystalline quality of the silicon nanocrystals [169]. This enhancement is further supported by the changes in the vibrational modes of silicon, as laser excitation increases the intensity of certain vibrational modes, which are crucial for photoluminescence [238].

1.6. Applications of Porous Silicon

PS has emerged as a diverse material with considerable potential in optoelectronic applications because of its distinctive optical, electrical, and structural characteristics. Features such as photoluminescence, a tunable band gap, and a large surface area have shown that PS is an essential tool in numerous light-based technologies. The ability to improve optical performance, effectively regulate heat and facilitate adjustable structural characteristics led to its use in essential applications, such as light-emitting devices, solar cells, and optical waveguides. This section explores the main optoelectronic applications of PS and highlights its contributions to the advancement of modern technologies.

1.6.1. Light-Emitting Diodes

The ability of PS to emit light efficiently at room temperature, attributed to quantum confinement effects, makes it highly valuable for light-emitting diodes (LEDs) [57]. By integrating PS into GaN-based LEDs, researchers have achieved significant improvements in optical performance through optimisation of the structural and morphological properties of the semiconductor [166].

A major challenge in LED performance is managing high junction temperatures, which reduce light emission efficiency and induce redshifts in emitted light, resulting in undesirable colour changes. PS can be engineered to optimise thermal management to enhancing localised heat transfer and reducing interfacial thermal resistance. These tailored properties make PS a promising material for improving the efficiency, stability, and reliability of LEDs in various applications [166].

1.6.2. Solar Cell

The PS has a unique structure that significantly enhances the performance of solar cells by reducing optical reflectivity and increasing light absorption. Simulation studies have shown that

incorporating a PS buffer layer in heterostructures can improve the efficiency of solar cells by approximately 10%, reaching up to 23.6% [53].

Furthermore, the high surface area of PS enhances light interaction, which improves the photovoltaic properties of solar cells [227]. This structural advantage not only maximises energy conversion efficiency but also minimises optical losses, making PS an essential material for advancing solar energy technologies.

1.6.3. Optical Waveguide

PS has the ability to tune the refractive index by controlling porosity through electrochemical etching, making PS a versatile material for the design of waveguides that can closely match the properties of conventional optical fibers [129].

Moreover, advanced fabrication techniques, such as laser irradiation, can create waveguiding regions within PS structures. These focused laser methods enable the formation of micrometre-sized channels, facilitating efficient light transmission and expanding the use of PS in integrated photonic circuits [167].

The unique characteristics of PS make it an essential material for various optoelectronic applications. The ability to optimise thermal management in LEDs, improve light absorption in solar cells, and help with tailored waveguide designs demonstrates its versatility and adaptability.

1.7. Summary

PS has evolved from an accidental discovery in the 1950s to a highly convertible material with wide applications in modern science and engineering. Early observations initially led researchers to hypothesise that the dark, matte layer formed on silicon was a subfluoride compound. Subsequent investigations, however, discovered a structure filled with voids, providing an extensive investigation of silicon's porous form. Its significance grew considerably in the 1990s, when it was shown that PS could emit visible light at room temperature, overturning the assumption that silicon was intrinsically inefficient for optoelectronic applications. This development sparked worldwide interest, revealing PS as a nanostructured material with tunable porosity, high internal surface area, and remarkable photoluminescence.

All of these properties are closely related to the morphology of PS, which can exhibit microporous, mesoporous, or macroporous structures. The size, shape, and density of the pores can be modified by adjusting various electrochemical etching parameters and other fabrication methods, which affect the interaction of PS with light, chemicals, and electric fields. The large surface

area provides abundant reactive sites for chemical functionalisation or biomolecular attachment, which is particularly beneficial in drug delivery, biosensing, and catalysis. Moreover, the quantum confinement effect within the silicon nanocrystallites gives PS unusual optical behaviour, including the ability to emit light across a broad spectral range. At the same time, defect-related mechanisms and surface passivation techniques offer further control over photoluminescence lifetime and quantum efficiency.

This flexibility comes in part from the variety of methods used in the creation of PS. Methods such as anodic etching, metal-assisted chemical etching, stain etching, reactive-ion etching, and laser ablation enable fine manipulation of pore geometry, thickness, and surface chemistry. The use of catalysts or oxidising agents, combined with control over factors such as current density or irradiation wavelength, leads to PS structures optimised for specific ends, whether high-aspect-ratio pores for microfluidic devices or heavily branched networks for enhanced thermal management. Additional processes, such as thermal oxidation, are used to stabilise PS against environmental degradation and to modify its optical and chemical properties.

The potential of PS extends multiple fields. In electronics and optoelectronics, the low thermal conductivity of the material and the important light-emitting properties enhance the efficiency of LEDs, solar cells, and optical waveguides. The adjustable refractive index has led to advances in antireflective coatings and sensor platforms, while controlled porosity makes it suitable for hosting active substances in drug delivery systems. PS can withstand temperature elevations up to a point before undergoing structural changes, thus offering the possibility of customised thermal management solutions. As fabrication strategies continue to refine its morphology and surface chemistry, PS remains at the forefront of modern materials science, facilitating breakthroughs in quantum information, energy conversion, sensing technologies, and beyond.

Chapter 2. Experimental Methodology

2.1. Introduction

This chapter provides methodologies for producing PS, with a particular emphasis on the anodisation of silicon wafers, and investigates the resultant material properties through various characterisation techniques. To optimise the fabrication process for specific applications (laser writing on PS), an illustration of the methodologies applied to analyse the crystal structure, surface morphology, and optical as well as electrical properties of the samples both before and after laser irradiation is presented.

Different methods were used to characterise the samples, including microscopy (optical microscopy, scanning electron microscopy) and spectroscopy (Fourier transform infrared spectroscopy, Raman spectroscopy, X-ray diffraction, X-ray photoelectron spectroscopy). In addition, secondary ion mass spectrometry was used to quantify the elements in the surface layers of a sample. Similarly, the electrical conductivity of the area processed by the laser was measured.

This chapter presents a fundamental understanding of PS formation and an overview of advanced techniques used to investigate and tailor PS.

2.2. Electrochemical Etching for Formation of Porous Silicon

The scientific community has shown significant interest in PS in recent decades due to its unique physical, chemical, and optical properties, which make it vital for many applications, including sensors, solar cells, microelectronics, and biomedical devices [74, 228]. The most common method used to form PS is electrochemical etching.

Electrochemical etching, also known as anodisation, involves applying an anodic bias to the wafer in a fluoride-based electrolyte solution due to the negative standard electrode potential of silicon, which leads to the formation of an oxide layer that is insoluble in aqueous solutions at a pH of ≤ 7. This oxide is soluble by strong alkaline solutions (e.g., hot, concentrated NaOH or KOH) and by HF solutions. Although silicon is chemically active in both alkaline and fluoride solutions, additional side reactions occur in alkaline environments alongside the anodic reaction.

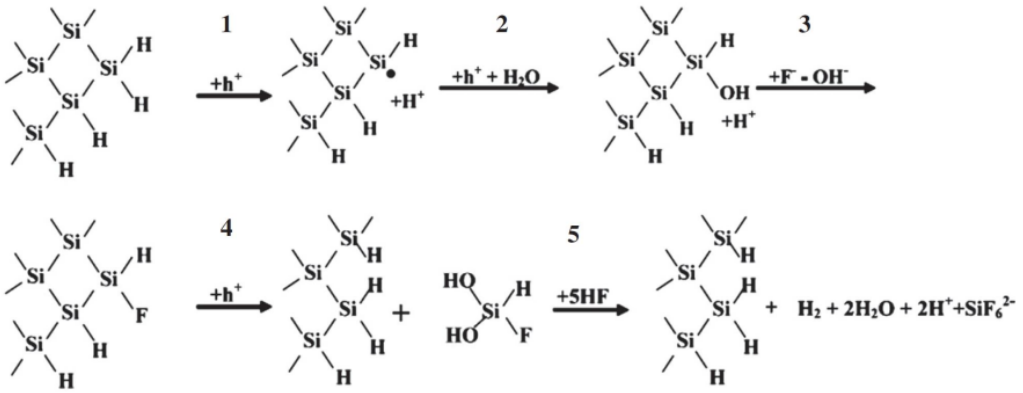

Figure 2.1 Electrochemical dissolution of a silicon atom in hydrofluoric acid solution. (adapted from [95]).

In contrast, hydrofluoric acid alone does not etch silicon without an oxidant, making it crucial for controlled etching and minimising unwanted side reactions [115].

Figure 2.1 shows the generally accepted reaction sequence for the anodic dissolution of silicon. The formation of PS by anodisation occurs in multiple stages that involve the reaction of $Si-Si$, $Si-H$, $Si-O$ and $Si-F$ bonds. Initially, the silicon surface is covered with a passivating layer of $Si-H$ bonds when immersed in HF solution. The free hole inside silicon reaches the silicon interface and $Si-H$ is replaced by $Si-OH$, creating two holes in the process, as the $Si-F$ bond is much stronger than the $Si-H$ bond. F^- ions replace the OH^- groups. The ionic $Si-F$ bonds make the Si atom more polarised, and the HF molecules will attack the weak $Si-Si$ back bonds. During the electrochemical etching process, a silicon atom is removed from the lattice, leaving the remaining silicon atoms bound to hydrogen. The selective removal of silicon results in microporous or mesoporous structures [101]. The general reaction can be expressed as:

$$\mathrm{Si} + 6\,\mathrm{HF}_2^- + 4\,\mathrm{h}^+ \longrightarrow \mathrm{SiF}_6^{2-} + 6\,\mathrm{HF}.$$

There are three configurations for electrochemical etching, as shown in Figure 2.2 lateral cell, single cell, and double cell. In the lateral cell, the silicon wafer serves as the anode, while a platinum electrode (or another HF-resistant material) acts as the cathode. The cell body is typically made of acid-resistant polymers such as Teflon. When the wafer is immersed in HF, any exposed silicon surface will be etched if the current density remains below the critical value. However, a key disadvantage of the lateral cell is its nonuniform porosity and thickness, which arise from a drop in the lateral potential across the wafer, leading to non-uniform current density.

The single-cell (single-tank) configuration is the most commonly used and was used in this project. In this setup, a metal contact is made on the back of the wafer, serving as an anode and

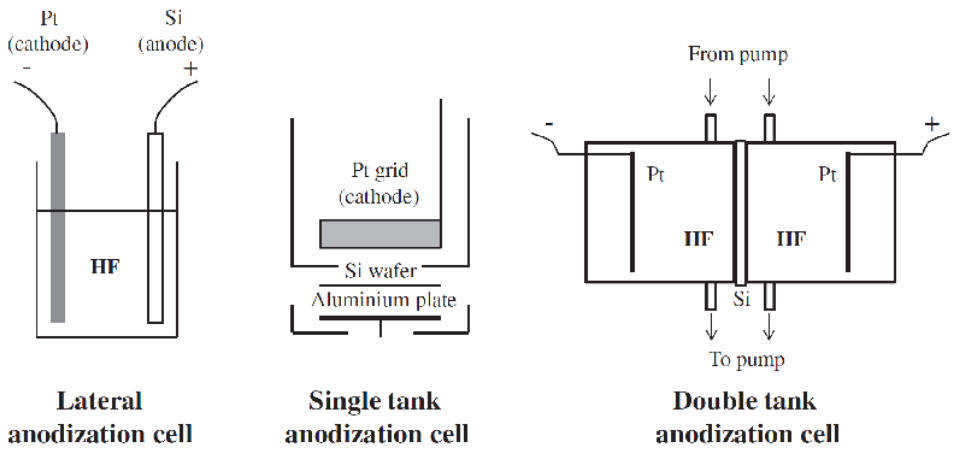

Figure 2.2 Cross-section of the Electrochemical Etching Cell Assembly: lateral, single and double tank anodisation cells. (Figure taken from [95]).

providing a uniform current density. The wafer is sealed with an O-ring so that only the front of the sample is exposed to the electrolyte, resulting in a more uniform porous layer.

Finally, the double-tank cell consists of two half-cells separated by the silicon wafer. The anode and cathode are large platinum electrodes immersed in both half-cells, and the electric current travels through the wafer. Both the front and rear sides of the wafer serve as the local anode and cathode, respectively. To prevent a drop in the local concentration of the electrolyte and eliminate hydrogen bubbles, chemical pumps are used to circulate the electrolyte between half cells [26].

2.3. Laser Writing

After characterising the PS layer, a laser was applied to the PS using the setup shown in Figure 2.3.

Figure 2.3 illustrates the laser writing assembly, which consists of:

1. A continuous wave CO_2 laser (manufacturer: Synrad). The laser power reaches 50 W, with a wavelength of 10.6 µm, and a 470 µm beam diameter at the lens.

2. An array of mirrors (m_1, m_2, and m_3) and a ZnSe convex lens (L) with a focal length of 101.6 mm.

3. A motorised XY stage, controlled via the Kinesis software.

4. A computer to manage stage speed.

5. Cooling system (not shown in the diagram).

6. Safety key.

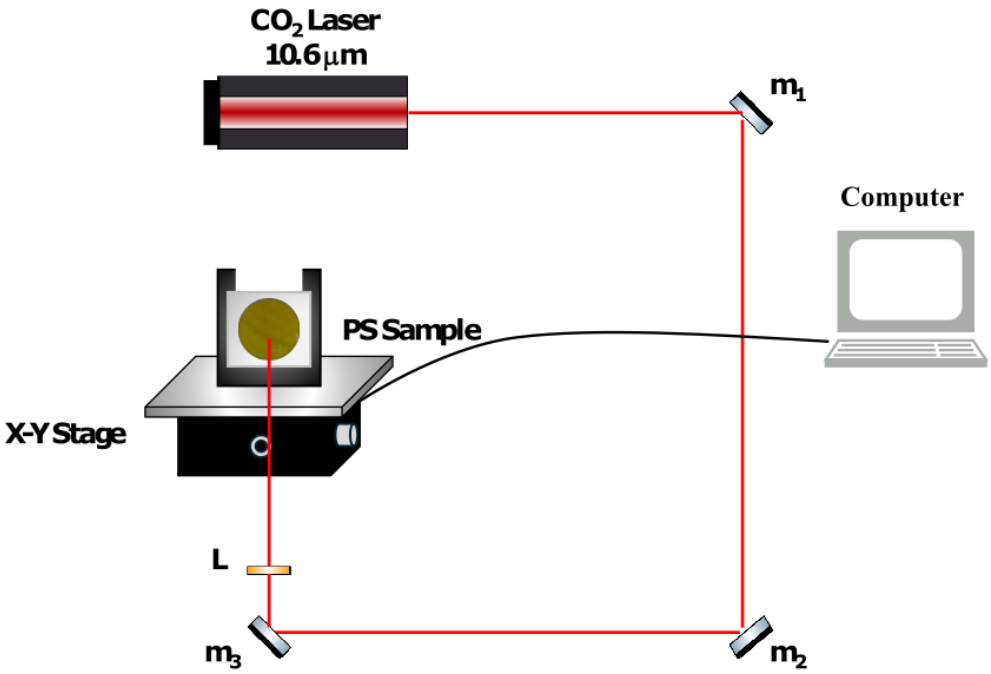

Figure 2.3 Laser writing setup

The principle of using a CO_2 laser is that its interaction with the semiconductor generates thermal heating through the excitation of lattice vibrations. The laser was used to write lines at different speeds (50, 20, 10, and 5 μm/s) with fixed power in each PS sample, within a laser power range of 5 to 30 W.

The sample was placed on the XY stage so that its surface was perpendicular to the laser beam. A laser beam was focused on the sample at a specified distance using the ZnSe convex lens, resulting in a beam diameter at the focus of 470 μm. A constant speed was applied to move the stage along the X-axis while maintaining constant laser power from the start to the end point, forming a line on the PS layer.

After forming the first line, the platform was raised by 1 mm, and the stage speed was reduced to 20 μm/s, with the laser power unchanged. The procedure was then repeated at 10 μm/s and 5 μm/s to increase the thermal effect by prolonging the exposure time. Subsequent samples were processed similarly, using higher laser powers for each trial.

2.4. Characterisation Techniques

2.4.1. Gravimetric Method for Measuring Porosity and Thickness

The gravimetric method was used to determine porosity and thickness. This method uses the fact that freshly etched PS dissolves quickly in simple aqueous solutions, for example, aqueous

NaOH or KOH solution [179]. In contrast, single-crystal silicon dissolves much more slowly. The definition of porosity, P, is the ratio of the volume of pores to the total apparent volume of the sample Equation (2.1)

$$P = \frac{V_{\text{pores}}}{V_{\text{total}}} \tag{2.1}$$

The volume of the pores is assumed to be equal to the volume of silicon that is removed during the electrochemical etch, given by Equation (2.2):

$$V_{\text{pores}} = \frac{m_1 - m_2}{\delta_{\text{Si}}} \tag{2.2}$$

where m_1 is the mass of the sample before the etch, m_2 is the mass of the sample after the etching, and δ_{Si} is the density of silicon (assumed to be 2.33 g/ml in this project [179]).

The sample was weighed before and after etching. Subsequently, the sample was placed in a beaker containing 10 ml of the 1 M aqueous ethanolic KOH solution for 5 minutes or until the PS layer dissolved. Subsequently, the sample was rinsed with ethanol, dried, and weighed again to obtain the final mass (m_3). Figure 2.4 shows a schematic of these steps.

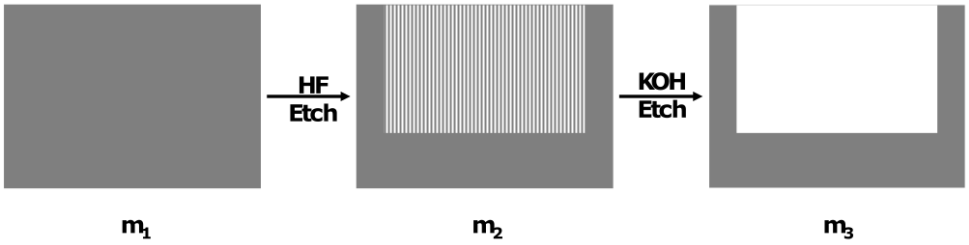

Figure 2.4 Diagram illustrating the steps of the gravimetric method for measuring the porosity and thickness of a PS layer. For visual clarity, the diagram is drawn with a layer of PS that is much thicker than the case. The PS layer was typically a thin film of 5-10 μm on top of a wafer with a 525 μm thickness.

The total volume required for the volume ratio equation 2.1 is the volume of PS, which was estimated by removing the PS film with KOH/ethanol and determining the difference in mass:

$$V_{\text{total}} = \frac{m_1 - m_3}{\delta_{\text{Si}}} \tag{2.3}$$

By substituting Equations (2.2) and (2.3) into Equation (2.1), the porosity is:

$$P = \frac{m_1 - m_2}{m_1 - m_3} \tag{2.4}$$

The thickness of the porous layer (T) depends on the density of the material and the planar area A of the wafer exposed to the etching solution, as shown in Equation (2.5):

$$T = \frac{m_1 - m_3}{A\delta_{\mathrm{Si}}} \tag{2.5}$$

where A represents the wafer area exposed to HF during electrochemical etching [179].

Although the gravimetric method is both inexpensive and straightforward, providing the measurement of thickness and porosity by assigning mass, it yields only average values across the sample. In cases where the PS membrane is non-uniform, the results may be inaccurate. Furthermore, gravimetric analysis can be susceptible to errors arising from contamination or material loss during sample handling, affecting the accuracy of the measurement [179].

2.4.2. Scanning Electron Microscope

Scanning electron microscopy (SEM) has become a standard technique for characterising materials from the microscale to the nanoscale. An SEM produces images by sweeping a high-energy electron beam across a sample. When the electron beam strikes the surface, it penetrates the sample to a depth of a few microns, depending on the accelerating voltage and sample density. This interaction generates multiple signals, including secondary electrons and X-rays, which are collected by specialised detectors to form an image that reveals surface topography, composition, and other properties.

The signal intensities are processed and converted into pixels on a display, producing a greyscale image in which variations in intensity indicate differences in surface features or composition. Several samples were tested to obtain cross-sectional images so the results would represent the process accurately [144]. In this research, SEM images were used to study the surface of PS and to determine the thickness of the PS layer before and after laser processing.

2.4.3. Fourier Transform Infrared Spectroscopy

Fourier-transform infrared spectroscopy (FTIR) measures how a sample absorbs light at different wavelengths to identify and quantify various materials. FTIR spectroscopy characterises the electromagnetic spectrum in the infrared (IR) region through the Fourier transform. Infrared radiation induces the molecules to vibrate. The absorption of IR radiation causes the bonds in the molecules to stretch and bend. During the stretch, the length of the bond will increase and decrease. The bend represents a variation of the angle between two bonds. The vibration will be infrared active only if the molecule's dipole moment changes to correspond to the vibration.

Therefore, symmetric vibrations are typically inactive in the infrared. The vibration frequency, ν, is given by:

$$\nu = (1/2\pi c)\sqrt{(k(m_1+m_2)/m_1m_2)} \tag{2.6}$$

where k is the spring constant, whilst m_1 and m_2 are the masses of the atoms [23]. The frequencies at which these vibrations occur provide information about the chemical bonds and molecular structure of the material.

FTIR uses a Michelson interferometer to convert the infrared spectrum into an interferogram, which is then transformed using the Fourier transformation to obtain the spectrum [76, 188]

The Michelson interferometer (Figure 2.5) comprises a beam splitter, a stationary mirror, and a moving mirror. Infrared light from the source is split into two beams, one reflected from the stationary mirror and the other from the moving mirror. When these beams recombine, they create an interferogram containing all the wavelength information. As the moving mirror changes position, a time-domain signal is recorded and then transformed to reveal the frequency-domain spectrum [76].

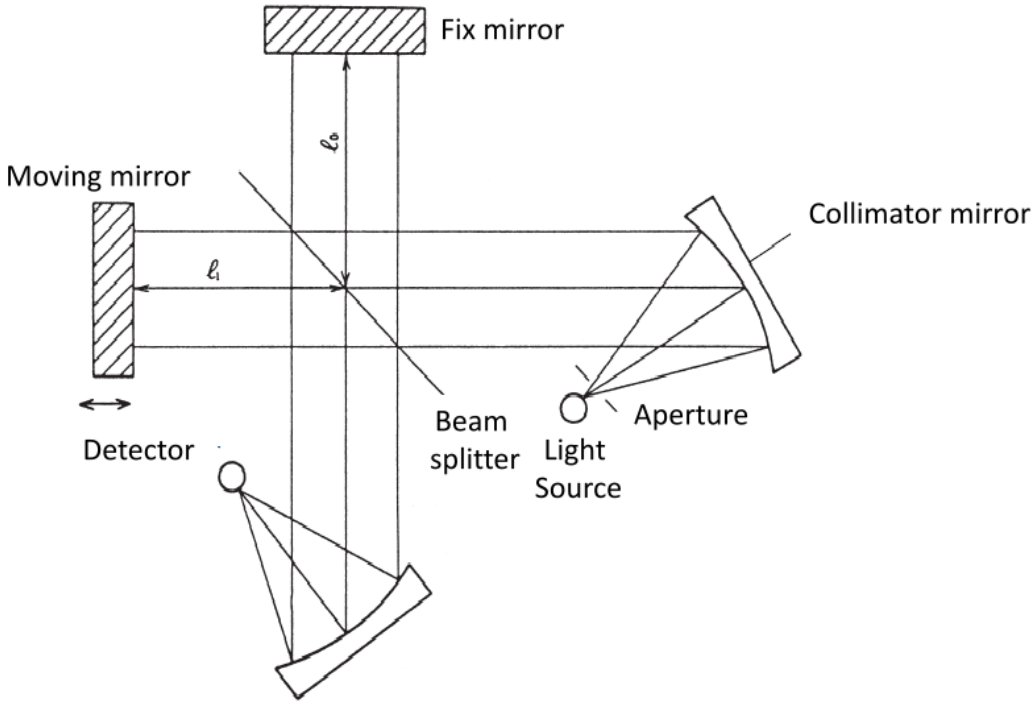

Figure 2.5 Michelson Interferometer, the core of FTIR spectrometers, which splits one beam of light into two beams. (adapted from [195]).

Fourier transform improves sensitivity, speed, and accuracy [83]. The infrared spectrum can be used to study the surface chemistry of PS [111]. IR spectra can identify specific functional groups and bonding types in a material. Each functional group absorbs IR radiation at character-

istic frequencies corresponding to its specific bond vibrations [86]. The location and intensity of the absorption bands in the IR spectrum correlate with the types of chemical bonds present. The functional groups and bonding environments can be identified by comparing the observed IR spectrum with the reference spectra. The IR spectrum is a fingerprint that is used to identify the chemical bond and atom in the sample [180].

To study the chemical structure of the PS surface, FTIR spectra were recorded using a Shimadzu IRAffinity-1S at room temperature in air and under N_2 flow to reduce humidity noise. Measurements were performed once the samples were etched. Measurements were taken daily for 30 days following the etching process to examine the progress of PS oxidation.

2.4.4. Raman Spectroscopy

Raman scattering has been used as a non-destructive tool that can provide extensive information on the structure of solids, such as strain, stress, crystallinity and disorder [44]. When a material is exposed to a monochromatic light source, the light interacts with the matter. It can transmit, reflect, absorb, or scatter. This interaction is influenced by both the material properties and the wavelength of the incident light.

Scattering occurs in two main categories: elastic and inelastic. In elastic scattering, the incident photon with energy E_0 interacts with molecular vibrations that cause the system to rise to some intermediate state. The system returns to its ground state and releases a photon. The scattering photon energy is E; following the energy conservation, the energy of the scattering photon should be equal to the energy of the incident photon ($E_0 = E$), and there is no change in frequency or momentum. This phenomenon is also known as Rayleigh scattering.

In inelastic scattering, the energy of the scattering photon differs from $E_0 = E$ due to the exchange of energy with a particle. If the system is excited from the ground state to a virtual state and then relaxes to a lower energy state, the photon energy increases ($E = E_0 + E_v$), producing anti-Stokes Raman scattering (higher frequency). Conversely, if the energy of the scattering photon decreases ($E = E_0 - E_v$), Stokes-Raman scattering occurs, yielding a lower frequency [45, 173, 88]. Figure 2.6 illustrates the energy-level diagram of the three scattering processes that can occur when light interacts with the phonon.

The full width at half maximum (FWHM) of the Raman peak is important because it provides valuable information in addition to the peak position. Raman peaks can become broader for various reasons. For instance, increasing the temperature can lead to more phonon-phonon interactions and reduce the phonon lifetime, resulting in broader Raman peaks [75].

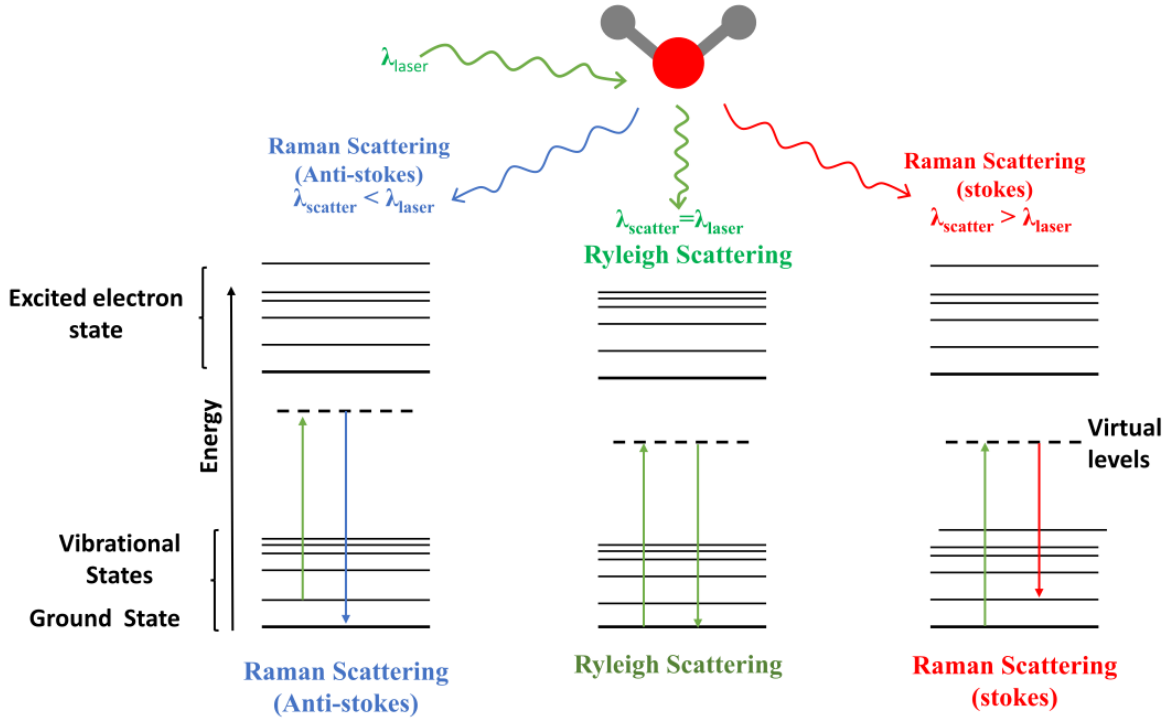

Figure 2.6 Three scattering processes that occur when light interacts with molecular vibrations. The diagram shows Rayleigh, Stokes, and anti-Stokes scattering pathways.

Additionally, higher temperatures cause intensified lattice vibrations and thermal turbulence, further contributing to the broadening of the Raman peak.

Stress and strain can change the distances and angles between atoms in a crystal lattice, leading to variations in phonon vibrational frequencies, which also results in the broadening of the Raman peak [70]. Additionally, stress can cause shifts and splitting of Raman peaks [201]. In an ideal crystal with translational symmetry, first-order Raman scattering arises from phonons at $\mathbf{q} = 0$ (the Brillouin zone centre). However, disorder or finite-size effects can relax momentum conservation, leading to downshifts and a broadening of the Raman peak [202].

In nanomaterials, a reduction in particle size increases the surface-to-volume ratio in nanoparticles, which affects the vibrational states and contributes to peak broadening. For example, crystalline silicon exhibits a sharp Raman peak at 520 cm $^{-1}$, nanocrystalline silicon shows a broadened peak in the range of 510–520 cm $^{-1}$, and amorphous silicon is characterised by a broad peak around 480 cm $^{-1}$ [90]. Bulk materials and nanostructures behave differently under Raman scattering, prompting models such as the phonon confinement model to explain these effects [172]. A phonon wave function in an infinite crystal is given by:

$$\Phi(\mathbf{q}_0, \mathbf{r}) = u(\mathbf{q}_0, \mathbf{r})\, e^{-i\mathbf{q}_0\mathbf{r}} \tag{2.7}$$

where r is the space vector. In the phonon confinement model, phonons in a nanocrystal of diameter L have a modified wave function:

$$\Psi(\mathbf{q}_0,\mathbf{r}) = W(\mathbf{r},L)\Phi(\mathbf{q}_0,\mathbf{r}) = \Psi'(\mathbf{q}_0,\mathbf{r})\,u(\mathbf{q}_0,\mathbf{r}) \tag{2.8}$$

where $W(\mathbf{r},L)$ is a Gaussian weighting function $\exp\left(-2r^2/L^2\right)$. The first-order Raman spectrum, $I(\omega)$, can be expressed as:

$$I(\omega) \cong \int \frac{|C(0,q)|^2 d^3q}{(\omega-\omega(q))^2+(\Gamma/2)^2} \tag{2.9}$$

where $|C(0,q)|^2$ is a weighting function, q is the wave vector of the phonon, $\omega(q)$ is the dispersion curve for optical phonons, and Γ is the natural linewidth [31].

In this research, Raman spectroscopy was used to study the crystal structure of PS and the effects of laser writing. Measurements were performed at a wavelength of 532 nm and room temperature, using low laser power to avoid local heating.

Surface-Enhanced Raman Spectroscopy

Surface-enhanced Raman spectroscopy (SERS) is an advanced form of Raman spectroscopy that significantly enhances the Raman scattering signal by several orders of magnitude. This enhancement is achieved through the electromagnetic interaction between light and rough metal surfaces, generally known as plasmon resonances. The molecules being analysed are attached to or located very close to the metal surface [121]. As explained previously, Raman scattering is the inelastic scattering of photons when they interact with matter. Because Raman scattering is typically weak, SERS provides a way to significantly enhance the signal. Theoretically, two mechanisms describe SERS: electromagnetic enhancement (EM) and charge transfer (CT), also known as chemical enhancement [140].

Electromagnetic enhancement in SERS occurs when localised surface plasmon resonances (LSPR) are excited on the metallic substrate. Localised surface plasmons are collective oscillations of conduction electrons confined to the surface of a metallic nanoparticle. Their resonance is determined by the size, shape, material and arrangement of the metallic nanostructures. If the incident light frequency matches the electrons' oscillation frequency, an intense electromagnetic field localises near the surface, known as LSPR [78, 173].

The chemical contribution to SERS comes from the charge transfer between the adsorbed molecule and the metal surface, amplifying the Raman signal. This mechanism involves the

formation of a chemical bond between the molecule and the metal surface, resulting in a resonant Raman process that increases the Raman scattering cross-section. Although this chemical enhancement is often smaller than the electromagnetic enhancement, it can be significant or molecules capable of strong chemical bonding with the metal [183].

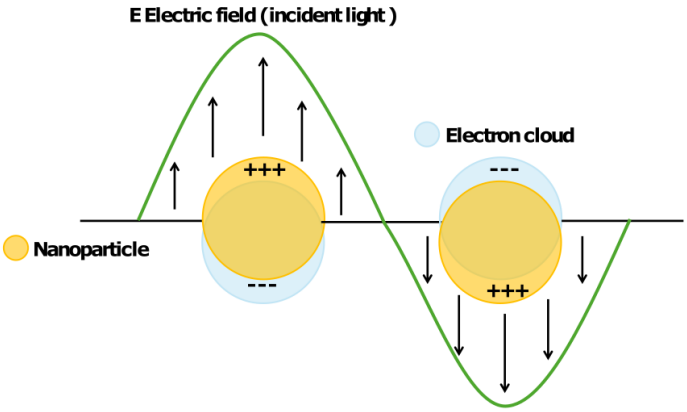

Figure 2.7 Collective oscillations of electrons in a nanoparticle under an external electric field.

Figure 2.7 shows the collective oscillations of electrons in a nanoparticle when exposed to an external electric field.

2.4.5. Atomic force microscopy

Atomic force microscopy (AFM) is a type of scanning probe microscopy (SPM), developed in 1985 [25], that uses a probe to measure localised characteristics (e.g., surface topography). It is widely applied to investigate the properties of grains, phases and surface layers in ceramics, metals, polymers, and composites [196].

The AFM probe features a sharp tip mounted on a flexible cantilever. Attractive and repulsive forces between the tip and the sample surface generate a high-resolution, three-dimensional topographic image. Resolutions of a few nanometres are achievable. Typically, the AFM setup includes a microscope stage, an electronic control system, and a computer interface. The microscope stage often incorporates an optical microscope for sample observation and is placed on a vibration isolation platform to reduce noise. The cantilever, usually made of silicon or silicon nitride, is attached to a piezoelectric (PZT) operator, and a position-sensitive photodetector receives a laser beam reflected from the cantilever tip. The detector signals provide feedback on the cantilever deflection, which the electronic control system uses to adjust the movement of the scanner. Hence, the AFM can maintain a consistent force or height above the sample [54]. Figure 2.8 presents a schematic of the AFM setup.

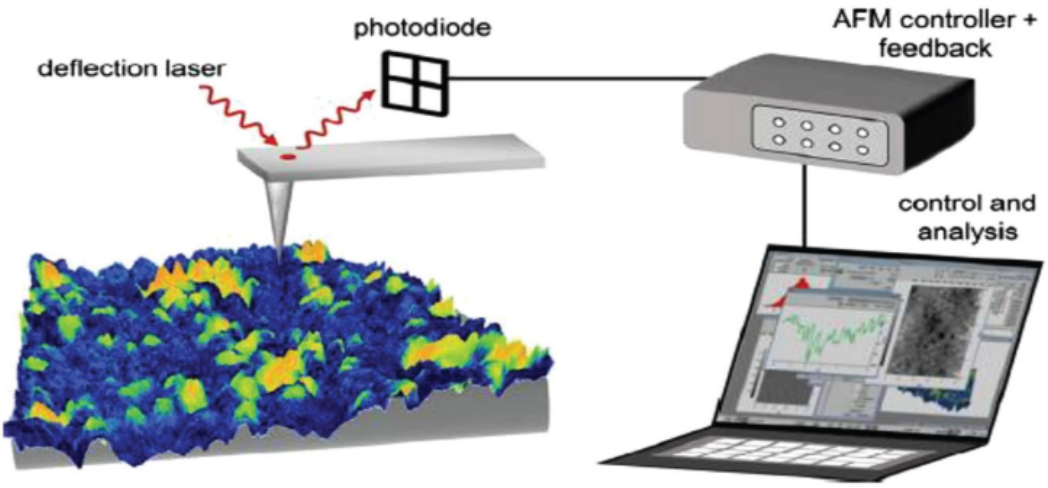

Figure 2.8 A schematic of the AFM setup, showing the main components for scanning and feedback control (adapted from [196]).

AFM involves continuously scanning a sharp tip across the surface of a sample. This scanning process is guided by feedback mechanisms that allow piezoelectric (PZT) scanners to precisely control the position of the tip, ensuring that it maintains a consistent force or height above the surface. AFM can be operated in three primary imaging modes: contact, tapping, and non-contact. In contact mode, the tip remains in continuous contact with the sample surface, and cantilever deflection provides topographical data. Tapping mode involves oscillating the cantilever near its resonance frequency so that the tip intermittently contacts the surface, reducing lateral forces and sample damage. Finally, non-contact mode keeps the tip oscillating slightly above the surface, detecting van der Waals forces to form the image.

Computer-defined parameters manage the scanning process. As the tip scans the surface, it moves vertically in response to surface contours. The deflection of the cantilever is measured by the deviation of the laser beam, and a photodiode records the difference in light intensities. This signal is used to adjust the scanner in real-time, ensuring consistent force or height. The constant force PZT transducer records height deviations, and in the constant height mode, the deflection force is measured on the sample [93].

AFM data are digital by default, making post-processing straightforward. Common steps include filtering, background subtraction, and levelling (also called flattening). If the substrate is tilted relative to the scanner, the background tilt can mask small height variations in the sample. Therefore, polynomial fitting and subtracting the substrate background is crucial to

ensure accurate measurements [231]. Figure 2.9 displays an example of flattening AFM images for clarity.

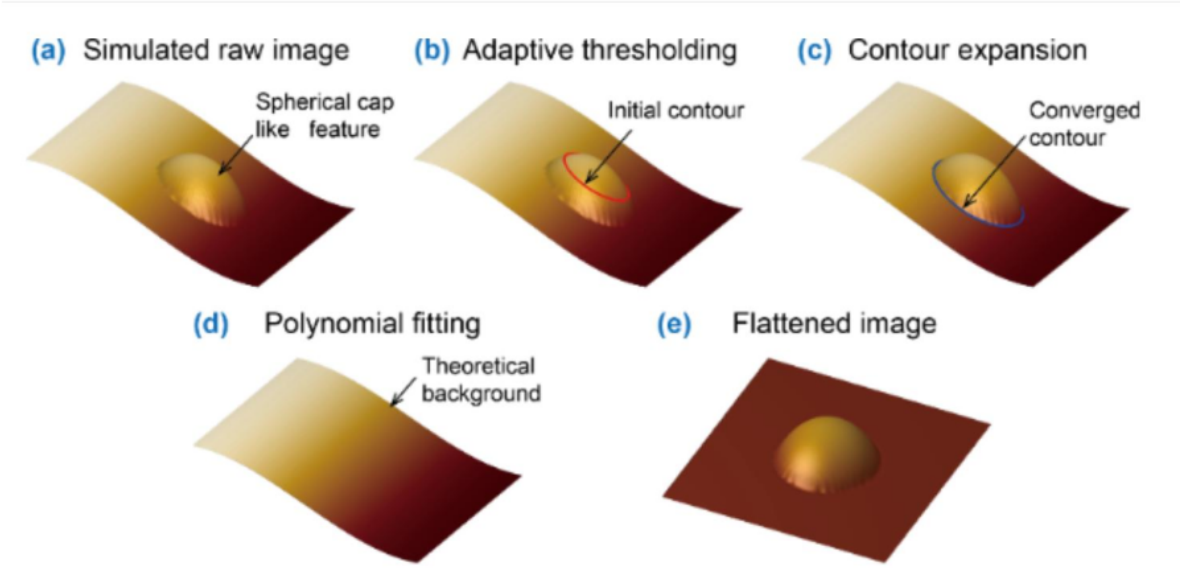

Figure 2.9 Illustration of the suggested technique for flattening AFM images. a) Sketch of an inflated AFM height image with a tilted background. b) The adaptive thresholding method is used to find a feature in the image. c) Find the edges of an object by expanding the contours to find the main mask area. d) The surface was made by fitting the background as a polynomial surface and leaving out the mask area for the centre. e) The image flattened by taking away the polynomial surface of the original image. (Figure taken from [231]).

A multimode-8 atomic force microscope with a Nanoscope V controller and (J) scanners (Bruker) was used to acquire AFM data. An active vibration isolation system (Nano Series, Accurion) was used to reduce vibrational noise. Nanoscope software version 9.2 was used to control the microscope. The system was operated in tapping mode in the air. The AFM data were processed with NanoScope Analysis 1.8 software (Bruker). Silicon tips on silicon cantilevers (NCHV, Bruker) were used to collect images. The nominal tip radius was approximately 8 nm, frequency 300 kHz, and spring constant $k = 42\ Nm^{-1}$.

2.4.6. Kelvin Probe Force Microscopy

Kelvin Probe Force Microscopy (KPFM) is a variation of Atomic Force Microscopy (AFM) used to measure the contact potential difference (CPD) between the sample surface and the tip. CPD reflects the difference in electric potential between two materials resulting from their different work functions. The work function is the energy required to remove an electron from a material's surface to a point in space, making it a fundamental material property.

During contact mode operation, the AFM tip physically contacts the sample surface, leading to tip cantilever bending due to the repulsive force between the tip and the sample. The cantilever deflection serves as a feedback signal. In tapping and non-contact mode at AFM, the tip oscillates above the surface, and changes in amplitude or frequency indicate attractive or repulsive forces. These variations are used as feedback signals to determine the topography of the sample surface [142].

In tapping mode, the change in amplitude reflects variations in tip-sample interactions. Because the tip and sample can function as two conductive surfaces separated by a small gap, they form a capacitor with capacitance C. The electrostatic force between the tip and the sample $F_{es}$is given by:

$$F_{es} = \frac{1}{2}\frac{dC}{dz}\left(V_{cpd}\right)^2 \tag{2.10}$$

where C is the capacitance between the tip and the sample surface, z is the distance between the tip and the sample, and V_{cpd} the contact potential difference, linked to the difference in work functions:

$$V_{cpd} = \frac{\Delta W}{e} \tag{2.11}$$

where ΔW is the difference in the work function and e is the electron charge [94]. In this project, the KPFM was used to investigate the electrical properties of laser-written samples and detect any changes in doping concentration in those regions.

2.4.7. X-ray Diffraction

X-ray diffraction (XRD) is a powerful technique for investigating the crystal structure and properties of materials. It relies on the principle of constructive interference of X-rays as they interact with atomic planes in a crystal. When X-rays encounter the lattice, they scatter. Due to the periodic arrangement of atoms, constructive interference occurs at specific angles, forming a distinctive diffraction pattern.

According to Bragg's law:

$$2d\sin\theta = n\lambda \tag{2.12}$$

where d is interplanar spacing, θ is the angle between the incident X-ray beam and the crystal plane, n is an integer representing the order of the diffraction peak, and λ is the X-ray wavelength. Measuring these diffraction angles and intensities reveals the crystal's atomic arrangement [104].

The method of XRD involves several steps. First, a crystal is prepared and placed in the path of an X-ray beam. The X-rays interact with the crystal lattice and scatter in different directions. A detector, such as a photographic plate or a modern electronic detector, records the pattern formed by the diffracted X-rays. The diffraction pattern consists of a series of spots or peaks, which correspond to the scattering of X-rays at specific angles and intensities. These spots can be analysed using mathematical techniques, such as Fourier transformation, to extract information about the atomic or molecular structure of the crystal.

2.4.8. Synchrotron X-ray radiation for Material Analysis

A synchrotron is a circular particle accelerator used to generate high-intensity electromagnetic radiation (the setup shown in Figure 2.10). Free electrons, produced by an electron gun (via a heated tungsten filament), the generated electrons were collected by an electric field and guided towards the linear accelerator (LINAC), then accelerated near-light speed. Once this speed is reached, the electrons are sent to a circular accelerator known as the booster ring. Inside the booster ring, the electrons move along a circular path and undergo controlled energy stimulation from radio frequency cavities. This stimulation enhances the energy of the electrons before they are transferred to the storage ring. The strength of the magnetic field in the booster ring increases as the electron velocity increases, following the relationship:

$$r = \frac{mv}{qB} \tag{2.13}$$

where r is the radius of the circular path on which the charged particle travels, m is the mass of the charged particle, v is the velocity of the particle, q is the charge of the particle and B is the magnetic field strength.

In the storage ring, electromagnetic dipoles cause the electrons to travel in curved paths. These electromagnetic dipoles, also called insertion devices, are placed in straight sections of the storage ring, which apply an alternating magnetic field to induce electron oscillation while maintaining an overall straight pathway. Then, electrons emit synchrotron radiation. Finally, the synchrotron radiation reaches the beamline tangential to the storage ring. At the beamline, radiation is usually (but not always) monochromatic and is focused using X-ray optics on a sample [158, 233].

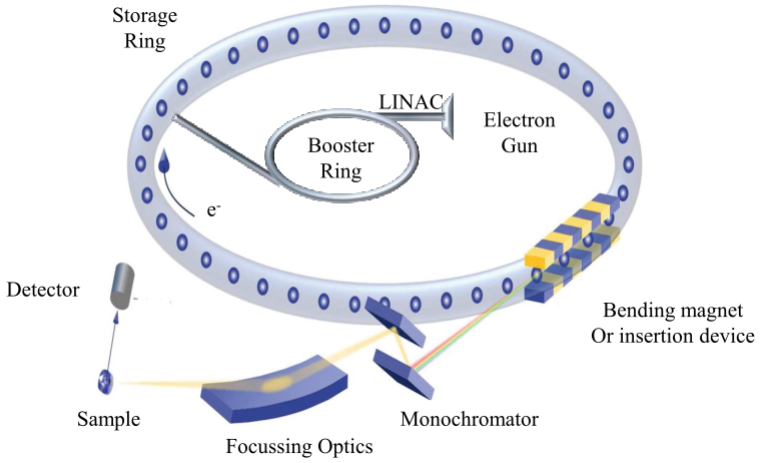

Figure 2.10 Schematic of a synchrotron accelerator: electrons are accelerated in the LINAC, boosted in the booster ring, and stored at high speed. Bending magnets direct the electron beam, which emits synchrotron radiation. (Modifications have been made to the Figure taken from [186]

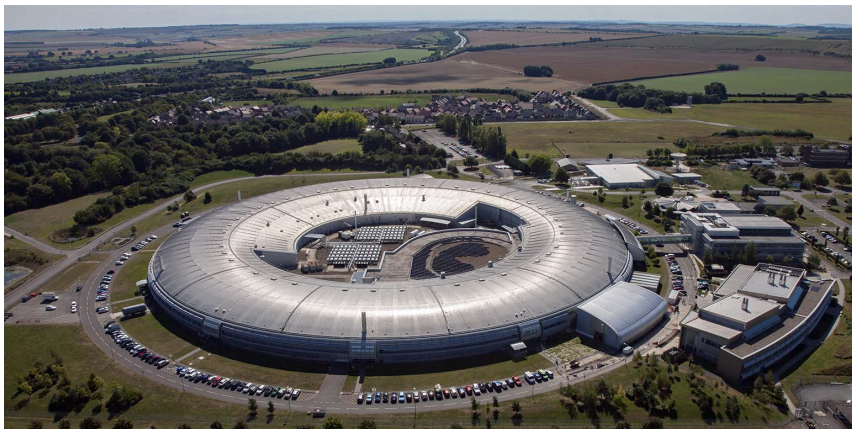

Figure 2.11 Diamond Light Source the UK's national synchrotron light source.(Figure taken from [127].

The properties of synchrotron radiation depend on the characteristics of the storage ring. Synchrotron radiation exhibits high intensity, a broad and continuous spectral range from infrared to hard x-rays, inherent narrow angular collimation, a high degree of polarisation, pulsed time structure, high brightness resulting from the small cross section of the electron beam, and a high degree of collimation of the emitted radiation. This phenomenon occurs in an extremely high vacuum environment and provides stability to the beam. All these characteristics can be quantitatively determined using quantitative methods [145].

Due to these properties, synchrotron radiation is suitable for studying the crystal structure of nanomaterials, including symmetry, bonding, unoccupied states densities, bond length, local disorder, and origin of luminescence from light-emitting materials [192]. In this project, the Diamond Light Source science facility located at the Harwell Science and Innovation Campus in Oxfordshire (UK) was used as the synchrotron light source to study the crystal structure of the laser writing line (Figure 2.11).

2.4.9. X-ray photoelectron Spectroscopy

X-ray photoelectron spectroscopy (XPS) is a technique used to analyse the chemical composition of the electronic state of the surface of a material (< 10 nm). The XPS is an ultra-high vacuum technique. It involves irradiating the sample with high-energy X-rays, causing the ejection of photoelectrons from the atoms of the material surface (see Figure 2.12).

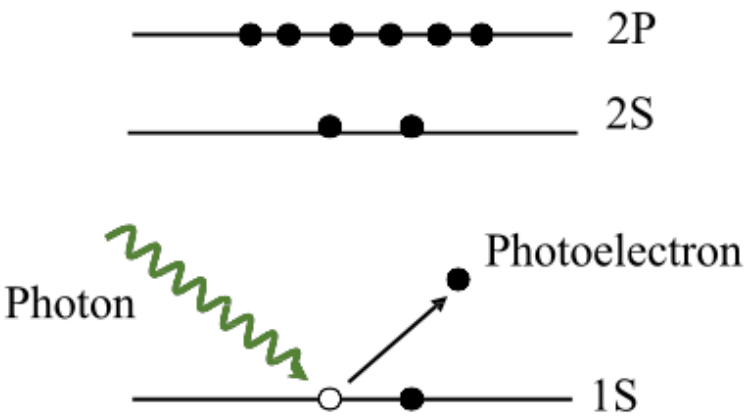

Figure 2.12 Diagram illustrating XPS photoelectron emission from a sample surface under X-ray irradiation.

The kinetic energy and a variation in the binding energy are measured by a hemispherical analyser; the Fermi level of an electron is dependent on a chemical shift, often referred to as a variation in the oxidation state or a change of the electronic charge distribution around the nucleus. This shift arises from variations in the chemical bonding of the element and its surrounding environment, following the relation

$$E_B = h\nu - E_k - \phi \tag{2.14}$$

where E_k is the kinetic energy and E_B is the binding energy. It is the difference in energy levels between the initial and final states after the emission of the photoelectron of the atom; h is Planck's constant, ν is the frequency of the X-ray photon, and ϕ is the work function of the spectrometer; both are constant for a given spectrometer [110]. The Fermi level is used as the reference energy level and represents the highest energy electrons that are normally occupied. In XPS, the sample and spectrometer are connected, so their Fermi levels line up. The work function ϕ is the energy needed to move an electron from the Fermi level to outside the spectrometer. Since kinetic energy is measured from the vacuum level of the spectrometer, the work function

must be subtracted to get the correct binding energy. Both $h\nu$ and ϕ stay the same for a given setup

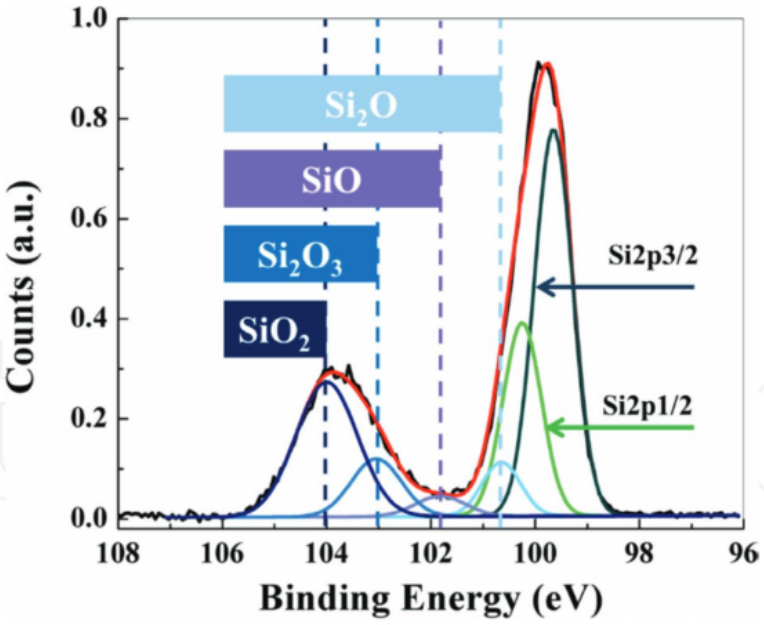

Figure 2.13 XPS spectrum of Si2p core-level emission showing two silicon and four oxide peaks (this Figure taken from [148]).

Chemical shifts reflect changes in the oxidation states or electronic environments. For instance, levels of p, d, and f will split after ionisation to $p_{1/2}, p_{3/2}$, $d_{3/2}$, $d_{5/2}$, $f_{5/2}$, and $f_{7/2}$. The spin-orbit splitting ratio is 1:2 for p levels, 2: 3 for d levels, and 3: 4 for f levels [36].

2.4.10. Secondary Ion Mass Spectrometry

Secondary Ion Mass Spectrometry (SIMS) is a nanoscale surface analysis technique. A high-energy primary ion beam bombards a solid surface, initiating a collision cascade beneath the surface (Figure 2.14).

Energy transfers from the primary ions to the surface atoms, breaking bonds and ejecting particles. This ejection process is known as sputtering. Most of the sputtered particles are neutral, but about 1% are ionised. Only these ionised particles can be analysed by a mass spectrometer.

The core principle of SIMS involves the high-energy ion beam striking the solid surface, which leads to the removal and ionisation of secondary ions from the surface of the sample. The collision cascade theory explains the sputtering and ionisation mechanisms. Using a mass analyser, an electric field extracts secondary ions from a mass spectrometer, sorting them according to their mass-to-charge (m/z) ratios. Finally, the separated ions are directed to a

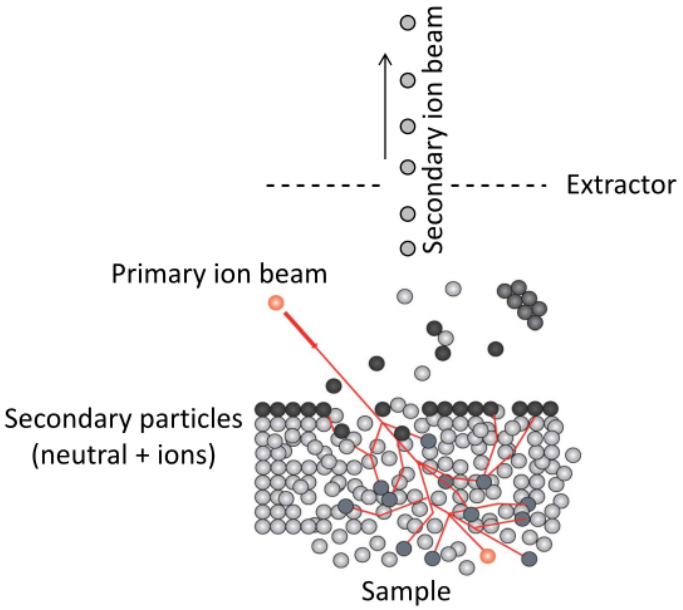

Figure 2.14 Diagram Illustration of primary-beam collisions in SIMS, leading to sputtered ions and the creation of a crater (adapted from [191]).

detector, which generates a mass spectrum by plotting the signal intensity of the detected ions against their m/z ratios [5, 191].

SIMS is a destructive technique because surface erosion occurs during measurements. It is extremely sensitive to surface contaminants that can interfere with analysis. Even minor contamination can significantly affect the results. Although SIMS excels at surface analysis, its depth resolution can be limited, particularly for very thin layers. The sputtering process may also cause layer mixing, decreasing depth accuracy. Furthermore, SIMS requires a high vacuum environment, restricting the samples that can be analysed and complicating preparation and handling [162].

2.4.11. Electrical Characterisation Measurements ((I-V) Measurements)

The electrical properties of semiconductors are determined by their ability to conduct an electric current which is influenced by parameters such as doping concentration, carrier mobility, and temperature. Resistance, a fundamental electrical characteristic, measures the extent to which a material impedes the flow of electric current. The concentration of charge carriers (electrons and holes) in semiconductors affects resistance, and this concentration can be controlled by doping. Doping involves the addition of impurities to a semiconductor to increase the concentration of electrons (n-type) or holes (p-type), thereby reducing the resistivity of the material.

The two-probe method is commonly used to measure the resistance of a semiconductor (Figure 2.15). This technique consists of applying an electrical current between two probes. A current is passed through the sample through one pair of contacts, while the voltage drop is measured across the same pair of contacts or another. Although straightforward, the two-probe method can be affected by the contact resistance between the metal probes and the semiconductor, leading to inaccuracies in resistance measurement. The quality of contacts and calibration are essential. The method allows measuring the resistance of an object with known geometry, limiting the comparison of results for devices of different sizes [118].

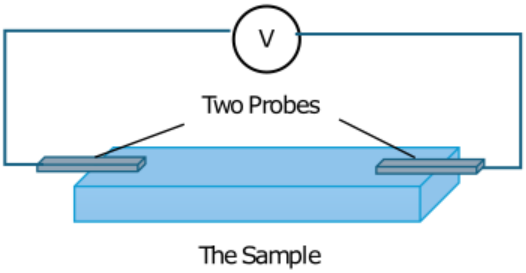

Figure 2.15 Two probe method for measuring electrical resistance.

In this study, electrical measurements were performed using a Cascade Microtech probe station and an Agilent B1500A semiconductor analyser. Tungsten probe tips (with 10 µmradius) contacted the sample. Current measurements spanned voltages from $-2V$ to $+2V$ in 50 mV increments, under nitrogen atmosphere and under dark conditions.

I-V curves at different temperatures were obtained at the probe station using a thermal chuck system (Model ETC-200 L, ESPEC, Japan). The samples were connected to the probe station, and the current-voltage curves were collected.

2.4.12. Temperature Dependence of Electrical Properties in Semiconductors and Porous Silicon

PS is created by electrochemical etching of silicon (a semiconductor). Semiconductors is a fundamental material in modern electronics, and the electrical properties for both PS and silicon are sensitive to temperature. Understanding how temperature affects their conductivity, carrier mobility, and resistance is critical to improving device performance in various applications. Although the temperature dependence of semiconductors has been extensively studied, PS presents additional complexity because of its porous structure and surface states. Temperature affects the concentration and mobility of charge carriers in semiconductors. For intrinsic semiconductors, the number of thermally generated electron-hole pairs increases exponentially

with temperature. Carrier concentration (n_i) can be expressed as:

$$n_i = AT^{3/2} \exp\left(-\frac{E_g}{2k_B T}\right) \tag{2.15}$$

where E_g is the bandgap energy, k_B is Boltzmann constant, and T is the temperature. A is a constant that depends on the properties of the semiconductor, such as the effective density of states in the conduction band (N_C) and the effective density of states in the valence band (N_V):

$$A = N_C N_V \tag{2.16}$$

Where N_C is the effective density of states in the conduction band:

$$N_C = 2\left(\frac{2\pi m_n^* k_B T}{h^2}\right)^{\frac{3}{2}} \tag{2.17}$$

where m_n^* is the effective mass of electrons, and h is Planck constant,and N_V is the effective density of states in the valence band:

$$N_V = 2\left(\frac{2\pi m_p^* k_B T}{h^2}\right)^{\frac{3}{2}} \tag{2.18}$$

where m_p^* is the effective mass of holes [207].

Temperature has a more nuanced effect on extrinsic semiconductors, which are doped with impurities that introduce free charge carriers. At low temperatures (the freeze-out region), thermal energy is insufficient to ionize the dopant atoms, resulting in a low carrier concentration. As the temperature increases to moderate levels, these dopant atoms become fully ionized, and the semiconductor enters the extrinsic region, where conductivity is primarily determined by dopant concentration. At higher temperatures, however, thermally generated carriers can outnumber those introduced by the dopants, further affecting the overall conductivity [197].

The electrical properties of PS, prepared by electrochemical etching of silicon, have gained interest as a result of its low conductivity compared to the conductivity of the substrate. Since the surface area and porosity of PS are large, the charge carriers will be trapped in the surface defects, called charge traps; as a consequence, conductivity will decrease [123].

Models developed to explain the temperature-dependent electrical conductivity in porous silicon (PS) often assume that conduction occurs only once a continuous network of silicon nanowires is formed. At low temperatures, these nanowires remain partially disconnected, resulting in low conductivity. As the temperature increases, more interconnections develop

among the nanowires, increasing conductivity [194]. Furthermore, at higher temperatures, some carriers escape from traps via a Poole-Frenkel field-assisted emission mechanism, which lowers the energy barrier for thermal emission [59]. This additional release of carriers further boosts conductivity. Such thermally activated behavior can be described by an Arrhenius-type model:

$$\sigma = \sigma_0 \exp\left(-\frac{E_a}{kT}\right) \tag{2.19}$$

where σ_0 is a pre-exponential factor, E_a is the activation energy required to release trapped carriers. In this project, I-v measurement (Section 2.4.11) has been done in the temperature range of 283˜273 K to study the electrical properties of the laser-irradiated area.

2.5. Conclusion

This chapter presents a comprehensive overview of PS, beginning with the electrochemical etching of silicon wafers and culminating in detailed characterisation and laser irradiation studies. Multiple techniques, including SEM, FTIR, Raman (including SERS), AFM, and KPFM, were employed to explore the microstructure, chemical bonding, and electronic features of PS. Advanced methods such as X-ray diffraction, synchrotron X-ray analysis, XPS, and SIMS further enabled insight into the crystallographic, compositional, and surface properties of both unprocessed and laser-processed PS.

The investigation also included the use of a continuous-wave CO_2 laser to modify selected regions of PS samples. Different power levels and scanning speeds were tested to study changes in surface morphology and potential alterations in material properties. Electrical I–V measurements, performed over a range of temperatures, provided data on the resistivity and conduction mechanisms. Additionally, KPFM was used to examine whether laser irradiation might affect doping concentration in the laser-irradiated areas, although no definitive conclusions about doping changes were drawn here.

Overall, the chapter underscores the versatility of porous silicon as a platform for laser-based modification, highlighting the value of multitechnique characterisation to capture morphological, chemical, and electronic nuances. These approaches lay the groundwork for further investigations into how laser processing may influence doping levels, surface chemistry, or device performance, indicating a broad spectrum of potential applications in sensors, microelectronics, and optoelectronic components.

Chapter 3. Porous Silicon Formation

3.1. Introduction

PS has become a significant material due to its unique optical [153], electrical [143] and structural properties [21], which generate considerable attention for a wide range of applications in fields such as optoelectronics, sensors [68] and biomedical devices [139]. The transformation of crystalline silicon into a porous structure through different fabrication techniques and procedures creates opportunities for customising the properties of the material for specific applications. The controllable porosity and thickness of the PS layer significantly influence the performance and applicability in numerous domains. Electrochemical etching is a widely used method for producing PS due to its cost effectiveness and ease of implementation [185]. Silicon is anodised in hydrofluoric acid under controlled current densities and etching times. Management of PS characteristics is carried out by modifying the density and duration of the oxidation current, which directly influences its thickness and porosity.

In this chapter, the effect of modification of the electrochemical process parameters on the structural properties of PS was analysed using techniques such as gravimetric methods, AFM and SEM. Surface chemistry influences those final characteristics of PS. FTIR spectroscopy and Raman spectroscopy are critical techniques for characterising the chemical bonding and vibrational features of the PS surface. In addition, XPS provides details about the chemical composition of the material. In this chapter, these characterisation methods were further explored to improve understanding of the structural and surface modifications occurring during PS formation.

AFM is widely used to investigate the surface structure of PS, providing significant information on the roughness and shape of the material at the nanoscale. Using FTIR, Raman and XPS analysis, AFM provides a deep understanding of the connection between fabrication conditions and the resulting properties of PS, supporting the optimisation of the material for specific applications.

3.2. Cleaning the Surface of the Substrate

Cleaning the surface of the silicon substrate is an essential step to eliminate organic and inorganic contaminants that could negatively impact subsequent electrochemical etching and laser processing. The substrate was cut into pieces approximately 1 cm × 1 cm, and the back surface was lightly abraded with sandpaper to prepare it for further processing. Figure 3.1a shows microscope images of the sample after cutting, while Figure 3.1b shows microscope images of the sample after polishing.

In the initial cleaning stage, the silicon pieces were immersed in acetone for five minutes to dissolve the dirt residues, followed by drying with nitrogen gas (Figure 3.1c). The silicon was then immersed in a piranha solution composed of sulfuric acid and hydrogen peroxide in a 4:1 ratio to remove any remaining organic contaminants [179]. After 20 minutes, the silicon pieces were thoroughly rinsed with deionised water to remove traces of the piranha solution. Finally, the samples were dried with nitrogen and a gallium-indium eutectic was applied to the rear surface (Figure 3.1d). It is important to note that even after these cleaning steps, the surface of the silicon substrate can still become contaminated with dust and other particles. This highlights the critical importance of thorough and meticulous cleaning procedures to ensure that the substrate is properly prepared for subsequent processes. Ensuring a clean surface is essential for achieving optimal results in etching and laser processing.

As shown in Figure 3.1, it was evident that the contamination on the silicon substrate was not due to any of the materials used in the cleaning or drying processes. After several attempts to address this issue, a new method was developed for this project to remove all contaminants from the surface effectively. This approach involves wiping the substrate surface with a cotton bud soaked in acetone after cutting and abrading the back surface with sandpaper before the piranha cleaning step, as shown in Figure 3.2d.

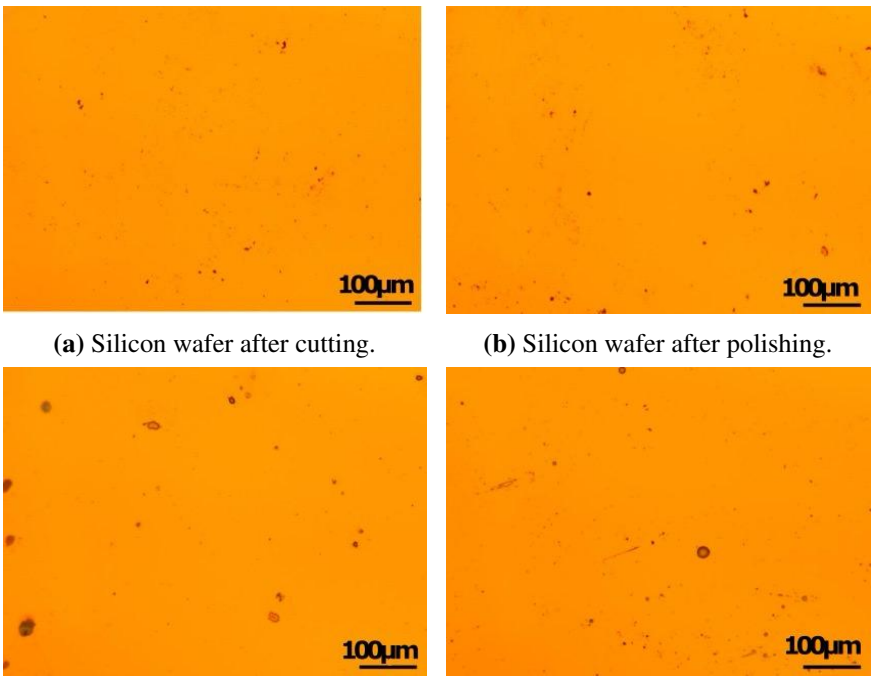

(a) Silicon wafer after cutting.

(b) Silicon wafer after polishing.

(c) Silicon wafer after cleaning with acetone.

(d) Silicon wafer after cleaning with piranha solution.

Figure 3.1 Microscope images showing the Si substrate surface after cutting and polishing without using a cotton bud: a) silicon wafer after cutting, b) silicon wafer after polishing, c) silicon wafer after cleaning with acetone, d) silicon wafer after cleaning with piranha solution.

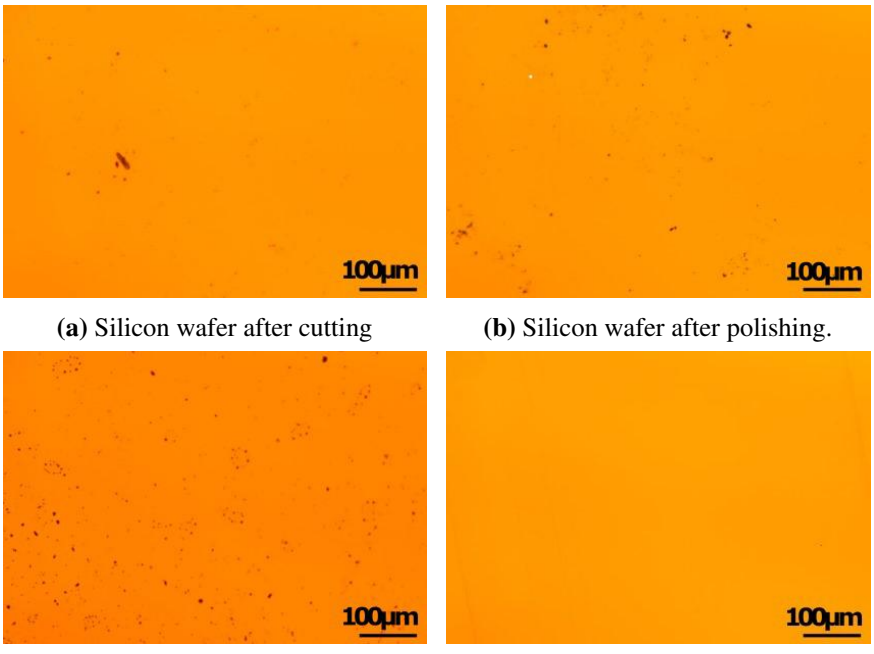

(a) Silicon wafer after cutting

(b) Silicon wafer after polishing.

(c) Silicon wafer after cleaned with acetone.

(d) Silicon wafer cleaned with cotton swab dipped in acetone.

Figure 3.2 Microscope images illustrating the Si substrate surface before and after cutting and polishing using cotton swab: a) silicon wafer after cutting, b) silicon wafer after polishing, c) silicon wafer after cleaned with acetone, d) silicon wafer cleaned with cotton swab dipped in acetone.

3.3. Electrochemical Etching for Formation of Porous Silicon

To create the PS layer, the boron-doped p-type silicon wafer (100) ($1 - 10$ Ω.cm, PI-KEM, Tamworth, UK) was cut to $1\ \text{cm} \times 1\ \text{cm}$ chips using a diamond scribe. The unpolished surface of the wafer was then treated with sandpaper in preparation for applying a coating of gallium-indium eutectic to enhance the back connection between the Si chip and copper plate. After this, the chips were soaked in acetone for five minutes and the shiny surface was wiped with acetone-soaked cotton buds to remove grease. Subsequently, a piranha etch (4:1) (H_2SO_4 30% w/w H_2O_2(aq)) was applied for 20 minutes to remove organic and inorganic contaminants. The chips were then rinsed multiple times with deionised water to ensure that no piranha etch solution remained. Subsequently, the gallium-indium eutectic was applied to the sanded surface. The chips were then placed with the shiny side facing in an electrochemical cell and etched using a solution of hydrofluoric acid (with a concentration of 40%) and absolute ethanol in a 1:1 ratio.

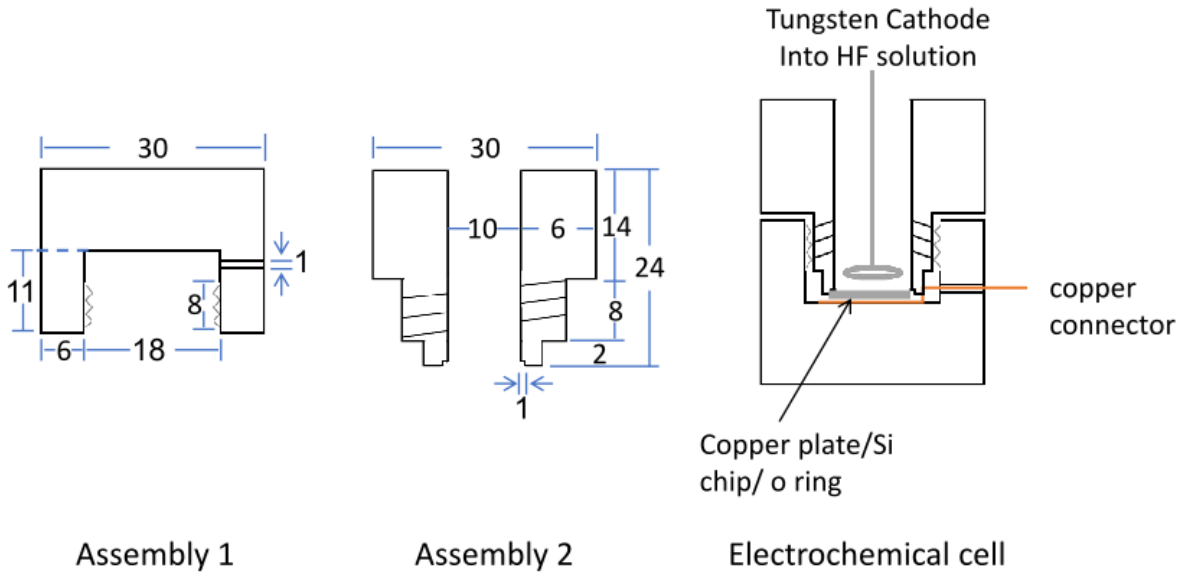

Figure 3.3 Schematic cross-section of Teflon electrochemical cell with the dimensions given in mm.

Figure3.3 shows the cross sections of the two parts of the electrochemical cell with the dimensions given in mm. Both assemblies were fabricated from polytetrafluoroethylene (PTFE). PTFE was chosen because it is resistant to HF. Assembly 1 consists of a cylindrical hole of 18 mm diameter and 11 mm height. The cylindrical hole has diagonal lines representing an internal thread of 8 mm. A copper plate was placed at the base of the PTFE connected to a copper wire that exits through a 1 mm diameter hole drilled in Assembly 1 to allow connection to the external circuit. Assembly 2 has a diagonal line that displays the external thread 8 mm. The exact size is the internal thread of Assembly 1. The two parts were securely attached using the thread. The

electrolyte solution of HF/ethanol is housed in Assembly 2 by a cylindrical hole with a diameter of 10 mm and a height of 24 mm (volume 2 mL). A Viton O-ring with an outer diameter 10 mm and an inner diameter 8 mm was installed in a radial groove that is 0.5 mm deep and 1 mm broad at the top end of Assembly 2. The Viton was chosen because of its resistance to HF.

The following method was employed for anodic electrochemical etching:

1. The Si chip was placed on the copper plate in Assembly 1 (clean side facing up), ensuring the top surface was clean and not contaminated.

2. Screw Assembly 2 and Assembly 1 together and keep the assemblies upright. To complete the electrochemical cell assembly as revealed in Figure 3.3, Assembly 2 was spun clockwise to push the silicon wafer on the O-ring against the copper anode to ensure contact once Assembly 1's inner thread and Assembly 2's internal thread made contact.

3. Deionised water was used for a five minute leakage test. The electrochemical cell impenetrability was then confirmed. A hydrofluoric acid (40% concentration) solution (HF: ethanol) (1:1) was prepared and transferred to the electrochemical cell using a plastic pipette.

4. The tungsten wire is used as a cathode in this electrochemical cell (immersed in HF/ethanol). A loop was made at the end of the wire to ensure an even distribution of the electric current during etching. The etching process was begun at room temperature using an electric bias for a fixed time.

5. Upon completion of the etching, the HF/ethanol electrolyte was replaced with deionised water. The sample was first laterally washed with HF to remove the eutectic, then washed with deionised water (type I with a nominal resistivity of > 18.2 MΩ.cm from a Millipore water system was used throughout). The chip was dipped in ethanol to remove the hydrofluoric acid residue from the porous chip and to remove the residual species in the pores. Finally, it was washed with hexane because hexane has a lower surface tension, which helps prevent the walls of the pores from being damaged by pressure (see Section 3.4).

Figure 3.4 is an image of the Teflon cell used in the electrochemical etching of silicon. Figure 3.4 a shows the two assemblies are fastened with the wire to connect to the external circuit, where Figure 3.4 b) shows the two assembled disconnect, the O-ring attached to Assembly 2, and the copper plate rests on the bottom of the groove of Assembly 1 to connect the back electrode.

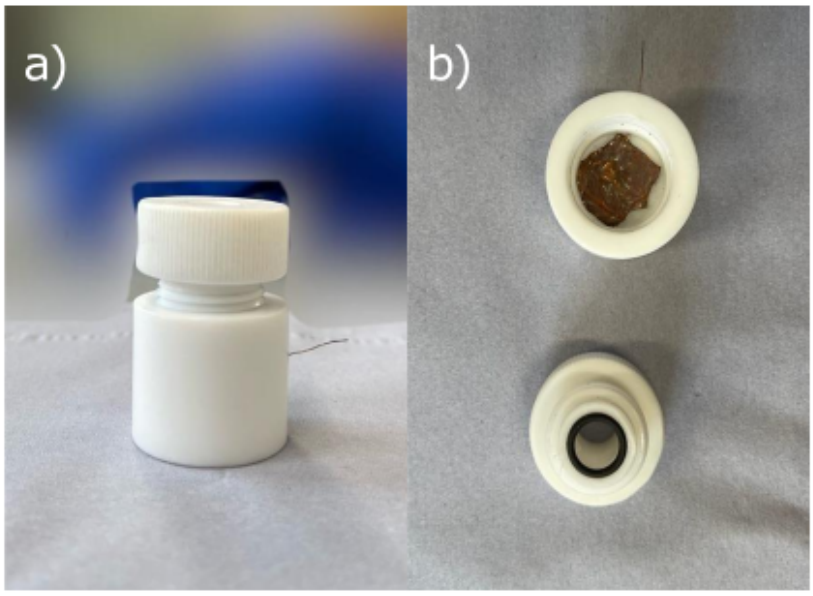

Figure 3.4 a) Teflon etch cell and copper wire. Copper wire be connected to the external circuit. b)The rubber o-ring seals the HF solution inside the vessel and copper contacts the back electrode.

A range of 1 to 10 mA as anode current was applied for 1 to 100 minutes in the etching process to avoid cracks and obtain a uniform thickness of the created PS layer [240]. After being allowed to dry, different methods were exploited to characterise the samples, regardless of whether the analysis was microscopic (optical microscope, SEM and AFM) or spectral (FTIR and Raman).

3.4. Rinsing and Drying a Porous Layer

After anodisation, a significant amount of toxic substances remain in the sample, including electrolyte (HF) and by-products such as silicon tetrafluoride and hexafluorosilicic acid . Considering the subsequent chemical reaction between H_2SiF_6 and water, this process can lead to the formation of metasilicic acid . Metasilicic acid can potentially undergo polymerisation, resulting in the formation of a less soluble gel known as polysilicate. Over time, this gel can solidify, effectively trapping any remaining fluoride species [130]. Such polymeric species were not observed at the applied current densities.

The anodised sample was rinsed with water. However, because of the inherent hydrophobic nature of the sample, water cannot enter the pores. Therefore, it is recommended to rinse the sample with alcohol before drying [131]. The PS layer exhibits a coloured reflection when wet, but collapses when exposed to air. During air drying, capillary forces arise from the evaporation of fluids within the pores, potentially leading to a breakdown of the microstructure of the material [20]. Figure 3.5 a is the photograph of the sample surface showing colour inhomogeneity

that indicates cracks in the PS layer, which is visible in the microscope image Figure 3.5 b. Figure 3.5 c is a cross-section image using SEM that shows the peeling of parts of the PS layer due to cracks. If the chip was washed with water after etching and then left to dry in the air, due to the high surface tension of water and the large force exerted by the meniscus on the porous structure during drying, the porous film will disintegrate (Figure 3.5).

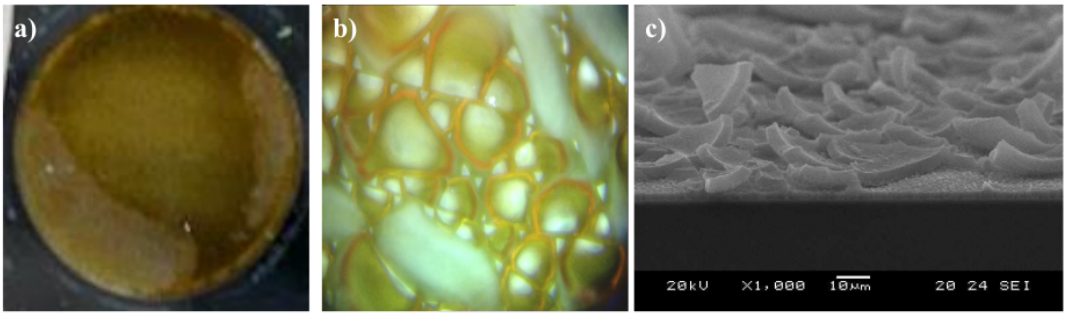

Figure 3.5 a) Photograph, b) optical microscope image, c) SEM image of the PS layer showing the cracking on the PS layer during air drying.

The pentane/hexane drying method was used to avoid cracking and reduce instability in the PS layer. The principle of this method is to exchange the aqueous medium that fills the pores with a low surface tension organic solvent. However, this cannot be done in a single step because water and hexane are not miscible. First, the water is exchanged in the pores for ethanol because these two are miscible. After that, ethanol is exchanged for hexane because those two solvents are miscible. Hexane has a much lower surface tension $(17.91\text{mN/m}\,(25°\text{C}))$ than ethanol $(22.39\text{mN/m}\,(25°\text{C}))$ [41]. This method has been shown to reduce PS cracking during drying [157]. Figure 3.6 a, is a photograph of the surface of the sample showing the homogeneity of the surface, indicating the absence of cracks in the PS layer, which is clearly shown in the microscope image (Figure 3.6 b). The cross-sectional image using SEM (Figure 3.6 c) shows the PS layer without cracks. The dark areas at the bottom represent the silicon substrate; the PS layer is above it.

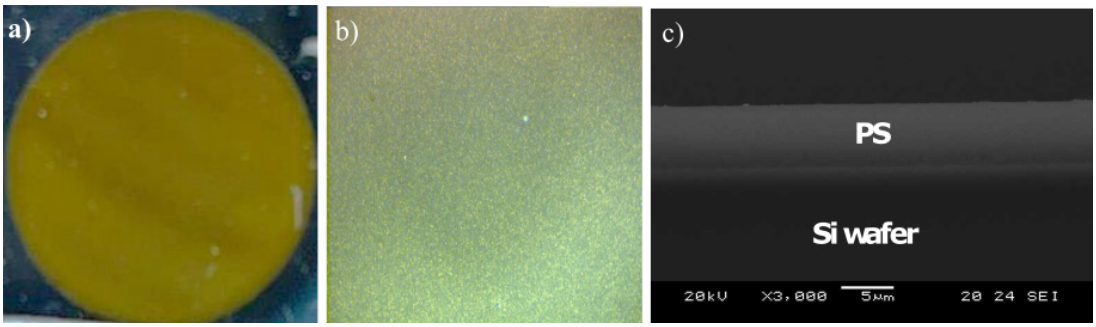

Figure 3.6 a) Photograph, b) optical microscope image, c) SEM image of the PS layer after the pentane drying method.

It is vital to mention an important point that plays a significant role in obtaining a layer of uniform, crack-free PS, which is the absence of any solution from the previous stage. This signifies the absence of residual HF when the sample is washed with water, the absence of water residues when the sample is immersed in ethanol, and the absence of ethanol residues in the final stage when the sample is immersed in hexane.

The optimal immersion time for each stage of the process was carefully evaluated. Figure 3.7 presents a photograph of the surface of a sample etched for 20 minutes at a current of 5 mA. The sample was immersed in three different liquids for equal durations of 15, 10, and 5 minutes, ensuring that the immersion time in each liquid was the same at the same stage. Figure 3.7 a) and b) after washing the sample for 15 and 10 minutes, respectively, some cracks appear in the PS layer, while the surface appears homogeneous and free of cracks when the sample is washed for five minutes Figure 3.7 c). A clean and crack-free PS layer is crucial for safe laser writing. Cracks and contaminants in the porous silicon layer can cause laser light to scatter, compromising the safety and effectiveness of the process.

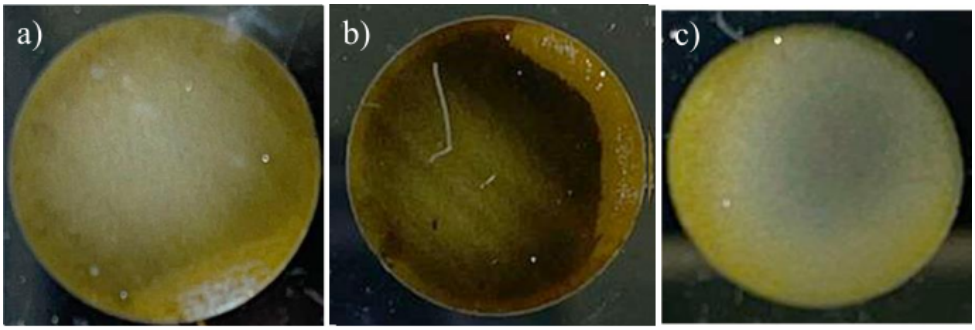

Figure 3.7 a), b) After immersion for 15 and 10 minutes, respectively, cracks were found due to the inhomogeneous surface colour. c)After immersion for 5 minutes, the surface homogeneity appears, indicating no cracks in the PS layer.

3.5. The Thickness and Porosity of PS

The geometry of PS, including the size, shape, thickness and porosity of the pores, is influenced by both the parameters of the silicon substrate (type of impurities [15], crystal orientation [72], and resistivity [11]) and the etching conditions (including the HF concentration [114], current density [164] and etching duration [18]) [101]. The goal is to achieve a stable PS layer with small pores (20–100 Å), which are suitable for laser writing. Using a p-type silicon substrate offers a significant advantage, as it eliminates the need for illumination during etching (required for n-type silicon) and produces smaller pores compared to n-type silicon, which typically has pore sizes of 100–1000 Å [150].

This section focusses on investigating the etching conditions and evaluating the impact of the etching current and duration on the thickness and porosity of the PS layer. The samples were prepared by anodic etching of p-type crystalline silicon wafers (100) (1–10 Ω·cm) in hydrofluoric acid (40% concentration) and absolute ethanol in a 1:1 ratio. The gravimetric method and cross-sectional SEM images were used to measure the thickness of the PS layer, while porosity was determined using the gravimetric method and AFM surface images. Ensuring the stability of the PS layer was crucial for the subsequent stage, where laser writing was applied.

3.5.1. Effects of Anodising Current Density on the Thickness and Porosity of PS

The anodising current density significantly influences the structural properties of the resulting porous layer, including the thickness and porosity. The effect of the anodisation current density on the thickness and porosity of the PS layer was studied wildly [164, 43]. To study the effect of the anodising current density on the thickness and porosity of PS, the varied anodising current (1, 2, 3, 4 and 5 mA) was applied once by etching all samples to a constant value of 100 Coulomb and once at a constant time of 20 min. The porosity and thickness of the PS samples were determined using the gravimetric method (equation 2.4 and equation 2.3). All the etching conditions and the resulting PS layer characteristics are summarised in Figure 3.8 and Figure 3.9.

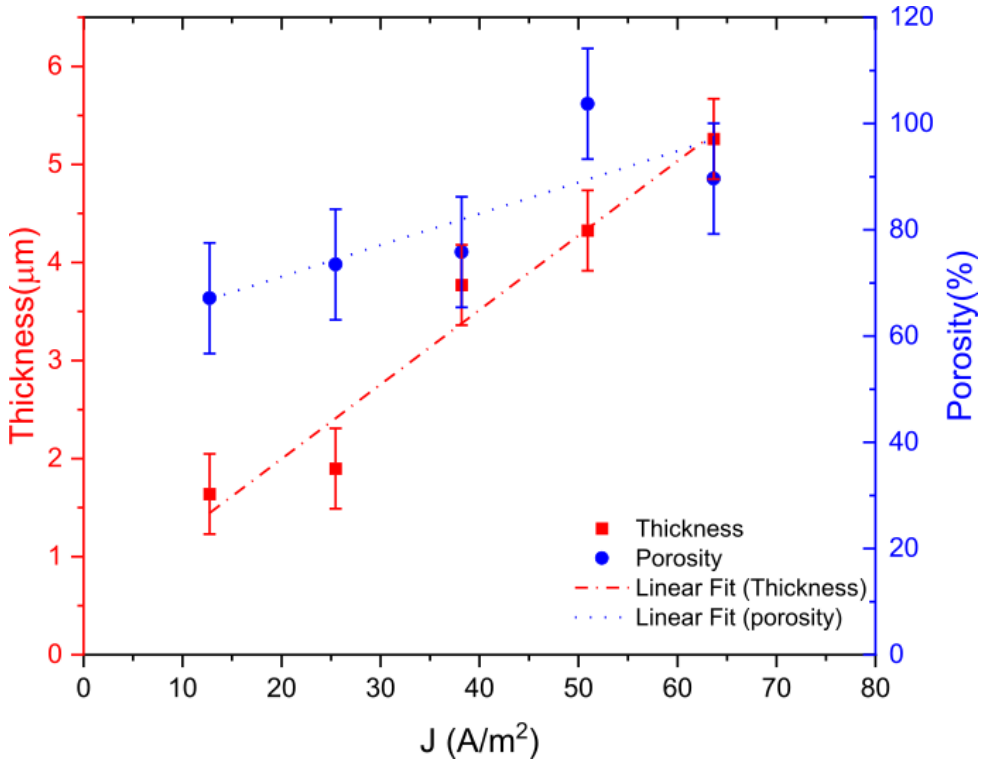

Figure 3.8 Dependence of PS thickness and porosity on anodising current density on a fixed electric charge for 100 C.

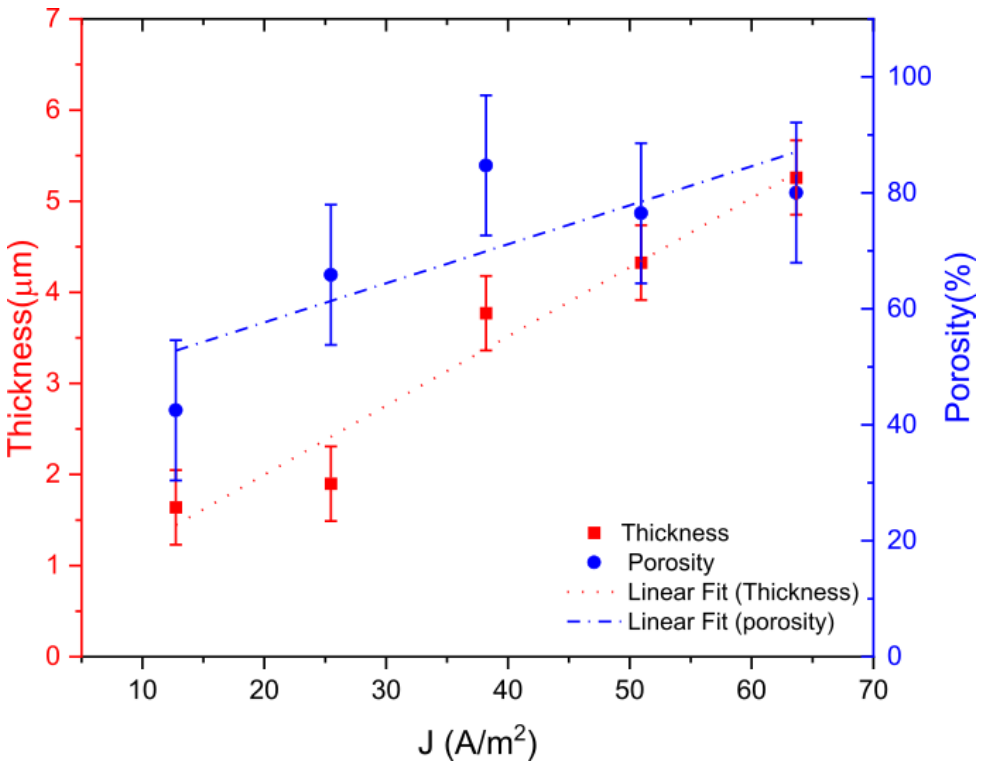

Figure 3.9 Dependence of PS thickness and porosity on anodising current density at a fixed etching time for 20 min.

The thickness and porosity of the PS layer increased linearly with current density [113]. The direction of porous growth strongly depends on the orientation of the substrate crystal, the type of doping, and the direction of the electric field [39]. In p-type silicon [100], the porous growth is perpendicular to the surface toward the interface between the PS layer and the silicon wafer in the direction of (100) if the structure is [100] [189]. The nature of the bonding for atoms at hydrogen-terminated (111) and (100) surfaces is responsible for orientation-dependent reactivity. On hydrogen-terminated surfaces (111), the low polarity of the Si-H bond and the fact that F^- is sterically inhibited from approaching Si atoms render the hydrogen-terminated surface (111) stable to etching [81]. The steps and edges are removed, and the result is (atomically flat) Si(111)-H. In contrast, the hydrogen-terminated surface (100) is more complex with monohydride and dihydride species, and etching proceeds more rapidly in this direction. However, as the anodic current density increases, the etching rate will increase towards the substrate, affecting the thickness of the PS layer. The relationship between thickness and anodising current density was confirmed by measuring thickness from SEM images (Figure 3.10 and Figure 3.11).

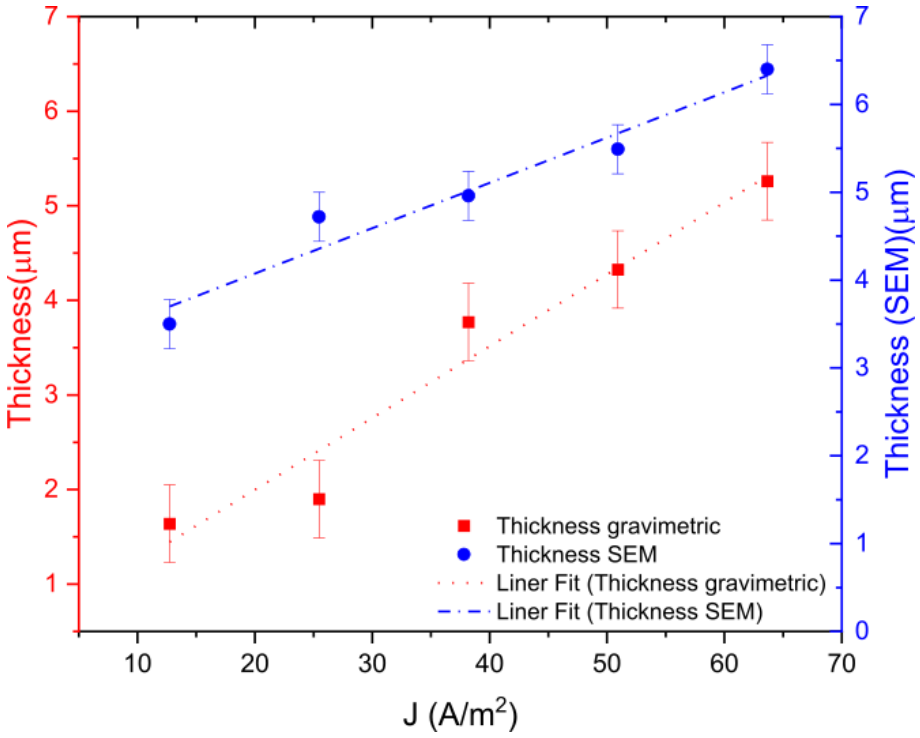

Figure 3.10 Comparison between measuring the thickness of the PS layer using the gravimetric method and from the SEM images with the current density at a fixed electric charge of 100 C. The correlation coefficient between data from gravimetric and data from SEM is 0.9, reflects a high level of agreement between the two methods

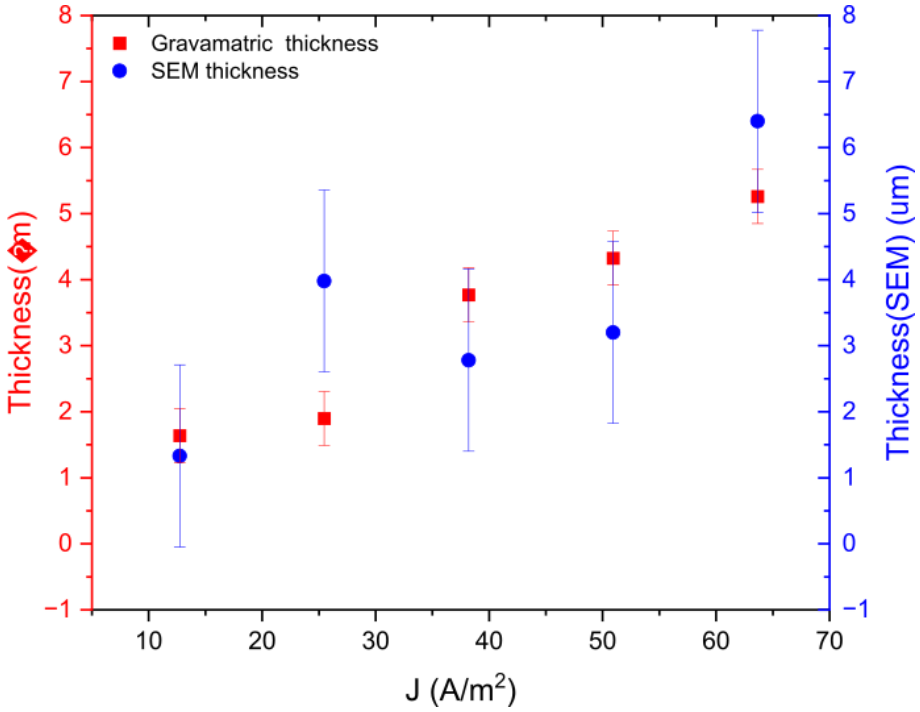

Figure 3.11 Comparison between measuring the thickness of the PS layer using the gravimetric method and from the SEM images with the current density at a fixed time of 20 minutes. The correlation coefficient between data from gravimetric and data from SEM is 0.6 this suggests a moderate linear relationship between the two data sets. It is not as strong as 0.9 but still indicates that the results from the two methods are related.

The stability and uniformity of the PS layer are affected by different anodising conditions (anodising current or anodising time), as the PS layer shows instability if the sample thickness exceeds 50 μm [40]. Figure 3.12 shows the effect of the oxidation current on the stability and uniformity of the PS layer. Structurally, cracking is less likely to occur in higher anodising currents. The porosity refers to the amount of silicon removed during the anodisation compared to before etching. If the thickness of the porous layer is increased, this indicates the removal of a more significant amount of silicon, thus increasing porosity [205].

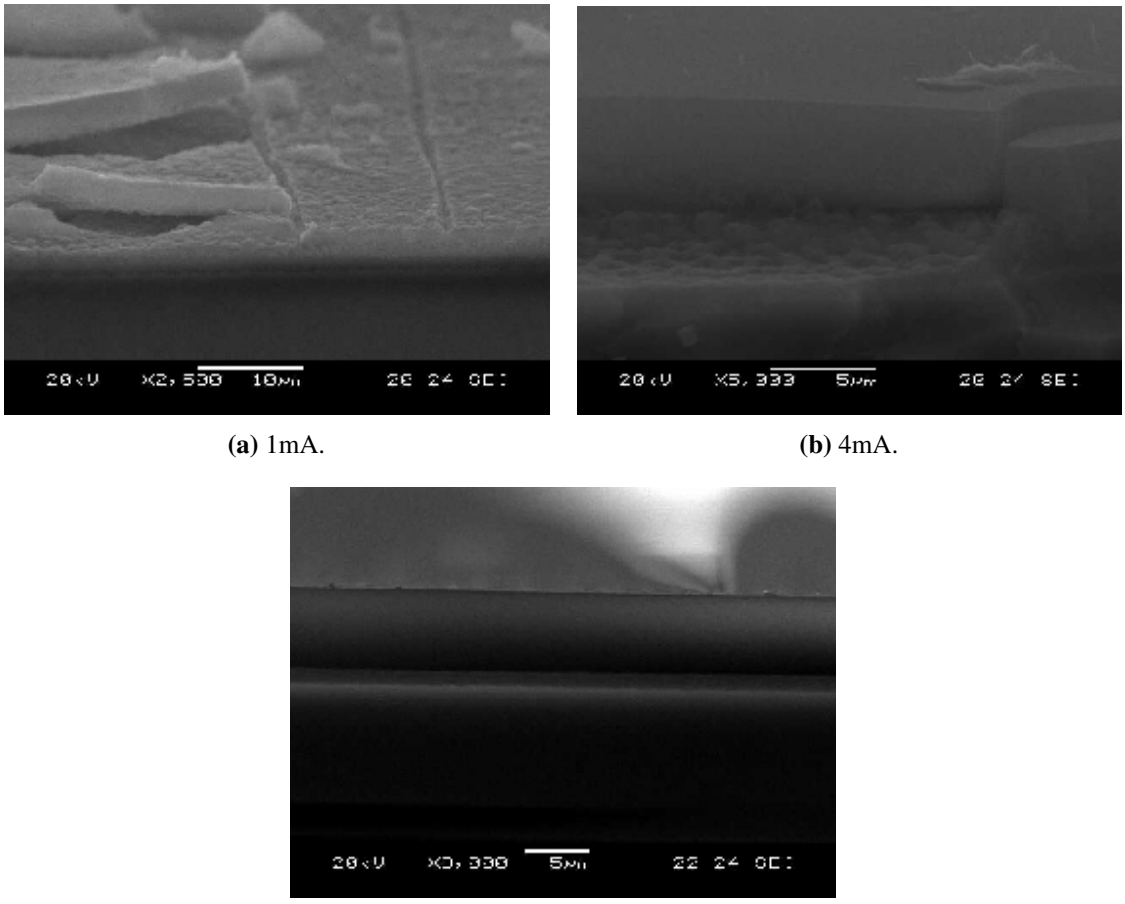

(a) 1mA. **(b)** 4mA.

(c) 5mA.

Figure 3.12 A PS layer formed at different anodising currents at a constant charge (100 C). a) Sample etched with 1 mA showing visible signs of cracking and flaking on the surface. b) with 4 mA applied, clusters of PS are formed. c) the PS layer is more homogeneous and uniform when 5 mA is applied.

3.5.2. Effect of the Duration of Electrochemical Anodisation on Thickness and Porosity of Porous Silicon

The relation between the duration of electrochemical anodisation at a constant current density and the thickness and porosity of the PS layers was investigated. The first sample was etched for 20 minutes; the second sample was etched for 30 minutes, and the etching time was increased by 10 minutes as each sample was prepared until it reached 100 minutes. The etching current

density was constant at approximately 63.6 A/m^2. Porosity and thickness were defined using gravimetric analysis (Section 2.4.1). The fluctuation porosity between 80% and 95% is shown in Figure 3.13.

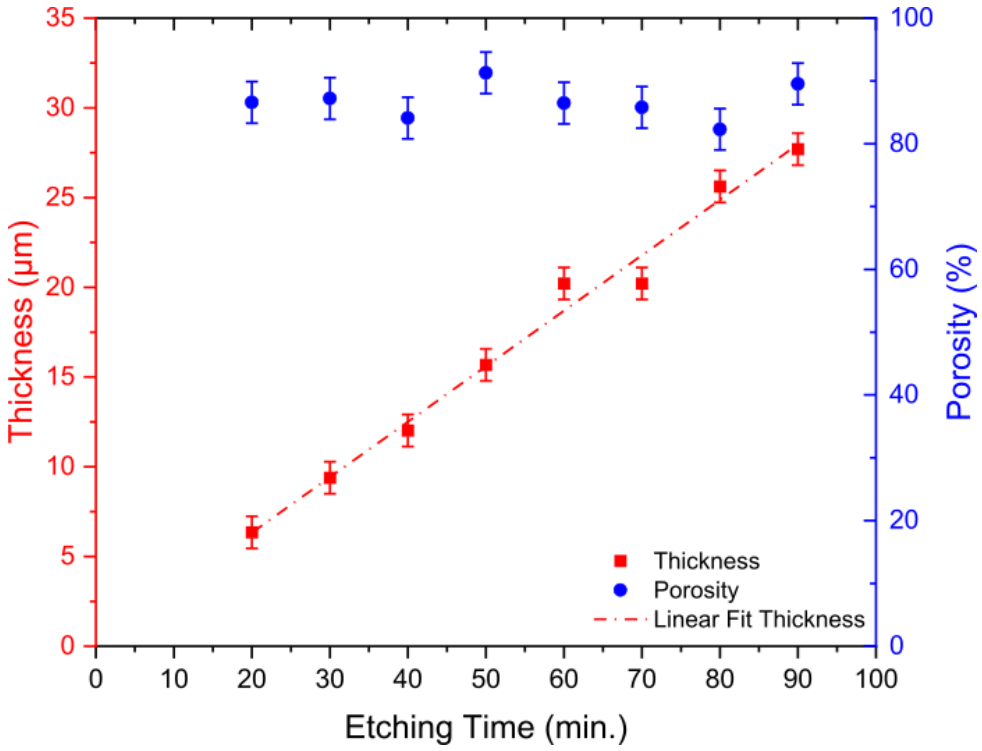

Figure 3.13 The variation of porosity and thickness with etching time at fixed etching current density

Increasing the etching time causes an increase in porosity. The size of the silicon structure decreases as the anodisation period increases on the surface, reducing as the anodisation period increases [18]. In addition, the increase in the etching time leads to an increase in the diameter of the pores (D) and a reduction in the inter-pore distance (porous wall) (W) (Figure 3.14). During the continuous electrochemical dissolution process, the dissolution also started in the (111) direction, forming side branches from the primary pore due to additional holes [163]. The continuous flow of the electrolyte leads to a gradual decrease in HF concentration from the surface to the PS/Si interface, resulting in a decrease in porosity at the surface and a decrease in porosity with depth [117].

The thickness (T) of the PS layer was calculated using the gravimetric method using equation (2.4). The results, illustrated in Figure 3.13 shows that the thickness increases linearly with the extension of the etching time. When the sample is exposed to etching for a longer period, the etching current density increases to maintain the same total charge ($Q = I \times t$, where the Q is the charge measured in coulombs (C), I is current and t is time) for each cycle, this is consistent with the principle that increasing the current density helps counteract changes at the silicon-HF interface, ensuring that the electrochemical reaction proceeds efficiently. The

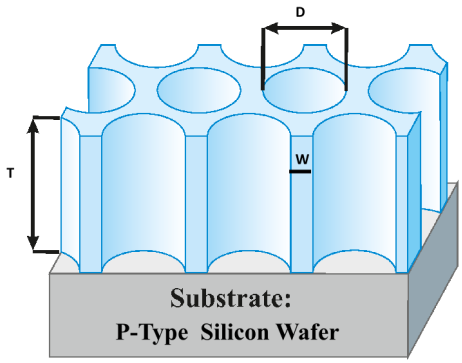

Figure 3.14 Diagram illustrating the diameter and wall of the pore.

increased current density amplifies the rate of the electrochemical reaction at this interface, enhancing the dissolution of silicon in hydrofluoric acid and resulting in a noticeable increase in the thickness of the PS layer [154, 132].

3.6. Porous Silicon Colour

Silicon wafers have a grey colour, where the colour of PS can vary depending on its structure and the substances trapped within its pores. The reduced refractive index and optical interference between the underlying bulk silicon and PS result in vibrant colours throughout the visible spectrum [33]. Figure 3.15 shows a PS sample under fluorescent conditions. Thickness affects the interference of light reflected from both the top and bottom surfaces. This interference determines the apparent colour in reflectance or fluorescence. The fluorescent colour emitted is determined by the wavelength of light that undergoes constructive interference, controlled by:

$$2n_{\text{eff}}\, t \cos\theta = m\lambda$$

where λ is the wavelength of the observed light, n_{eff} is the effective refractive index of the PS layer, t is the thickness of the PS, m is the interference order (integer) and θ is the angle of observation [135]. Thicker layers shift constructive interference towards longer wavelengths, resulting in redder reflection. Thinner layers increase shorter wavelengths, resulting in a bluer reflection [174].

The analysis of colours has shown that for thicknesses up to 500 nm, the interference colour is directly proportional to the thickness and porosity of the PS layer [159]. The colour of the PS layer is also affected when the silicon layer is exposed to an ambient atmosphere saturated with vapours of different organic solvents [27].

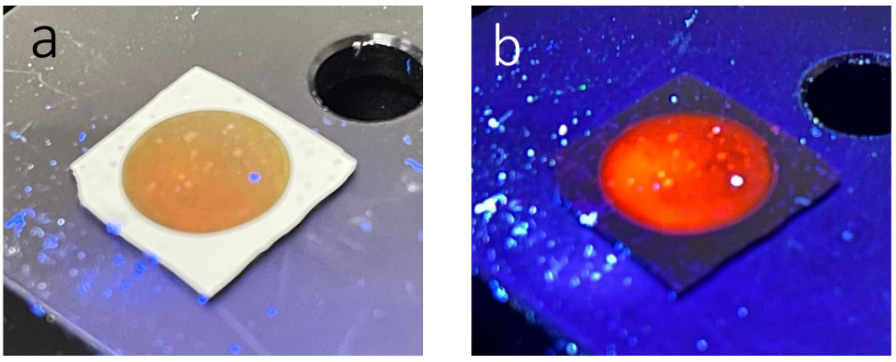

Figure 3.15 Photographs showing the colours of a PS sample of 1 cm diameter and 6μm thickness under different light sources. a) Colour under a yellow LED lamp (5 to 7 watts). b) The sample emits orange light when illuminated by a 365 nm hand-held UV lamp

3.7. Atomic Force Microscopy (AFM) as an Alternative Method to The Gravimetric Method

The accuracy of the gravimetric method to measure the thickness and porosity of the PS layer is relatively poor when the layer thickness is more than 200 nm, and the area of the removed silicon is 1 cm^2. The error rate can easily reach 100% [120].

Therefore, an alternative method must be found to measure thickness and porosity. This could be a visual method, since SEM images were used to measure the thickness of the porous layer, or a numerical method such as AFM image analysis [7, 149]. However, using AFM images to determine thickness can be challenging due to the limited length of the AFM silicon cantilever, which is less than 6 μm and thus unsuitable to accurately calculate the thickness of the PS layer (Figure 3.16).

In the current study, ImageJ software was used to determine the porosity of PS. When applying this method, it is crucial to choose an appropriate threshold that is not low because that would lead to the ignore of some pores at a slight depth from the surface (Figure 3.17).

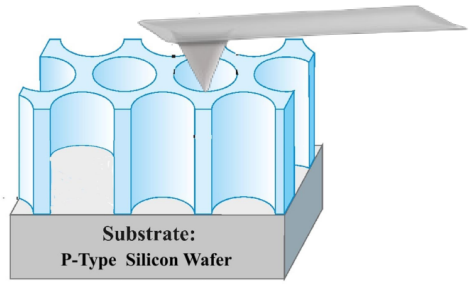

Figure 3.16 The diagram shows the limitations of AFM in measuring the thickness of the PS.

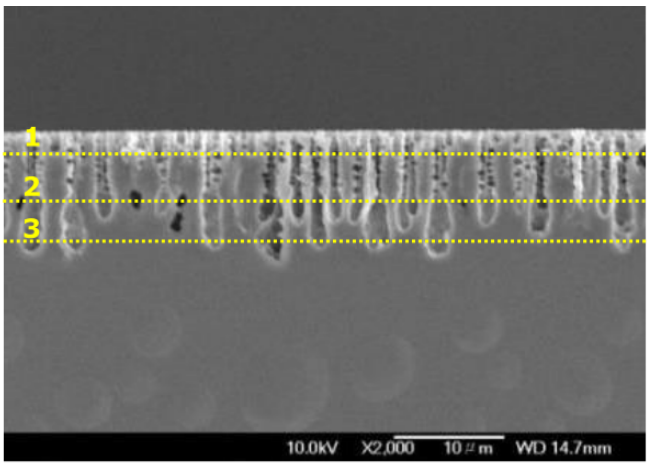

Figure 3.17 The Figure illustrates the importance of the threshold position during porosity measurement. 1) The measurement will cover most pores if the threshold is close to the surface. In contrast,2) and 3) The threshold is located far from the surface of pores and missed some of the pores in the porosity measurement. Thus, the further away from the surface, the greater the error in the porosity measurement. (SEM from [203]).

AFM images were used to measure the porosity of samples prepared with an anodising current of 63.7 A/m^2 and an etching time of 20 min. The value of porosity calculated using AFM images was 60 %. The porosity value calculated using the gravimetric technique was around 82 %. The experimental error was calculated using equation (3.1) and was found to equal 36 %.

$$R_P = \frac{\text{Porosity}_{\text{gravimetric}} - \text{Porosity}_{AFM}}{\text{Porosity}_{AFM}} \times 100\% \tag{3.1}$$

where $\text{Porosity}_{\text{gravimetric}}$ and $\text{Porosity}_{\text{AFM}}$ are the values of the porosity of PS determined using the gravimetric method and AFM, respectively.

3.8. Surface Chemistry of Porous Silicon

Surface chemistry is essential to determine the properties and performance of the material. The porous material has the potential to act as a template or host for other substances, such as carbon, metals and magnetic nanoparticles. The main reactions in porous Si lead to the formation of Si-O, Si-C, Si-N, or Si -meta surface bonds. Critical reactions include Si-O or Si-C bonds, as they allow the bonding of functional molecules, such as drugs, proteins, targeting agents or biological sensor molecules, to PS surfaces [33].

The absorption mode of FTIR was employed to investigate the surface chemistry of PS samples before and after exposure to humid air at room temperature. After the PS was formed, the FTIR spectra were immediately taken after the sample was dried. The lifetime of PS oxidation

was determined by studying the change in the FTIR spectrum when the measurement was taken over 30 days by exposing the sample to air, resulting in oxidation at room temperature.

An infrared spectrum (Shimadzu IRAffinity-1S) with a wavelength of CW 632.8 nm was used. The measurements were performed under a continuous flow of atmospheric nitrogen to decrease the humidity in the atmosphere because the water vapour strongly absorbs in the infrared region, which can cause unwanted peaks in the spectrum. Absorption curves versus wavenumber for freshly formed PS, after 15 days and after 30 days from 400 cm^{-1} to 3000 cm^{-1}, shown in Figure 3.18, and in Figure 3.19. The freshly prepared PS shows well-defined silicon-hydrogen (SiH_2 scissor mode) at 910 cm^{-1} (Figure 3.18). The appearance of SiH_2 deformation mode at 662 cm^{-1} [111] (Figure 3.18), and the absorbance in the wavenumber range 2087-2138 cm^{-1} is attributed to SiH_x (x = 3, 1, 2) stretching modes [12] (Figure 3.19). In addition, the absorption peak at 624 cm^{-1} is associated with the Si-H wagging bond (Figure 3.18), are an indication of the formation of PS.

Changes are seen over 30 days. The first change observed in the FTIR spectrum after the sample is exposed to air at room temperature is the growth of a peak in 470 cm^{-1} (Figure 3.18). This is assigned to an out-of-plane rocking mode of the Si-O-Si group. The intensity increased as the exposure time increased [134]. Further evidence of oxidation was observed in the changes in the SiHx modes, as indicated by a decrease in the intensity of the SiH_x stretching modes. This was accompanied by the detection of a broad absorbance band around 2110 cm^{-1} [138] and the appearance of SiH_x absorption peaks to clarify the physical observation (Figure 3.19). The main vibration modes occur at a wavenumber of 1072, 1110, and 1163 cm^{-1}. The signal observed at a wavenumber of 1072 cm^{-1} corresponds to the stretching vibrations of the Si-O-Si bridges in the SiO_x compound. The peak observed at 1110 cm^{-1} results from the asymmetrical strained of the Si-O-Si bonds. The intensity at 1072 and 1163 cm^{-1} increased with the degree of oxidation. These frequencies are related to the highly stressed SiO_2 -Si interface or defective silicon oxide on the surface of the PS. However, these modes are the symmetrical and asymmetric vibration modes of the Si-O-Si bridges [6].

Based on these results, it is concluded that the oxidation of PS at room temperature is considerable, and attention should be given to ensuring long-term oxidation stability.

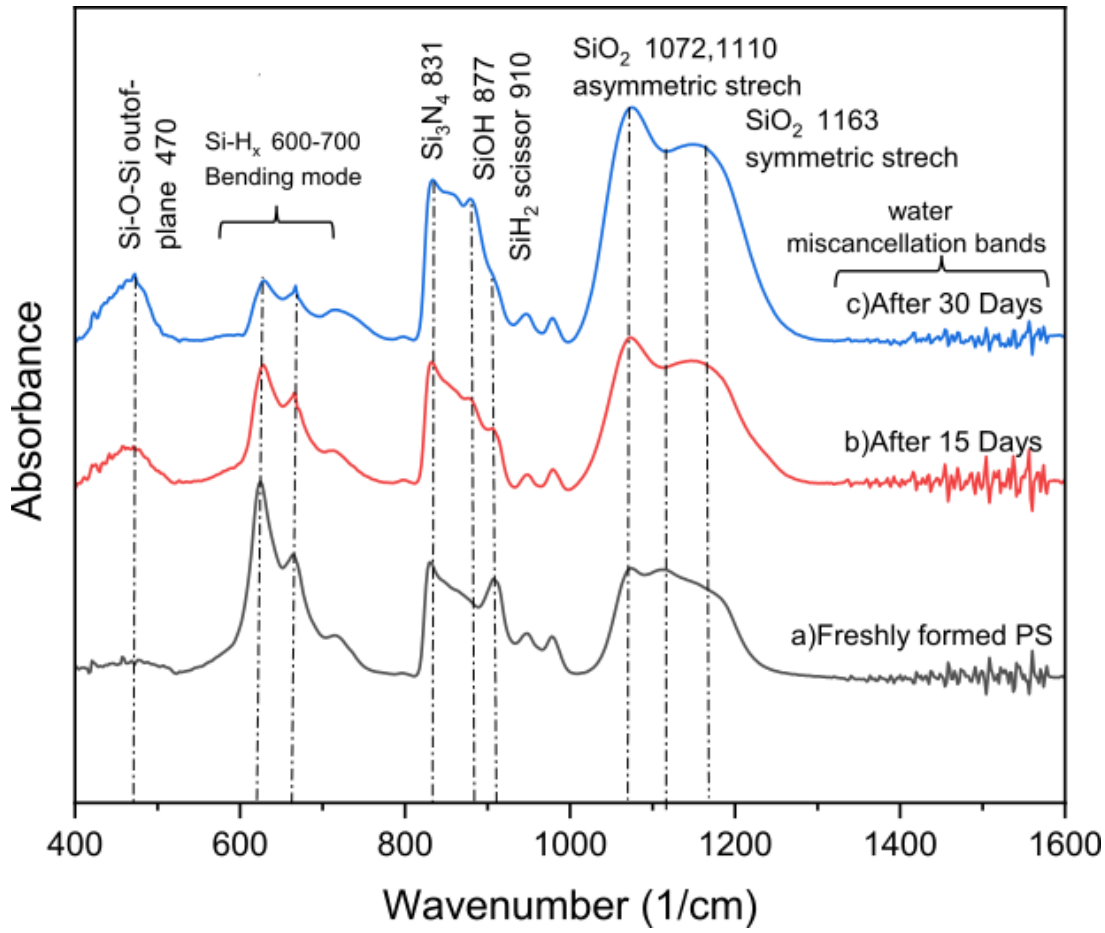

Figure 3.18 FTIR spectra were taken for three different stages of surface modification: (a) freshly prepared PS, (b) oxidised PS after 15 days, and (c) oxidised PS after 30 days. The spectra indicate the growth in asymmetric Si-O-Si stretch modes, bulk oxide modes, and oxidised silicon-hydride deformation modes formed by surface oxidation.

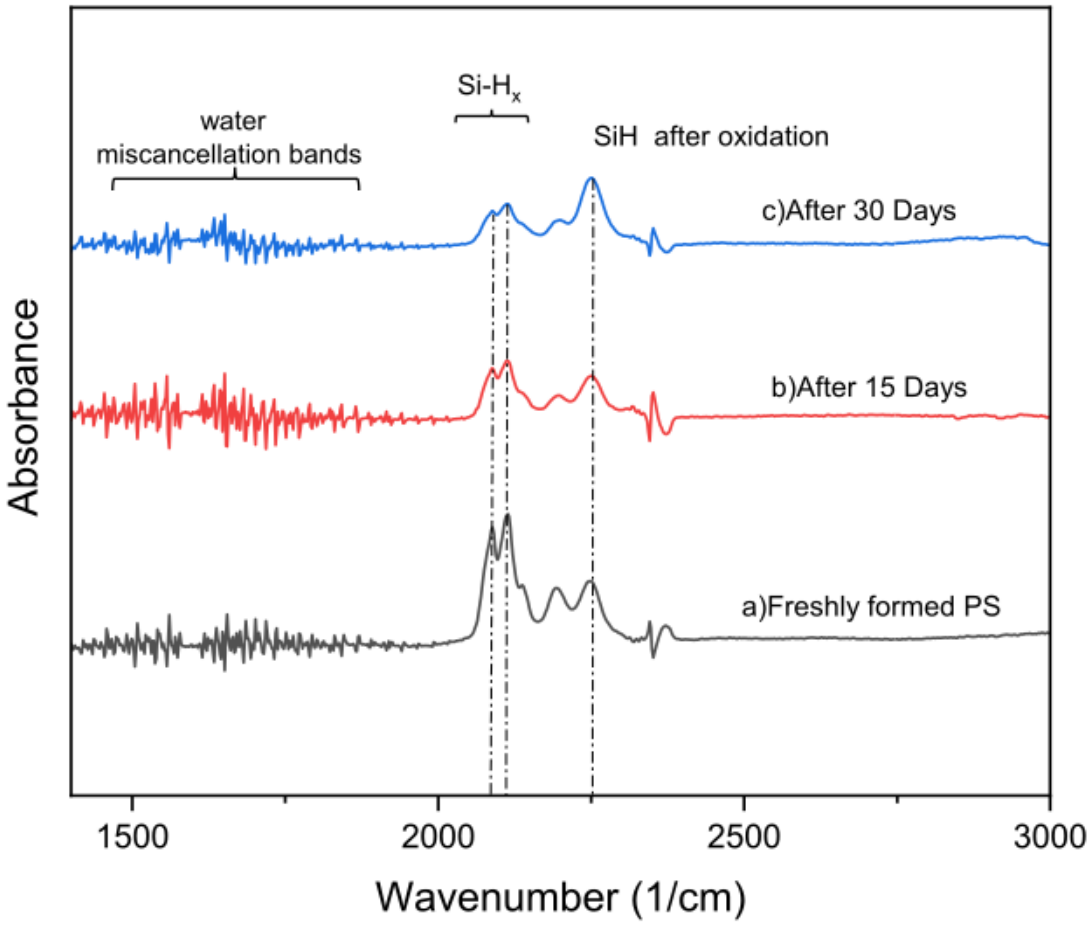

Figure 3.19 The development of oxidised silicon hydride extension bands indicates oxidation. There is a continuous growth of oxidised silicon hydride expansion bands over time.

Raman spectra can help determine the degree of crystallinity, the size of the nanocrystal, and the presence of amorphous phases, providing essential information on structural transformations and material quality [213].

Variations in the Raman spectrum of PS have often been attributed to contributions from both crystalline silicon and amorphous silicon. Typically, amorphous silicon displays a broad peak around 480 cm^{-1}, which contrasts sharply with the well-defined peak of crystalline silicon [213]. This shift and broadening of PS spectra is mainly attributed to the large surface area-to-volume ratio in PS, which promotes the formation of interfaces between crystalline silicon and silicon oxides. The formation of silicon oxides was shown to occur more rapidly in the amorphous regions of PS than in crystalline silicon, resulting in Raman spectra that exhibit characteristics associated with amorphous phases [44].

Additionally, as the size of the nanocrystals within the PS decreases, a shift in the Raman peak toward lower frequencies relative to the bulk crystalline silicon is observed [239]. This shift is caused by phonon confinement, where wave vectors extend beyond the Brillouin zone

when the crystal sizes drop below 100 Å. In such nanoscale crystals, the restricted movement of phonons alters the vibrational modes, resulting in a red shift in the Raman signal. This phenomenon is demonstrated by the phonon confinement model, which has been extensively used in theoretical analyses to explain the impact of reduced crystal size on the Raman spectra of PS [14]. As nanocrystals decrease in size, their vibrational properties diverge from those of bulk silicon, explains the observed changes in the spectra [200, 69].

For this study, the nature of PS and the structural transformations in crystalline silicon were evaluated using Raman scattering. Raman measurements were conducted using a LabRAM HR Evolution confocal microscope spectrometer with a DPSS 532 nm laser. The laser power at the sample was carefully controlled to prevent overheating. In Raman scattering, a fraction of the monochromatic laser's energy is used to induce lattice vibrations. The residual energy is emitted as a photon with energy slightly lower than that of the incident photon, creating a Raman shift.

Figure 3.20 shows the normalised intensity (the measured intensity divided by its maximum value) on the X-axis and the Raman shift on the y-axis. The Raman spectrum of crystalline silicon, shown by the solid black line, features a sharp and symmetric peak. This results from well-defined lattice vibrations, because the long-range atomic order in bulk silicon is preserved, minimising defects and disorder. The narrow peak at 521 cm^{-1} with a FWHM of 2.7 cm^{-1} is attributed to optical phonons in Si-Si bonds of the bulk crystal [44].

In contrast, the Raman spectrum of PS, represented by the red dashed line in Figure 3.20, exhibits a peak with FWHM broader than that of crystalline silicon. This broadening can be linked to a decrease in the crystalline dimensions within PS, which reduces the coherence length of the phonons. As the crystalline dimensions decrease, the phonon confinement effects become more pronounced, particularly for phonons propagating perpendicular to the smaller crystal dimensions. This generally results in a redshift of the Raman peak because of altered phonon behaviour. However, in this case, the absence of a significant redshift may indicate that the PS layer retains relatively large nanocrystals or possesses minimal structural disorder, both of which would reduce the extent of phonon confinement and preserve vibrational characteristics similar to bulk silicon. Additionally, phonons travelling along the longer dimensions of the microcrystals may retain frequencies close to those of crystalline silicon, further contributing to the lack of noticeable redshifting.

Studies using high-resolution electron microscope (HREM) images have disproven the theory that the Raman spectrum in PS is purely due to amorphous silicon. HREM confirmed the presence of microcrystals, as indicated by lattice fringes [77]. Therefore, the Raman spectrum of PS can be understood by focussing on the coherence length of phonons and the microcrystalline

structure, as shown in Figure 3.21, which illustrates the possible coherence lengths of phonons in relation to the dimensions of pores.

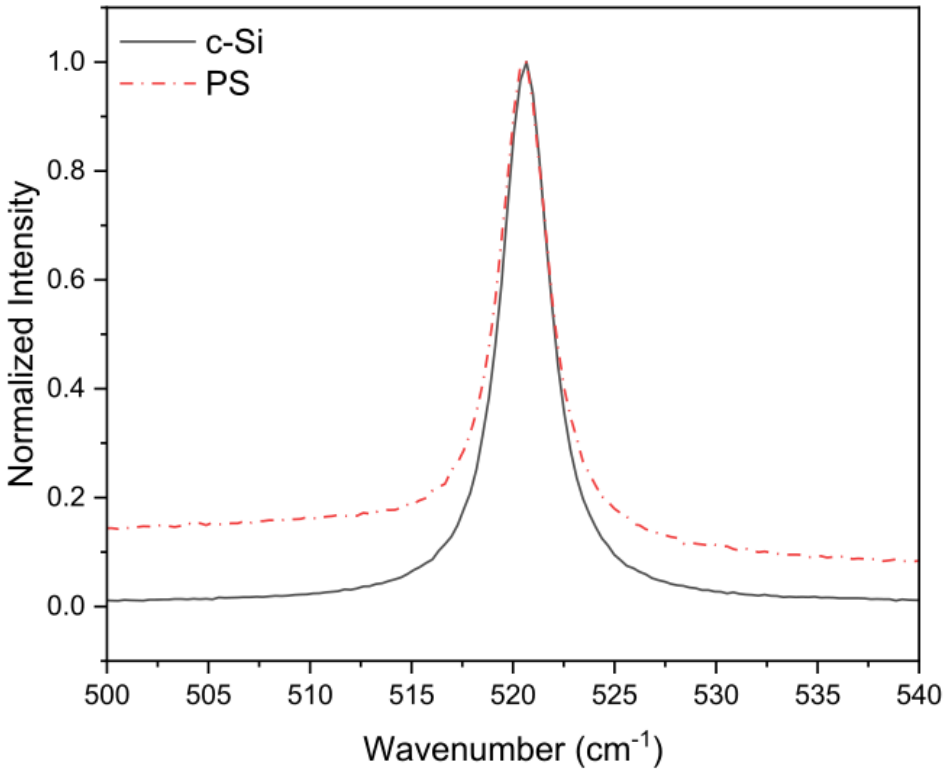

Figure 3.20 Raman spectra of crystalline silicon (c-si) (black solid line) and PS (red dash-dotted line).

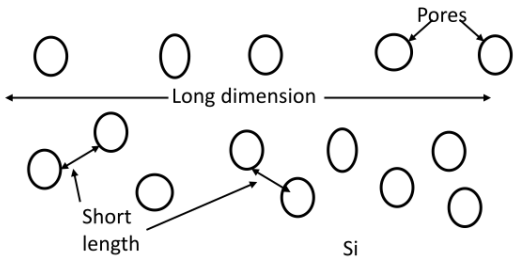

Figure 3.21 The expected coherence length of phonons within a plane that is perpendicular to the direction of the pores (this Figure taken from [69]).

3.9. The Surface Structure of Porous Silicon

The PS layer formed by electrochemical etching consists of a network of silicon particles in the nanometre range, separated by voids. Consequently, the surface of PS has mechanical roughness that facilitates the study of its morphology [149]. After PS preparation, AFM (section 2.4.5) in contact mode was used to image the surface structure of the samples.

According to the International Union of Pure and Applied Chemistry classification of pore size [175], pores with diameters less than 2 nm are of the micro type, 2-50 nm are of the meso type and more than 50 nm are of the macro type. Figure 3.22 shows a pore diameter of approximately 40 nm.

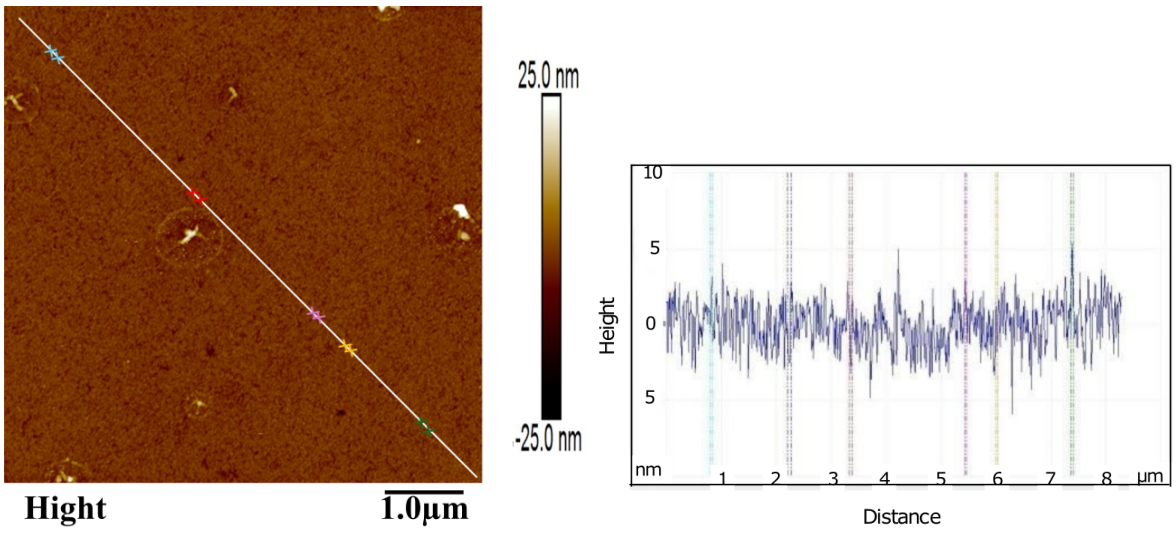

Figure 3.22 Pore size determination from AFM line profile. The horizontal distance between two vertical lines of the same colour indicates the width of a single pore. The average of these distances is used to estimate the pore size of the porous silicon sample.

Figure 3.23a shows the surface of the PS layer illustrating many uniformly distributed holes on the surface of the PS layer grown on the sample of p-type c-Si (100) (Figure 3.23c). The surface of the c-Si sample had complete etching, which formed numerous tiny pores across the thin wall. The PS layer has a higher surface roughness with a root mean square (RMS) of 1.48 nm within a sample size 6 µm $\times$ 6 µm compared to the silicon wafer showing a surface roughness at an RMS of 0.37 nm within a sample size 6 µm $\times$ 6 µm (Figuuer 3.23d).

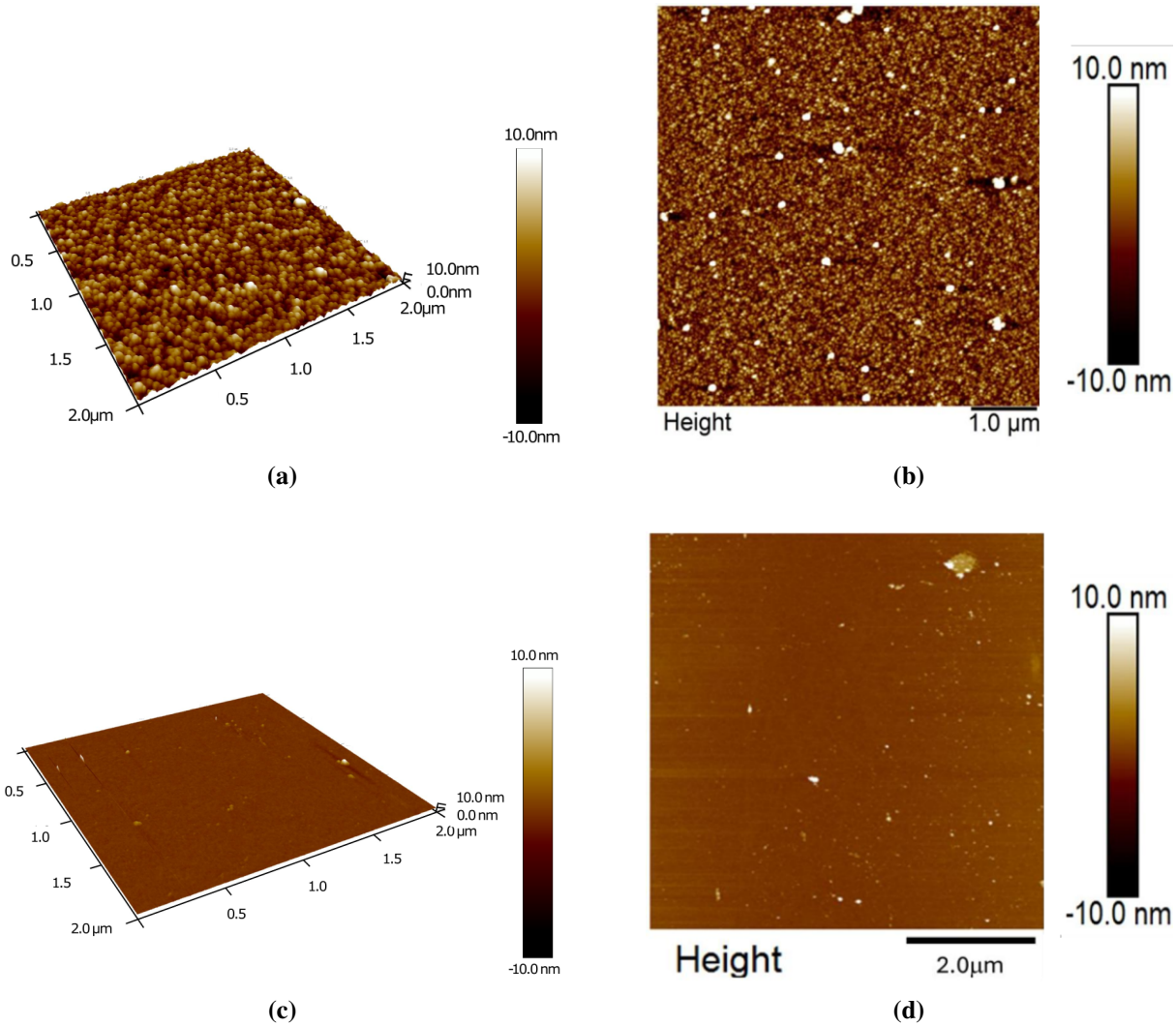

Figure 3.23 AFM images of PS and silicon wafer: (a) 2 µm × 2 µm PS morphology. b) 6 µm × 6 µm topography images of PS. c) 2 µm × 2 µm silicon wafer morphology. b) 6 µm × 6 µm topography images of silicon wafer

3.10. Chemical Composition

The chemical composition of the surface has a impact on the optical properties of the sample. The chemical composition of the sample surface was investigated using XPS. When an X-ray hits a material, the atoms within the material become excited and release electrons. The kinetic energy of these electrons can be measured to determine the strength of the chemical bonds within the material. This is done by measuring the energy required to remove an electron from an atom, called the binding energy. The measurement was taken after writing the PS with a laser and again after partially etching the sample in HF acid diluted with water (1:2) for 10 seconds to remove the silicon oxide layer. Al K_α XPS with a spot diameter of 400 µm was used to emit the X-rays, and the analyser mode used was a CAE constant energy analyser with a pass energy of 200.0 eV. Data were processed using the CasaXPS computer programme.

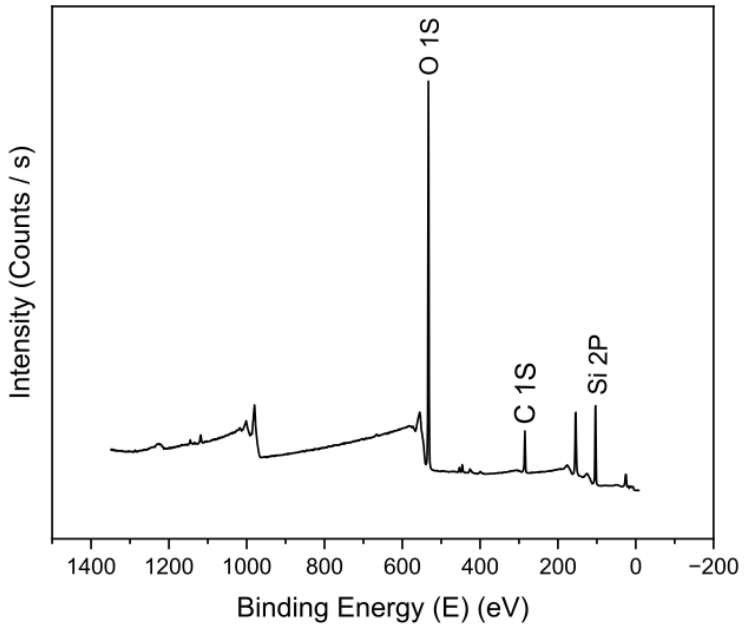

Figure 3.24 A widespread XPS spectrum of HF etched porous Si for 20 min at current density of 63.6 A/m^2.

Figure 3.24 shows the XPS spectrum of HF etched porous Si for 20 min at current density 63.6 A/m^2. The spectrum shows silicon dioxide and silicon with small concentrations of carbon. Figure 3.25 compares the XPS survey for the sample before and after etching. Generally, the O/Si ratio in the etched sample is greater than in the unetched sample [124].

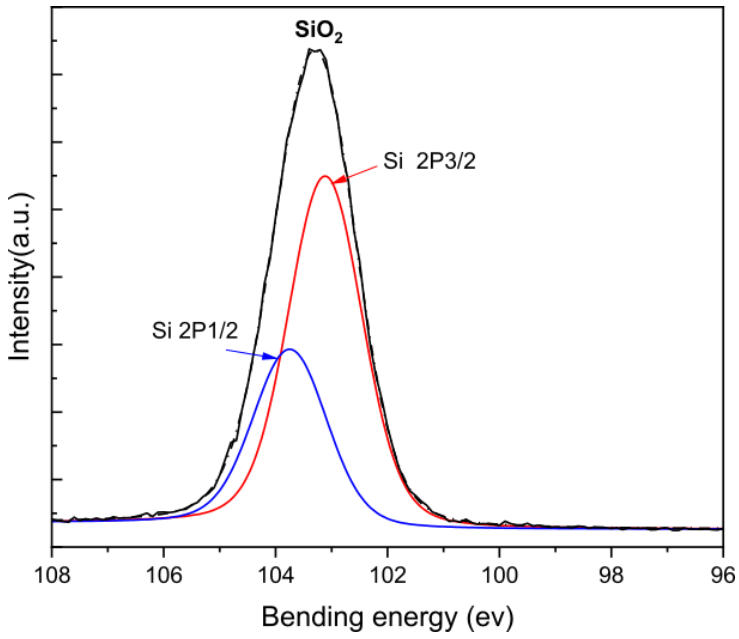

(a) Non etched PS

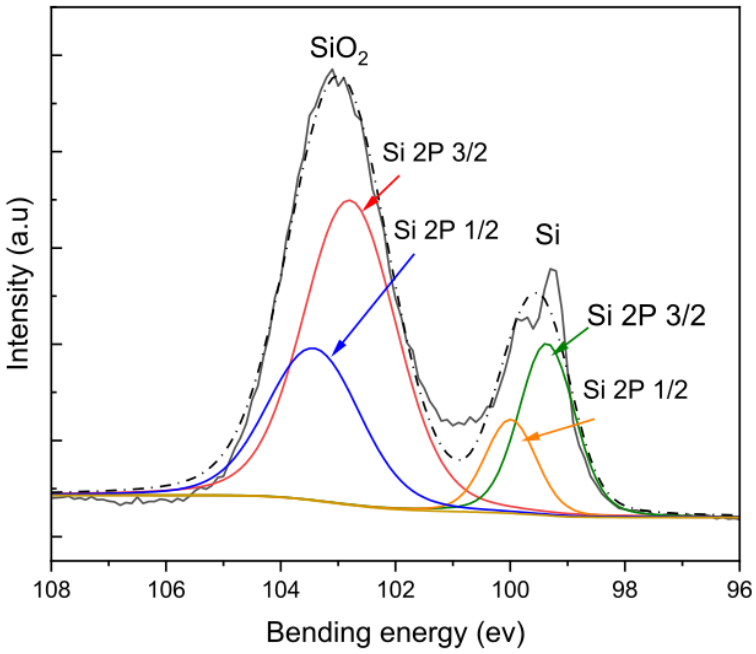

(b) Etched PS for 10 second in HF

Figure 3.25 a) The Si 2p XPS. The spectrum of the PS sample is shown as oxidised (b), which is the corresponding spectrum after etching porous Si in dilute HF to remove the SiO layer. The spectrum is shown as oxidised and elemental peaks in the porous layer.

The PS spectrum (Figure 3.25a) shows the Si 2p spectra of the etched PS sample with a peak at 103 eV that corresponds to the formation of Si-O bonds. The second spectra of PS Si 2p, after partly etching to remove the SiO_2, are shown in Figure 3.25b. This was done to determine the phase composition of the porous layer. Si 2p spectra for pure silicon were obtained, proving that PS samples consist of two components: pure silicon with a peak at 99.3 eV and SiO_2 [51].

3.11. Conclusions

This chapter focused on the comprehensive characterisation of the PS layer, employing a range of techniques to evaluate its structural, morphological, and chemical properties. The gravimetric method revealed that the thickness and porosity of the PS layer increased linearly with the density of the oxidation current. While porosity remained relatively unaffected by etching time, the thickness showed a direct linear relationship, with longer etching times producing thicker porous layers. These findings were corroborated by AFM and SEM imaging, which provided detailed information on the morphological nature of PS.

AFM images were also used to quantify porosity and analyse the surface morphology of PS etched in HF for 20 minutes at 5 mA. Furthermore, UV radiation experiments confirmed the integrity of the sample, as exposure of a 6.4 μm thick porous layer to UV light resulted in a characteristic orange colour, indicative of its stable optical properties.

Spectroscopic techniques, including FTIR and Raman spectroscopy, were employed to study the crystal structure and vibrational properties of PS. Notably, exposure of the PS layer to air, humidity, and laser interaction led to the formation of a silicon oxide layer on the surface. FTIR and XPS analyses successfully tracked the oxidation process and provided a detailed chemical composition of the material.

These findings provide valuable information on the structural and chemical behaviour of PS under varying conditions. The ability to tailor porosity and thickness through controlled etching and oxidation processes highlights the potential of PS for applications in optoelectronics, sensing, and other advanced technologies.

Chapter 4. Consolidation of Porous Silicon Using CO_2 Laser

4.1. Introduction

In the previous chapter, the methods used to characterise the PS layer and analyse its crystalline and chemical structures were discussed in detail. The findings revealed that the optical and physical properties of the PS layer are strongly influenced by its crystalline structure and surface chemistry, which can be tailored through variations in the etching parameters, such as the etching current and the etching duration [3].

This chapter investigates how low-power (5-10 W) continuous-wave (CW) CO_2 laser processing affects the physical, structural, and chemical properties of the PS layer. By systematically varying irradiation parameters, including laser power density and duration (controlled via stage traversal speed), the study aims to understand the interplay between laser-induced heating and the resultant material modifications. In this power regime, the result shows that the material is not melted but is heated to the extent that it consolidates.

A combination of imaging techniques, optical microscopy, SEM and AFM, was employed to evaluate structural changes, while Raman spectroscopy provided molecular-level insights into chemical transformations. These analyses collectively shed light on the mechanisms of thermal processing and the tunability of PS properties under controlled laser irradiation, laying the groundwork for potential applications in optoelectronics, sensing, and other fields.

4.2. Thermal and Optical Properties of Silicon and Porous Silicon

PS exhibits a thermal conductivity (k) substantially lower than that of bulk crystalline silicon, ranging from 0.2 to 0.5 W m^{-1} K^{-1} compared to approximately 130 W m^{-1} K^{-1} for bulk silicon [193, 232]. This reduction is attributed to the porous structure, which disrupts heat transfer by introducing interfaces and voids that scatter phonons, thereby reducing thermal transport efficiency [67]. Consequently, heat generated in the irradiated regions of PS is less efficiently dissipated, leading to localised hot spots [61]. These effects are exacerbated by structural defects

and impurities within the pores [84], which enhance absorption at specific wavelengths, such as 10.6 µm.

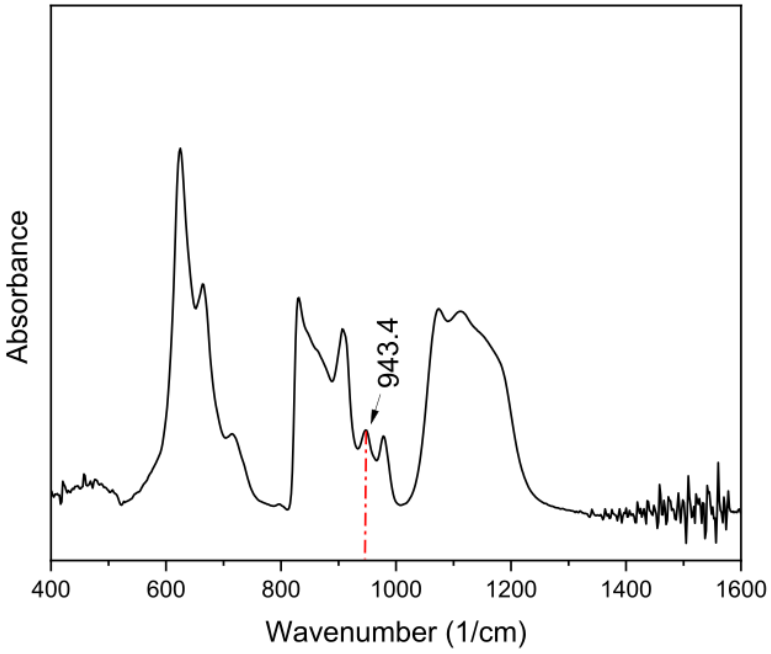

Figure 4.1 FTIR spectrum of porous silicon showing the characteristic absorption peak at 10.6 µm (943.4 cm^{-1}), corresponding to the wavelength of the CO_2 laser used for irradiation.

The absorption mechanism of the CW CO_2 laser (10.6 µm wavelength, 943.4 cm^{-1} wavenumber) in PS is clarified through its FTIR spectrum (Figure 4.1), which displays a significant absorption peak at the laser resonance wavenumber. This absorption results from two synergistic processes: free-carrier absorption and the excitation of resonant lattice vibrations. Infrared photons are first absorbed by free carriers (electrons or holes) within the silicon matrix, transmitting kinetic energy to them. Subsequently, these carriers transfer energy to the lattice, causing localised heat generation. The 943.4 cm^{-1} band corresponds to the vibration modes of silicon lattice bonds, possibly affected by surface-terminating species such as Si-O or Si-H, which are common in PS due to its high surface-to-volume ratio. The nanostructured morphology of PS enhances these effects: it is interconnected pores and surface defects increase the free carrier density by quantum confinement and trap states, while the disordered lattice promotes phonon localisation, reducing thermal conductivity and enhancing energy retention. In addition, light trapping within the porous structure by multiple internal reflections extends the effective absorption path, enhancing the photon-phonon interaction. The combination of these mechanisms, augmented by impurities and structural heterogeneity, leads to effective localised thermalisation, essential for applications that require spatially controlled heating [1].

Localised hot spots form in regions where the temperature significantly exceeds that of the surrounding material. These hot spots arise from photon-structure interactions, where the porous morphology restricts heat dissipation because of the reduced thermal conductivity of PS. This concentrated heat intensifies vibrational and thermal activity, leading to an uneven temperature distribution and potential structural modifications or phase changes. These phenomena are critical for understanding the structural transformations associated during laser-induced consolidation.

4.3. Heat Distribution in The Porous Silicon Layer

A model was created to analyse the heat dispersion in the PS layer undergoing laser processing.

$$\frac{\partial T}{\partial t} - \frac{k}{\rho C}\nabla^2 T = \dot{q}_v \tag{4.1}$$

Equation 4.1 is the heat conduction equation. It describes the temperature distribution T (K) in a material over time t, where k is the thermal conductivity, ρ is the density of the material, C is the specific heat capacity and $\dot{q}_v$ is the rate of volumetric heat generation, representing the amount of heat generated per unit volume of the material. The $\dot{q}_v$ is given by $\dot{q}_v = \alpha I$, where α is the inverse absorption length, and I is the intensity of light at position $r,\ z$, where r is the radial distance from the focus, and z is the depth below the surface of the sample.

Assuming a Gaussian beam focused at the surface of the sample,

$$I = I_0 \left(\frac{\omega_0}{\omega(z)}\right)^2 \exp\left(-\frac{r^2}{\omega(z)^2}\right) \exp(-\alpha z) \tag{4.2}$$

where $\exp(-\alpha z)$ is attenuated by a factor due to absorption within the sample. $\omega(z)$ is expressed in terms of the beam waist ω_0 as,

$$\omega(z) = \omega_0 \sqrt{1 + \left(\frac{z}{z_R}\right)^2} \tag{4.3}$$

and the Rayleigh range is $z_R = \pi\omega_0^2 n/\lambda$ where n is the refractive index and λ is the wavelength. The calculation can be easily updated if a more appropriate expression for the intensity is available than the equation (4.2), which assumes that the only effect of absorption is to attenuate the intensity independent of r.

Equation 4.1 may be cast in a more convenient form after defining the dimensionless variables: $u = T/T_0$, $R = r/\omega_0$, $Z = z/\omega_0$, and $\tau = t/\Delta t$. The Equation 4.1 then becomes

$$\frac{\partial u}{\partial \tau} - \frac{k\Delta t}{\rho C \omega_0^2} \nabla_{R,Z}{}^2 u = \frac{\alpha I_0 \Delta t}{\rho C T_0} \left(\frac{\omega_0}{\omega(z)} \right)^2 \exp\left(-\frac{2R^2}{\omega(Z)^2} \right) \exp\left(-\alpha \omega_0 Z\right) \tag{4.4}$$

Equation 4.4 was discretised on an exponentially expanding grid in the R and Z directions with the boundary conditions,

$$\left| \frac{\partial u}{\partial Z} \right|_{Z=0} = 0 : \text{no heat lost to the surroundings above the sample.} \tag{4.5}$$

$$\left| \frac{\partial u}{\partial R} \right|_{R=0} = 0 : \text{radial symmetry.} \tag{4.6}$$

$$u \to 1 : \text{as } R \to \infty \text{ or } Z \to \infty \tag{4.7}$$

The initial condition is taken as a uniform sample temperature of $u = 1$. Equation (4.4) was solved by a fully implicit finite difference scheme using the method of successive over-relaxation to solve the elliptic equations at each time step on a R, Z grid of 100×100 points. This grid size was found to be sufficient to converge the temperature values to approximately 1%.

Optical and material parameters

Only three parameters are needed for the Gaussian beam model used to describe the irradiation: ω_0, the beam waist. n the refractive index and α the inverse absorption length. The beam waist can be estimated as half of the spot diameter. The optical properties of porous silicon are taken from the literature [105, 67]. The thermal conductivity of porous silicon is much lower than that of single-crystal silicon by several orders of magnitude [9, 67]. A range of different values was tried, from the bulk silicon value of 130 W m^{-1} K^{-1} to 0.1 W m^{-1} K^{-1}. The density of silicon was adjusted for porosity, but the specific heat capacity (0.71 J g^{-1} K^{-1}) of bulk silicon was used because this should be approximately independent of porosity. Finally, the beam power at sample I_{meas} was measured for the 10.6 µm laser on the confocal microscope and used to determine I_0.

$$I_{meas} = 2\pi I_0 \int_0^\infty \exp\left(-\frac{2r^2}{\omega_0^2} \right) r dr = \frac{\pi \omega_0^2}{2} I_0 \tag{4.8}$$

Limitations and assumptions of the model

- The beam profile is assumed to remain Gaussian as it penetrates the PS.
- Suppose that the beam is focused so that the beam waist coincides with the top of the PS layer.
- Two-photon absorption effects are ignored.
- The porosity of the PS layer is not precisely known. This means that there is also uncertainty in the optical parameters of PS.
- The precise doping concentration of the silicon substrate is unknown, as the resistance of the substrate ranges from $(1 - 10\ \Omega.\text{cm})$.
- Assumption that no heat is lost to the air above the sample.
- The PS layer is assumed to be homogeneous, which simplifies heat conduction modelling and aligns with the uniform etching process used during fabrication.

The temperature increases steadily and reaches a stable state determined by the balance between absorption and thermal diffusion away from the focal point at $R = 0,\ Z = 0$. Figure 4.2 shows a graph of the temperature in focus against time for a beam waist of 235 μm, a thermal conductivity of 0.1 W m^{-1} K^{-1}, and an inverse absorption length of 10^5 m^{-1}. The temperature T is normalised by an initial temperature of $T_0 = 293$ K. The beam power integrated into the sample was set to the measured value of 5 W and 15 W in steps of 5 W. Based on the porosity measurement in the last chapter, the porosity of the layer was estimated as 80%, and it was assumed that the depth of the layer was large. The steady-state temperature profile in the porous silicon layer (at 500 μs) is shown in Figure 4.2.

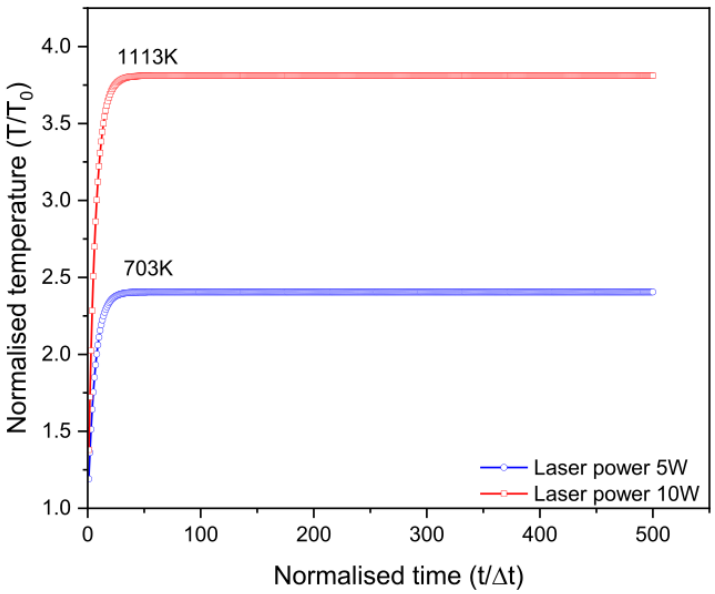

Figure 4.2 Normalised temperature $u = \frac{T}{T_0}$ against normalised time $\tau = t/\Delta t$ at the focus of laser power 5 W and 10 W. The laser beam of λ=10.6 µm on a porous silicon layer $k = 0.1$ $Wm^{-1}K^{-1}$. The beam waist was 235 µm.

The values chosen for this simulation include realistic optical parameters and realistic thermal conductivity, although perhaps at the low end of the data range for porous silicon [67]. Notably, the temperature rises to 703 K and 1113 K for 5 W and 10 W laser powers, respectively. The simulation shows that when PS is processed by a laser at a power of up to 10 W, the temperature reaches 1113 K, lower than the melting point of the bulk silicon (1687K)[104].

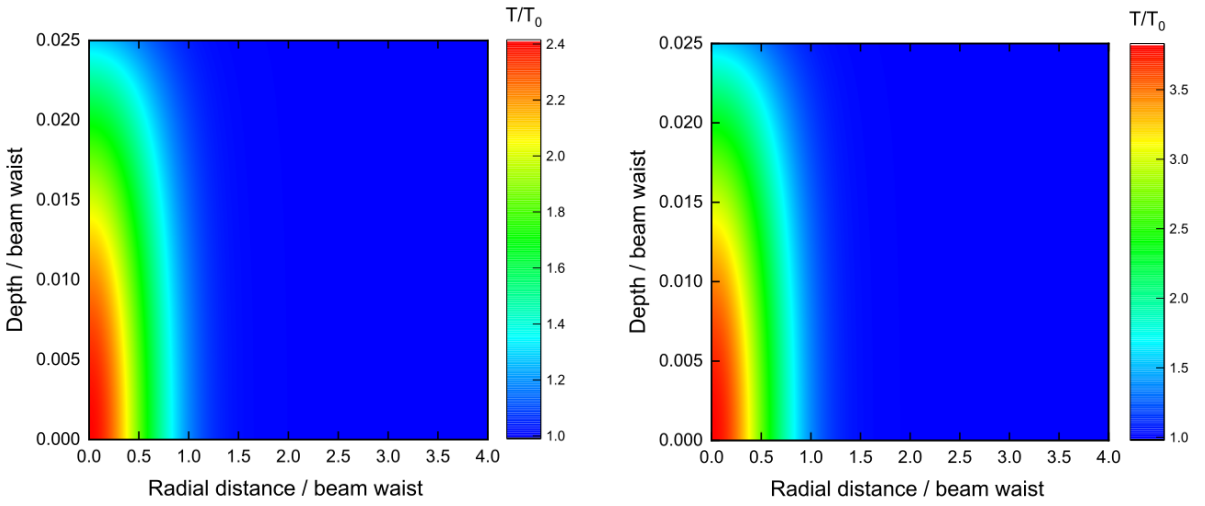

(a) Laser power 5 W

(b) Laser power 10 W

Figure 4.3 Cross-sectional temperature profiles in porous silicon layer during CO_2 laser processing.

Figure 4.3 shows the temperature distribution profiles for CW CO_2 laser irradiation on PS at 5 W and 10 W revealing the distinctive thermal behaviours influenced by the interaction of laser power, material structure, and heat dissipation processes. At 5 W irradiation, the peak normalised

temperature (T/T_0) reaches approximately 2.4 at the beam centre ($r/\omega_0 = 0$), decaying smoothly to $T/T_0 \approx 1.0$ at a radial distance of $r/\omega_0 \approx 1.0$. This profile indicates an effective radial heat distribution that is constrained by the inherently low thermal conductivity of PS (0.2 to 0.5 W m^{-1} K^{-1}) [193, 218], this is the result of phonon scattering at the pore interfaces and defects [46]. In contrast, the 10 W laser provides a significantly higher peak temperature ($T/T_0 \approx 3.5$) at the centre of the beam, with a sharper radial decay to $T/T_0 \approx 1.0$ at $r/\omega_0 = 1.0$. This narrower, more intense heating zone underscores the nonlinear relationship between laser power and thermal accumulation [109], influenced by increased photon-phonon coupling and free-carrier absorption at high-energy densities.

The depth-dependent temperature profiles further distinguish the two regimes. For the 5 W case, the temperature at a depth of $z/\omega_0 = 0.025$ remains moderate ($T/T_0 \approx 1.2$), indicative of limited subsurface heating and effective lateral dissipation. At 10 W, however, the steeper thermal gradient ($T/T_0 \approx 1.5$ at the same depth) demonstrates a deeper penetration of energy and reduced heat dispersion, probably resulting from the intensification of the phonon localisation by the structural disorder. The porous network allows photon trapping through multiple internal reflections, which enhances absorption at higher power, increasing the effective interaction path and intensifying localised thermalisation [38].

The difference arises from the distinct PS morphologies. At 10 W, the higher power density increases the absorption of the free carrier and causes nonlinear effects, including defect-assisted multiphonon processes. The voids and impurities in the porous structure concurrently reduce thermal conductivity, developing a self-reinforcing cycle of heat retention. This differs from the 5 W regime, in which reduced energy deposition allows for a more gradual redistribution of heat, thus minimising the risks of thermal runaway.

The results of the materials vary accordingly. The 5 W irradiation regime, characterised by moderate and uniform heating, is appropriate for applications necessitating controlled surface modifications, including oxidation or annealing, while preventing structural degradation. The 10 W regime extreme localised temperatures ($T/T_0 > 3$) present a risk of phase transitions or melting at the pore interfaces, which may lead to microcracking or delamination as a result of differential thermal expansion. These conditions are beneficial for processes such as laser-induced consolidation, where precise energy deposition is essential for pore closure or densification.

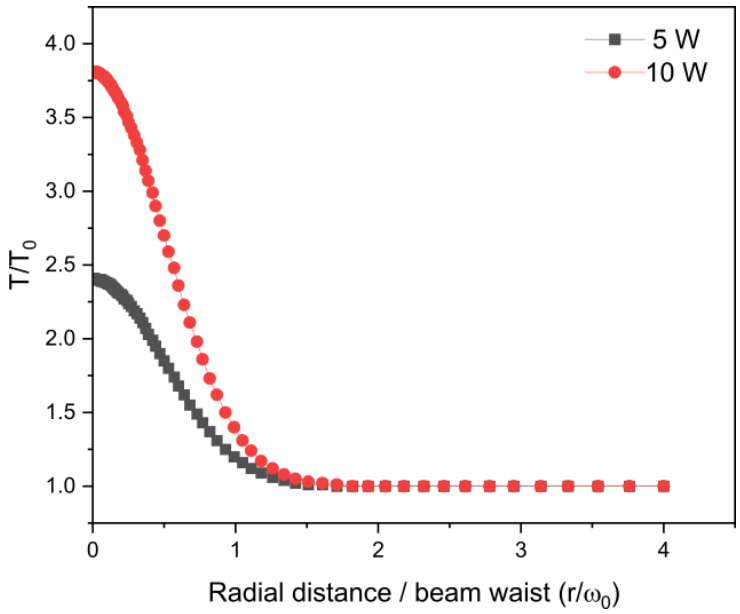

Figure 4.4 Temperature–distance profiles for 5 W and 10 W CW CO_2 laser irradiation on PS.

Figure 4.4 illustrates the temperature-distance profiles for CW CO_2 laser irradiation on porous silicon at 5 W and 10 W. In particular, for both power levels, the normalised temperature (T/T_0) remains significantly elevated within $r/\omega_0 \leq 1.5$, indicating a confined region of heat accumulation. Under 5 W irradiation, the temperature gradually decreases from a moderate peak at the beam center ($r/\omega_0 = 0$) to ambient levels by $r/\omega_0 = 1.0$. This broad and uniform thermal profile reflects the low thermal conductivity of PS owing to effective phonon scattering at the pore interfaces and supports controlled surface modifications such as oxidation or annealing without inducing structural damage.

In contrast, the 10 W profile exhibits a sharper temperature gradient, with a higher peak (approximately $T/T_0 \approx 3.5$) in the centre and a rapid decay to the baseline by $r/\omega_0 = 1.0$. This more intense localised heating is consistent with the enhanced photon–phonon coupling and defect-assisted absorption at elevated power levels. The porous network further amplifies energy deposition through multiple internal reflections, increasing the risks of microcracking or phase transitions if the energy is not carefully managed.

Overall, these observations emphasise that while moderate laser power produces a broad, evenly distributed thermal field conducive to precision processing, higher power intensities lead to more confined and intense heating, necessitating meticulous calibration to avoid thermal runaway and structural degradation.

4.4. Experimental Procedure and Analysis

Initially, the PS sample was created by electrochemical etching with a current of 5 mA for 20 minutes. The resulting PS layer had a thickness of approximately 6.5 µm. The setup shown in Figure 2.3 was used for laser processing. The PS sample was mounted on a holder perpendicular to the X-Y stage holder, positioned 10.16 cm from the lens to ensure optimal beam focus. The laser beam, operating at 5 W power, was directed onto the PS surface. The stage was programmed to move along the x-axis at an initial speed of 50 µm/s, producing a laser-written line on the PS. Subsequently, the sample was raised by 1 mm along the z-axis to avoid overlap. The platform was reset to its starting position along the x-axis. The process was repeated at progressively slower speeds of 20 µm/s, 10 µm/s and 5 µm/s.

Slower stage speeds increased the localised laser exposure time, enhancing thermal energy deposition per unit area. This resulted in four distinct lines on the PS sample, each corresponding to a specific speed and exposure duration.

These lines were examined using microscopic and spectroscopic analysis. The process was repeated in the PS sample using a higher power (10 W). Figure 4.5 shows that the laser-writing lines have a texture and a colour different from the surrounding PS.

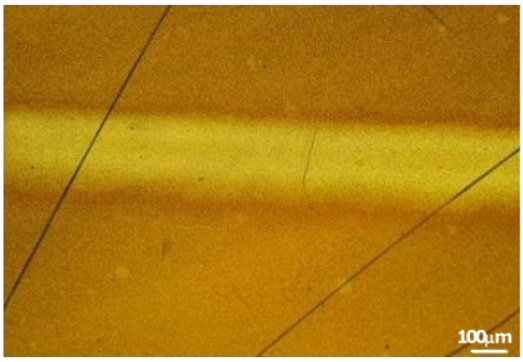

(a) Laser power 10 W at speed 50 µm/s

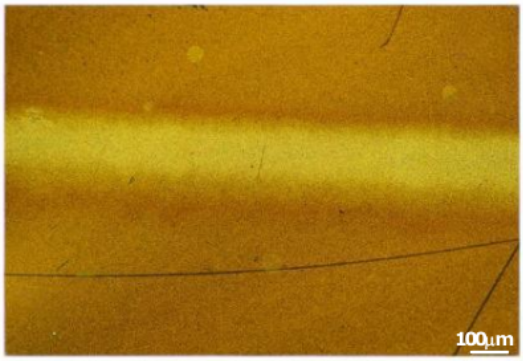

(b) Laser power 10 W at speed 20 µm/s

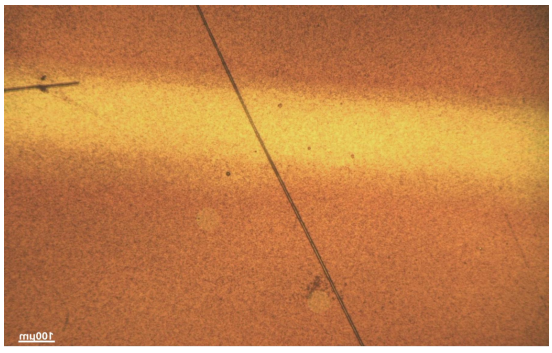

(c) Laser power 10 W at speed 10 µm/s

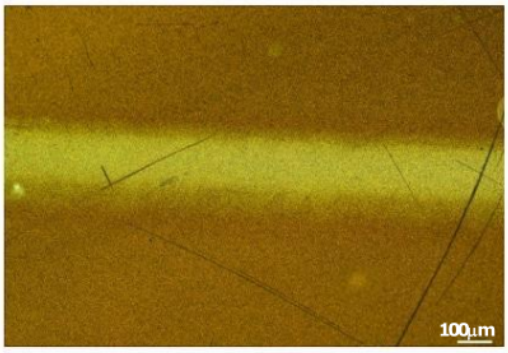

(d) Laser power 10 W at speed 5 µm/s

Figure 4.5 Optical microscope images for porous silicon exposed to CO_2 laser at power 10 W using different speeds.

4.5. Laser-Induced Thermal Consolidation of Porous Silicon

As the material is heated, the nanoporous structure experiences softening of the pore walls due to increased atomic mobility and reduced mechanical stability [210]. Structural reorganisation induced by elevated temperatures drives the consolidation of PS under thermal exposure [178]. Thermal activation increases viscous flow and localised sintering in the nanostructured silicon matrix, resulting in wall thickening, pore collapse, and a subsequent decrease in overall porosity [222]. The process involves densification, where the PS layer shifts from a high-surface-area morphology to a more compact, continuous phase. Laser irradiation acts as a focused thermal source, allowing rapid energy deposition that specifically changes the PS microstructure. The transient thermal gradients produced during laser writing improve non-equilibrium phase transformations, with consolidation confined to the irradiated areas because of the spatial precision of the energy input (Figure 4.6a).

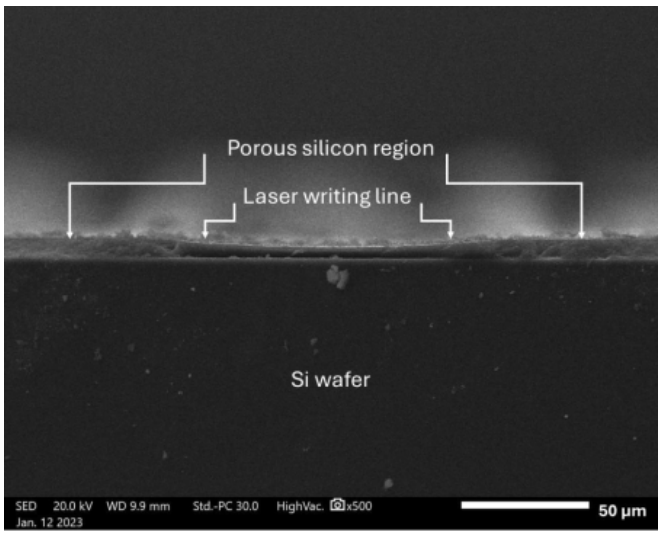

(a)

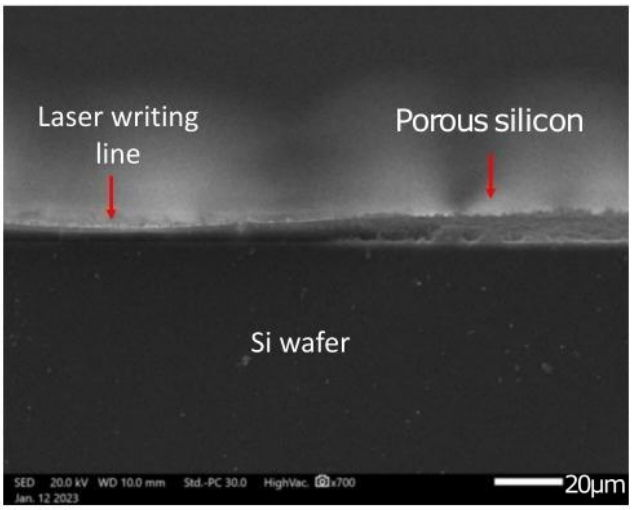

(b)

Figure 4.6 SEM image for cross-section shows the difference between the thickness of PS and laser writing line (laser power 5W).

Analysis of the laser-processed PS layer using SEM demonstrated apparent morphological differences between consolidated and unprocessed areas. Cross-sectional imaging demonstrated a reduction in layer thickness from approximately 7 µm in native porous silicon to 4 µm within the laser-written line (Figure 4.6b). The observed disparity is directly connected to the densification mechanism when pore collapse and material redistribution lead to a reduction in void volume and an increase in packing density. The consolidated zone showed a uniform microstructure with reduced pore connectivity, in contrast to the interconnected porosity of the unprocessed PS. The observed structural changes indicate that laser-induced thermal effects facilitate localised consolidation, offering a method of developing density gradients in silicon-based substrates for applications requiring spatially modulated optoelectronic or mechanical properties.

Unfortunately, the resolution of SEM does not allow for the study of the sample's surface morphology, so the structure was studied using AFM.

4.6. Structural Characterisation of Consolidated Porous Silicon

Optical microscope images of PS after CO_2 laser processing (Figure 4.5) show marked changes in both colour and texture. These changes appear as consolidated regions within the PS layer, visually distinct from unprocessed areas (Figure 4.6). The increased temperature from laser exposure improves crystallisation, causing adjacent pores to merge and their separating walls to thicken [181].

Figure 4.7 presents an AFM image of a laser-written line on a 6 µm × 6 µm PS sample, where the average pore diameter has increased to 67 nm, substantially wider than the 41 nm observed in the unprocessed PS. These larger pores, coupled with thicker pore walls, underscore the structural reorganisation induced by laser processing. Furthermore, Figure 4.8e provides a three-dimensional AFM image that illustrates this consolidation effect.

Laser processing also reduces surface roughness. As shown in Figure 4.8f, the laser-processed surface exhibits an RMS roughness of 0.72 nm over a 6 µm×6 µm area, which is considerably lower than the 1.48 nm measured for unprocessed PS (Figure 4.8d), yet still higher than the 0.372 nm of bulk silicon (Figure 4.8b). Collectively, these findings highlight the dual effects of CO_2 laser processing: pore merging and wall thickening, leading to a consolidated network, and significant smoothing of the PS surface.

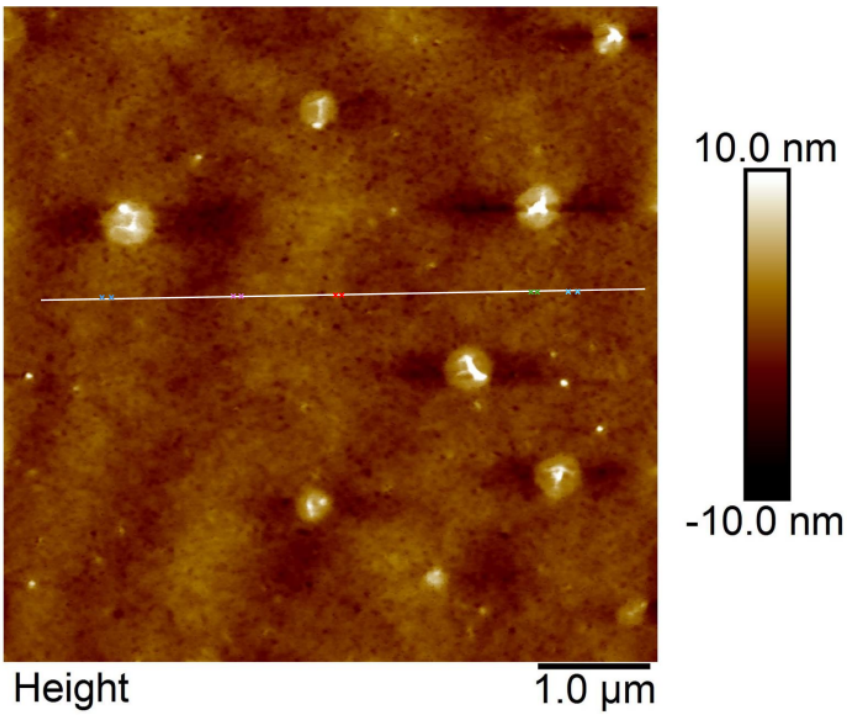

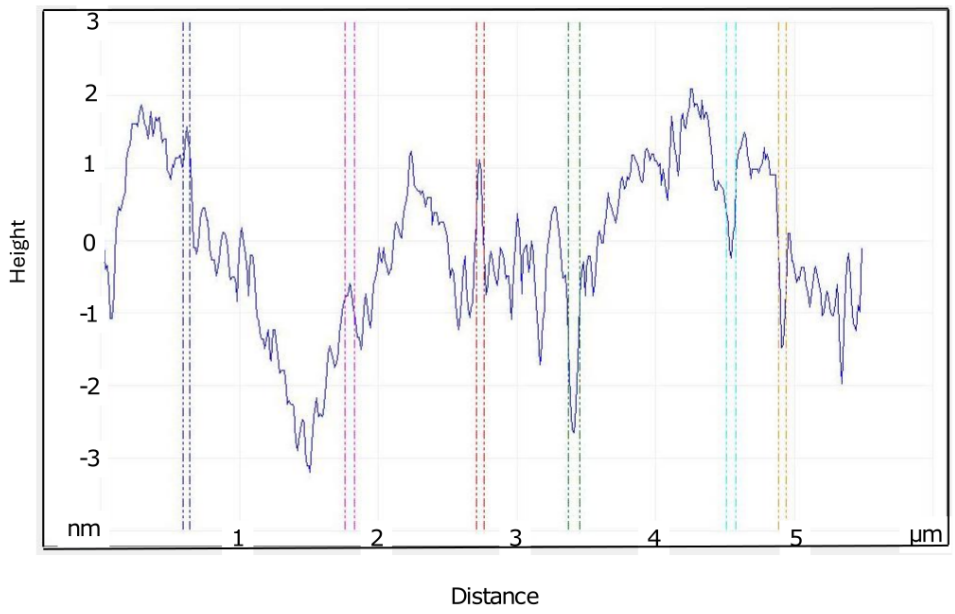

Figure 4.7 The coloured dots on the line in the upper Figure represent the pore size (the lines in the down Figure) after laser writing at power 10 W as determined from the AFM image.

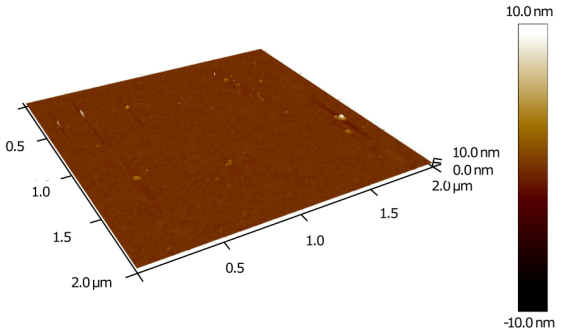

(a) 3D Image Si.

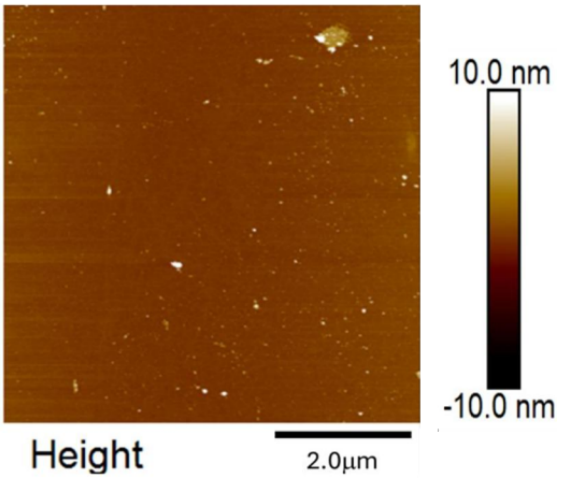

(b) Si roughness

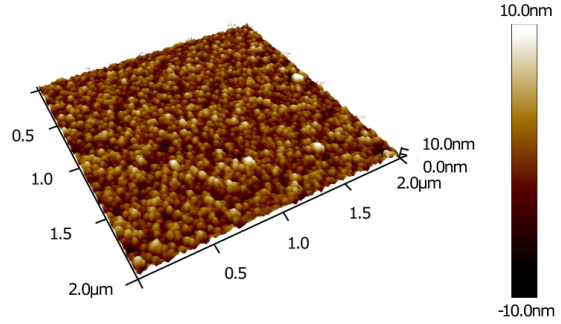

(c) 3D Image PS.

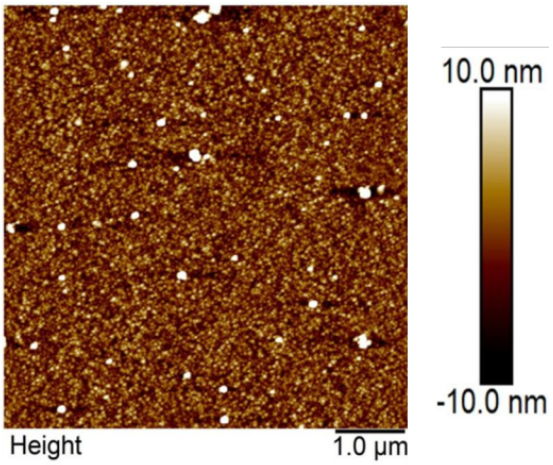

(d) PS roughness.

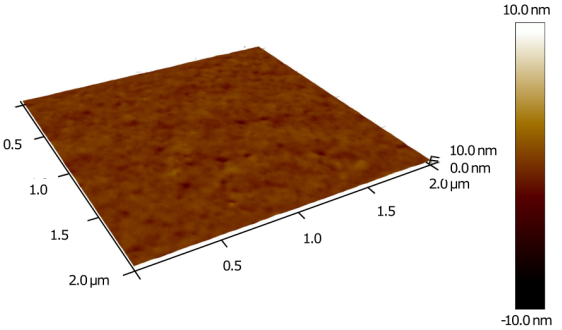

(e) 3D Image(laser power 10W).

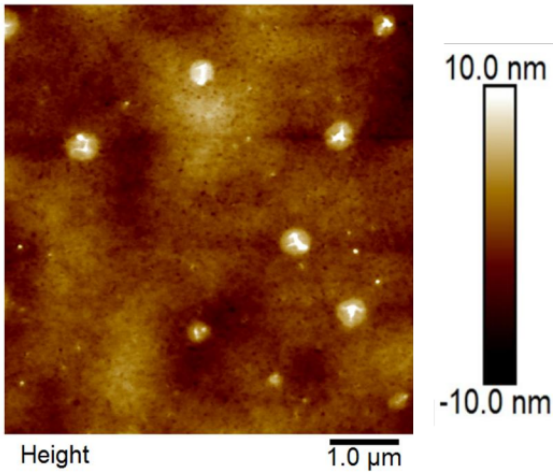

(f) laser power 10W roughness.

Figure 4.8 AFM images of porous silicon, silicon, and laser writing lines at a power of 10 W: (a) 2 µm × 2 µm silicon morphology; (b) 6 µm × 6 µm topography image of silicon; (c) 2 µm × 2 µm porous silicon morphology; (d) 6 µm × 6 µm topography image of porous silicon; (e) 2 µm × 2 µm laser writing line morphology; (f) 6 µm × 6 µm topography image of the laser writing line.

4.7. Raman Spectrum of the Consolidation Porous Silicon.

The application of a CW CO_2 laser to PS leads to changes in the structural and optical properties of the material. Raman spectroscopy is a crucial technique for investigating these changes, providing valuable insights into the phonon behaviour of PS after laser exposure. By analysing the Raman spectra, one can assess the crystallinity, nanocrystal size, and presence of amorphous phases, thereby defining structural transformations and material quality.

PS samples were fabricated by electrochemical etching of a p-type silicon wafer ($1 - 10\ \Omega$.cm). Etching was performed by applying a current of 5 mA for 20 minutes. The thermal threshold for laser-induced melting of porous silicon decreases from 35 to 11 mJ/cm^2 as porosity increases from 45% to 82% [209]. This thermal sensitivity influences the size of the pores and the thickness of the wall. The heating effects of the laser can be precisely controlled by adjusting the laser power and irradiation duration, enabling fine-tuning of the material's properties.

4.7.1. Effect of Laser Power on Raman Spectrum

To investigate the impact of laser power on the Raman spectra, PS samples were processed to 5 W and 10 W laser irradiation at various stage speeds (50, 20, 10 and 5 μm/s). Figure 4.9a and Figure 4.9b show the normalised Raman spectra for crystalline silicon, unprocessed PS, and laser-processed PS under different combinations of power speeds. All spectra were normalised to their maximum intensity, facilitating effective comparison by removing variations unrelated to the material. The reference spectrum for crystalline Si (solid black line) shows a sharp, well-defined peak at around 520 cm^{-1}, which corresponds to the characteristic phonon mode of silicon [137]. In contrast, the unprocessed PS spectrum (dashed red line) has a broader, lower intensity peak, reflecting its porous structure and a higher proportion of disordered silicon regions [98]. When PS is exposed to laser radiation, the Raman peak starts to narrow and becomes almost symmetric near the 520 cm^{-1} position. This observation suggests that local annealing or recrystallisation is occurring within the porous network, effectively increasing the crystalline fraction of silicon.

The changes become stronger with an increase in laser power (from 5 W to 10 W) or a decrease in stage speed (from 50 μm/s to 5 μm/s), suggesting that the total energy delivered per unit area is important for providing structural reorganisation. Increased power or reduced speeds result in improved heating and longer reaction durations, which supports further crystallisation or densification [119]. There is a slight shift in peak position, and there are changes in the FWHM of crystalline silicon versus laser-processed PS signals. That can further quantify the degree of structural transformation. A narrower, more defined peak implies a reduction in disorder

and a higher concentration of well-ordered crystal domains. These spectra provide evidence of increased crystallinity in PS after laser processing.

Overall, the Raman data confirm that laser processing alters the crystalline and porous characteristics of PS.

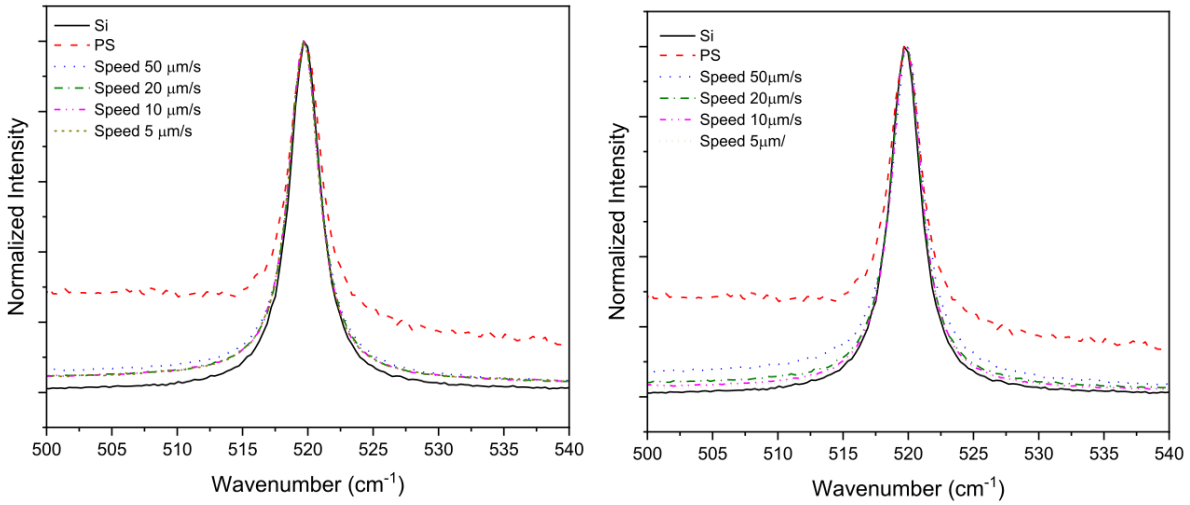

(a) Laser power 5 W. **(b)** Laser power 10 W.

Figure 4.9 The Raman peaks with two samples (laser power 5 W and 10 W). Laser writing used different speeds 50, 20, 10 and 5 µm/s.

4.7.2. Effect of Laser Writing Speed on Raman Spectrum

The laser writing speed plays a crucial role in determining the structural and optical properties of PS. Reducing the scanning rate results in an extended laser-substrate interaction, which increases the creation of heat in the material. The thermal input helps with partial densification and recrystallisation of the porous network, as demonstrated by the changes observed in the Raman spectra.

Figure 4.10 compares normalised Raman peaks of PS for two laser powers (5 W and 10 W) at writing speeds of 50, 20, 10, and 5 µm/s. At slower speeds, the characteristic peak near 520 cm^{-1} approaches the sharper profile of the bulk silicon, indicating a higher crystalline fraction. In contrast, accelerated scanning preserves wider peaks similar to those of unprocessed PS, indicating a more disordered and porous structure.

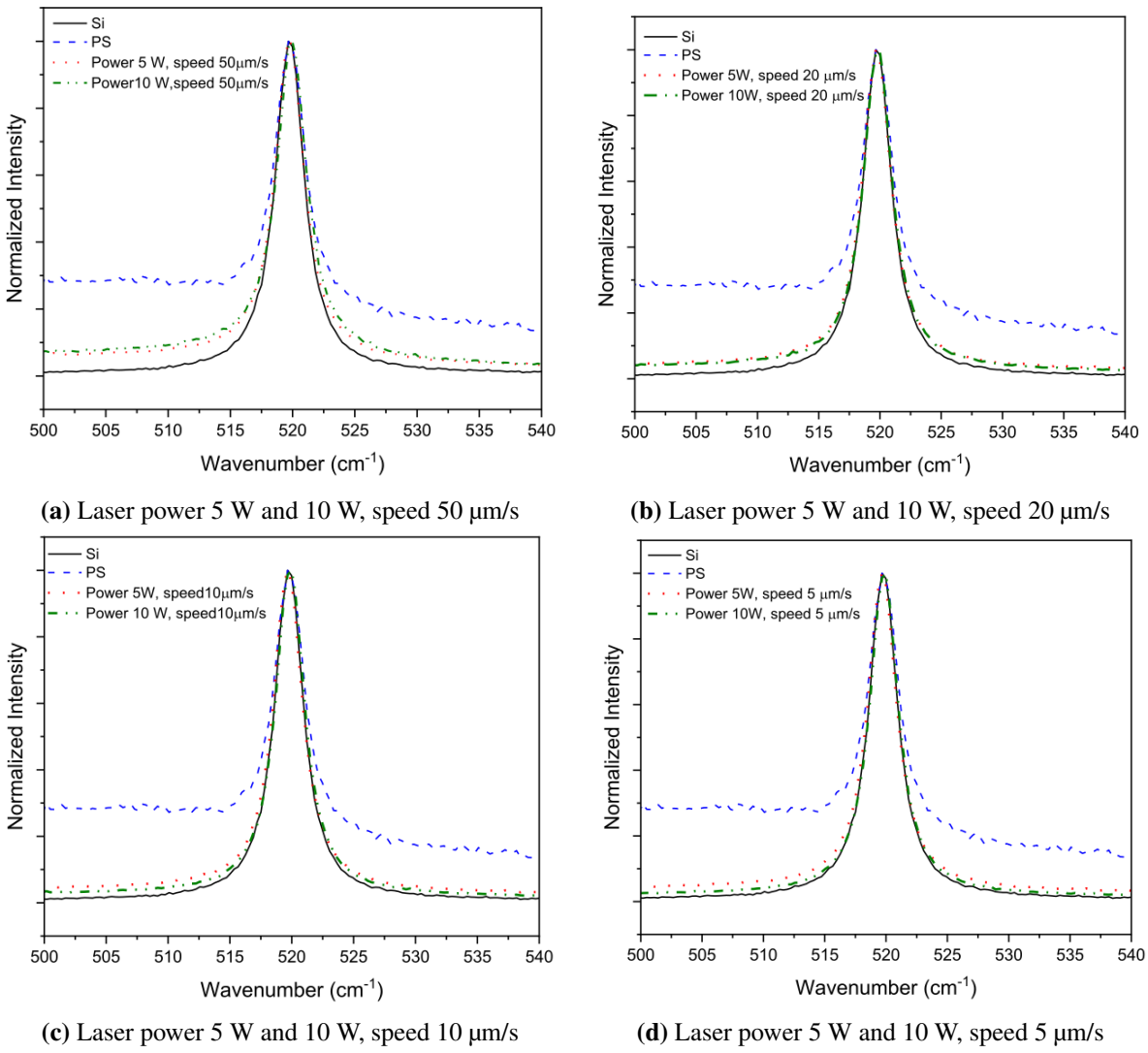

(a) Laser power 5 W and 10 W, speed 50 µm/s

(b) Laser power 5 W and 10 W, speed 20 µm/s

(c) Laser power 5 W and 10 W, speed 10 µm/s

(d) Laser power 5 W and 10 W, speed 5 µm/s

Figure 4.10 Raman peaks for laser writing at different speeds (50, 20, 10, and 5 µm/s) for each laser power: 5 W and 10 W.

Figure 4.11 provides additional evidence through the Voigt fitting. In sub-Figure 4.11a, the Raman peak of the bulk silicon is accurately modelled using a Voigt function with a fixed Lorentzian linewidth $\Gamma = 2.7$ cm^{-1} [80]. Applying this fixed parameter to the laser-processed PS spectra (from sub-Figure 4.11b to sub-Figure 4.11i) highlights how the shape of the material lines evolves under different thermal conditions. Slower writing speeds and higher laser powers produce a narrower overall profile, reflecting enhanced crystallinity. Moreover, any slight shifts in the peak position may indicate localised strain induced by the laser process.

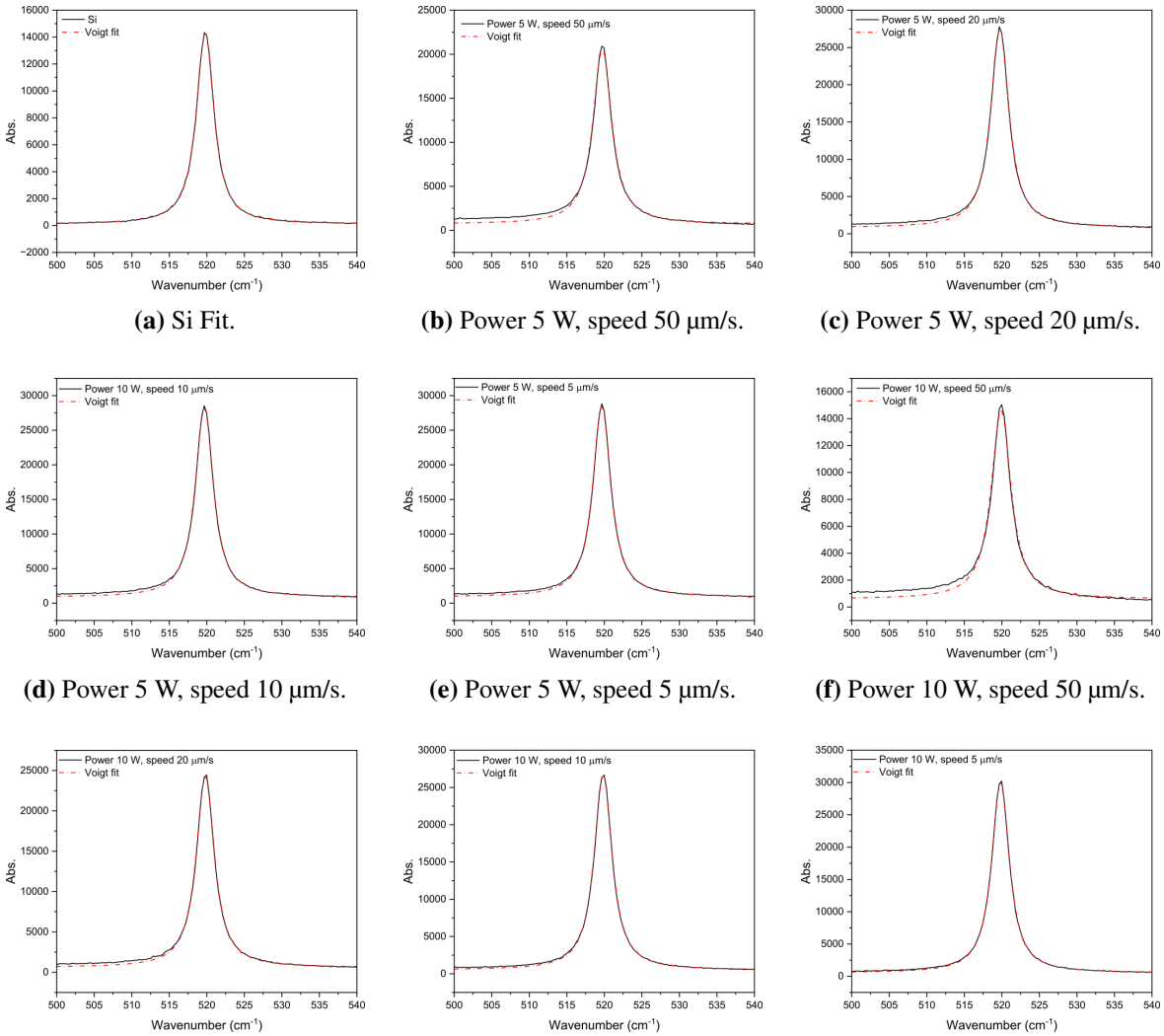

(a) Si Fit. **(b)** Power 5 W, speed 50 µm/s. **(c)** Power 5 W, speed 20 µm/s.

(d) Power 5 W, speed 10 µm/s. **(e)** Power 5 W, speed 5 µm/s. **(f)** Power 10 W, speed 50 µm/s.

(g) Power 10 W, speed 20 µm/s. **(h)** Power 10 W, speed 10 µm/s. **(i)** Power 10 W, speed 5 µm/s.

Figure 4.11 Voigt Fit Analysis: (a) Voigt fit of the bulk silicon Raman spectrum using a linewidth parameter of $\Gamma = 2.7$ cm^{-1}. (b), (c), (d), and (e) show the Voigt fitting of Raman spectra for laser-written lines at a power of 5 W, processed at different speeds: 50, 20, 10, and 5 µm/s, respectively. (f), (g), (h), and (i) represent the Voigt fitting of Raman spectra for laser-written lines at a power of 10 W, processed at the same speeds (50, 20, 10, and 5 µm/s).

The FWHM plot (Figure 4.12) quantifies these observations. For each laser power, the FWHM increases with increasing scan speed, confirming that rapid scanning reduces the net thermal exposure and limits the reorganisation of the material into a denser, more crystalline state. Notably, the 10 W data show a steeper climb in FWHM, emphasising that higher power intensifies the interplay between speed and local heating. These findings collectively demonstrate how judicious control of laser parameters can tune the microstructure and optical response of porous silicon for advanced applications.

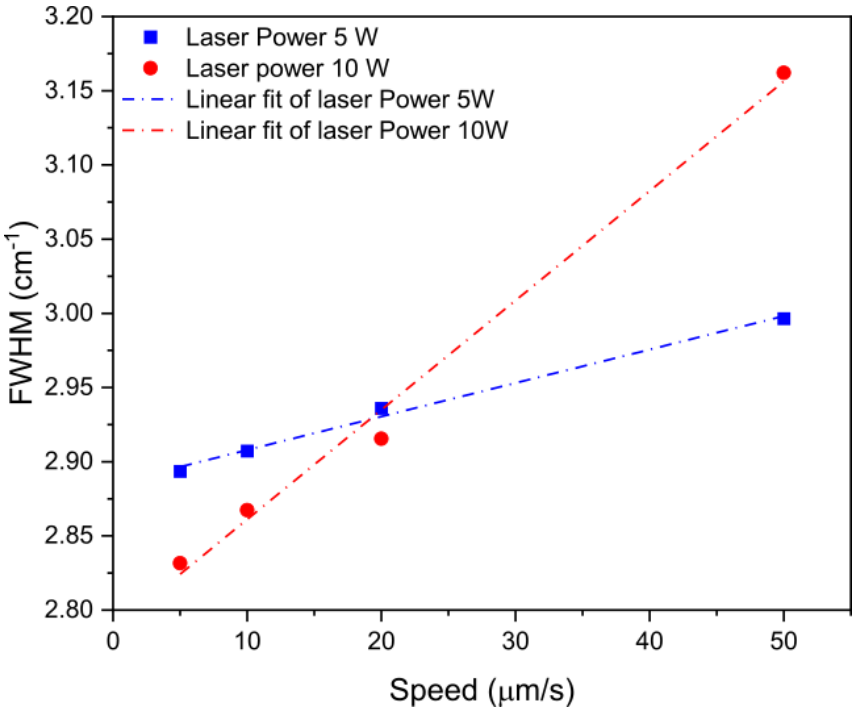

Figure 4.12 Graph showing the FWHM versus speeds for laser writing applications at different laser powers.

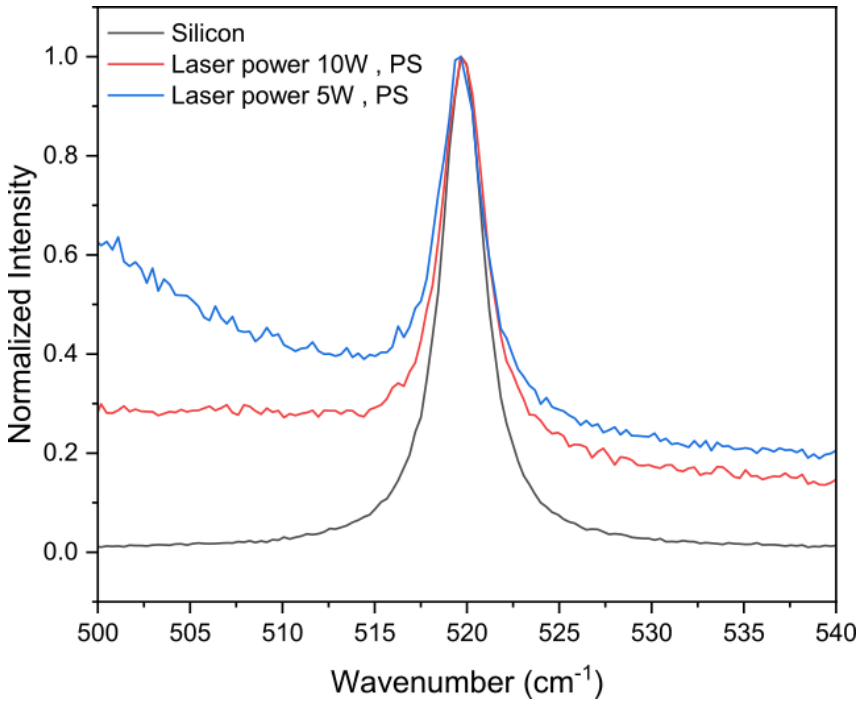

Figure 4.13 Comparison of initial porosity among porous silicon samples before to laser processing.

The FWHM plot (Figure 4.12) shows a slight crossing between the 5 W and 10 W data sets, indicating differences in the initial porosity or microstructure (Figure 4.13). These differences can overshadow the simpler assumption that higher power invariably leads to a narrower FWHM. In certain speed regimes, the nominally higher-powered sample exhibits a broader FWHM if its baseline microstructure does not support effective heat distribution or stable consolidation.

In contrast, at slower speeds, the higher power of the same sample leads to a more pronounced narrowing. Taken together, these observations underscore that both the laser power and the intrinsic properties of the porous substrate dictate the extent of thermal reorganisation and, consequently, the final crystallinity.

In summary, lower laser writing speeds and higher laser powers strongly affect the material by raising local temperatures, reducing porosity, and enhancing crystallinity in the processed regions. These effects are consistently observed across various experimental results, with slower speeds and higher powers leading to more pronounced structural changes. The interaction between laser speed and power underscores their importance as critical parameters for tailoring the structural and optical properties of porous silicon.

4.8. Conclusion

The study showed the effects of the CW CO_2 laser writing on PS, which depend on the laser power and writing speed. Reducing the laser writing speed increased the exposure time, resulting in higher localised heating. The significantly lower thermal conductivity of porous silicon compared to crystalline silicon led to uneven heat distribution and limited heat dissipation. This created localised hot spots within the laser-irradiated regions, which enhanced crystallinity.

Modelled temperature profiles indicated that increasing the laser power could elevate temperatures to just below the melting point of silicon, explaining some of the observed structural changes. SEM revealed a decrease in material density along the laser-irradiated lines, signifying the consolidation of the porous structure. Longer laser exposure times, achieved through reduced writing speeds, resulted in greater heating, which increased the thickness of the pore walls and enhanced the crystallinity of the PS layer.

Moreover, the temperature rise led to an expansion of the pore diameters, as confirmed by AFM topographic analyses of the laser-processed areas. Raman spectroscopy further validated these findings, demonstrating a spectral shift and narrowing, indicating a structural transition toward crystalline silicon. The decrease in the FWHM with slower writing speeds further supported the improvement in crystallinity.

The results underscore the critical role of laser-induced thermal effects in driving the consolidation of porous silicon. The reduction in porosity and enhancement of crystallinity, as evidenced by Raman spectroscopy and AFM, demonstrate that the consolidation process can effectively alter the structural and optical properties of porous silicon. The expansion of silicon

nanowires, as observed in the laser-processed regions, highlights the potential for fine-tuning material properties through controlled laser parameters.

The findings of this study demonstrate that the CW CO_2 laser processing is a versatile tool to induce consolidation in porous silicon. By carefully controlling laser parameters such as power and writing speed, it is possible to tailor the structural and optical properties of PS, making it suitable for applications in optoelectronics, sensing, and nanotechnology. Future work could explore higher laser powers, alternative wavelengths, and other material systems to further expand the scope of this technique.

Chapter 5. Laser Induced Melting and Recrystallisation of Porous Silicon

5.1. Introduction

It was previously explained that when a CW CO_2 laser is applied to a PS layer, localised heat zones are formed. This localised heating raises the temperature, resulting in the thickening of the pore walls and the expansion of pore sizes, ultimately leading to the consolidation of the laser-processed PS layers.

The absorption of laser energy induces localised heating, which significantly alters the optical and structural properties of PS. These changes include thermal expansion, stress development, and, in some cases, fracture of the silicon structure. Consolidation through controlled laser parameters enhances the uniformity and crystallinity of the PS layer, making it suitable for advanced applications such as optoelectronic devices [226] and biosensors [47].

In contrast, when the PS layer is exposed to temperatures near or exceeding the melting point of silicon (1687 K), it undergoes pronounced transformations. These include a significant and reversible improvement in optical absorption in oxidised PS layers, attributed to a thermally induced decrease in the band gap and an increase in Si-Si bonding states [108, 2]. Furthermore, exposure to high temperatures affects the morphology of PS, leading to notable changes in the Raman and photoluminescence (PL) spectra. These spectral modifications highlight laser-assisted surface interactions that influence the structural and chemical characteristics of the material [165, 181].

This chapter focusses on the effects of temperatures exceeding the melting point of silicon. By examining the thermal processes initiated by CW CO_2 laser irradiation, the study investigates how elevated temperatures drive structural, morphological, and chemical transformations in porous silicon. Understanding these thermally induced changes provides critical insight into the mechanisms of consolidation and material refinement under extreme conditions. The discussion explores how these elevated temperatures contribute to the crystallisation and densification of the PS structure, while also highlighting potential limitations such as stress and fracture.

5.2. Heat Distribution and Phase Transitions in Porous Silicon Under Laser Irradiation

The preceding chapter (Section 4.3) analysed the distribution of heat within a PS layer at a low-intensity laser. Several interconnected factors, including porosity, thermal conductivity, and laser intensity, influence the thermal distribution. Each of these components significantly affects the distribution and deposition of heat within the porous silicon, eventually affecting its thermal behaviour during laser exposure.

Porosity, which denotes the volume of a void within the silicon, affects the heat conductivity. With an increase in porosity, the thermal conductivity of the material decreases, which limits the ability of porous silicon to transfer heat effectively. The decrease in thermal conductivity arises from air-filled voids, which disrupts the pathways for phonon transport, the primary mechanism of heat conduction in semiconductors. Structural alterations result in localised heat when the material is exposed to laser radiation [116]. The low thermal conductivity of the material, combined with the thermal barriers created by its uniformly distributed pores, produces a distinctive pattern of thermal confinement. By increasing the laser intensity, the porous silicon undergoes a significant temperature rise, reacting to the energy input. The simulations shown in Figure 5.1 demonstrate that at laser power levels ranging from 15 W to 30 W, the internal temperature of the PS layer could exceed the melting point of crystalline silicon(1687 K) [176]. The transition from solid to liquid at high temperatures is important because melting can change the structure of the material and possibly lead to the collapse of the porous network.

When the laser power P nears 30 W, the temperature increases, potentially exceeding the boiling point of silicon of 2628 K [42], as shown in Figure 5.1 At this point, significant phase changes, such as vaporisation, can occur within the porous silicon, resulting in structural alteration or potential failure if the material is unable to disperse heat swiftly enough. This behaviour underscores the sensitivity of porous silicon to laser intensity, where incremental power increases can lead to significant thermal alterations and phase transitions.

Figures 5.2a to 5.2d shows the temperature distribution profiles of a CW CO_2 laser irradiating PS at 15 W, 20 W, 25 W and 30 W, highlighting distinct thermal responses at progressively higher powers while sharing the feature that (T/T_0) returns to unity at $r/\omega_0 = 1.0$ for each case. At 15 W, the peak normalised temperature at the beam centre $(r/\omega_0 = 0)$ approaches about 5 before dropping to the baseline of the ambient by one radius of the beam. This moderate increase suggests that, although phonon scattering at the pore interfaces [193] restricts the flow of radial heat, there is sufficient dissipation to prevent large-scale heating beyond $r/\omega_0 = 1.0$. At 20 W, the central peak reaches approximately $T/T_0 \approx 6$, again decaying to $T/T_0 = 1.0$ by the

beam radius. These observations are consistent with established findings that increased power intensifies photon–phonon coupling, yet the low thermal conductivity of PS (0.2–0.5 W m^{-1} K^{-1}) concentrates heat near the beam core [234, 37].

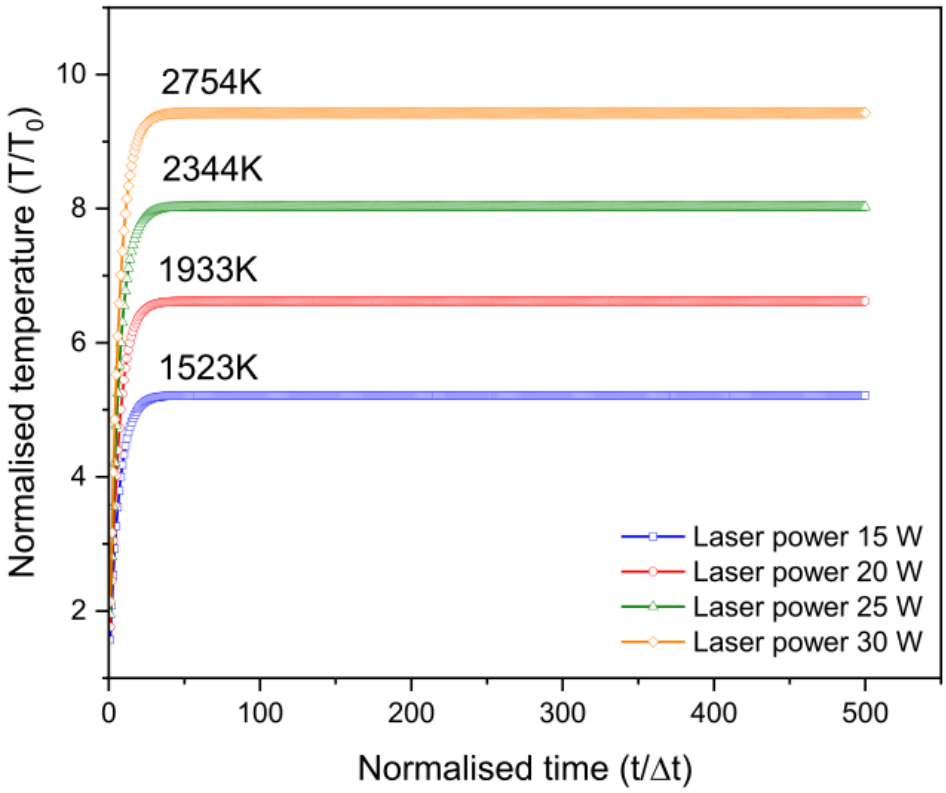

Figure 5.1 Normalised temperature $u = \frac{T}{T_0}$ against normalised time $\tau = t/\Delta t$ at the focus of laser power 15 W, 20 W, 25 W, and 30 W. The laser beam has a wavelength λ = 10.6 µm on a PS layer with thermal conductivity $k = 0.1$ $Wm^{-1}K^{-1}$. The beam waist was 235 µm.

In the higher-power regimes, 25 W and 30 W exhibit more pronounced localised heating in the centre, with T/T_0 values of approximately 8 and 9, respectively, before converging to the baseline within $r/\omega_0 = 1.0$. This reflects enhanced free-carrier absorption and multiphonon processes triggered by larger energy densities, as structural voids in the PS matrix promote recurrent photon trapping [37]. Despite the intense thermal zone, the ambient boundary at $r/\omega_0 = 1.0$ remains a clear demarcation, suggesting that the heat is largely confined within the beam footprint and does not propagate further radially.

Depth-dependent temperature maps corroborate the trend of deeper subsurface heating at higher powers. At 15 W, the region around $z/\omega_0 \approx 0.025$ retains a moderate temperature ($T/T_0 < 2.0$), implying that a significant portion of heat disperses radially near the surface. In contrast, steeper gradients at 20 W and beyond indicate more substantial penetration of energy, raising concerns about localised thermal runaway and structural changes, especially when defect-rich pore networks slow heat conduction. Nevertheless, these higher temperatures

can be harnessed for applications like laser-assisted sintering or densification, provided that the rapid rise does not induce microcracking or delamination caused by differential thermal expansion.

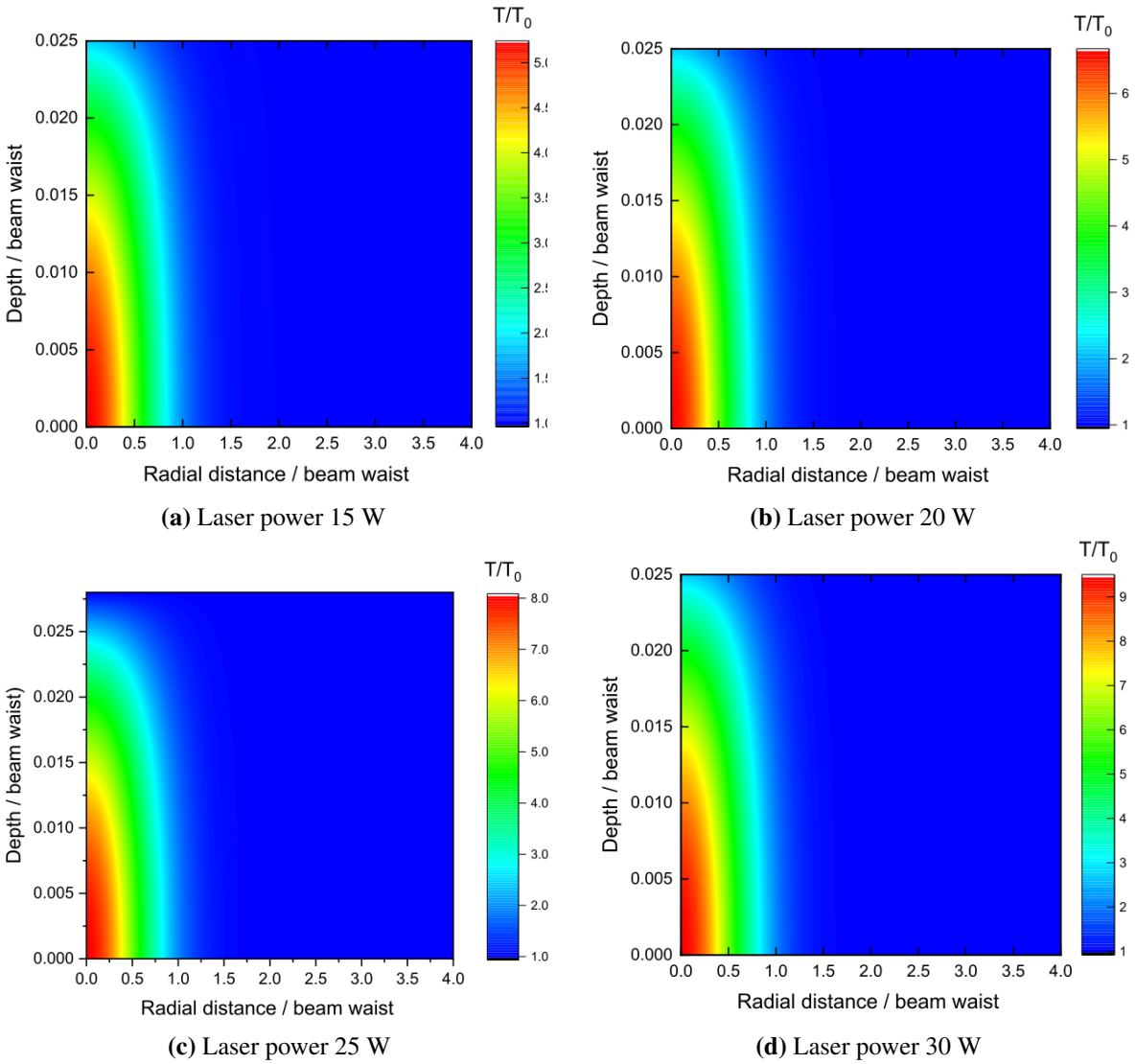

(a) Laser power 15 W

(b) Laser power 20 W

(c) Laser power 25 W

(d) Laser power 30 W

Figure 5.2 Temperature distribution of a CO_2 laser in a porous silicon layer for varying laser powers.

Overall, although the maximum centre temperature increases significantly with power, each profile reverts to $T/T_0 = 1.0$ by $r/\omega_0 = 1.0$, indicating a sharp thermal boundary defined by the radius of the laser beam. The interplay of PS porosity, phonon scattering, and multiple internal reflections ensures that heating remains confined within a limited radial domain, permitting precise thermal modifications at the beam core without extensively affecting the surrounding material.

The temperature–distance profiles in Figure 5.3 illustrate how PS responds to 15 W, 20 W, 25 W, and 30 W CW CO_2 laser irradiation. For all four power levels, the normalised temperature (T/T_0) remains significantly elevated within $r/\omega_0 \leq 1.5$, reflecting a localised heat zone that

intensifies with increasing laser power. At 15 W, T/T_0 peaks around 5 near the centre of the beam ($r/\omega_0 = 0$) and drops back to 1.0 at approximately $r/\omega_0 = 1.5$. This relatively broad decay aligns with the characteristic low thermal conductivity of PS, where phonon scattering at pore boundaries promotes radial heat dispersion without allowing extreme hotspots.

By contrast, the 20 W curve exhibits a higher central temperature around $T/T_0 = 6.6$, coupled with a more pronounced drop by $r/\omega_0 = 1.5$. This finding suggests that increasing power intensifies free carrier absorption and photon-phonon coupling, while the porous architecture still constrains the main heat zone within 1.5 beam radii. The 25 W and 30 W profiles reach even steeper peaks of roughly $T/T_0 = 8$ and 9.5, respectively, underscoring the nonlinear effect of higher energy density. Although the temperature returns again to the baseline beyond $r/\omega_0 = 1.5$, the significantly hotter core increases the potential for thermal stress, microcracking, or phase transitions, in line with prior observations that such elevated temperatures can cause localised damage if not carefully managed.

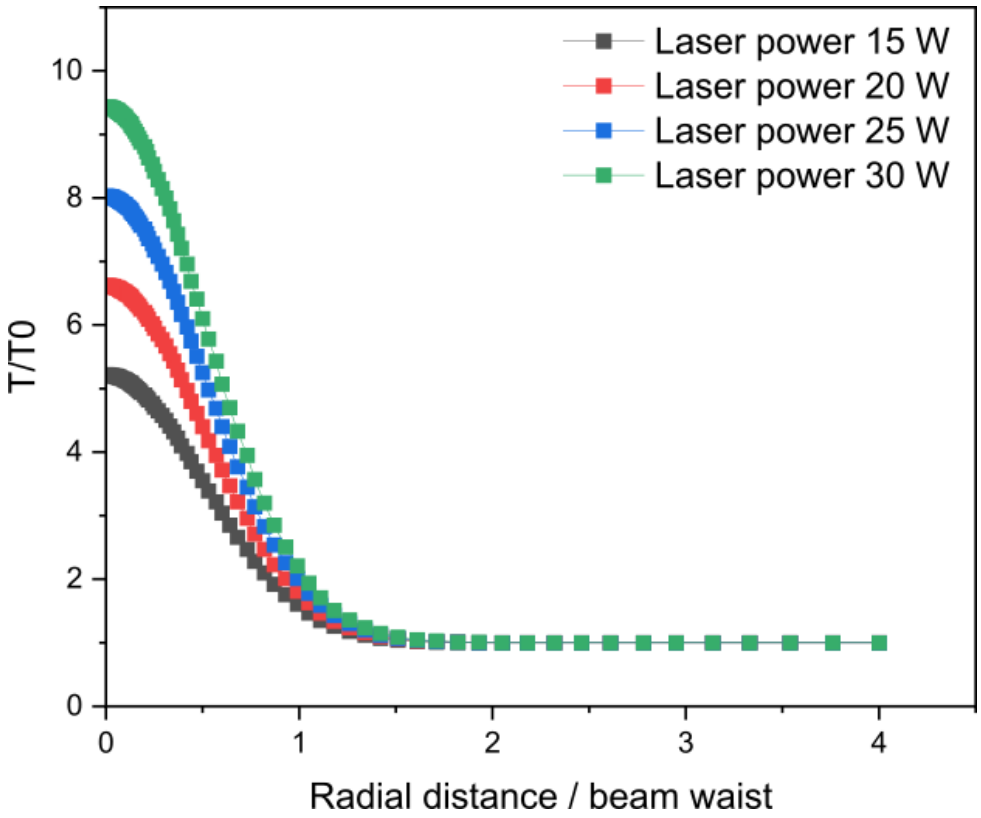

Figure 5.3 Temperature–distance profiles for 15, 20, 25 and 30 W CW CO_2 laser irradiation on PS

Together, these curves reveal how power scaling affects the interplay between heat retention and radial dissipation in porous silicon. Although moderate power levels (15 W–20 W) may support controlled surface modifications or mild annealing without significant structural risks, pronounced heating at 25 W–30 W could facilitate laser-assisted consolidation, densification or melting-recrystallisation - although with an increased likelihood of thermal runaway near the

centre of the beam. Consequently, tailoring the laser power to remain within safe temperature thresholds is essential for achieving the desired outcome, whether for uniform surface processing or for aggressive restructuring within a confined focal region.

5.3. Microscopic and Optical Changes in Porous Silicon After Laser Exposure

The PS sample was fabricated by electrochemical etching a 1 cm $\times$ 1 cm p-type silicon wafer with $\langle 100 \rangle$ orientation and resistivity of 1–10 $\Omega \cdot$ cm, using a current of 5 mA for 20 minutes. After cleaning and drying the sample, CW CO_2 laser irradiation was applied at intensities ranging from 8.65×10^{-5} to 1.73×10^{-4} W/µm^2, corresponding to laser powers from 15 W to 30 W in 5 W increments. This irradiation was performed at various stage speeds (50, 20, 10, and 5 µm/s) to vary the duration of the exposure, producing four distinct lines on the surface of the PS. Microscopic analyses revealed structural and colour changes after laser irradiation, as shown in Figure 5.4, along with the disappearance of UV light illumination in irradiated areas (Figure 5.5).

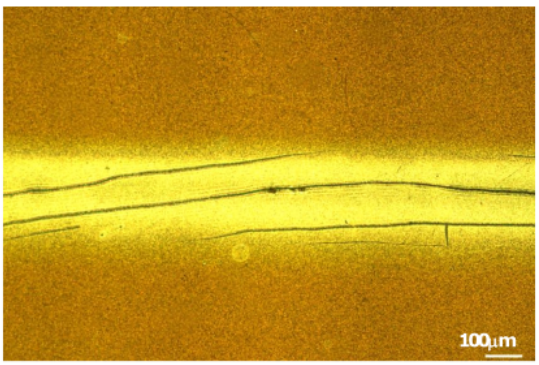

(a) Laser power 15 W at speed 50 μm/ s

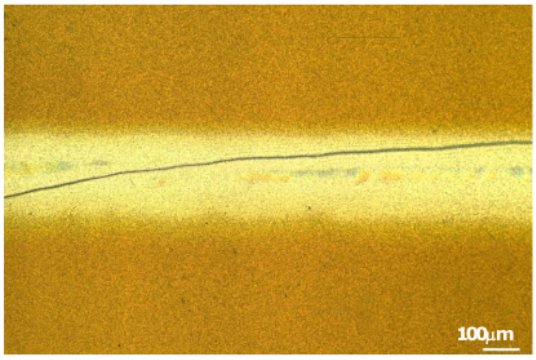

(b) Laser power 15 W at speed 20 μm/ s

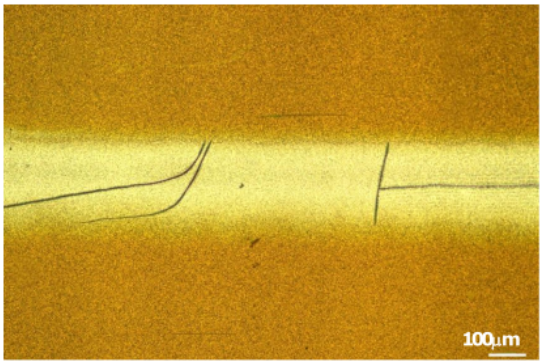

(c) Laser power 15 W at speed 10 μm/ s

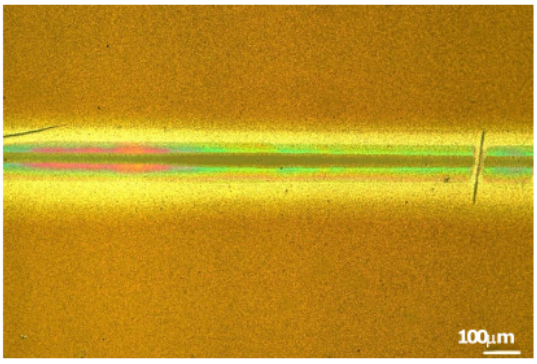

(d) Laser power 15 W at speed 5 μm/ s

Figure 5.4 Optical microscope images for porous silicon exposed to CO_2 in power 15 W (I=8.65×10^{-5} W/µm^2) using different speeds.

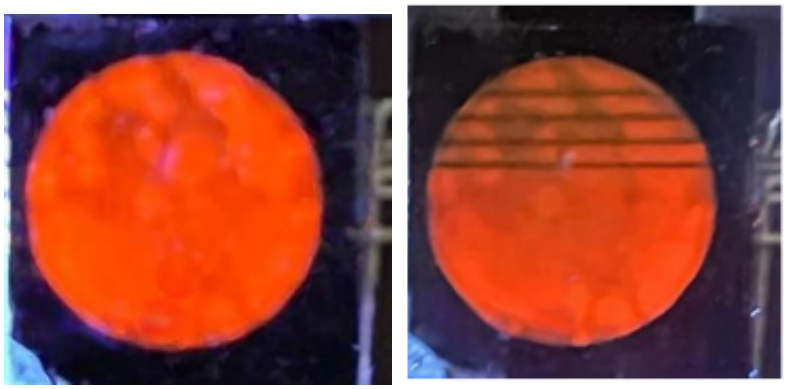

(a) Sample before laser writing. **(b)** Sample after laser writing

Figure 5.5 Photographs of a porous silicon sample, 1 cm in diameter and about 7 µm thick, illuminated under UV light sources: a) The sample emits orange light. b) The laser-writing line does not emit orange light.

5.4. Thermal Effects and Melting of Porous Silicon Under Laser Irradiation

Simulation of the temperature distribution for laser power above 15 W shows that the temperature exceeds the melting point of silicon. This significantly changes the crystal structure of PS, as evident in the microscope image (Figure 5.6a). Additionally, laser irradiation of PS at this stage leads to notable densification in the irradiated region, reducing the thickness of the silicon layer from approximately 7 µm to 2 µm after irradiation (Figure 5.6a). This final thickness is less than that observed after laser exposure during the consolidation stage, which was approximately 4 µm (Figure 4.6). These results indicate that laser-induced melting significantly modifies the PS layer [50].

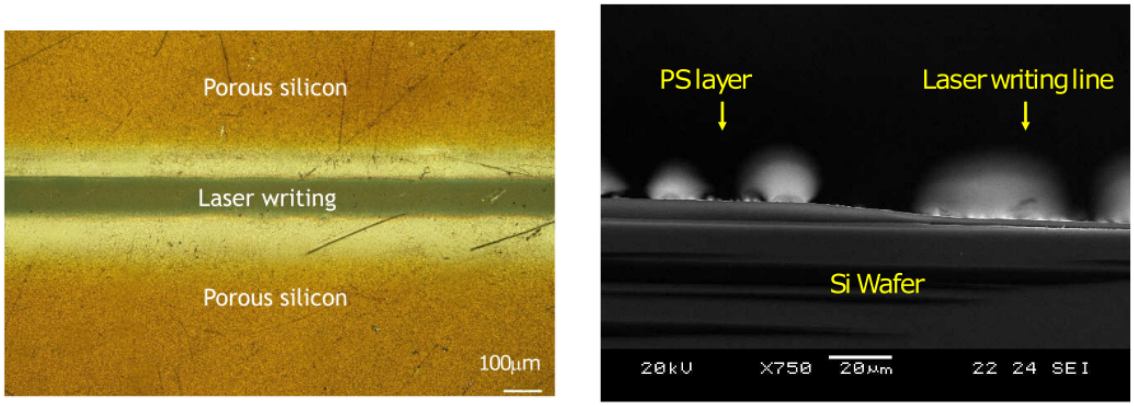

(a) Microscope image of PS irradiated with increased laser power **(b)** SEM cross-section image of the PS layer showing the laser-irradiated region

Figure 5.6 Crystal structure variation in porous silicon after CW CO_2 laser irradiation with increased power

Due to the limited resolution of SEM images, it is challenging to clearly visualise changes in the crystal structure, such as variations in the pore diameter or wall thickness between pores. To address this, an AFM was used to image the sample surface and monitor these structural changes.

5.5. Impact of Laser-Induced Melting on Porous Silicon Surface

Figure 5.7 presents three-dimensional AFM images and the corresponding topographical maps of *P* for several states: pristine PS, consolidated PS, and laser-melted (molten) PS, along with a reference silicon wafer. In particular, the RMS roughness for the molten PS sample was measured on a SiO_2 layer that formed along the laser writing line as a result of the laser irradiation. Both the consolidated and laser-melted samples exhibit comparable low surface roughness. Specifically, the molten PS sample shows an RMS roughness of approximately 0.8 nm over a $6\ \mu m \times 6\ \mu m$ area (Figure 5.7e), which is very similar to the 0.72 nm RMS roughness observed for the consolidated PS sample (Figure 5.7d). Furthermore, the 3D topography of the molten PS (Figure 5.7f) reveals a surface quality that closely resembles that of the silicon substrate, whose RMS roughness is as low as 0.37 nm over a $6\ \mu m \times 6\ \mu m$ area (Figure 5.7g). These results indicate that the laser-induced melting process, which produces a SiO_2 layer along the laser writing line (this will be discussed in detail later), effectively smooths the PS surface, achieving a finish nearly comparable to that of the original silicon wafer. This outcome is particularly promising for high-performance microelectronic and optoelectronic devices that require minimal surface roughness.

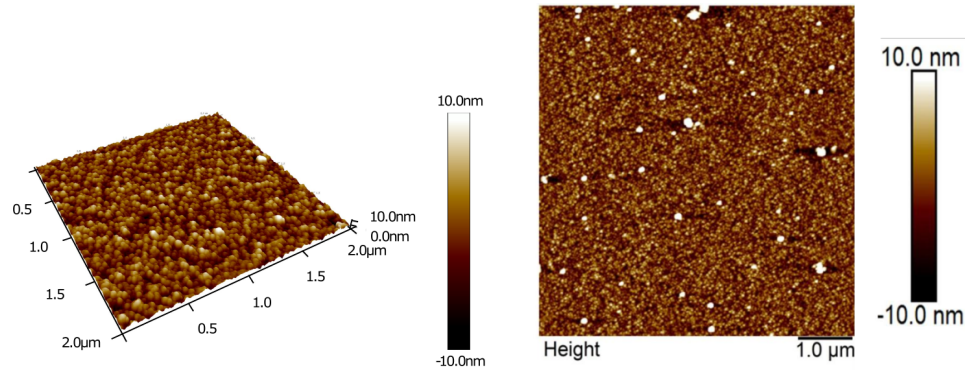

(a) 3D Image (PS) **(b)** Roughness (PS)

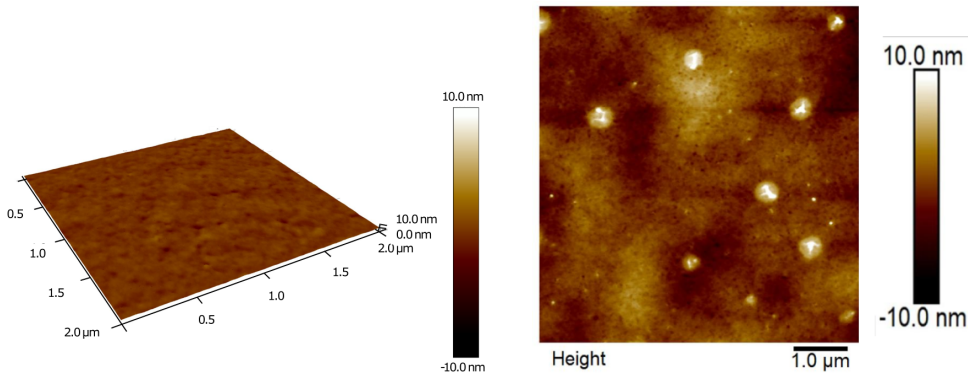

(c) 3D Image (10W) **(d)** Roughness (10W)

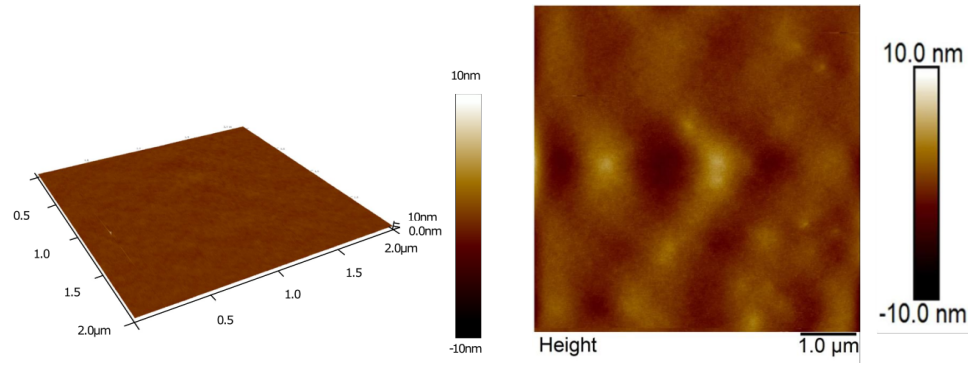

(e) 3D Image (20W) **(f)** Roughness (20W)

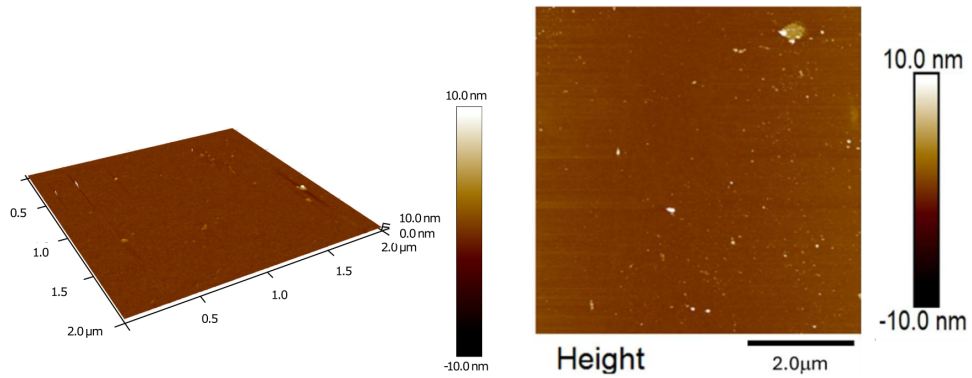

(g) 3D Image (Si) **(h)** Roughness (Si)

Figure 5.7 AFM images of porous silicon, showing laser writing lines at 10 W, 20 W, and 30 W: (a) $2\,\mu\text{m} \times 2\,\mu\text{m}$ morphology of the laser writing line at 10 W; (b) $6\,\mu\text{m} \times 6\,\mu\text{m}$ topography image of the laser writing line at 10 W; (c) $2\,\mu\text{m} \times 2\,\mu\text{m}$ morphology of the laser writing line at 20 W; (d) $6\,\mu\text{m} \times 6\,\mu\text{m}$ topography image of the laser writing line at 20 W; (e) $2\,\mu\text{m} \times 2\,\mu\text{m}$ morphology of the laser writing line at 30 W; (f) $6\,\mu\text{m} \times 6\,\mu\text{m}$ topography image of the laser writing line at 30 W; (g) $2\,\mu\text{m} \times 2\,\mu\text{m}$ morphology of Si substrate; (h) $6\,\mu\text{m} \times 6\,\mu\text{m}$ topography of Si substrate.

5.6. Raman Spectroscopic Analysis of Melting and Structural Changes in Laser-Processed Silicon

AFM images revealed variations in surface morphology between unprocessed PS and regions subjected to low-power laser irradiation. Additionally, morphological differences were observed between areas processed at the melting stage of laser irradiation and those processed at the consolidation stage, highlighting variations in crystal structure across these regions. Raman spectroscopy is one of the most effective methods for studying structural changes because of its non-destructive and contactless characteristics.

Figures 5.8a and 5.8b present the Raman spectra obtained when a laser was applied at intensities of 2.2 $\times 10^{-5}$ W/μm^2 and 3.0 $\times 10^{-5}$ W/μm^2, corresponding to laser powers of 15 W and 20 W, respectively. These measurements were conducted at varying speeds, where the exposure time increased as the laser writing speed decreased. The Raman peak for silicon exhibited a sharp and strong signal at 520 cm^{-1} with a symmetric line shape. Upon laser application, the Raman peak displayed a redshift (indicating a decrease in the frequency of phonons interacting with the incident photon) of approximately 1 cm^{-1}. Furthermore, a secondary peak appeared at a higher wavenumber, around 524 cm^{-1}, as the exposure time increased.

The redshift could occur due to several factors: strain effect [201], doping [24], temperature effects [71], phase transitions [71], and defects [24]. These factors can interact complexly, resulting in the observed red-shift behaviour in the Raman peak of silicon.

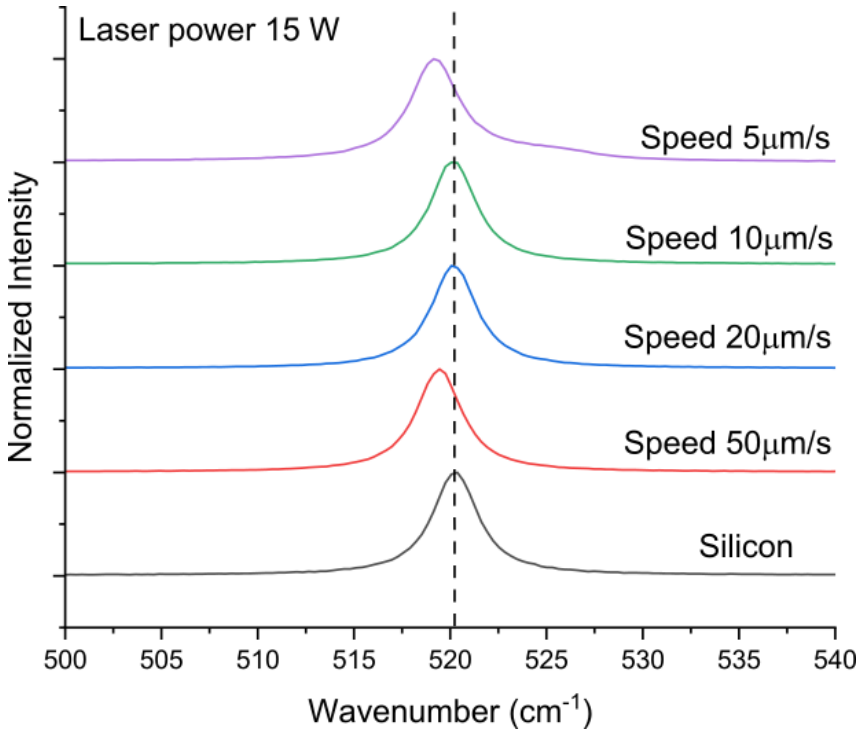

(a) Laser power 15 W.

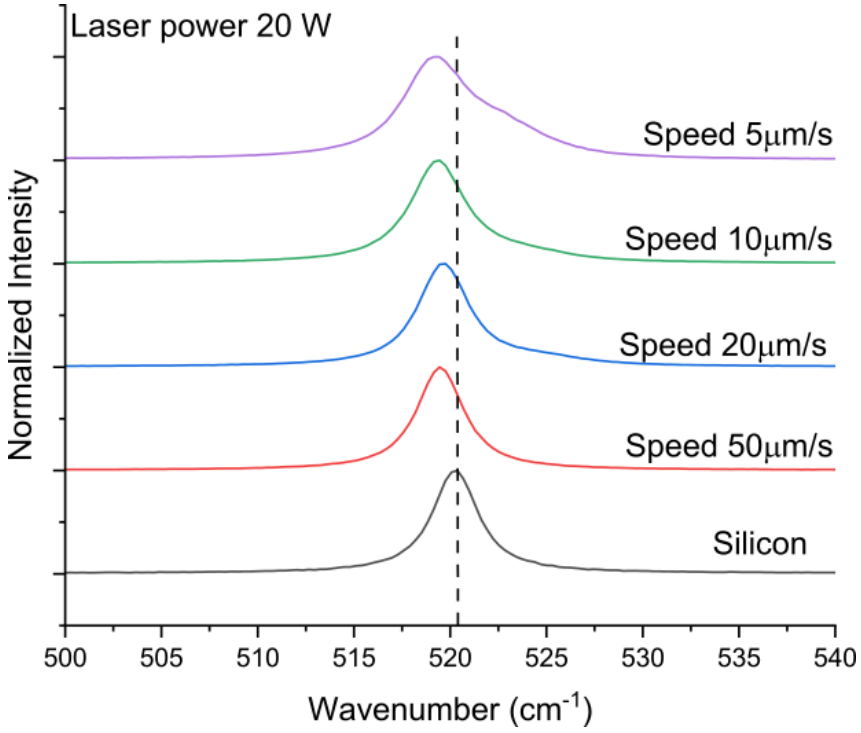

(b) Laser power 20 W.

Figure 5.8 Raman spectra of two samples processed with laser powers of 15 W and 20 W, using laser writing speeds of 50, 20, 10, and 5 μm/s.

It is evident from Section 4.2 that exposure of the sample to CW CO_2 laser creates localised hot spots, leading to the creation of tensile stress, which in turn causes the observed redshift [73]. The possibility of silicon dioxide (SiO_2) formation due to laser writing cannot be excluded.

This deformation at the interface between Si and SiO_2 contributes to the observed effects. The symmetry on the Raman peak is an indicator of recrystallisation [151]. Additionally, tensile strain caused by boron doping disrupts the silicon lattice structure, influencing vibrational modes and contributing to redshift [182].

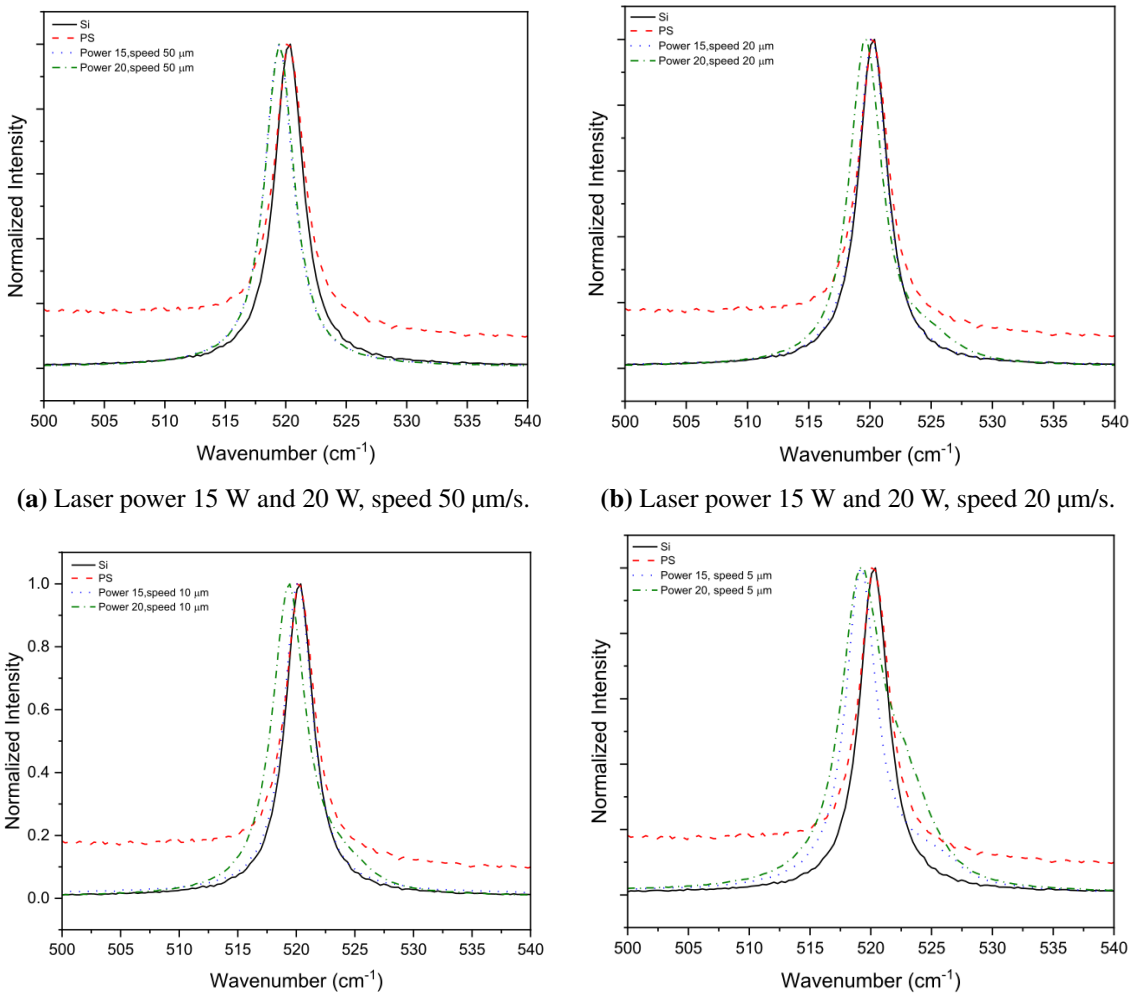

(a) Laser power 15 W and 20 W, speed 50 µm/s.

(b) Laser power 15 W and 20 W, speed 20 µm/s.

(c) Laser power 15 W and 20 W, speed 10 µm/s.

(d) Laser power 15 W and 20 W, speed 5 µm/s.

Figure 5.9 Raman spectra obtained for laser writing conducted at different speeds (50, 20, 10, and 5 µm/s) for each laser power: 15 W and 20 W.

The differences in Raman shifts and peak shapes across speeds for each power are shown in Figure 5.9. The figure emphasises that slower speeds, corresponding to longer laser exposure, result in more pronounced redshifts due to increased localised heating. Additionally, new peak growth at high power and low speeds suggests possible structural or phase changes caused by laser-induced stress. A Voigt fit, combining Gaussian and Lorentzian functions, was used to analyse the bulk silicon peak with $\Gamma = 2.7$ cm^{-1} (Figure 5.10). A similar Voigt fit was applied to the Raman peaks for 15 W and 20 W at slower speeds (where a secondary peak appears) using

$\Gamma = 2.7$ cm^{-1} for both peaks (Figure 5.11). The full width at half maximum (FWHM) for the bulk silicon of this fit is 2.8 cm^{-1}.

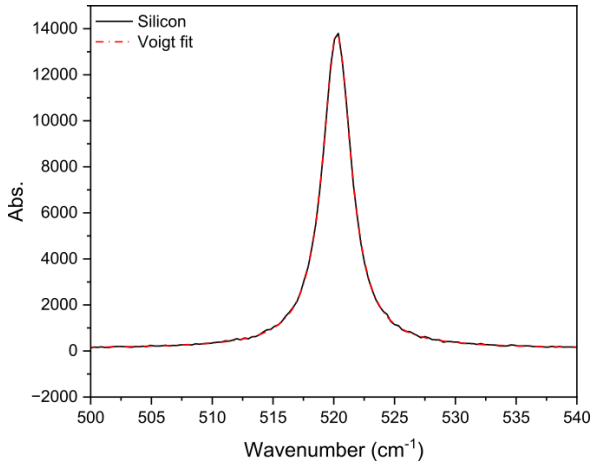

Figure 5.10 Voigt fitting of Raman shift for Silicon.

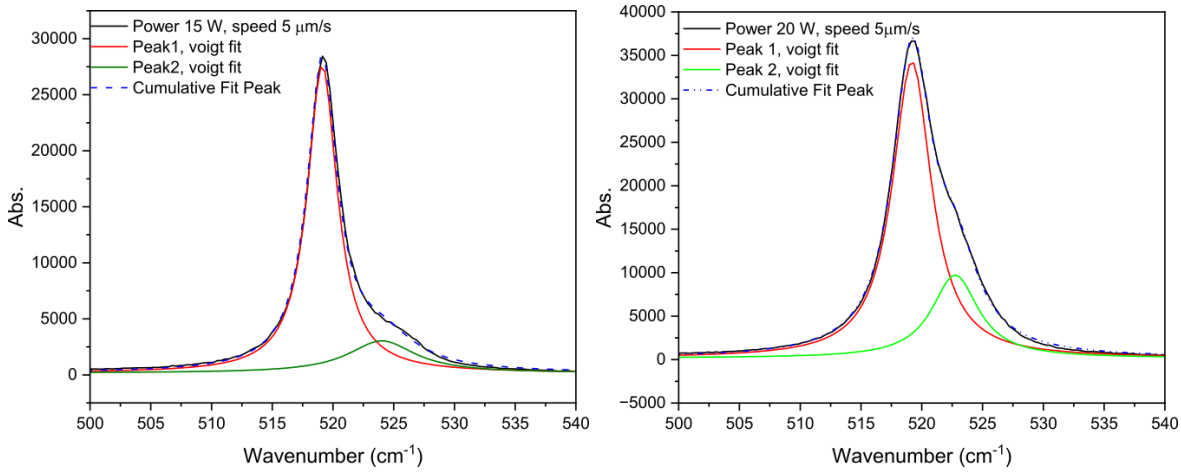

(a) Laser power 15 W.

(b) Laser power 20 W.

Figure 5.11 Raman fit with two samples (laser power 15 W and 20 W). Laser writing used speed 5 µm/s.

Tables 5.1 shows the FWHM and the poison of the Raman peak for silicon substrate and laser writing at power 15 W using speed (50, 20, 10 and 5 µm/s).

Condition	Peak (cm^{-1})	FWHM (cm^{-1})
Si (substrate)	520.2	2.8
Speed 50 µm/s	519.4	2.9
Speed 20 µm/s	520.2	2.9
Speed 10 µm/s	520.1	2.9
Speed 5 µm/s, Peak 1	519.2	3.1
Speed 5 µm/s, Peak 2	524.4	6.0

Table 5.1 FWHM and Raman peak wavenumbers for laser power 15 W and silicon substrate

5.7. XRD Study of Silicon Recrystallisation and Stress Induced by Laser Melting

Raman microscopy and SEM images reveal significant variations in the surface morphology of silicon, demonstrating recrystallisation after high-intensity laser irradiation of porous silicon. XRD is a powerful technique for investigating crystal structures and assessing the degree of crystallinity within a sample. Figure 5.12 presents an XRD profile showing the relationship between XRD intensity and d-spacing for both silicon substrates and laser-processed regions. A Gaussian function was used to fit the XRD peaks. The d-spacing for the unprocessed silicon substrate is 1.048 Å, whereas for laser-processed regions, it is 1.043 Å. This reduction in d-spacing for laser-processed regions indicates the presence of compressive stress, which arises from the reduced interplanar spacing within the crystal lattice. Furthermore, the symmetric shape of the peak suggests that the stress is homogeneously distributed [215].

The intensity of XRD peaks provides critical insight into the structural characteristics of the material, including crystallinity, phase composition, and the presence of defects or heterogeneities. High intensity peaks correspond to highly ordered crystalline structures, indicating fewer structural defects [79].

The FWHM of XRD peaks serves as an important indicator of material properties such as residual stress, crystallite size, and microstrain. Generally, FWHM is positively correlated with residual stress; higher stress levels lead to broader peaks [221]. However, thermal processing, such as laser-induced heating, can alleviate internal stresses, reduce defects, and increase crystallite size. This relaxation process sharpens the XRD peaks, resulting in reduced FWHM values [49]. According to the Scherrer equation (Equation 5.1), the crystallite size is inversely

proportional to the FWHM. As crystallite size increases due to recrystallisation during laser processing, the corresponding reduction in FWHM reflects improved material order [146].

$$d = \frac{K\lambda}{\beta \cos\theta} \tag{5.1}$$

Here, d represents the crystallite size, K is the Scherrer constant, β is the FWHM, λ is the wavelength of the X-rays and θ is the diffraction angle.

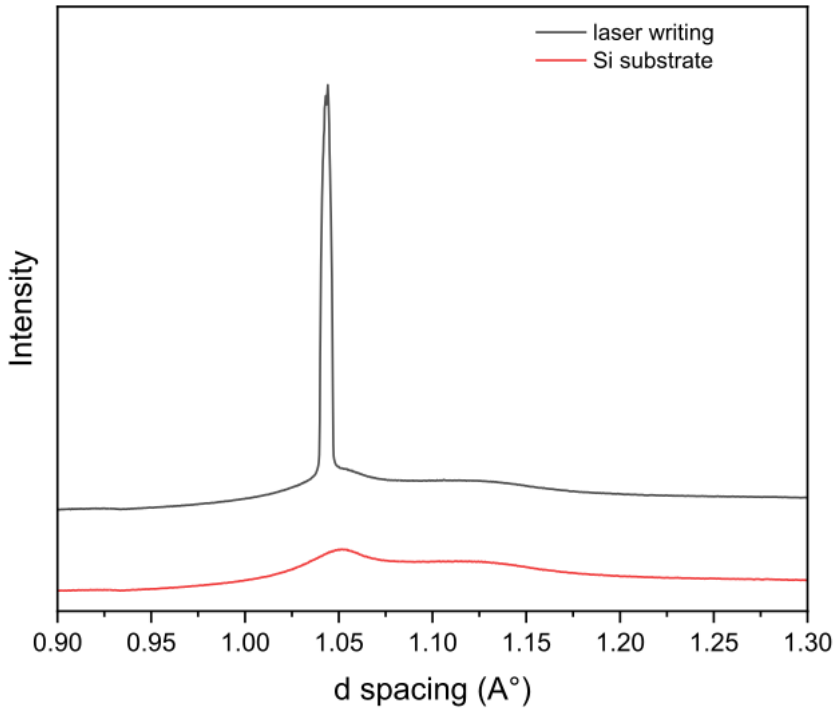

Figure 5.12 XRD profile for laser writing and silicon substrate (intensity as a function of d-spacing).

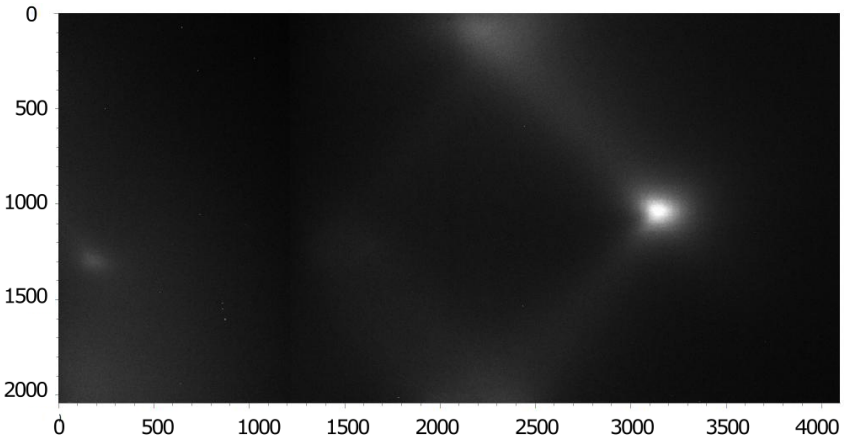

(a) Si substrate.

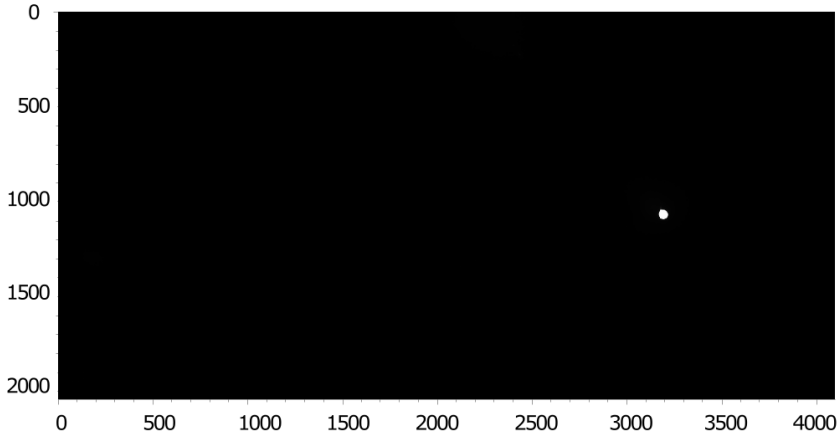

(b) Laser writing.

Figure 5.13 a) XRD pattern of silicon substrate. b) XRD pattern of laser writing. The axes are numbered by pixel number

Figures 5.13a and 5.13b show the XRD patterns for a silicon substrate and laser-written silicon, respectively. The silicon substrate exhibits a sharp, bright, and symmetric diffraction spot, indicating a highly ordered single-crystalline structure characteristic of the diamond-cubic lattice. Likewise, the laser-written silicon pattern displays a similarly sharp diffraction spot aligned with the substrate orientation, confirming epitaxial growth. To verify this alignment quantitatively, the angle of the diffraction spot was measured from the center of the pattern using Gwyddion. The measured angle matches the crystallographic orientation of the substrate, demonstrating that the original single-crystal structure of the substrate is retained after laser writing.

In contrast, the XRD pattern for the laser-written silicon displays a single sharp diffraction spot without any observable diffuse scattering. This indicates a highly ordered crystalline structure with strongly preferred orientation. The absence of diffuse scattering further highlights

the recrystallisation process induced by laser writing, demonstrating its capability to transform porous silicon into a more ordered and crystalline state.

5.8. Oxidation Dynamics in Porous Silicon Induced by Laser Melting: XPS and Raman Analysis

XRD analysis of laser-written results indicates recrystallisation of silicon within the PS layer after exposure to a high-intensity laser. To further interpret the Raman spectra, which exhibit redshifts and the growth of new peaks, to identify the sources of stress, XPS was performed to determine the chemical composition of the laser-written surface.

Figure 5.14 displays the XPS spectrum of the laser-written region. The prominent peak at 103.35 eV is attributed to SiO_2 [208], while no silicon peak is observed, indicating complete oxidation of the surface. The formation of a silicon oxide layer is expected due to CO_2 laser-induced oxidation [28].

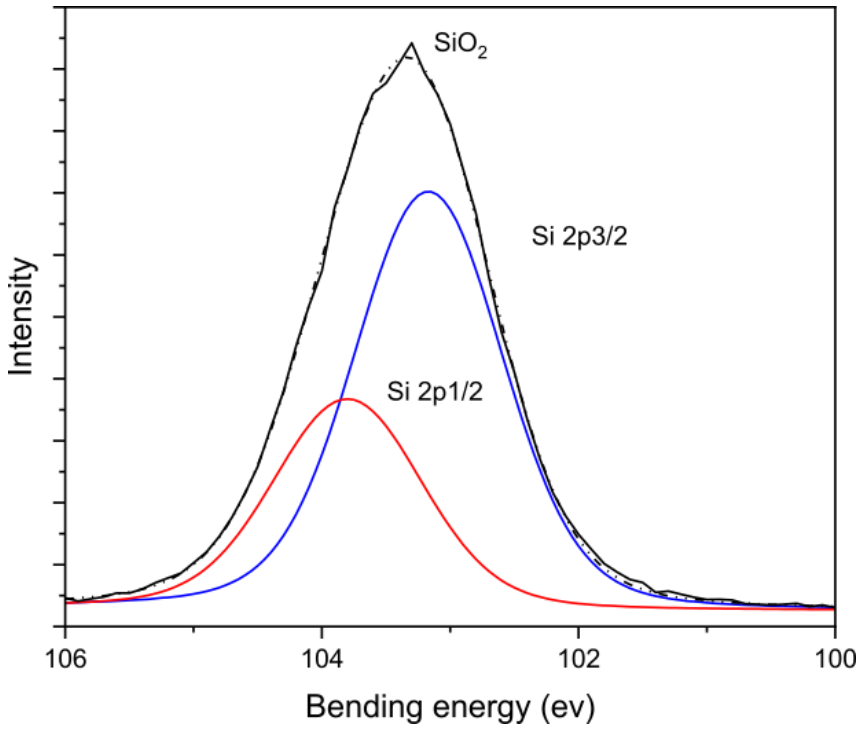

Figure 5.14 XPS spectra of porous silicon sample exposed to high-intensity CO_2 laser.

To remove the SiO_2 layer, the sample was etched in a dilute HF solution without applying an electric current. Although silicon, with its strong covalent Si–Si bonds, remains inert to HF, SiO_2, with its weaker Si–O bonds, is susceptible to chemical attack. As a result, HF selectively dissolves SiO_2 without affecting the underlying silicon.

Figure 5.15a shows that after etching the sample in dilute HF acid for 30 seconds, the silicon oxide layer was only partially removed. Therefore, further etching was required to completely

dissolve the oxide layer and reveal the underlying composition. Figure 5.15b shows two peaks at 99.3 eV and 103.35 eV, attributed to Si and SiO_2, respectively [208]. These findings confirm that high-intensity CW CO_2 laser exposure induces recrystallisation of silicon, consistent with XRD and Raman results, while also forming a silicon oxide layer.

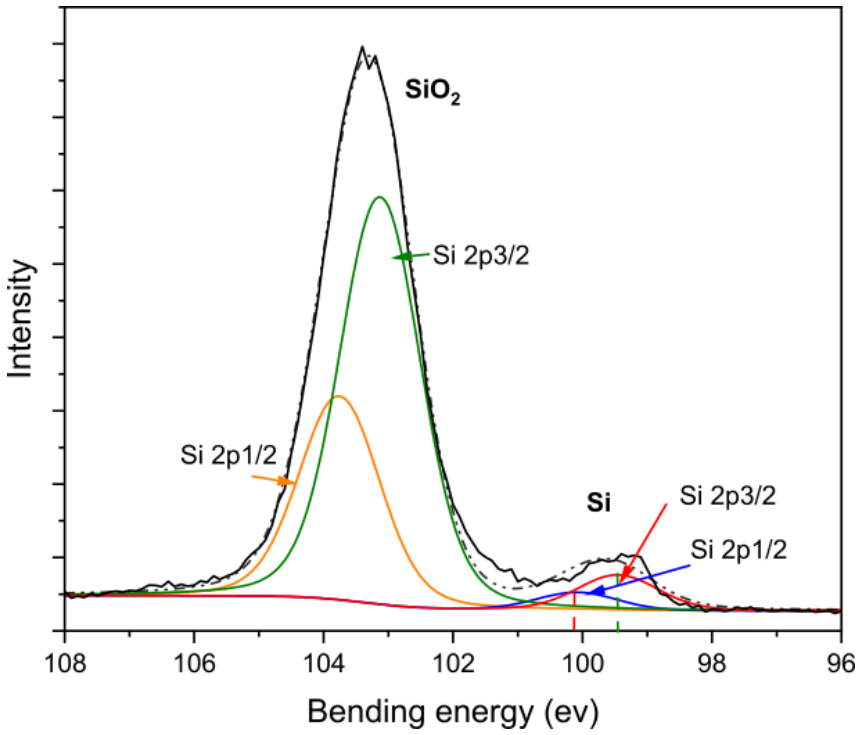

(a) XPS spectra after etching the sample in dilute HF acid for 30 seconds.

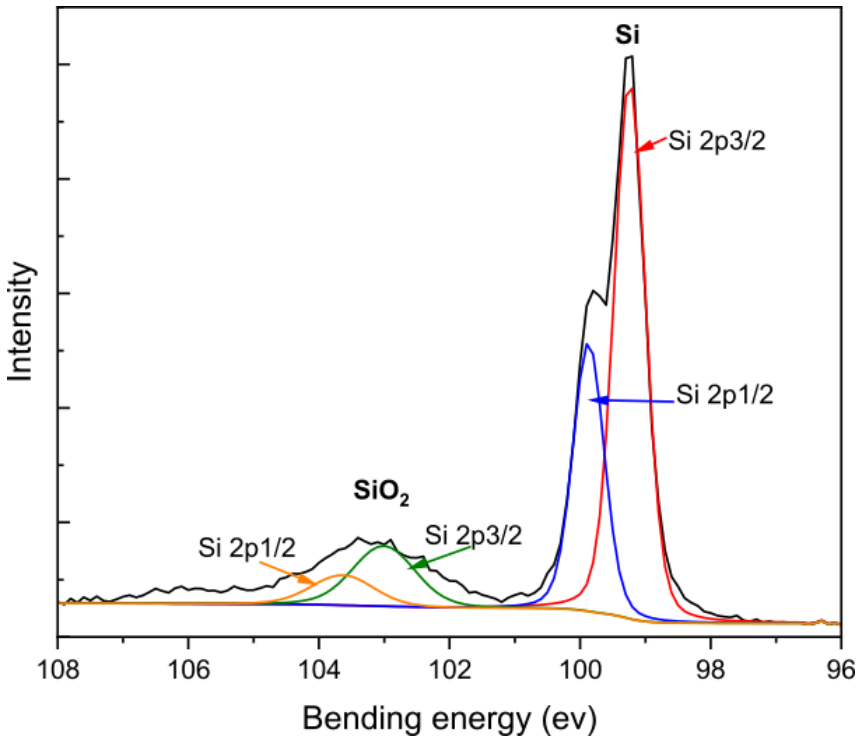

(b) XPS spectra after etching the sample in dilute HF acid for three hours.

Figure 5.15 XPS spectra of porous silicon samples exposed to high-intensity CO_2 laser after etching in dilute HF acid.

Notably, the redshift and the development of peaks at higher wavenumbers in the Raman spectra observed after laser exposure (Figure 5.16) disappeared after the removal of the SiO_2 layer. This highlights the influence of the silicon oxide layer on the Raman spectral features.

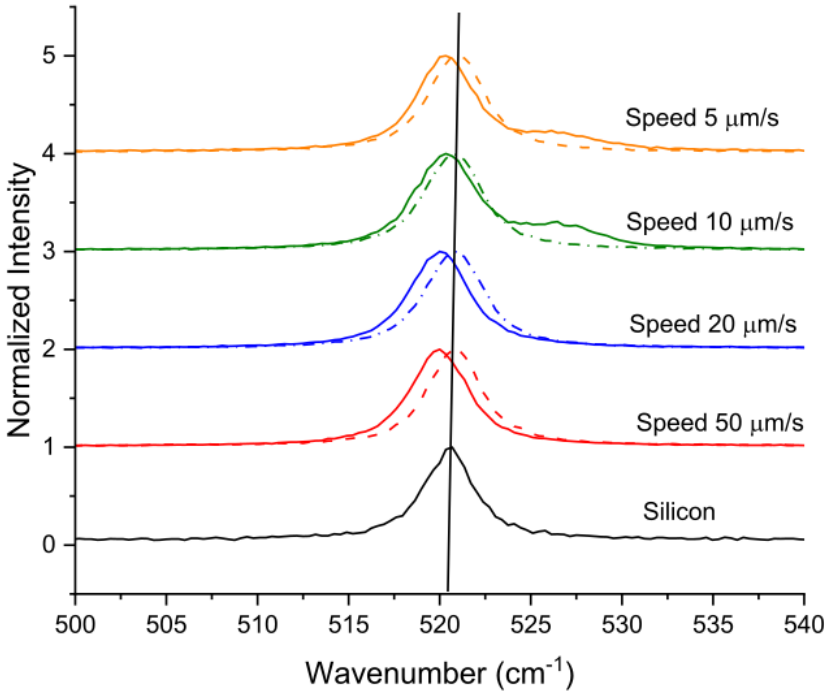

Figure 5.16 Raman spectra of laser writing at high intensity before (solid lines) and after etching SiO_2 for three hours (dashed lines).

Table 5.2 present the Raman peak wavenumber and FWHM of the PS laser-irradiated regions at various scanning speeds, measured before and after etching. The data reveal that the redshift observed in the Raman spectra prior to etching was eliminated following removal of the SiO_2 layer. Additionally, the spectral peaks became sharper and more defined after etching, as evidenced by the reduced FWHM values, indicating a decrease in lattice strain and improved crystallinity.

	Before Etching		After Etching	
Condition	**Peak (cm^{-1})**	**FWHM (cm^{-1})**	**Peak (cm^{-1})**	**FWHM (cm^{-1})**
Si (substrate)	520.5	3.3	520.5	3.3
Speed 50 µm/s	519.9	3.7	520.8	3.5
Speed 20 µm/s	519.9	3.9	520.8	3.8
Speed 10 µm/s, Peak 1	520.3	3.9	520.7	3.7
Speed 10 µm/s, Peak 2	526.3	4.6	–	–
Speed 5 µm/s, Peak 1	520.3	3.6	520.9	3.6
Speed 5 µm/s, Peak 2	526.6	4.9	–	–

Table 5.2 FWHM and Raman peak wavenumbers for laser power 20 W and silicon substrate, before and after etching

5.9. Conclusion

In this chapter, the effects of the CW CO_2 laser interaction with PS were thoroughly investigated. The study demonstrated that laser exposure induces significant morphological, structural, and chemical changes in PS.

Laser exposure led to densification of the PS layer, significantly reducing its thickness, as observed in SEM images. AFM analysis revealed that the regions exposed to the laser exhibited a smooth and soft surface, with the disappearance of pores attributed to the melting of silicon. These changes suggest a transformation of PS into a more compact and uniform material.

The heat generated during the laser interaction was highly localised, resulting in substantial temperature increases sufficient to melt and vaporise silicon. This localised heating is advantageous for precision applications as it minimises thermal effects in adjacent areas.

Raman spectroscopy revealed redshifts and peak broadening, indicating tensile stress and potential phase transitions in the silicon structure. XRD analysis confirmed recrystallisation of silicon, with changes in d-spacing suggesting compressive stress. further corroborating the structural transformations observed.

XPS analysis identified the formation of a silicon oxide layer on the laser-modified surface, which could be selectively removed using dilute HF acid to reveal the underlying silicon. This

highlights the potential for controlled surface modification and chemical tailoring of PS using laser technology.

These findings provide valuable insights into the potential applications of laser-modified PS in advanced technologies, including microelectronics, optoelectronic devices, and sensors, where precise control over thermal and structural properties is critical. Future research could focus on optimising the laser parameters to further refine the material properties and expanding the study to explore additional functional applications of laser-modified PS.

Chapter 6. Electrical Characterisation of The Melting Porous

6.1. Introduction

The previous chapter investigated the effects of oxidation on Raman scattering resulting from laser-induced melting of PS. Building on this, the present chapter examines the structural and spectroscopic changes resulting from the melting and recrystallisation processes. Specifically, this chapter explores how these processes influence the Raman scattering behaviour, with a particular emphasis on understanding the mechanisms behind the observed surface-enhanced Raman scattering (SERS).

Upon exceeding the melting point of silicon by laser irradiation, the laser-irradiated region appeared black, as shown in Figure 5.6a. After the oxide layer was removed, the irradiated region remained black (Figure 6.1), confirming that the silicon dioxide layer is not responsible for the black colouration. XPS spectra did not reveal the presence of any elements that could explain the black appearance (Figure 5.15). To investigate the origin of the dark colouration, which could not be resolved using SEM, the surface morphology was analysed using AFM. Additionally, current-voltage (I-V) curve measurements were performed to evaluate the electrical properties of the regions, while Kelvin Probe Atomic Microscopy (KFAM) was employed to map surface potential variations. Together, these analyses provide a comprehensive understanding of the structural, electrical, and spectroscopic changes induced by laser melting and recrystallisation.

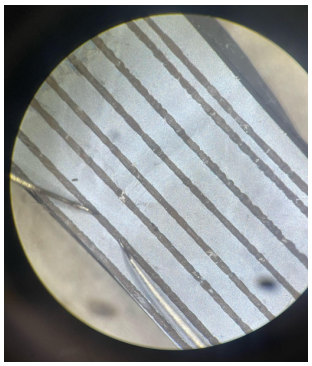

Figure 6.1 microscope image of the laser-irradiated region after the oxide layer was removed. The dark appearance indicates that the black colouration is not solely due to silicon dioxide.

6.2. Effects of Melting and Recrystallisation on Raman Scattering

Figure 6.2 shows the Raman spectra for both the laser-exposed region (red curve) and the silicon substrate (black curve). In both spectra, the principal peak near 520 cm^{-1} corresponds to the first-order Raman mode of crystalline silicon, indicating that the dominant phase remains crystalline in both regions. However, the laser-processed area exhibits a significantly higher intensity and a modest broadening of this peak. Such broadening commonly arises from either nanocrystalline domains or lattice strain introduced by the rapid melting and recrystallisation process. In addition, smaller crystallites can induce quantum confinement effects, shifting and broadening the phonon modes in the Raman spectrum [64, 106].

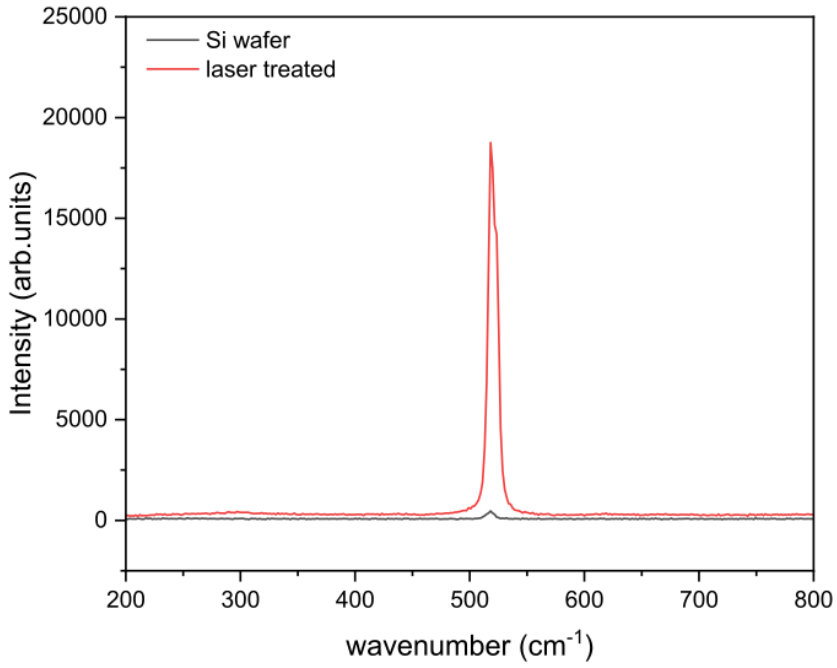

Figure 6.2 Raman spectra of the silicon substrate (black) and laser-irradiated region (red), showing enhanced Raman intensity in the laser-irradiated region due to surface modifications

Beyond these structural changes, the pronounced enhancement of the Raman signal in the laser-exposed region is indicative of surface-enhanced Raman scattering (SERS) mechanisms. In conventional SERS, the presence of metallic nanostructures or other plasmonic materials generates strong localised electromagnetic (EM) hot spots, dramatically amplifying the Raman cross section. In this case, two primary factors may contribute to SERS:

1. Nanostructured surface morphology.

   Laser-induced etching and subsequent melting/recrystallisation processes can form rough surfaces, pores, nanoshells, or other topographical features. These surface nanostructures create localised regions with high electromagnetic fields when illuminated. Molecules

(including residual electrolyte adsorbates or ambient contamination) situated near these (hot spots) experience a strong enhancement of the electric field, thus producing higher Raman signals [198].

2. Boron rich regions and plasmon-like effects.

   The initial electrochemical etching process may partially deplete silicon at the surface, leaving behind regions enriched in boron. Upon laser melting and fast solidification, boron can become highly concentrated (or more uniformly distributed at high levels) near the surface. Heavily-doped semiconductors, particularly when dopant concentrations approach or exceed the metallic / insulator transition, can support localised plasmon-like resonances in certain spectral regimes. Although classical (metallic) plasmons are typically associated with noble metals, heavily doped silicon can similarly exhibit free carrier resonances that enhance local EM fields [155]. As a result, areas enriched in boron formed by laser processing may act as pseudo plasmonic domains, further strengthening Raman scattering [219].

Together, these effects, including the morphological modification plus dopant-related plasmon-like behaviour, can explain the observed increase in Raman intensity. The surface roughness amplifies the electromagnetic contribution to SERS, while boron enrichment boosts the local free carrier density, creating additional hot spots and enhancing light-matter interactions on the laser-processed surface. These findings confirm that laser-induced morphological and dopant modifications can strongly influence optical and electrical properties, a theme further explored in the following sections.

6.3. Electrical Characterisation of Laser-Processed Porous Silicon after Etching

The spectroscopic results indicate that laser-induced morphological and dopant-related modifications significantly amplify the Raman signal. However, it is important to understand how these variations affect the electrical characteristics of silicon. Specifically, changes in dopant concentration and structural imperfections can strongly affect charge transport. To investigate these effects, current-voltage (I–V) measurements were conducted in the same laser-processed areas. A two-probe setup (Figure 6.3) was used to demonstrate the effects of laser processing on electrical conductivity and to discover the relationship between structural modifications, doping enhancement, and electrical performance.

Figure 6.3 Photograph of the two-probe used for the I–V measurements on laser-processed PS.

Figure 6.4 shows that all curves are approximately symmetric around $V = 0$ and do not exhibit rectifying (diode-like) behaviour [82], indicating primarily ohmic conduction. In a two-probe setup, any significant barriers (such as Schottky contacts) would appear as strong non-linearities or asymmetries [230], which are not observed here.

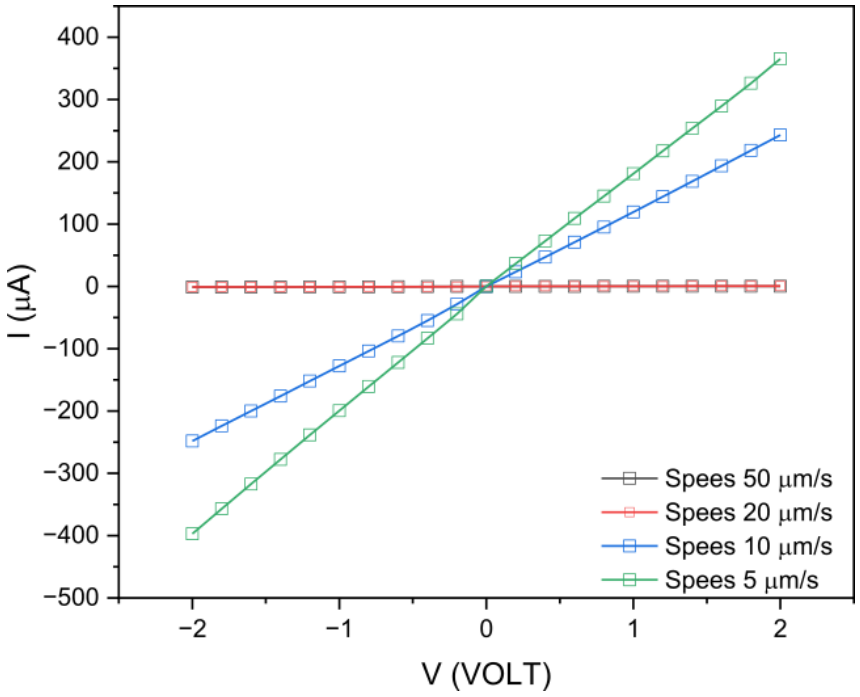

Figure 6.4 Current–voltage (I–V) curves at different laser scan speeds at laser power 30 W.

Since the laser power remains constant, the scan speed is the only variable. Figure 6.5 shows that slower scanning (longer exposure) leads to a significant decrease in resistance, indicating an improvement in conductivity. In contrast, faster scans result in comparatively minor conductivity changes. At slower speeds, more extensive boron redistribution or surface enrichment can occur during melting and recrystallisation, which increases the density of free carriers (holes in this case) and potentially forms conductive nanostructures or grain boundaries. These structural

modifications lower the overall resistance. In contrast, at higher scan speeds, there is insufficient time for extensive dopant redistribution or microstructural reorganisation, so the electrical properties of the sample remain nearer to their initial condition, leading to less pronounced enhancements in conductivity.

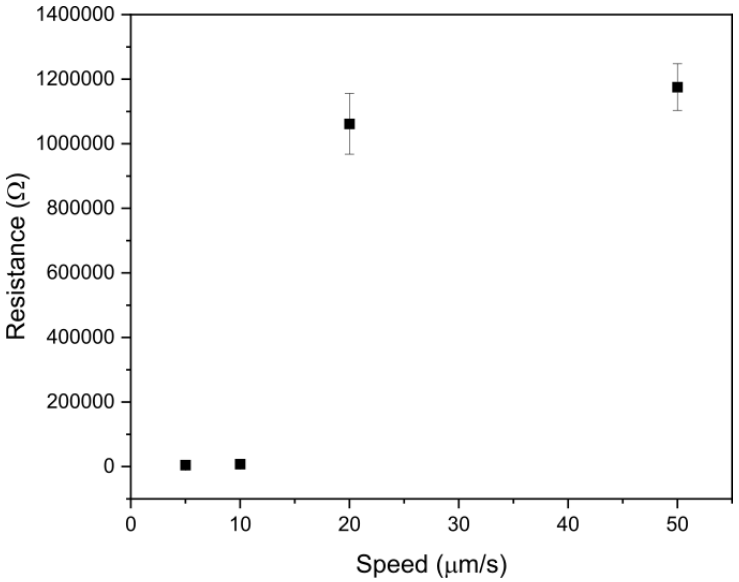

Figure 6.5 Resistance versus scan speed.

6.4. The Temperature Dependence of Electrical Properties

Temperature has a profound influence on the electrical properties of semiconductors, particularly those with dopants or structural modifications [160]. In this study, the current-voltage (I–V) response of laser-modified PS in a temperature range of 20 °C to 100 °C was studied. The objective was to understand the evolution of thermally activated conduction channels and to find any unique characteristics delivered by the laser process.

A sample featuring laser-written lines at 10 μm/s speeds was placed on a temperature controlled stage in a continuously flowing nitrogen atmosphere to prevent oxidation or contamination, thus ensuring cleaner, more stable and more reproducible temperature-dependent electrical data. After each temperature setpoint was reached, the sample was allowed several minutes to equilibrate before the I–V curves were recorded. A two-probe method was used, with the same probe spacing maintained throughout, ensuring that any observed changes in conduction were primarily related to temperature rather than geometric factors. Room-temperature measurements confirmed that the electrical contacts were ohmic.

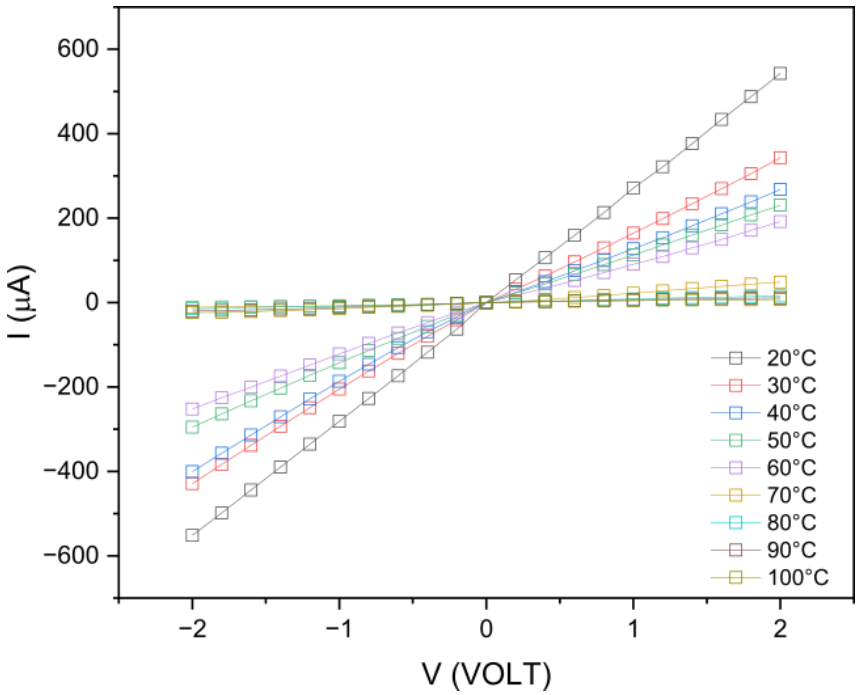

Figure 6.6 I-V curves of the laser withe scan speed 10 μm/s modified PS at different sample temperatures.

Figure 6.6 shows the I–V curves obtained between 20 °C and 100 °C. The I-V curves exhibit a progressive decrease in slope as the temperature increases, indicating an increase in resistance with increasing temperature. This suggests that charge carrier mobility is temperature-dependent and is being increasingly hindered as thermal effects become more pronounced. This is probably caused by an increase in scattering events [229]. The linearity of the I–V curves across the measured voltage range suggests that conduction follows an Ohmic response in this regime, meaning that there are no strong rectifying or non-linear transport effects within the investigated voltage window [30].

In the Drude model, electrical conductivity (σ) of a material is expressed as:

$$\sigma = \frac{ne^2\tau}{m^*}$$

where n is the concentration of the charge carrier, e is the elementary charge, τ is the mean free time between scattering events (relaxation time), and m^* is the effective mass of the charge carriers [48]. Since the material under investigation is extrinsic at these temperatures, the carrier concentration n is expected to remain relatively constant [147]. However, the mean free time τ decreases with increasing temperature due to enhanced phonon scattering, leading to a reduction in carrier mobility and, consequently, an increase in resistance, consistent with observations in the I-V data [22].

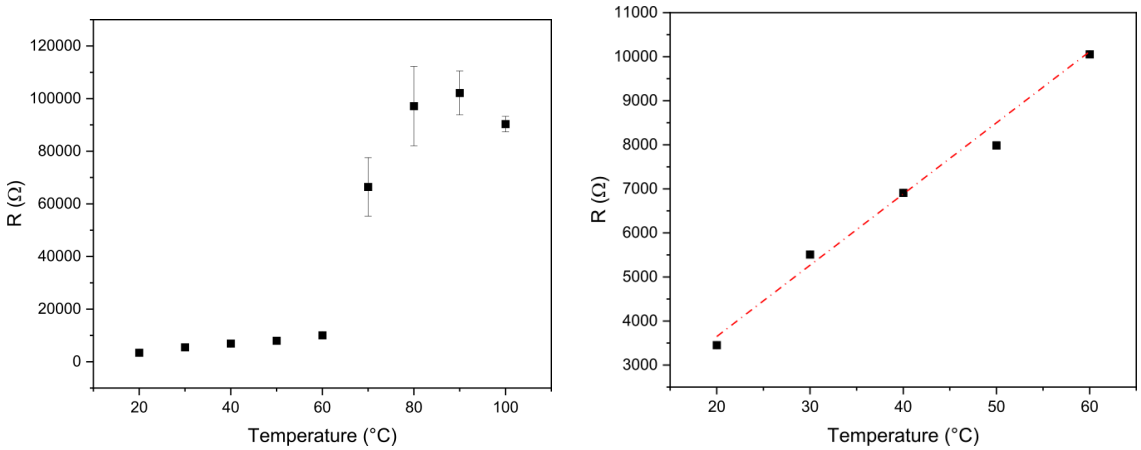

(a) R VS T in the range 20-100 °C

(b) R VS T for at 20-60 °C

Figure 6.7 Resistance (R) versus temperature (T) for laser scanning speeds of 10 µm/s.

To quantify the I–V data, the resistance near $V = 0$ was extracted. Figure 6.7a shows the relationship between resistance R and temperature T. The data indicate various regimes rather than a basic monotonic increases, the resistance follows a linear trend up to approximately 60 °C, which is characteristic of metallic behaviour. Beyond this point, the resistance exhibits a deviation from linearity, suggesting the emergence of additional conduction-limiting mechanisms.

This behaviour can be explained using the Matthiessen rule, which states that the total resistivity (ρ) of a material is the sum of different contributions to the scattering:

$$\rho(T) = \rho_{\text{impurity}} + \rho_{\text{phonon}}(T) + \rho_{\text{grain boundary}}(T) + \rho_{\text{contact}}(T)$$

where ρ_{impurity} is the temperature-independent contribution of the ionised dopants and defects, $\rho_{\text{phonon}}(T)$ is the temperature-dependent resistivity due to phonon scattering, $\rho_{\text{grain boundary}}(T)$ accounts for structural barriers to charge flow, and $\rho_{\text{contact}}(T)$ represents additional resistance from the metal-semiconductor interfaces [52].

In the linear regime (below 60 °C) (Figure 6.7b), the resistance behaves according to the Drude model for a simple metal. In this case, the impurity scattering is approximately temperature-independent at ambient temperature, but the phonon contribution is directly proportional to temperature. The grain and contact resistances would be expected to decrease as temperature rises, therefore they do not appear to be significant. Overall, a linear increaes of resistance with temperature is expected at ambient temperature for metal-like behaviour. Such an interpretation is also consistent with the KPFM data (Figures 6.8and 6.9 below) and the observed Raman enhancement (Figure 6.2).

However, beyond 60 °C, the deviation from linearity suggests the emergence of additional resistive mechanisms. One possible explanation is the increased influence of phonon scattering.

At higher temperatures, the phonon population grows non-linearly, leading to more frequent electron-phonon interactions, which impede charge carrier mobility. As a result, resistance increases faster than observed in the lower temperature regime, according to Matthiessen's rule [62].

Another contributing factor could be changes in contact resistance. Metal-semiconductor interfaces are particularly susceptible to thermal degradation, which can lead to variations in Schottky barrier height or diffusion-related modifications in contact resistivity. These changes introduce additional resistance at the electrode-material junction, further exacerbating the deviation from the initial linear trend [112].

Additionally, microstructural and grain boundary effects may play a role in the increase in observed resistance. In polycrystalline or porous materials, elevated temperatures can induce thermal expansion, which alters the arrangement of grains and boundaries. Dopant redistribution at these interfaces can further influence charge transport, modifying conductive pathways, and introducing additional scattering events that contribute to increased resistivity [170].

Another possible mechanism is carrier freeze-out at the interface states. At high temperatures, surface states or charge-trapping effects may lead to local carrier depletion, reducing the number of available charge carriers and thereby increasing resistance. This effect is particularly relevant in materials with significant surface roughness or defect states, where localised charge trapping can alter conduction characteristics and further contribute to the nonlinear increase in resistance beyond 60 °C [141].

6.5. Work Function Mapping of Recrystallised Silicon

KPFM is known as a powerful mode of AFM for defining local surface potentials (or contact potential differences) at a micrometre-scale resolution. It is used to identify electrostatic interactions between a conductive tip and the sample. By generating a feedback loop that removes the tip-sample potential difference, a spatially defined work function map of the surface can be generated.

This technique is especially relevant when doping or morphological modifications create local variations in electrical properties. Previous measurements indicated that laser irradiation at varying scanning speeds affects the crystallinity and dopant distribution of silicon, leading to changes in temperature-dependent conductivity and total resistivity. Although a strong link was established between reduced laser scan speeds and enhanced electrical conduction, direct visual evidence of dopant or defect distributions on the microscale was not previously demonstrated.

KPFM was therefore used on the laser-irradiated samples to identify regions with varying surface potentials that reflect local doping levels, chemical composition, or defect states. This localised mapping enhances earlier macroscopic conductivity data and offers a further understanding of how extended laser exposure may lead to dopant enhancement, defect formation, or other structural alterations. If a mixed or inhomogeneous potential distribution is seen in the KPFM images, it would support the idea that slower laser scans lead to more significant doping or crystallinity alterations, consistent with the findings from the temperature-dependent electrical tests.

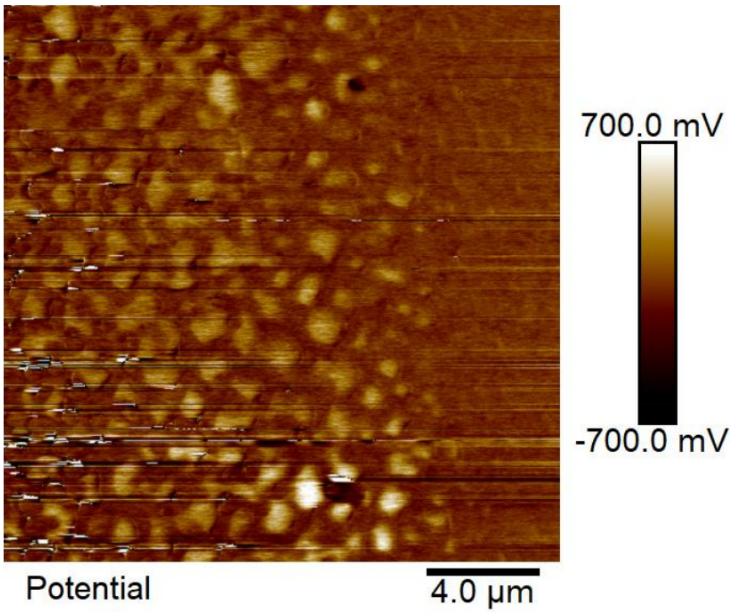

Figure 6.8 KPFM surface potential map of the laser-irradiated silicon sample at a scanning speed of 5 µm/s.

Figure 6.8 shows the KPFM map for the sample exposed to the lowest laser scanning speed of 5 µm/s. The colour scale represents the local surface potential, varying from around -700 mV (dark regions) to $+700$ mV (bright regions). The image indicates a population of bright regions interspersed with darker regions, indicating considerable local changes in the work function and electronic properties.

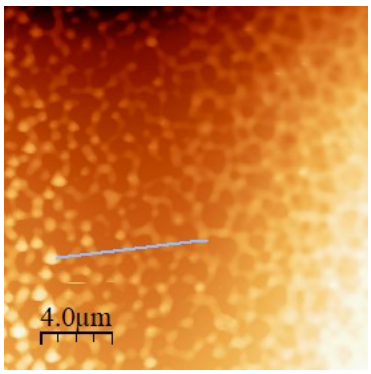

(a) AFM topography

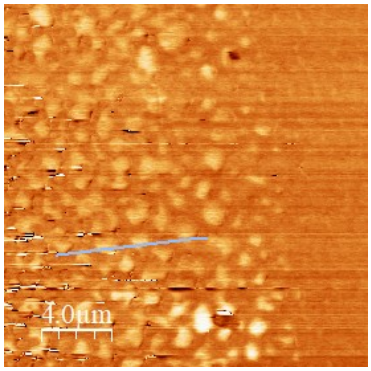

(b) KPFM surface potential map

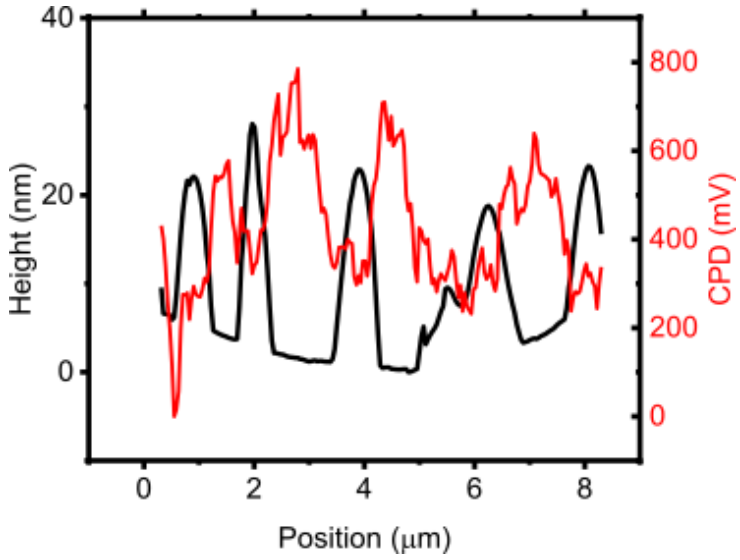

(c) Contact potential difference (CPD) distribution

Figure 6.9 AFM and KPFM analyses of the laser-irradiated silicon sample

Figure 6.9a is an AFM measurement of the same region as KPFM 6.9b. AFM reveals noticeable morphological changes in the laser-written area, often manifesting as slight elevations or texture variations. In addition, the contact potential difference (CPD) in Figure 6.9c shows a wide range in contact potential difference, extending from approximately -700 mV to $+700$ mV, which suggests significant shifts in the local Fermi level or band bending at the surface. The elevated or restructured regions observed in the AFM topography often align with higher CPD values in the KPFM map, indicating that prolonged laser exposure can induce both morphological and electronic modifications in the silicon surface. These findings strongly correlate with improved electrical conduction measured at slower scan speeds, reinforcing the notion that enhanced dopant incorporation or defect restructuring occurs under extended laser–material interaction.

These results are consistent with previous temperature-dependent conductivity measurements, confirming that samples processed at lower speeds exhibit improved electrical conduction. The

KPFM data suggest that local doping or surface chemistry undergoes substantial modification, possibly as a result of extended interaction between laser and material. The brighter areas might indicate areas of increased hole concentration or boron enrichment, while the darker regions could indicate less doping levels or defect-rich domains.

Overall, these results indicate that longer laser exposure on the silicon surface enhances dopant distribution and/or modifies crystallinity, which agrees with the increased conductivity noted in the temperature-dependent measurements. The KPFM image shows that longer laser exposure creates locally different surface potentials, thereby confirming the concept of higher dopant penetration or structural restructuring. The conclusion that slow-speed laser processing provides inhomogeneous but generally more conductive regions comes from the relationship between the KPFM potential map and previously measured electrical conductivity.

6.6. Charge Carrier Concentration in Laser-Processed Silicon

To evaluate the impact of laser processing on dopant concentration, SIMS was performed on both the unprocessed PS region and laser-processed regions. An analysis of these depth profiles offers insight into the impact of laser irradiation on dopant incorporation, redistribution, or activation. The SIMS data are linked with KPFM and I-V electrical measurements to find out if the observed trends correspond to fluctuations in surface potential and enhancements in conductivity.

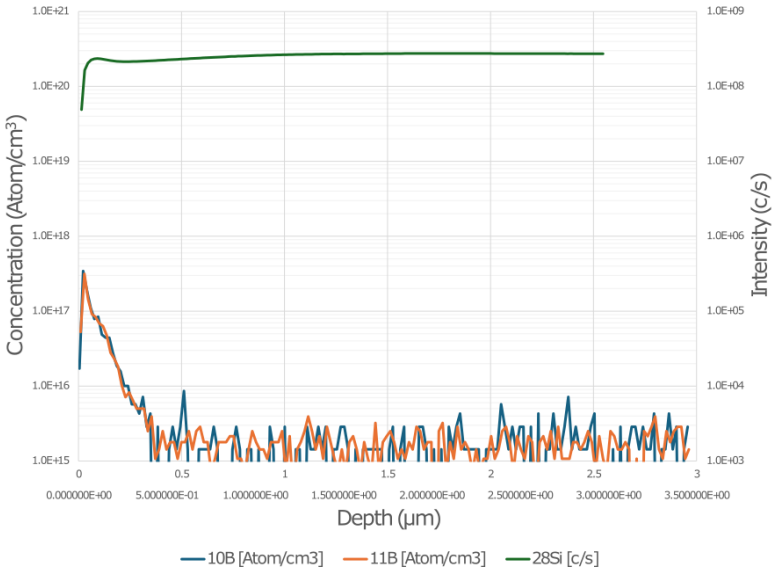

(a) SIMS depth profile for the silicon substrate after etched PS.

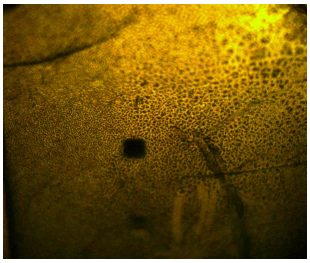

(b) Microscope image of the measurement spot.

Figure 6.10 SIMS depth profile for the etched silicon substrate alongside the microscope image of the measurement spot.

The SIMS depth profile for the unprocessed substrate (Figure 6.10a) indicates a high boron concentration at the surface (10^{17} atoms/cm^3), which decreases rapidly within the first 0.5 µm before stabilising at approximately 10^{15} atoms/cm^3 at greater depths. This trend is consistent with the expected doping profile of a p-type silicon wafer with a resistivity of $1 - 10$ Ω.cm, which confirms the intrinsic dopant distribution within the material. The ^{28}Si signal remains stable (around 10^{20} atoms/cm^3) throughout the depth range, indicating the uniformity of the silicon matrix.

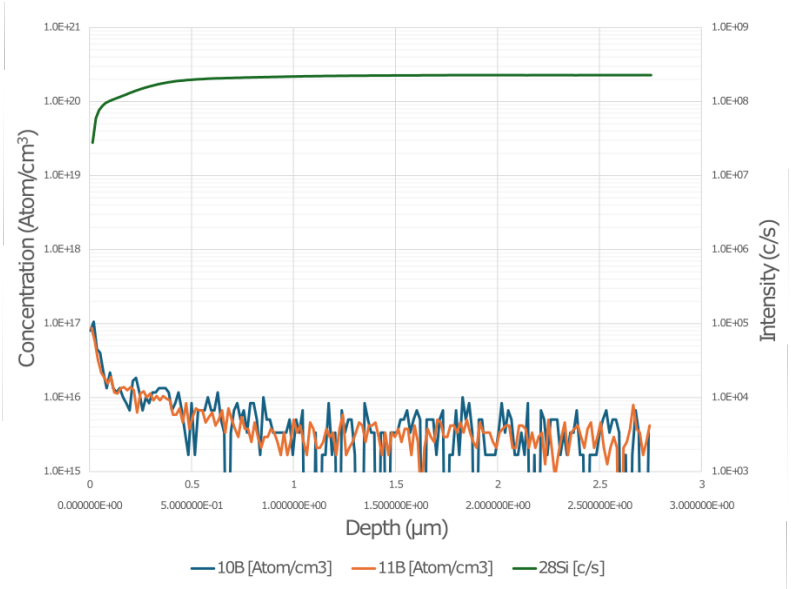

(a) SIMS depth profile of laser-processed area (the black trake) after PS engraving.

(b) Microscope image of the measurement spot on the black trake.

Figure 6.11 SIMS depth profile for the etched laser processed area alongside the microscope image of the measurement spot.

The SIMS profile for laser-processed regions (Figure 6.11) shows a similar concentration of boron and a depth-dependent decay, with no significant increase in dopant incorporation compared to the unprocessed substrate. However, greater fluctuations in boron concentration beyond 0.5 µm may indicate localised variations in dopant distribution or structural modifications induced by laser processing.

Although SIMS does not indicate a significant increase in boron concentration, I-V measurements demonstrate improved conductivity in laser-processed regions. This suggests that laser irradiation influences charge carrier behaviour, likely through dopant activation or structural modifications. Similarly, KPFM mapping has revealed variations in surface potential across laser-processed areas, which may be attributed to dopant redistribution, defect formation, or crystallinity changes.

Several limitations must be considered when interpreting these results. SIMS measures the total boron content but does not determine the fraction of boron atoms that contribute to electrical conduction. The finite depth resolution of SIMS may obscure sharp concentration changes, particularly if dopant redistribution occurs at the nanometre scale. Sputter artefacts can broaden the boron profile, potentially masking small-scale redistribution effects. Additionally, fluctuations in boron concentration beyond 0.5 µm may arise from measurement noise at low dopant levels rather than true compositional variations. Post-laser oxidation or surface contamination may also alter secondary ion yields, affecting detection accuracy.

6.7. Morphological Transformations of Recrystallised Silicon

Previous SIMS, KPFM, and I-V measurements described dopant distribution, surface potential variations, and electrical conductivity in laser-processed regions. However, none of these methods directly explained the black colouration observed in certain areas after laser exposure. Since surface morphology strongly influences optical absorption, AFM was applied to determine whether laser processing induced significant surface roughening, potentially leading to enhanced light trapping and reduced reflectivity, characteristic of black silicon formation.

AFM analysis was performed after the SiO_2 layer was etched in dilute HF to confirm that the observed surface features were related to laser-induced modifications rather than oxide-related artefacts. The investigation focused on comparing surface roughness and morphological changes before and after etching, particularly in regions where black silicon formation was suspected.

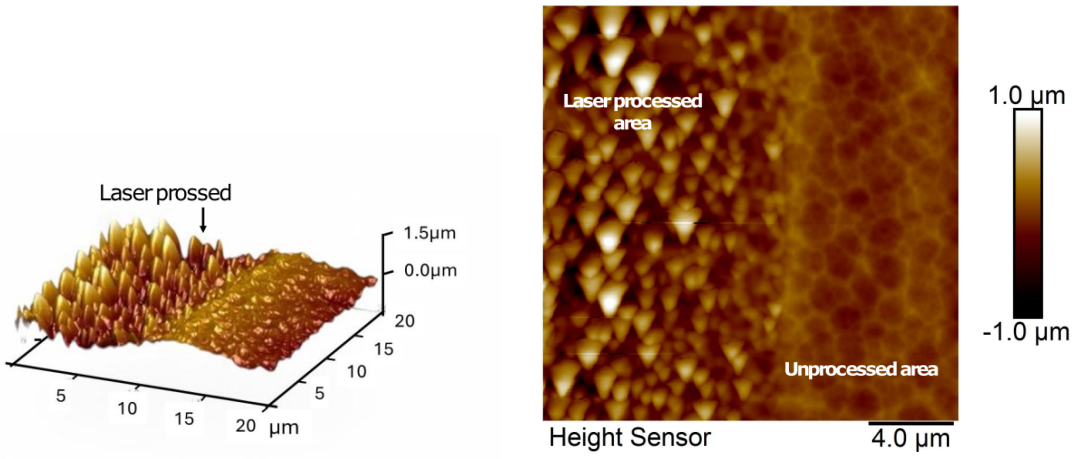

(a) 3D Image etched sample morphology. **(b)** Etched sample topography.

Figure 6.12 AFM images of black Silicon PS region (a) 20 μm $\times$ 20 μm laser writing line morphology; (b) 20 μm $\times$ 20 μm topography image of the laser writing line.

AFM imaging demonstrates a significant transformation in surface morphology after laser processing and etching. The three-dimensional AFM map (Figure 6.12a) shows the different surface textures of black silicon and porous silicon. The black silicon zone displays tightly arranged pyramidal structures, whereas the porous silicon appears to be comparatively smoother. The corresponding two-dimensional topography map (Figure 6.12b) further emphasises the distinct structuring, showing the increased surface roughness in laser-processed regions. These images confirm that laser exposure has significantly modified the surface, forming a morphology that enhances optical absorption.

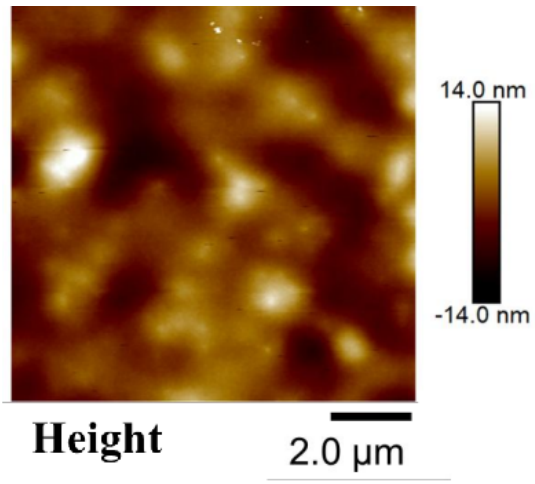

(a) Non-etched sample roughness.

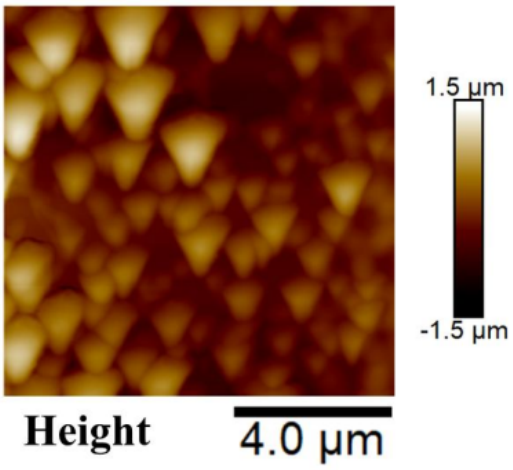

(b) Etched sample roughness.

Figure 6.13 Comparison of surface roughness between non-etched and etched samples, highlighting morphological differences.

A direct comparison between the non-etched and etched samples further demonstrates the structural transformation. The AFM height map of the non-etched sample (Figure 6.13a) shows a relatively smooth surface with an RMS roughness of 2.11 nm over a 10 µm $\times$ 10 µm area, showing no surface structure. In contrast, the etched sample shows a considerable increase in roughness, reaching 314.8 nm over the same scan area, as shown in Figure 6.13b. This substantial difference indicates that the oxide layer initially covered the laser-induced microstructures, which became fully exposed only after etching.

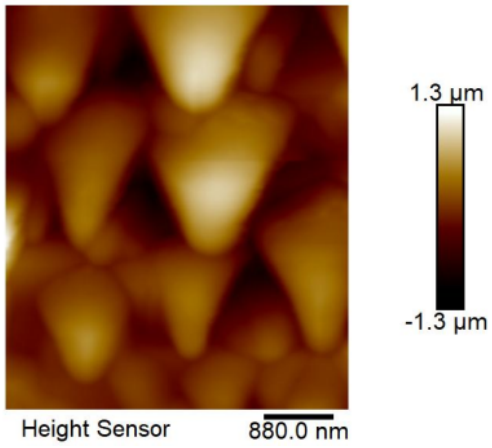

Figure 6.14

An in-depth analysis of individual black silicon features provides additional insight into their high-aspect ratio morphology. Figure 6.14 shows that the structures show an average base width of about 1.8 µm and a height that exceeds 1.3 µm, resulting in distinct pyramidal microstructures that improve optical absorption.

The black colouration of the laser-processed regions correlates directly with the increased surface roughness observed in the AFM measurements. The densely pyramidal microstructures modify the optical response of the surface in multiple ways. First, they enhance light absorption by increasing the probability of multiple internal reflections, causing incident light to be repeatedly scattered and absorbed rather than reflected. Second, the roughened black silicon surface disrupts coherent reflection, preventing specular reflection, which is characteristic of smooth silicon. A polished silicon surface generally reflects 30–40% of incident light, resulting in a metallic sheen, while the structured black silicon region scatters light in various directions, greatly decreasing overall reflectivity. Finally, the development of high-aspect-ratio features enhances broadband optical absorption, reducing reflectivity over a broad spectral range.

AFM analysis confirms that laser processing led to the creation of pyramidal structures with a high aspect ratio, which considerably increased surface roughness. This transformation explains the black colouring observed in laser-processed regions, as the structured surface improves light trapping, reduces reflectivity, and increases absorption, all important properties of black silicon. These results strongly suggest that the effect is primarily morphological rather than chemical, since previous studies in SIMS, KPFM, and I-V did not show chemical changes that may explain the black appearance.

6.8. Hypothesis: Boron Enrichment and Enhanced Conductivity

The results obtained in this study provide partial confirmation of the hypothesis that HF etching of silicon to form PS promotes boron enrichment at or near the surface, which is subsequently reorganised by laser melting and recrystallisation to form a boron-rich network. This network, in turn, is posited to enhance the electrical conductivity of the material. Several lines of experimental evidence support this notion. First, AFM imaging reveals notable surface restructuring, consistent with a mechanism by which boron, left behind by selective silicon removal in HF, becomes locally concentrated as the silicon matrix is re-etched or melted. Secondly, KPFM mapping indicates pronounced variations in surface potential that would be expected if higher doping levels or doping activation were present at the surface. Lastly, I–V measurements show improved conductivity in these laser-processed regions, aligning with the concept that boron is both accessible and activated by the melting–recrystallisation cycle.

However, SIMS depth profiling did not detect a marked increase in overall boron concentration, underscoring the complexity of the hypothesised mechanism. It is possible that boron enrichment occurs in regions too thin or localised for conventional SIMS resolution, or that dopant activation rather than net dopant addition is the driving factor. In addition, other structural evolutions, such as improved crystallinity, reduced defect densities, or the creation of conductive pathways along grain boundaries, may also contribute to the observed rise in conductivity. The balance of evidence thus supports the view that HF etching and subsequent laser-induced melting create conditions under which boron can be redistributed or activated at the surface, even if large-scale dopant concentration increases are not observed.

Further clarification may be achieved by more targeted techniques (for example, nanoSIMS or TEM–EDX mapping) designed to resolve dopant distributions at the nanometre scale. Nevertheless, the current results support the idea that selectively etched PS, followed by laser melting and recrystallization, creates a surface environment that improves electrical performance partly because of boron activation and local enrichment.

6.9. Conclusion

This chapter investigated the structural, spectroscopic, and electrical modifications induced by laser processing in PS. An interesting observation was the persistent black colouration of the laser-irradiated areas, previously considered to be oxidation. However, AFM analysis confirmed that the colouration resulted mainly from surface roughening and the formation of high-aspect

ratio pyramidal microstructures. These structures enhanced light trapping and reduced reflectivity, leading to the observed optical changes.

Raman spectroscopy provided further insight into the crystallographic transformations, revealing peak broadening and shifts indicative of nanocrystalline domain formation and lattice strain. The enhanced Raman signal indicated SERS effects associated with modifications in the silicon surface structure. Despite these changes, SIMS depth profiling indicated that laser processing did not introduce additional dopant incorporation, but likely influenced dopant redistribution and activation, which contributed to electrical modifications.

The KPFM results offered crucial proof that the surface potential fluctuation is connected to the observed changes in electrical behaviour. The laser-processed areas demonstrated localised modifications in surface potential, supporting the hypothesis that dopant activation and crystallinity modifications influenced charge carrier behaviour. The observed changes were in agreement with the V measurements, which indicated increased conductivity in the irradiated areas, supporting that surface restructuring and potential redistribution contributed to improvements in electrical performance.

Overall, this chapter provides a comprehensive understanding of how laser-induced melting and recrystallisation impact both the morphology and electrical properties of silicon.The combined results of AFM, Raman, SIMS, and KPFM analysis demonstrate that CO_2 CW laser irradiation modifies the silicon surface at the nanoscale and influences its electrical properties.

Chapter 7. Conclusions and Future Directions

7.1. Thesis Conclusion

This thesis has thoroughly investigated the transformative potential of CW CO_2 laser processing in modifying the structure and properties of PS. The research initially involved fabricating PS through electrochemical etching, carefully controlling key parameters such as pore size, thickness, porosity and surface chemistry. Detailed characterisation using SEM, FTIR, AFM and XRD confirmed the successful formation of reproducible and uniform porous silicon layers, providing a critical baseline for evaluating subsequent modifications induced by laser irradiation.

The main focus of this thesis was the controlled application of CW CO_2 laser processing to induce significant phase transitions and structural transformations within PS. Systematic experimentation that varied the laser power and scanning speed enabled precise control over the recrystallisation process. Raman spectroscopy was instrumental in elucidating these structural modifications, highlighting enhanced Raman signals indicative of improved crystallinity and the occurrence of nanostructural changes. The observed Raman spectral enhancements and characteristic shifts strongly suggested SERS effects resulting from laser-induced alterations in the silicon surface morphology and crystallinity.

Despite to initial expectations, SIMS depth profiling did not confirm an increase in dopant concentration due to laser processing. However, SIMS analysis indicated significant redistribution of dopants and possible activation, leading to improved electrical characteristics. KPFM provided additional insight, demonstrating changes in surface potential distribution consistent with enhanced dopant activity and improved charge-transport properties.

Electrical characterisation through I–V measurements supported these findings, revealing a marked improvement in conductivity in laser-treated regions. This enhancement is primarily attributed to the observed structural recrystallisation and dopant activation rather than a direct increase in dopant incorporation. Additionally, morphological analysis by AFM and SEM confirmed the densification and structural refinement of the laser-modified porous silicon. These structural changes improved the electrical properties.

The comprehensive set of experimental outcomes presented in this thesis clearly demonstrates the effectiveness of CW CO_2 laser irradiation as a versatile tool for precisely engineering structural and electrical properties of porous silicon. This work has provided valuable new insights into the mechanisms underlying laser-induced phase transitions, highlighting its potential for advanced applications in optoelectronics, microelectronics, and sensing technologies. By correlating the detailed morphological, structural, and electronic analyses, this research has significantly advanced our understanding of the interactions between laser processing and porous silicon.

Electrical measurements further support the efficacy of the laser processing technique. I-V analyses demonstrated a marked improvement in conductivity for the laser-irradiated samples. The observed enhancements in electrical performance are attributed to the improved charge transport mechanisms that result from a more ordered crystalline structure and a higher concentration of dopants. In addition, KPFM provided complementary evidence by mapping variations in surface potential that align with enhanced doping levels. The convergence of these different characterisation methods reinforces the conclusion that the CW CO_2 laser processing effectively modifies both the microstructure and the electronic properties of porous silicon.

7.2. Future Work

While the results are promising, there is still work to be done. Future research should focus on fine-tuning the CO_2 laser process to achieve more consistent modifications across the porous silicon. This means further optimising the laser power, scanning speed, and exposure time to reduce surface irregularities and maximise electrical performance. Additionally, testing the long-term stability of the modified material under real operating conditions will be crucial.

Another important direction is to integrate laser-processed porous silicon into actual device prototypes. By doing so, we can better assess its performance in practical applications, whether in microelectronics, optoelectronics, or sensor technologies. Although SIMS analysis in this study did not confirm an increase in the concentration of boron, future work should explore alternative or complementary techniques to investigate this aspect further. Techniques such as high-resolution Time-of-Flight SIMS, atom probe tomography (APT), or electron energy loss spectroscopy (EELS) in transmission electron microscopy (TEM) may offer the enhanced sensitivity and spatial resolution required to detect subtle changes in the boron distribution. Further investigation into the role of boron enrichment in enhancing conductivity could lead to better material models and more refined processing strategies.

In summary, the insights gained in this thesis provide a strong foundation for future studies aimed at transitioning from laboratory research to real-world applications in next-generation silicon-based technologies.

Appendix A. Heat Distribution in The Porous Silicon Simulation

```
import numpy as np
import matplotlib.pyplot as plt
from numba import jit, prange
import numpy as np
import matplotlib.pyplot as plt

# Constants
PI = np.pi

def save_data_txt(data, filename):
    with open(filename, 'w') as file:
        for item in data:
            file.write(str(item) + '\n')

# Function for plotting 2D heatmap
def plot_heatmap(r, z, u, xlabel="", ylabel=""):
    plt.figure(figsize=(10, 7))
    X, Y = np.meshgrid(r, z)
    plt.contourf(X, Y, u.T, 20, cmap='magma')  # Transpose u for correct orientatio
    plt.colorbar(label='Temperature (u)')
    plt.xlabel(xlabel)
    plt.ylabel(ylabel)
    plt.title('Temperature Distribution')
    plt.show()

# Function for plotting 1D data (temperature vs. time)
def plot(x, y, xlabel="", ylabel=""):
```

```
    plt.figure(figsize=(8, 5))
    plt.plot(x, y)
    plt.xlabel(xlabel)
    plt.ylabel(ylabel)
    # plt.title('Temperature Change Over Time')
    # plt.legend()
    plt.grid()
    plt.show()


w0 = 2.35e-4  # Beam waist (m)
lambda_ = 1.06e-5  # Wavelength (m)
nr = 3.67  # Refractive index of silicon
por = 0.8  # Porosity
T0 = 293.0  # Initial temperature (K)
kT = 0.5e-1  # Thermal conductivity (W/mK)
asym = 1.0  # Axial to radial thermal conductivity ratio
cp = 0.710  # Specific heat capacity (J/gK)
dens = 2.33e6  # Density (g/m³)
inp = input("Enter the measured laser power (W):")
if inp:
    I_meas = float(inp)
else:
    I_meas = 2.5e1
abv = 8.59e4  # Inverse absorption length (1/m)
zd = 0.0  # Depth below surface (units of w0)
beta = 0.0e-6  # Two-photon absorption coefficient

# Grid parameters
dr = 0.01
Rmax = 4
dz = 0.0004
Zmax = 0.028
omega = 1.990  # Overrelaxation parameter
dt = 2.0e-5  # Time step (s)
```

```
maxits = 10000  # Max iterations for SOR
eps = 1.0e-5  # Precision for relaxation method

# Grid setup
imax = 100
jmax = 100
tmax = 500
r = np.zeros(imax)
z = np.zeros(jmax)
u = np.ones((imax, jmax))
q = np.zeros((imax, jmax))

# Compute I0 from the measured laser power, I_meas
I0 = 2.0 * I_meas / (np.pi * (w0 ** 2))
print(I0, 'W m^-2')

# Compute dimensionless groups
gA = (kT * dt) / (dens * (1.0 - por) * cp * (w0 ** 2))
print(gA, 'Dimensionless diffusivity')

gB = (abv * I0 * dt) / (dens * cp * T0)
print(gB, 'Dimensionless factor for volumetric heat - 1 photon')

gBB = (beta * I0 * I0 * dt) / (dens * cp * T0)
print(gBB, 'Dimensionless factor for volumetric heat - 2 photon')

gC = (np.pi * w0 * nr * (1.0 - por)) / lambda_
print(gC, 'Dimensionless Rayleigh range, ZR')

gD = (abv * w0) * (1.0 - por)
print(gD, 'Dimensionless inverse absorption length')

# Exponentially expanding grid generation
r_exp = (np.log((Rmax / dr) + 1)) / (imax - 1)
```

```
z_exp = (np.log((Zmax / dz) + 1)) / (jmax - 1)

for i in range(imax):
    r[i] = dr * (np.exp(r_exp * i) - 1)

for j in range(jmax):
    z[j] = dz * (np.exp(z_exp * j) - 1)

# Compute the heat term due to absorption of a Gaussian beam
for i in range(imax):
    for j in range(jmax):
        zqtemp = 1.0 + ((z[j] - zd) / gC) ** 2
        q[i, j] = gB * (abv / ((abv + beta * I0) * np.exp(gD * z[j]) - beta * I0)) * np.
        q[i, j] += gBB * (abv / ((abv + beta * I0) * np.exp(gD * z[j]) - beta * I0)) * n

# Setup fully implicit difference equation coefficients
a = np.zeros((imax, jmax))
b = np.zeros((imax, jmax))
c = np.zeros((imax, jmax))
d = np.zeros((imax, jmax))
e = np.zeros((imax, jmax))
f = np.zeros((imax, jmax))

for i in range(1, imax - 1):
    for j in range(1, jmax - 1):
        rtemp = 2 / (r[i + 1] - r[i - 1])
        ztemp = 2 / (z[j + 1] - z[j - 1])
        rt1 = 1 / (r[i + 1] - r[i])
        rt2 = 1 / (r[i] - r[i - 1])
        zt1 = 1 / (z[j + 1] - z[j])
        zt2 = 1 / (z[j] - z[j - 1])
        a[i, j] = gA * (rtemp * rt1 + (1 / r[i] / (r[i + 1] - r[i - 1])))
        b[i, j] = gA * (rtemp * rt2 - (1 / r[i] / (r[i + 1] - r[i - 1])))
        c[i, j] = asym * gA * ztemp * zt1
```

```
        d[i, j] = asym * gA * ztemp * zt2
        e[i, j] = -(a[i, j] + b[i, j] + c[i, j] + d[i, j]) - 1
        f[i, j] = -u[i, j] - q[i, j]

@jit(nopython=True, parallel=True)
def solve_heat_equation(u, q, a, b, c, d, e, f, maxits, eps, omega, tmax, imax, jma
    t = np.zeros(tmax)
    torigin = np.zeros(tmax)
    for k in range(tmax):
        n = 1
        pstop = 0
        for i in range(1, imax - 1):
            for j in range(1, jmax - 1):
                f[i, j] = -u[i, j] - q[i, j]
        while pstop == 0:
            n += 1
            change = 0.0
            u[:, 0] = u[:, 1]  % Boundary condition
            u[0, :] = u[1, :]  % Boundary condition
            for i in range(1, imax - 1):
                for j in range(1, jmax - 1):
                    before = u[i, j]
                    resid = a[i, j] * u[i+1, j] + b[i, j] * u[i-1, j] + c[i, j] * u
                    u[i, j] = u[i, j] - omega * resid / e[i, j]
                    after = u[i, j]
                    change += abs(after - before)
            if change < eps:
                pstop = 1
            elif n > maxits:
                pstop = 1
            else:
                pstop = 0
        t[k] = k+1
        torigin[k] = u[0, 0]
```

```
    return u, t, torigin


# Execute the calculations
u, t, torigin = solve_heat_equation(u, q, a, b, c, d, e, f, maxits, eps, omega, tmax, im


plot_heatmap(r, z, u, 'Radial distance / beam waist', 'Depth / beam waist')
plot(t, torigin, 'Normalised time ( t/dt )', 'Normalised temperature( T/T0)')
plot(r, u[:,0], 'Radial distance / beam waist', 'Normalised temperature( T/T0)')


save_data_txt(u, "uI={I_meas}.txt")
save_data_txt(r, "rI={I_meas}.txt")
save_data_txt(z, f"z with I={I_meas}.txt")
save_data_txt(t, "time.txt")
save_data_txt(torigin, "temperature_origin.txt")
data = np.stack([t, torigin])
print(data.shape)
np.savetxt(f"Heat Distribution with I={I_meas}.txt", np.round(data.T, 2), fmt="%.2e", de
data = np.stack([r, u[:,0]])
np.savetxt(f"Plot3  with I={I_meas}.txt", np.round(data.T, 2), fmt="%.2e", delimiter=","
```

Bibliography

[1] Takahiro Abe, Takashi Yasuda, Masaaki Tanizaki, Shigeru Yamaguchi, Kenzo Nanri, Naoomi Miyakawa, and Tomoo Fujioka. Gas temperature analysis of laser gain medium in a slab-type radio-frequency-discharge-excited co_2 laser. *The Review of Laser Engineering*, 36(APLS):1261–1264, 2008.

[2] Ali L. Abed and Bassam G. Rasheed. Study of the effect of co_2 laser annealing on silicon nanostructures. *Modern Applied Science*, 4(12):56, 2010.

[3] H. K. Abood and F. A. H. Mutlak. Structural, morphological, and optical properties of n-type porous silicon: Effect of etching current density. *IOP Conference Series: Materials Science and Engineering*, 757(1):012065, 2020.

[4] Gunjan Aggarwal, Prabhash Mishra, Bipin Joshi, Harsh, and S. S. Islam. Porous silicon surface stability: A comparative study of thermal oxidation techniques. *Journal of Porous Materials*, 21:23–29, 2014. doi: 10.1007/s10934-013-9747-5.

[5] Paola Agüi-Gonzalez, Sebastian Jähne, and Nhu T. N. Phan. Sims imaging in neurobiology and cell biology. *Journal of Analytical Atomic Spectrometry*, 34(7):1355–1368, 2019.

[6] G. Aguila Rodríguez, G. García-Salgado, G. Romero-Paredes, R. Peña-Sierra, et al. Ftir and photoluminescence studies of porous silicon layers oxidized in controlled water vapor conditions. *Revista Mexicana de Física*, 53(6):431–435, 2007.

[7] Faten Alfeel, Fowzi Awad, Ibrahim Alghoraibi, and Fadi Qamar. Using afm to determine the porosity in porous silicon. *Journal of Materials Science and Engineering A*, 2(9A): 579, 2012.

[8] Zeid A. ALOthman. A review: Fundamental aspects of silicate mesoporous materials. *Materials*, 5(12):2874–2902, 2012.

[9] Francesc Xavier Alvarez, David Jou, and Antonio Sellitto. Pore-size dependence of the thermal conductivity of porous silicon: A phonon hydrodynamic approach. *Applied Physics Letters*, 97(3), 2010.

[10] Abebaw Abun Amanu. Electronic electrical conductivity in n-type silicon. *Latin-American Journal of Physics Education*, 9(2):9, 2015.

[11] Rolfe C. Anderson, Richard S. Muller, and Charles W. Tobias. Investigations of the electrical properties of porous silicon. *Journal of the Electrochemical Society*, 138(11): 3406, 1991.

[12] Rolfe C. Anderson, Richard S. Muller, and Charles W. Tobias. Chemical surface modification of porous silicon. *Journal of the Electrochemical Society*, 140(5):1393, 1993.

[13] Emily J. Anglin, Lingyun Cheng, William R. Freeman, and Michael J. Sailor. Porous silicon in drug delivery devices and materials. *Advanced Drug Delivery Reviews*, 60(11): 1266–1277, 2008.

[14] Roman Anufriev, Jeremie Maire, and Masahiro Nomura. Review of coherent phonon and heat transport control in one-dimensional phononic crystals at nanoscale. *APL Materials*, 9(7), 2021.

[15] Yoshinobu Arita and Yoshio Sunohara. Formation and properties of porous silicon film. *Journal of the Electrochemical Society*, 124(2):285, 1977.

[16] V. M. Aroutiounian and M. Zh. Ghulinyan. Electrical conductivity mechanisms in porous silicon. *Physica Status Solidi (a)*, 197(2):462–466, 2003.

[17] Nikola Baran, Sanja Renka, Matea Raić, Davor Ristić, and Mile Ivanda. Effects of thermal oxidation on sensing properties of porous silicon. *Chemosensors*, 10(9):349, 2022. doi: 10.3390/chemosensors10090349.

[18] Kasra Behzad, Wan Mahmood Mat Yunus, Zainal Abidin Talib, Azmi Zakaria, Afarin Bahrami, and Esmaeil Shahriari. Effect of etching time on optical and thermal properties of p-type porous silicon prepared by electrical anodisation method. *Advances in Optical Technologies*, 2012, 2012.

[19] Ali Belarouci, Roman Tkach, and Dmytro Averin. Engineering high aspect-ratio silicon nanostructures. *Physical Sciences and Technology*, 10(3-4):87–94, 2023.

[20] Daniel Bellet and Leigh Canham. Controlled drying: The key to better quality porous semiconductors. *Advanced Materials*, 10(6):487–490, 1998.

[21] I. Berbezier and A. Halimaoui. A microstructural study of porous silicon. *Journal of Applied Physics*, 74(9):5421–5425, 1993.

[22] Olivia M. Berengue, Adenilson J. Chiquito, Livia P. Pozzi, Alexandre J. C. Lanfredi, and Edson R. Leite. Electron–phonon scattering in sn-doped in_2o_3 fet nanowires probed by temperature-dependent measurements. *Nanotechnology*, 20(24):245706, 2009.

[23] Catherine Berthomieu and Rainer Hienerwadel. Fourier transform infrared (ftir) spectroscopy. *Photosynthesis Research*, 101:157–170, 2009.

[24] G. M. Bhalerao, M. K. Singh, A. K. Sinha, and Haranath Ghosh. Optical redshift in the raman scattering spectra of fe-doped multiwalled carbon nanotubes: Experiment and theory. *Physical Review B—Condensed Matter and Materials Physics*, 86(12):125419, 2012.

[25] Gerd Binnig, Calvin F. Quate, and Christoph Gerber. Atomic force microscope. *Physical Review Letters*, 56(9):930, 1986.

[26] Olmes Bisi, Stefano Ossicini, and Lorenzo Pavesi. Porous silicon: A quantum sponge structure for silicon-based optoelectronics. *Surface Science Reports*, 38(1–3):1–126, 2000.

[27] Robert B. Bjorklund, Shahin Zangooie, and Hans Arwin. Color changes in thin porous silicon films caused by vapor exposure. *Applied Physics Letters*, 69(20):3001–3003, 1996.

[28] I. W. Boyd and John I. B. Wilson. Oxidation of silicon surfaces by co_2 lasers. *Applied Physics Letters*, 41(2):162–164, 1982.

[29] Mark B. H. Breese and Dharmalingam Mangaiyarkarasi. Porous silicon bragg reflectors with sub-micrometer lateral dimensions. *Optics Express*, 15(9):5537–5542, 2007.

[30] Richard A. Butera and David H. Waldeck. The dependence of resistance on temperature for metals, semiconductors, and superconductors. *Journal of Chemical Education*, 74(9): 1090, 1997.

[31] I. H. Campbell and Ph. M. Fauchet. The effects of microcrystal size and shape on the one phonon raman spectra of crystalline semiconductors. *Solid State Communications*, 58(10): 739–741, 1986.

[32] L. T. Canham, T. I. Cox, A. Loni, and A. J. Simons. Progress towards silicon optoelectronics using porous silicon technology. *Applied Surface Science*, 102:436–441, 1996.

[33] Leigh Canham. *Handbook of porous silicon*. Springer International Publishing, 2014.

[34] Leigh T. Canham. Silicon quantum wire array fabrication by electrochemical and chemical dissolution of wafers. *Applied Physics Letters*, 57(10):1046–1048, 1990. doi: 10.1063/1.103561.

[35] F. Severiano Carrillo, G. García-Salgado, and M. Salazar Villanueva. Optical, morphological, and structural properties of tablets obtained from porous silicon. *Silicon*, pages 1–7, 2022.

[36] Jill Chastain and Roger C. King Jr. Handbook of x-ray photoelectron spectroscopy. *Perkin-Elmer Corporation*, 40:221, 1992.

[37] Liang-yao Chen, Xiao-yuan Hou, Da-ming Huang, Ping-hai Hao, Fu-long Zhang, Xing-wei Feng, You-hua Qian, and Xun Wang. Optical study of photon-trapped porous silicon layer. *Japanese Journal of Applied Physics*, 33(4R):1937, 1994.

[38] Liang-yao Chen, Xiao-yuan Hou, Da-ming Huang, Fu-long Zhang, Xing-wei Feng, Min Yang, Yi Su, You-hua Qian, and Xun Wang. Study of photon-trapping phenomenon in porous silicon layer. *Acta Physica Sinica (Overseas Edition)*, 3(8):595, 1994.

[39] S-F Chuang, SD Collins, and RL Smith. Preferential propagation of pores during the formation of porous silicon: A transmission electron microscopy study. *Applied Physics Letters*, 55(7):675–677, 1989.

[40] Wayne A. Churaman and Luke Currano. *Preparation of nanoporous silicon*. Army Research Laboratory, 2007.

[41] Inc CiteDrive. The engineering toolbox, 2005. URL https://www.engineeringtoolbox.com/surface-tension-d_962.html. [Online; accessed 26-OCTOBER-2023].

[42] Creative Chemistry. Periodicity and properties of period 3 elements, 2024. URL https://www.creative-chemistry.org.uk/alevel/core-inorganic/periodicity/trends8. Accessed: October 23, 2024.

[43] F. Secco d'Aragona. Dislocation etch for (100) planes in silicon. *Journal of the Electrochemical Society*, 119(7):948, 1972.

[44] R. S. Dariani and Z. Ahmadi. Study of porous silicon structure by raman scattering. *Optik*, 124(22):5353–5356, 2013.

[45] Ruchita S. Das and Y. K. Agrawal. Raman spectroscopy: Recent advancements, techniques and applications. *Vibrational Spectroscopy*, 57(2):163–176, 2011.

[46] Higo de Araujo Oliveira, Zheyong Fan, Ari Harju, and Luiz Felipe C. Pereira. Tuning the thermal conductivity of silicon phononic crystals via defect motifs: Implications for thermoelectric devices and photovoltaics. *ACS Applied Nano Materials*, 2024.

[47] Gero Decher, Birgit Lehr, Klaus Lowack, Yuri Lvov, and Johannes Schmitt. New nanocomposite films for biosensors: Layer-by-layer adsorbed films of polyelectrolytes, proteins or dna. *Biosensors and Bioelectronics*, 9:677–684, 1994.

[48] L. Degiorgi. The drude model in correlated systems. *Annalen der Physik*, 518(7–8): 571–584, 2006.

[49] D. Dimova-Malinovska. Structural and optical properties of poly-si thin films obtained by aluminium induced crystallization. *Journal of Physics: Conference Series*, 223(1): 012013, 2010.

[50] Th. Dittrich, I. Sieber, W. Henrion, S. Rauscher, N. Wanderka, and J. Rappich. Selective laser-induced melting of ultrathin nanoporous silicon layers. *Applied Physics A*, 63: 467–470, 1996.

[51] E. P. Domashevskaya, V. M. Kashkarov, E. Yu Manukovskii, A. V. Shchukarev, and V. A. Terekhov. Xps, usxs and pls investigations of porous silicon. *Journal of Electron Spectroscopy and Related Phenomena*, 88:969–972, 1998.

[52] J. S. Dugdale and Z. S. Basinski. Mathiessen's rule and anisotropic relaxation times. *Physical Review*, 157(3):552, 1967.

[53] Alena Dyadenchuk, Natalia Domina, and Roman Oleksenko. Simulation of solar element characteristics based on porous silicon. In *2022 IEEE 4th International Conference on Modern Electrical and Energy Systems (MEES)*, pages 1–4, 2022.

[54] Peter Eaton and Paul West. *Atomic force microscopy*. Oxford University Press, 2010.

[55] Paz Elia, Einat Nativ-Roth, Yehuda Zeiri, and Ze'ev Porat. Determination of the average pore size and total porosity in porous silicon layers by image processing of sem micrographs. *Microporous and Mesoporous Materials*, 225:465–471, 2016.

[56] Linda M. Ephrath. Reactive ion etching for vlsi. *IEEE Transactions on Electron Devices*, 28(11):1315–1319, 1981.

[57] P. M. Fauchet, L. Tsybeskov, C. Peng, S. P. Duttagupta, J. Von Behren, Y. Kostoulas, J. M. V. Vandyshev, and K. D. Hirschman. Light-emitting porous silicon: Materials science, properties, and device applications. *IEEE Journal of Selected Topics in Quantum Electronics*, 1(4):1126–1139, 1995.

[58] Aleksandr S. Fedorov and Anastasiia S. Teplinskaia. Thermal properties of porous silicon nanomaterials. *Materials*, 15(23):8678, 2022.

[59] A. Fejfar, I. Pelant, E. Šípek, J. Kočka, G. Juška, T. Matsumoto, and Y. Kanemitsu. Transport study of self-supporting porous silicon. *Applied Physics Letters*, 66(9):1098–1100, 1995.

[60] M. N. Filippov, M. A. Ermakova, V. P. Gavrilenko, A. A. Kuzin, A. Yu. Kuzin, A. A. Kuzmin, V. B. Mityukhlyaev, A. V. Rakov, P. A. Todua, and A. V. Zablotskiy. Natural oxide thickness measurements on the test silicon relief pitch structure. *Proceedings of the International Conference on Micro- and Nano-Electronics 2012*, 8700:257–262, 2013.

[61] A. Florakis, E. Verrelli, Damiano Giubertoni, G. Tzortzis, and D. Tsoukalas. Non-melting annealing of silicon by co_2 laser. *Thin Solid Films*, 518(9):2551–2554, 2010.

[62] R. Fogelholm and O. Rapp. High-temperature deviation from matthiessen's rule in incd alloys. *Journal of Physics F: Metal Physics*, 7(4):667, 1977.

[63] Helmut Föll, Martin Christophersen, Jürgen Carstensen, and Gerd Hasse. Formation and application of porous silicon. *Materials Science and Engineering: R: Reports*, 39(4): 93–141, 2002.

[64] Yukun Gao and Penggang Yin. Origin of asymmetric broadening of raman peak profiles in si nanocrystals. *Scientific Reports*, 7(1):43602, 2017.

[65] Gaël Gautier and Sébastien Kouassi. Integration of porous silicon in microfuel cells: A review. *International Journal of Energy Research*, 39(1):1–25, 2015.

[66] Daohan Ge, Ahmed Rezk, Chengxiang Zhao, Zhou Hu, and Liqiang Zhang. Experimental research on damage and formation limits on porous silicon materials by electrochemical etching method. *Journal of Materials Research*, 37(4):876–886, 2022.

[67] G. Gesele, J. Linsmeier, V. Drach, J. Fricke, and R. Arens-Fischer. Temperature-dependent thermal conductivity of porous silicon. *Journal of Physics D: Applied Physics*, 30(21): 2911, 1997.

[68] James L. Gole and Stephen E. Lewis. Porous silicon—sensors and future applications. In *Nanosilicon*, pages 149–175. Elsevier, 2008.

[69] S. R. Goodes, T. E. Jenkins, M. I. J. Beale, J. D. Benjamin, and C. Pickering. The characterisation of porous silicon by raman spectroscopy. *Semiconductor Science and Technology*, 3(5):483, 1988.

[70] T. Gries, L. Vandenbulcke, P. Simon, and A. Canizares. Stresses in textured and polycrystalline cubic films by raman spectroscopy: Application to diamond. *Journal of Applied Physics*, 102(8), 2007.

[71] M. X. Gu, L. K. Pan, B. K. Tay, and Chang Q. Sun. Atomistic origin and temperature dependence of raman optical redshift in nanostructures: A broken bond rule. *Journal of Raman Spectroscopy*, 38(6):780–788, 2007.

[72] M. Guendouz, P. Joubert, and M. Sarret. Effect of crystallographic directions on porous silicon formation on patterned substrates. *Materials Science and Engineering: B*, 69: 43–47, 2000.

[73] Lihao Han, Miro Zeman, and Arno H. M. Smets. Raman study of laser-induced heating effects in free-standing silicon nanocrystals. *Nanoscale*, 7(18):8389–8397, 2015.

[74] Farid A. Harraz. Porous silicon chemical sensors and biosensors: A review. *Sensors and Actuators B: Chemical*, 202:897–912, 2014.

[75] T. R. Hart, R. L. Aggarwal, and Benjamin Lax. Temperature dependence of raman scattering in silicon. *Physical Review B*, 1(2):638, 1970.

[76] Kazuki Hashimoto, Venkata Ramaiah Badarla, and Takuro Ideguchi. High-speed fourier-transform infrared spectroscopy with phase-controlled delay line. *Laser & Photonics Reviews*, 15(1):2000374, 2021.

[77] Shinji Hayashi and Hiroya Abe. Implication of amorphous-like raman spectra of gas-evaporated si and ge microcrystals. *Japanese Journal of Applied Physics*, 23(11A):L824, 1984.

[78] Christy L. Haynes, Adam D. McFarland, and Richard P. Van Duyne. Surface-enhanced raman spectroscopy. *The Journal of Physical Chemistry B*, 2005.

[79] Bob B. He. Materials characterization from diffraction intensity distribution in the γ-direction. *Powder Diffraction*, 29(2):113–117, 2014.

[80] Noel Healy, Sakellaris Mailis, Nadezhda M. Bulgakova, Pier J. A. Sazio, Todd D. Day, Justin R. Sparks, Hiu Y. Cheng, John V. Badding, and Anna C. Peacock. Extreme electronic bandgap modification in laser-crystallized silicon optical fibres. *Nature Materials*, 13(12):1122–1127, 2014.

[81] G. S. Higashi, Y. J. Chabal, G. W. Trucks, and Krishnan Raghavachari. Ideal hydrogen termination of the si (111) surface. *Applied Physics Letters*, 56(7):656–658, 1990.

[82] Yoshihiro Hishikawa, Takuya Doi, Michiya Higa, Kengo Yamagoe, Hironori Ohshima, Takakazu Takenouchi, and Masahiro Yoshita. Voltage-dependent temperature coefficient of the i–v curves of crystalline silicon photovoltaic modules. *IEEE Journal of Photovoltaics*, 8(1):48–53, 2017.

[83] J. Michael Hollas. *Modern spectroscopy*. John Wiley & Sons, 2004.

[84] Patrick E. Hopkins, Charles M. Reinke, Mehmet F. Su, Roy H. Olsson III, Eric A. Shaner, Zayd C. Leseman, Justin R. Serrano, Leslie M. Phinney, and Ihab El-Kady. Reduction in the thermal conductivity of single crystalline silicon by phononic crystal patterning. *Nano Letters*, 11(1):107–112, 2011.

[85] Yu-Jen Hsu, Hsing-Yu Wu, Wei-Che Chang, and Yung-Tang Nien. Machining fused silica surface by continuous-wave co2 laser beams and their nanostructure characterizations. *Materials Letters*, 306:130960, 2022. doi: 10.1016/j.matlet.2021.130960.

[86] Allan Hynes, David A. Scott, Angela Man, David L. Singer, Michael G. Sowa, and Kan-Zhi Liu. Molecular mapping of periodontal tissues using infrared microspectroscopy. *BMC Medical Imaging*, 5:1–10, 2005.

[87] Vladimir Iancu, Magdalena Lidia Ciurea, and Mihai Draghici. Modeling of optical charging spectroscopy investigation of trapping phenomena in nanocrystalline porous silicon. *Journal of Applied Physics*, 94(1):216–223, 2003.

[88] Nathan Ida and Norbert Meyendorf. *Handbook of advanced nondestructive evaluation*, volume 10. Springer, 2019.

[89] Raid A. Ismail, Alwan M. Alwan, and Ahmed S. Ahmed. Preparation and characteristics study of nano-porous silicon uv photodetector. *Applied Nanoscience*, 7:9–15, 2017.

[90] Mile Ivanda, Svetozar Musić, Marijan Gotić, Aleksandra Turković, A. M. Tonejc, and Ozren Gamulin. The effects of crystal size on the raman spectra of nanophase tio_2. *Journal of Molecular Structure*, 480:641–644, 1999.

[91] Haneen D. Jabbar, Mohammed Jalal AbdulRazzaq, and Makram A. Fakhri. Synthesis porous silicon substrates using electrochemical etching method assisted by laser. In *AIP Conference Proceedings*, volume 2660, 2022.

[92] Jaroslaw Jakubowicz. Porous silicon formation by mechanical means. In *Handbook of Porous Silicon*, pages 3516–3526. Springer, 2014. doi: 10.1007/978-3-319-05744-6_9. URL https://link.springer.com/referenceworkentry/10.1007/978-3-319-05744-6_9.

[93] Nader Jalili and Karthik Laxminarayana. A review of atomic force microscopy imaging systems: Application to molecular metrology and biological sciences. *Mechatronics*, 14 (8):907–945, 2004.

[94] I. R. Jankov, I. D. Goldman, and Roberto Nunes Szente. Principles of the kelvin probe force microscopy. *Revista Brasileira de Ensino de Física*, 22:503–509, 2000.

[95] Karyn L. Jarvis, Timothy J. Barnes, and Clive A. Prestidge. Surface chemistry of porous silicon and implications for drug encapsulation and delivery applications. *Advances in Colloid and Interface Science*, 175:25–38, 2012.

[96] Ivan Jelínek, Tomáš Chvojka, Vladimír Vrkoslav, Jindřich Jindřich, Miroslav Lorenc, Daniel Nižňanský, Ivan Němec, Vladimír Král, and Juraj Dian. Nanostructured porous silicon—optical properties, surface modification and sensor applications. *Chimia*, 59(5): 222–222, 2005.

[97] Y. Q. Jia, L. Z. Zhang, J. S. Fu, B. R. Zhang, J. C. Mao, and G. G. Qin. Characterization of stain etched porous si with photoluminescence, electron paramagnetic resonance, and infrared absorption spectroscopy. *Journal of Applied Physics*, 74(12):7615–7617, 1993.

[98] Magdaléna Kadlečíková, Juraj Breza, L'ubomír Vančo, Miroslav Mikolášek, Michal Hubeňák, Juraj Racko, and Ján Greguš. Raman spectroscopy of porous silicon substrates. *Optik*, 174:347–353, 2018.

[99] Yoshihiko Kanemitsu, Takahiro Matsumoto, Toshiro Futagi, and Hidenori Mimura. Porous silicon: Microstructure, optical properties and application to light emitting diodes. In *Porous Silicon*, pages 363–392. World Scientific, 1994.

[100] Samra Kanwal, Chun Yun Kee, and L. K. Ang. Analytical model of space charge current for a cylindrical porous trap-limited dielectric. *arXiv preprint arXiv:2307.16136*, 2023.

[101] Farshid Karbassian. Porous silicon. In *Porosity: Process, technologies and applications*. IntechOpen, 2018.

[102] Farshid Karbassian, Shima Rajabali, Abbas Chimeh, Shams Mohajerzadeh, and Ebrahim Asl-Soleimani. Luminescent porous silicon prepared by reactive ion etching. *Journal of Physics D: Applied Physics*, 47(38):385103, 2014.

[103] M. Khardani, M. Bouaïcha, W. Dimassi, M. Zribi, S. Aouida, and B. Bessaïs. Electrical conductivity of free-standing mesoporous silicon thin films. *Thin Solid Films*, 495(1-2): 243–245, 2006.

[104] Charles Kittel and Paul McEuen. *Introduction to solid state physics*. John Wiley & Sons, 2018.

[105] Krisztian Kordas, Andrea Edit Pap, Szabolcs Beke, and Seppo Leppävuori. Optical properties of porous silicon. part i: Fabrication and investigation of single layers. *Optical Materials*, 25(3):251–255, 2004.

[106] Simona Kouteva-Arguirova, Tz Arguirov, Dirk Wolffframm, and Jürgen Reif. Influence of local heating on micro-raman spectroscopy of silicon. *Journal of Applied Physics*, 94(8): 4946–4949, 2003.

[107] Andras Kovacs, Dirk Meister, and Ulrich Mescheder. Investigation of humidity adsorption in porous silicon layers. *physica status solidi (a)*, 206(6):1343–1347, 2009. doi: 10.1002/pssa.200824521.

[108] Hideki Koyama and Philippe M. Fauchet. Very large continuous-wave-laser-induced optical absorption in porous silicon films: Evidence for thermal effects. *Applied Physics Letters*, 73(22):3259–3261, 1998.

[109] Hideki Koyama and Philippe M. Fauchet. Laser-induced thermal effects on the optical properties of free-standing porous silicon films. *Journal of Applied Physics*, 87(4):1788–1794, 2000.

[110] D. Nanda Gopala Krishna and John Philip. Review on surface-characterization applications of x-ray photoelectron spectroscopy (xps): Recent developments and challenges. *Applied Surface Science Advances*, 12:100332, 2022.

[111] K. Kulathuraan, K. Mohanraj, and B. Natarajan. Structural, optical and electrical characterization of nanostructured porous silicon: Effect of current density. *Spectrochimica Acta Part A: Molecular and Biomolecular Spectroscopy*, 152:51–57, 2016.

[112] A. K. Kulkarni and B. M. Post. Degradations in the electrical and structural characteristics of schottky diodes and ohmic contacts to gaas due to thermal aging. *Thin Solid Films*, 123 (1):1–8, 1985.

[113] Pushpendra Kumar and Patrick Huber. Effect of etching parameter on pore size and porosity of electrochemically formed nanoporous silicon. *Journal of Nanomaterials*, 2007: 089718, 2007.

[114] Pushpendra Kumar, Peter Lemmens, Manash Ghosh, Frank Ludwig, and Meinhard Schilling. Effect of hf concentration on physical and electronic properties of electrochemically formed nanoporous silicon. *Journal of Nanomaterials*, 2009:728957, 2009.

[115] Orest Kuntyi, Galyna Zozulya, and Mariana Shepida. Porous silicon formation by electrochemical etching. *Advances in Materials Science and Engineering*, 2022:1482877, 2022.

[116] B. Kurbanova, D. Chakraborty, A. Abdullaev, A. Shamatova, O. Makukha, A. Belarouci, V. Lysenko, A. Azarov, A. Kuznetsov, Y. Wang, et al. Multiscale phonon thermal transport in nano-porous silicon. *Applied Physics Letters*, 124(25), 2024.

[117] Julie Lascaud, Thomas Defforge, Dominique Certon, Damien Valente, and Gaël Gautier. In-depth porosity control of mesoporous silicon layers by an anodization current adjustment. *Journal of Applied Physics*, 122(21), 2017.

[118] J.-F. Lataste. Electrical resistivity for the evaluation of reinforced concrete structures. In *Non-destructive evaluation of reinforced concrete structures*, pages 243–275. Elsevier, 2010.

[119] Jonathan Lawrence. A comparative analysis of the wear characteristics of glazes generated on the ordinary portland cement surface of concrete by means of co2 and high power diode laser radiation. *Wear*, 257(5–6):590–598, 2004.

[120] S. Lazarouk, P. Jaguiro, S. Katsouba, G. Maiello, S. La Monica, G. Masini, E. Proverbio, and A. Ferrari. Visual determination of thickness and porosity of porous silicon layers. *Thin Solid Films*, 297(1–2):97–101, 1997.

[121] Eric Le Ru and Pablo Etchegoin. *Principles of surface-enhanced Raman spectroscopy: and related plasmonic effects*. Elsevier, 2008.

[122] Ching-Ting Lee, Yi-Fu Chen, and Chun-Hung Lin. Phase-separated si nanoclusters from si oxide matrix grown by laser-assisted chemical vapor deposition. *Nanotechnology*, 20 (2):025702, 2008. doi: 10.1088/0957-4484/20/02/025702.

[123] V. Lehmann, F. Hofmann, F. Möller, and U. Grüning. Resistivity of porous silicon: A surface effect. *Thin Solid Films*, 255(1–2):20–22, 1995.

[124] F. Leisenberger, R. Duschek, R. Czaputa, F. P. Netzer, G. Beamson, and J. A. D. Matthew. A high resolution xps study of a complex insulator: The case of porous silicon. *Applied Surface Science*, 108(2):273–281, 1997.

[125] Aleksandr S. Lenshin, Yaroslav A. Peshkov, Konstantin A. Barkov, Margarita V. Grechkina, Anatoliy N. Lukin, Sergey V. Kannykin, Dmitriy A. Minakov, and Olga V. Chernousova. Features of the composition and photoluminescent properties of porous silicon depending on its porosity index. *Coatings*, 13(2):385, 2023. doi: 10.3390/coatings13020385.

[126] Yaoping Liu, Han Xu, Lingqian Zhang, and Wei Wang. Microfabrication of micropore array for cell separation and cell assay. *Micromachines*, 9(12):620, 2018.

[127] Live Science Staff. Secrets of the synchrotron. https://www.livescience.com/secrets-of-the-synchrotron.html, n.d. Accessed: 03 March 2025.

[128] D. J. Lockwood. Optical properties of porous silicon. *Solid State Communications*, 92 (1-2):101–112, 1994. doi: 10.1016/0038-1098(94)90862-X.

[129] A. Loni, L. T. Canham, M. G. Berger, R. Arens-Fischer, H. Munder, H. Luth, H. F. Arrand, and T. M. Benson. Porous silicon multilayer optical waveguides. *Thin Solid Films*, 276 (1-2):143–146, 1996.

[130] Armando Loni et al. Porous silicon formation by anodization. *Handbook of Porous Silicon*, 1, 2014.

[131] Dusan Losic and Abel Santos. *Electrochemically engineered nanoporous materials*, volume 220. Springer, 2015.

[132] Jingmei Lu and Xuan Cheng. Effect of etching time on porous silicon formation. *ECS Transactions*, 11(11):9, 2008.

[133] Frieder Lucklum, Alexander Schwaiger, and Bernhard Jakoby. Development and investigation of thermal devices on fully porous silicon substrates. *IEEE Sensors Journal*, 14(4): 992–997, 2013.

[134] G. Lucovsky, J. Yang, S. S. Chao, J. E. Tyler, and W. Czubatyj. Oxygen-bonding environments in glow-discharge-deposited amorphous silicon-hydrogen alloy films. *Physical Review B*, 28(6):3225, 1983.

[135] V. A. Makara, V. A. Odarych, O. V. Vakulenko, and O. I. Dacenko. Ellipsometric studies of porous silicon. *Thin Solid Films*, 342(1–2):230–237, 1999.

[136] Raúl J. Martín-Palma, Miguel Manso-Silván, and Vicente Torres-Costa. Biomedical applications of nanostructured porous silicon: A review. *Journal of Nanophotonics*, 4(1): 042502, 2010.

[137] Narasimha Rao Mavilla, Chetan Singh Solanki, and Juzer Vasi. Raman spectroscopy of silicon-nanocrystals fabricated by inductively coupled plasma chemical vapor deposition. *Physica E: Low-Dimensional Systems and Nanostructures*, 52:59–64, 2013.

[138] Douglas B. Mawhinney, John A. Glass, and John T. Yates. Ftir study of the oxidation of porous silicon. *The Journal of Physical Chemistry B*, 101(7):1202–1206, 1997.

[139] Steven J. P. McInnes and Rachel D. Lowe. Biomedical uses of porous silicon. *Electrochemically Engineered Nanoporous Materials: Methods, Properties and Applications*, pages 117–162, 2015.

[140] Graeme McNay, David Eustace, W. Ewen Smith, Karen Faulds, and Duncan Graham. Surface-enhanced raman scattering (sers) and surface-enhanced resonance raman scattering (serrs): A review of applications. *Applied Spectroscopy*, 65(8):825–837, 2011.

[141] Simon Meaney, A. V. Pan, Antony Jones, and S. A. Fedoseev. Partial carrier freeze-out at the $laalo_3$/$srtio_3$ oxide interface. *APL Materials*, 7(10):101104, 2019.

[142] Wilhelm Melitz, Jian Shen, Andrew C. Kummel, and Sangyeob Lee. Kelvin probe force microscopy and its application. *Surface Science Reports*, 66(1):1–27, 2011.

[143] Samuel Ménard, Angélique Fèvre, Jérôme Billoue, and Gael Gautier. P-type porous silicon resistivity and carrier transport. *Journal of Applied Physics*, 118(10), 2015.

[144] Joseph R. Michael, Craig Y. Nakakura, Tomasz Garbowski, Anna Lena Eberle, Thomas Kemen, and Dirk Zeidler. High-throughput sem via multi-beam sem: Applications in materials science. *Microscopy and Microanalysis*, 21(S3):697–698, 2015.

[145] Settimio Mobilio, Federico Boscherini, Carlo Meneghini, et al. *Synchrotron radiation*. Springer, 2016.

[146] K. Mongkolsuttirat and J. Buajarern. Uncertainty evaluation of crystallite size measurements of nanoparticles using x-ray diffraction analysis (xrd). *Journal of Physics: Conference Series*, 1719(1):012054, 2021.

[147] F. J. Morin and J. P. Maita. Electrical properties of silicon containing arsenic and boron. *Physical Review*, 96(1):28, 1954.

[148] Riam Abu Much, Prakash Natarajan, Awad Shalabny, Sumesh Sadhujan, Sherina Harilal, and Muhammad Y. Bashouti. Heterojunction-based hybrid silicon nanowires solar cell. In *Solar Cells*. IntechOpen, 2019.

[149] Uday Muhsin Nayef and Mohammed Waleed Muayad. Typical morphological properties of porous silicon. *International Journal of Basic and Applied Sciences*, 13(2), 2013.

[150] H. Ohji, P. J. French, and K. Tsutsumi. Fabrication of mechanical structures in p-type silicon using electrochemical etching. *Sensors and Actuators A: Physical*, 82(1–3):254–258, 2000.

[151] D. J. Olego, H. Baumgart, and G. K. Celler. Strains in si-on-sio_2 structures formed by oxygen implantation: Raman scattering characterization. *Applied Physics Letters*, 52(6): 483–485, 1988.

[152] Andrea E. Pap, Kriztián Kordás, Geza Tóth, Juhani Levoska, Antti Uusimäki, Jouko Vähäkangas, Seppo Leppävuori, and T. F. George. Thermal oxidation of porous silicon: Study on structure. *Applied Physics Letters*, 86(4), 2005.

[153] Andrea Edit Pap, Krisztián Kordás, Jouko Vähäkangas, Antti Uusimäki, Seppo Leppävuori, Laurent Pilon, and Sándor Szatmari. Optical properties of porous silicon. part iii: Comparison of experimental and theoretical results. *Optical Materials*, 28(5):506–513, 2006.

[154] V. P. Parkhutik, L. K. Glinenko, and V. A. Labunov. Kinetics and mechanism of porous layer growth during n-type silicon anodization in hf solution. *Surface Technology*, 20(3): 265–277, 1983.

[155] Alexander V. Pavlikov, Pavel A. Forsh, Sergey E. Svyakhovskiy, Anna N. Matsukatova, Ekaterina A. Forsh, Andrey G. Kazanskii, and Pavel K. Kashkarov. Giant enhancement of free charge carrier concentration in boron-doped amorphous hydrogenated silicon under femtosecond laser crystallization. *Applied Physics Letters*, 113(20):201903, 2018.

[156] Atzin David Ruíz Pérez, M. B. de la Mora, J. L. Benítez, R. Castañeda-Guzmán, Jorge Alejandro Reyes-Esqueda, and M. Villagrán-Muniz. In situ study of porous silicon thin films thermal oxidation by pulsed laser photoacoustics. *Semiconductor Science and Technology*, 33(8):085001, 2018. doi: 10.1088/1361-6641/aad009.

[157] Monuko du Plessis. A decade of porous silicon as nano-explosive material. *Propellants, Explosives, Pyrotechnics*, 39(3):348–364, 2014.

[158] Gustavo Prado, Jorge C. L. Arthuzzi, Gabriel L. Oses, Flavia Callefo, Lara Maldanis, Paula Sucerquia, Bruno Becker-Kerber, Guilherme R. Romero, Francy R. Quiroz-Valle, and Douglas Galante. Synchrotron radiation in palaeontological investigations: Examples from brazilian fossils and its potential to south american palaeontology. *Journal of South American Earth Sciences*, 108:102973, 2021.

[159] E. Proverbio and A. Ferrari. Visual determination of thickness and porosity of porous silicon layers. *Thin Solid Films*, 297:97–101, 1997.

[160] Shuang Qiao, Yu-Ning Wu, Xiaolan Yan, Bartomeu Monserrat, Su-Huai Wei, and Bing Huang. Temperature effect on charge-state transition levels of defects in semiconductors. *Physical Review B*, 105(11):115201, 2022.

[161] M. Ben Rabha, M. Hajji, S. Belhadj Mohamed, A. Hajjaji, M. Gaidi, H. Ezzaouia, and B. Bessais. Stain-etched porous silicon nanostructures for multicrystalline silicon-based solar cells. *The European Physical Journal - Applied Physics*, 57(2):21301, 2012.

[162] Henry H. Radamson, Anders Hallén, Ilya Sychugov, and Alexander Azarov. *Analytical methods and instruments for micro-and nanomaterials*. Springer, 2023.

[163] Martha Ramesh and H. S. Nagaraja. The effect of etching time on structural properties of porous silicon at room temperature. *Materials Today: Proceedings*, 3(6):2085–2090, 2016.

[164] Martha Ramesh and H. S. Nagaraja. Effect of current density on morphological, structural, and optical properties of porous silicon. *Materials Today Chemistry*, 3:10–14, 2017.

[165] A. Ramzy, K. Omar, Z. Hassan, and H. Abu Hassan. Laser effects on porous silicon synthesis by photoelectrochemical etching process. *Optoelectronics and Advanced Materials - Rapid Communications*, 3(11):1190–1194, 2009.

[166] Muna E. Raypah, Anas A. Ahmed, and Ahmad Fairuz Omar. Application of porous materials and structures for improving optical and thermal performance of inorganic and organic light-emitting diodes: A review. *Sensors and Actuators A: Physical*, 347:113966, 2022.

[167] Ilaria Rea, Antigone Marino, Mario Iodice, Giuseppe Coppola, Ivo Rendina, and Luca De Stefano. A porous silicon bragg grating waveguide by direct laser writing. *Journal of Physics: Condensed Matter*, 20(36):365203, 2008.

[168] Seyed Javad Rezvani, Nicola Pinto, Emanuele Enrico, L. D'Ortenzi, A. Chiodoni, and Luca Boarino. Thermally activated tunnelling in porous silicon nanowires with embedded si quantum dots. *Journal of Physics D: Applied Physics*, 49(10):105104, 2016.

[169] Lukas Janos Richter, Ulrich Ross, Michael Seibt, and Jürgen Ihlemann. Excimer laser surface patterning for photoluminescence enhancement of silicon nanocrystals. *Photonics*, 10(4):358, 2023.

[170] Mark Rodder. Increased resistance in p-type poly-si resistors by thermal anneal reduction interface charge. *IEEE Electron Device Letters*, 12(4):160–162, 1991.

[171] Jon Rodriguez, Hyun-Cheol Shin, Eric Stava, Paul V. Gwozdz, Minrui Yu, José R. Sánchez Pérez, Max G. Lagally, and Robert H. Blick. Ablating nanoscale pores in crystalline quartz using laser-induced micro-plasmas in tri-layer structures. *Optical Materials Express*, 10(8):1991–1998, 2020.

[172] K. Roodenko, I. A. Goldthorpe, P. C. McIntyre, and Y. J. Chabal. Modified phonon confinement model for raman spectroscopy of nanostructured materials. *Physical Review B: Condensed Matter and Materials Physics*, 82(11):115210, 2010.

[173] Paul Rostron, Safa Gaber, and Dina Gaber. Raman spectroscopy: Review. *Laser*, 21:24, 2016.

[174] C. Rotaru, N. Tomozeiu, and G. Craciun. Optical properties of porous silicon thin films. *Journal of Molecular Structure*, 480:293–296, 1999.

[175] Jean Rouquerol, David Avnir, Craig W. Fairbridge, Douglas H. Everett, J. M. Haynes, Nicola Pernicone, John D. F. Ramsay, Kenneth Stafford William Sing, and Klaus K. Unger. Recommendations for the characterization of porous solids (technical report). *Pure and Applied Chemistry*, 66(8):1739–1758, 1994.

[176] Royal Society of Chemistry. Silicon - element information, properties and uses | periodic table. https://www.rsc.org/periodic-table/element/14/silicon, 2024. Accessed: October 20, 2024.

[177] M. Saadoun, N. Mliki, H. Kaabi, K. Daoudi, B. Bessais, H. Ezzaouia, and R. Bennaceur. Vapour-etching-based porous silicon: A new approach. *Thin Solid Films*, 405(1-2):29–34, 2002.

[178] R. Sabet-Dariani and D. Haneman. Heat-treatment effects on porous silicon. *Journal of Applied Physics*, 76(2):1346–1348, 1994.

[179] Michael J. Sailor. *Porous silicon in practice: Preparation, characterization and applications*. John Wiley & Sons, 2012.

[180] Walter Jaimes Salcedo, F. J. Ramirez Fernandez, and Elisabete Galeazzo. Structural characterization of photoluminescent porous silicon with ftir spectroscopy. *Brazilian Journal of Physics*, 27:158–161, 1997.

[181] Walter Jaimes Salcedo, Francisco J. Ramirez Fernandez, and Joel C. Rubim. Changes in the porous silicon structure induced by laser radiation. *Journal of Raman Spectroscopy*, 32(3):151–157, 2001.

[182] Rosari Saleh and N. H. Nickel. The influence of boron concentrations on structural properties in disordered silicon films. *Applied Surface Science*, 254(2):580–585, 2007.

[183] T. A. Saleh. Pharmaceutical characterization and detection using surface-enhanced raman scattering. *International Archives of Clinical Pharmacology*, 3(10), 2017.

[184] Christian Sämann, Jürgen R. Köhler, Morris Dahlinger, Markus B. Schubert, and Jürgen H. Werner. Pulsed laser porosification of silicon thin films. *Materials*, 9(7):509, 2016.

[185] Abel Santos and Tushar Kumeria. Electrochemical etching methods for producing porous silicon. *Electrochemically Engineered Nanoporous Materials: Methods, Properties and Applications*, pages 1–36, 2015.

[186] Shwetha Satish. Structural characterization of fibre foam materials using tomographic data, 2024.

[187] Sebastian P. Scheeler, Simon Ullrich, Stefan Kudera, and Claudia Pacholski. Fabrication of porous silicon by metal-assisted etching using highly ordered gold nanoparticle arrays. *Nanoscale Research Letters*, 7:1–7, 2012.

[188] Martin Schnell, Monika Goikoetxea, Iban Amenabar, P. Scott Carney, and Rainer Hillenbrand. Rapid infrared spectroscopic nanoimaging with nano-ftir holography. *ACS Photonics*, 7(10):2878–2885, 2020.

[189] P. C. Searson, J. M. Macaulay, and S. M. Prokes. The formation, morphology, and optical properties of porous silicon structures. *Journal of the Electrochemical Society*, 139(11): 3373, 1992.

[190] Antonio Sellitto, David Jou, and Vito Antonio Cimmelli. A phenomenological study of pore-size dependent thermal conductivity of porous silicon. *Acta Applicandae Mathematicae*, 122:435–445, 2012.

[191] Mathias Senoner and Wolfgang E. S. Unger. Sims imaging of the nanoworld: Applications in science and technology. *Journal of Analytical Atomic Spectrometry*, 27(7):1050–1068, 2012.

[192] T. K. Sham. Nanoparticles and nanowires: Synchrotron spectroscopy studies. *International Journal of Nanotechnology*, 5(9–12):1194–1246, 2008.

[193] H. R. Shanks, P. D. Maycock, P. H. Sidles, and G. C. Danielson. Thermal conductivity of silicon from 300 to 1400 k. *Physical Review*, 130(5):1743, 1963.

[194] F. G. Shi, K. Okuyama, et al. Electrical conduction in porous silicon: Temperature dependence. *Microelectronics Journal*, 31(3):187–191, 2000.

[195] *Shimadzu Fourier transform infrared spectrophotometer IRAffinity-1S instruction manual*. Shimadzu, 2013. Published August 2013.

[196] Kebede W. Shinato, Feifei Huang, and Ying Jin. Principle and application of atomic force microscopy (afm) for nanoscale investigation of metal corrosion. *Corrosion Reviews*, 38 (5):423–432, 2020.

[197] Michael Shur and Jasprit Singh. Physics of semiconductor devices, 1990.

[198] Vasyl Shvalya, Gregor Filipič, Janez Zavašnik, Ibrahim Abdulhalim, and Uroš Cvelbar. Surface-enhanced raman spectroscopy for chemical and biological sensing using nanoplasmonics: The relevance of interparticle spacing and surface morphology. *Applied Physics Reviews*, 7(3), 2020.

[199] R. S. Smerdov, A. S. Mustafaev, Yu M. Spivak, and V. A. Moshnikov. Porous silicon and graphene-based composite nanostructures for plasma energy systems. In *Proceedings of the 45th EPS Conference on Plasma Physics*, pages 921–924, 2018.

[200] Christian Smit, R. A. C. M. M. Van Swaaij, H. Donker, A. M. H. N. Petit, W. M. M. Kessels, and M. C. M. Van de Sanden. Determining the material structure of microcrystalline silicon from raman spectra. *Journal of Applied Physics*, 94(5):3582–3588, 2003.

[201] David A. Strubbe, Eric C. Johlin, Timothy R. Kirkpatrick, Tonio Buonassisi, and Jeffrey C. Grossman. Stress effects on the raman spectrum of an amorphous material: Theory and experiment on a-si:h. *Physical Review B*, 92(24):241202, 2015.

[202] Zhifeng Sui, Patrick P. Leong, Irving P. Herman, Gregg S. Higashi, and Henryk Temkin. Raman analysis of light-emitting porous silicon. *Applied Physics Letters*, 60(17):2086–2088, 1992.

[203] A. A. Sulaimana, M. M. Alyas, and A. M. Muhammed. Porous silicon (p-type) prepared by electrochemical etching and study of structure and morphology properties and effect of neutron irradiation. *Digest Journal of Nanomaterials and Biostructures*, 15:9–14, 2020.

[204] Peng Sun, Ming Hu, Ming-Da Li, and Shuang-Yun Ma. Microstructure, electrical and gas sensing properties of meso-porous silicon and macro-porous silicon. *Acta Physico-Chimica Sinica*, 28(2):489–493, 2012.

[205] R Suryana, DK Sandi, and O Nakatsuka. The morphological study of porous silicon formed by electrochemical anodization method. In *IOP Conference Series: Materials Science and Engineering*, volume 333, page 012034. IOP Publishing, 2018.

[206] Risa Suryana, Tasya Az-Zahra Setyorini, and Markus Diantoro. The formation of porous silicon using vertical photoelectrochemical method with laser energy variation. *Diffusion Foundations and Materials Applications*, 36:47–54, 2024.

[207] Simon M. Sze, Yiming Li, and Kwok K. Ng. *Physics of semiconductor devices*. John Wiley & Sons, 2021.

[208] Thermo Fisher Scientific. Silicon - element information, properties and uses | periodic table, n.d. URL https://www.thermofisher.com/uk/en/home/materials-science/learning-center/periodic-table/metalloid/silicon.html. Accessed: November 17, 2024.

[209] V. Yu Timoshenko, Th. Dittrich, I. Sieber, J. Rappich, B. V. Kamenev, and P. K. Kashkarov. Laser-induced melting of porous silicon. *Physica Status Solidi (a)*, 182(1):325–330, 2000.

[210] A. C. To, J. Tao, Mesut Kirca, and L. Schalk. Ligament and joint sizes govern softening in nanoporous aluminum. *Applied Physics Letters*, 98(5), 2011.

[211] Vicente Torres-Costa and R. J. Martín-Palma. Application of nanostructured porous silicon in the field of optics: A review. *Journal of Materials Science*, 45:2823–2838, 2010.

[212] L. Tsybeskov and P. M. Fauchet. Correlation between photoluminescence and surface species in porous silicon: Low-temperature annealing. *Applied Physics Letters*, 64(15): 1983–1985, 1994.

[213] David Tuschel. Why are the raman spectra of crystalline and amorphous solids different? *MJH Life Sciences*, 2017.

[214] J. Tuura, M. Björkqvist, J. Salonen, and V. P. Lehto. Long-term stability of thermally-carbonized porous silicon humidity sensor. *MRS Online Proceedings Library (OPL)*, 876: R8–8, 2005. doi: 10.1557/PROC-0876-R08-08.

[215] UCL Department of Chemistry. Crystallite size and strain, n.d. URL http://pd.chem.ucl.ac.uk/pdnn/peaks/size.htm. Accessed: November 15, 2024.

[216] A. Uhlir. Electrolytic shaping of germanium and silicon. *Bell System Technical Journal*, 35:333–347, 1956.

[217] Aliyaa A. Urabe, Uday M. Nayef, and Randa Kamel. Influence study of etching time for porous silicon on morphological, optical, electrical and spectral responsivity properties. *Al-Mustansiriyah Journal of Science*, 34(2):113–120, 2023.

[218] K. Valalaki and A. G. Nassiopoulou. Low thermal conductivity porous si at cryogenic temperatures for cooling applications. *Journal of Physics D: Applied Physics*, 46(29): 295101, 2013.

[219] Alix Valdenaire, Alaa Eldin Giba, Mathieu Stoffel, Xavier Devaux, Loïc Foussat, Jean-Marie Poumirol, Caroline Bonafos, Sonia Guehairia, Rémi Demoulin, Etienne Talbot, et al. Heavily doped si nanocrystals formed in p-(sio/sio_2) multilayers: A promising route for si-based infrared plasmonics. *ACS Applied Nano Materials*, 6(5):3312–3320, 2023.

[220] David Van der Heggen, Jonas J. Joos, and Philippe F. Smet. Importance of evaluating the intensity dependency of the quantum efficiency: Impact on leds and persistent phosphors. *ACS Photonics*, 5(11):4529–4537, 2018.

[221] M. Vashista and S. Paul. Correlation between full width at half maximum (fwhm) of xrd peak with residual stress on ground surfaces. *Philosophical Magazine*, 92(33):4194–4204, 2012.

[222] L. Vazquez and J. M. Sanchez. Influence of titanium diboride additions on the sintering behavior of nanoporous fumed silica composites. *Composites Part B: Engineering*, 90: 416–423, 2016.

[223] Didac Vega, Jordi Reina, and Ángel Rodríguez. Macroporous silicon photonic crystals for gas sensing. In *2013 Spanish Conference on Electron Devices*, pages 143–146. IEEE, 2013.

[224] Toshimasa Wadayama, Tuyoshi Arigane, and Aritada Hatta. In-situ photoluminescence, raman, and ir spectral study of porous silicon during exposure to thermoelectrons/h atoms,/h_2o and/o_3. *Materials Transactions*, 44(7):1394–1399, 2003. doi: 10.2320/matertrans.44.1394.

[225] Ekram A. Wahabaalla, E. M. El-Menyawy, T. Abdallah, and G. M. Youssef. Improving the photoelectrical conversion efficiency of silicon solar cells using zno: Al/porous silicon double antireflective layers. *Applied Physics A*, 125(12):842, 2019. doi: 10.1007/s00339-019-3128-5.

[226] Haiyang Wang, Yaozhuo Xu, Xinhong Yu, Rubo Xing, Jiangang Liu, and Yanchun Han. Structure and morphology control in thin films of conjugated polymers for an improved charge transport. *Polymers*, 5:1272–1324, 2013.

[227] Man Wang, Wei-Cheng Ou, and Zhen-Tao Yu. Porous silicon-supported catalytic materials for energy conversion and storage. *ChemSusChem*, 17(1):e202401459, 2024. doi: 10.1002/cssc.202401459.

[228] Man Wang, Wei-Cheng Ou, and Zhen-Tao Yu. Porous silicon-supported catalytic materials for energy conversion and storage. *ChemSusChem*, 18(3):e202401459, 2025.

[229] Xiao Wang and Ananth Dodabalapur. Trapped carrier scattering and charge transport in high-mobility amorphous metal oxide thin-film transistors. *Annalen der Physik*, 530(12):1800341, 2018.

[230] Y. G. Wang, B. S. Zou, T. H. Wang, N. Wang, Y. Cai, Y. F. Chan, and S. X. Zhou. I–v characteristics of schottky contacts of semiconducting znse nanowires and gold electrodes. *Nanotechnology*, 17(9):2420, 2006.

[231] Yuliang Wang, Tongda Lu, Xiaolai Li, and Huimin Wang. Automated image segmentation-assisted flattening of atomic force microscopy images. *Beilstein Journal of Nanotechnology*, 9:975–985, 2018.

[232] Jeffrey M. Weisse, Amy M. Marconnet, Dong Rip Kim, Pratap M. Rao, Matthew A. Panzer, Kenneth E. Goodson, and Xiaolin Zheng. Thermal conductivity in porous silicon nanowire arrays. *Nanoscale Research Letters*, 7:1–5, 2012.

[233] Philip Willmott. *An introduction to synchrotron radiation: Techniques and applications*. John Wiley & Sons, 2019.

[234] R. F. Wood, C. W. White, and R. T. Young. Laser processing of semiconductors: An overview. *Semiconductors and Semimetals*, 23:1–41, 1984.

[235] Dongsheng Xu, Lin Sun, Hongliang Li, Lei Zhang, Guolin Guo, Xinsheng Zhao, and Linlin Gui. Hydrolysis and silanization of the hydrosilicon surface of freshly prepared porous silicon by an amine catalytic reaction. *New Journal of Chemistry*, 27:300–306, 2003.

[236] Junwen Xu, Shuang Liu, Yapei Yang, Jiacheng Li, Chunhui Tian, Lina Guo, Shangjian Zhang, Yong Liu, and Zhiyong Zhong. Preparation of porous silicon by electrochemical etching methods and its morphological and optical properties. *International Journal of Electrochemical Science*, 14(6):5188–5199, 2019.

[237] Suriani Yaakob, Mohamad Abu Bakar, Jamil Ismail, N. H. H. A. Bakar, and Kamarulazizi Ibrahim. The formation and morphology of highly doped n-type porous silicon: Effect of short etching time at high current density and evidence of simultaneous chemical and electrochemical dissolutions. *Journal of Physical Science*, 23(2):17–31, 2012.

[238] D. T. Yan and N. G. Galkin. Mechanism of luminescence from porous silicon. In *Asia-Pacific Conference on Fundamental Problems of Opto-and Microelectronics*, volume 10176, pages 514–523. SPIE, 2016.

[239] C. C. Yang and S. Li. Size-dependent raman red shifts of semiconductor nanocrystals. *The Journal of Physical Chemistry B*, 112(45):14193–14197, 2008.

[240] Xi Yang, Fengshuo Xi, Xiuhua Chen, Shaoyuan Li, Xiaohan Wan, Wenhui Ma, Peng Dong, Jianguo Duan, and Yuanchih Chang. Porous silicon fabrication and surface cracking behavior research based on anodic electrochemical etching. *Fuel Cells*, 21(1):52–57, 2021.

[241] S. Zairi, C. Martelet, N. Jaffrezic-Renault, F. Vocanson, R. Lamartine, R. M'gaïeth, H. Maâref, and M. Gamoudi. p-type porous-silicon transducer for cation detection: Effect of the porosity, pore morphology, temperature, and ion valency on the sensor response and generalisation of the nernst equation. *Applied Physics A*, 73:585–593, 2001.

[242] XG Zhang. Morphology and formation mechanisms of porous silicon. *Journal of the Electrochemical Society*, 151(1):C69, 2003.